

ISTANBUL TECHNICAL UNIVERSITY ★ GRADUATE SCHOOL OF SCIENCE
ENGINEERING AND TECHNOLOGY

**PRODUCTION AND CHARACTERIZATION OF SPARK PLASMA
SINTERED BORON CARBIDE CERAMIC COMPOSITES SUITABLE
FOR BALLISTIC USE**



Ph.D. THESIS

Burcu APAK GÜLSEVER

Metallurgical and Materials Engineering Department

Metallurgical and Materials Engineering Programme

FEBRUARY 2018

ISTANBUL TECHNICAL UNIVERSITY ★ GRADUATE SCHOOL OF SCIENCE
ENGINEERING AND TECHNOLOGY

**PRODUCTION AND CHARACTERIZATION OF SPARK PLASMA
SINTERED BORON CARBIDE CERAMIC COMPOSITES SUITABLE
FOR BALLISTIC USE**

Ph.D. THESIS

Burcu APAK GÜLSEVER
(506112402)

Metallurgical and Materials Engineering Department

Metallurgical and Materials Engineering Programme

Thesis Advisor: Prof. Dr. Filiz ÇINAR ŞAHİN

FEBRUARY 2018

İSTANBUL TEKNİK ÜNİVERSİTESİ ★ FEN BİLİMLERİ ENSTİTÜSÜ

**BALİSTİK KULLANIMA UYGUN BOR KARBÜR SERAMİK
KOMPOZİTLERİNİN SPARK PLAZMA SİNERLEME YÖNTEMİ İLE
ÜRETİMİ VE KARAKTERİZASYONU**

Doktora TEZİ

**Burcu APAK GÜLSEVER
(506112402)**

Metalurji ve Malzeme Mühendisliği Anabilim Dalı

Metalurji ve Malzeme Mühendisliği Programı

Tez Danışmanı: Prof. Dr. Filiz ÇINAR ŞAHİN

ŞUBAT 2018

Burcu APAK GÜLSEVER, a Ph.D. student of ITU Graduate School of Science Engineering and Technology student ID 506112402, successfully defended the thesis/dissertation entitled “Production and Characterization of Spark Plasma Sintered Boron Carbide Ceramic Composites Suitable for Ballistic Use”, which she prepared after fulfilling the requirements specified in the associated legislations, before the jury whose signatures are below.

Thesis Advisor : **Prof. Dr. Filiz ÇINAR ŞAHİN**
İstanbul Technical University

Jury Members : **Prof. Dr. Onuralp YÜCEL**
İstanbul Technical University

Prof. Dr. Gültekin GÖLLER
İstanbul Technical University

Prof. Dr. Nilgün KUŞKONMAZ
Yildiz Technical University

Prof. Dr. Gökhan ORHAN
İstanbul University

Date of Submission : 05 February 2018

Date of Defense : 27 February 2018





To my beloved family,



FOREWORD

It is a great pleasure for me to express my deepest gratitude;

To my dearest adviser, Prof. Dr. Filiz ÇINAR ŞAHİN, who has undertaken the administration of my doctoral thesis work. She means more than a supervisor to me. I am always trying to walk through the path that she leads me through.

To my respectable professors, Prof. Dr. Onuralp YÜCEL and Prof. Dr. Gültekin GÖLLER, for giving valuable advices and letting me use their laboratory facilities.

To my precious colleagues, Dr. Meral CENGİZ, Dr. Mehtap Deniz AKARSU, Met. Eng. MSc. Seyran SARIDAŞ, Met Eng. MSc. Esin ALYAZ KORKMAZ, Asst. Barış YAVAŞ, Met. Eng. MSc. Can Burak DANIŞMAN, Met. Eng. MSc. Burak Çağrı OCAK, for their support and help.

To Tech. Hüseyin SEZER who has been very helpful during my characterization stages.

To my beloved mother, Binnur APAK, for her unconditional love, patience and care and my dear father, Sudi APAK who inspired me not to give up with his endless support. I am always proud of being their daughter. They made possible everything I wanted, all my life long.

To my unique spouse, Onur GÜLSEVER, who has always reminded the strength within me to finish my thesis.

To TUBITAK for their financial support within the scope of 213M163 coded “The Optimization of Single Step Spark Plasma Sintered Various Boron Carbide – Metal Composites for Ballistic and Nuclear Use” named project.

I am very thankful. Without them, this thesis would be impossible to finish.

February, 2018

Burcu APAK GÜLSEVER
Met. Eng. MSc.



TABLE OF CONTENTS

	<u>Page</u>
FOREWORD	ix
TABLE OF CONTENTS	xi
ABBREVIATIONS	xv
SYMBOLS	xvii
LIST OF TABLES	xix
LIST OF FIGURES	xxi
SUMMARY	xxix
ÖZET	xxxiii
1. INTRODUCTION	1
2. BORON CARBIDE	5
2.1 Crystal Structure of Boron Carbide.....	6
2.2 Characteristics and Properties of Boron Carbide	7
2.3 Applications of Boron Carbide	8
2.3.1 Boron carbide as an armour material	9
2.4 Production of Boron Carbide	12
2.4.1 Carbothermal reduction of boron oxide	12
2.4.2 Magnesiothermic reduction of boron oxide	13
2.4.3 Synthesis from elements	14
3. SINTERING	17
3.1 The Sintering Process	18
3.2 Thermodynamics and Stages of Sintering.....	20
3.3 Kinetics and Mechanisms of Sintering.....	23
3.3.1 Solid state sintering	24
3.3.2 Liquid phase sintering	26
3.4 Sintering Techniques	28
3.4.1 Hot pressing	29
3.4.2 Hot isostatic pressing	32
3.4.3 Spark plasma sintering	34
3.4.3.1 Processing parameters of SPS	37
3.4.3.2 Comparison of SPS with hot pressing.....	40
3.4.3.3 Basic mechanisms involved in spark plasma sintering.....	41
3.4.3.4 Processing issues of spark plasma sintering.....	51
4. BORON CARBIDE BASED MATERIALS IN LITERATURE	53
4.1 Consolidation Techniques Used in Boron Carbide Sintering	54
4.1.1 Pressureless sintered boron carbide	54
4.1.2 Hot pressed boron carbide.....	55
4.1.3 Hot isostatic pressed boron carbide	57
4.1.4 Spark plasma sintered boron carbide	57
4.2 Sintering Additives Used in Boron Carbide Sintering.....	58
4.2.1 Carbon addition.....	58
4.2.2 Metal addition	59
4.2.2.1 Al addition.....	60

4.2.2.2 Si addition	63
4.2.2.3 Ti addition	65
5. EXPERIMENTAL PROCEDURE.....	69
5.1 Powders Used in Experiments.....	69
5.2 Production of Boron Carbide Based Composites.....	73
5.2.1 Powder preparation	73
5.2.2 Spark plasma sintering stage.....	75
5.2.3 Characterization of boron carbide ceramic composites	77
5.2.3.1 Density	77
5.2.3.2 XRD analysis.....	77
5.2.3.3 Hardness and fracture toughness measurements.....	78
5.2.3.4 Microstructure observations.....	79
5.2.4 Ballistic test.....	79
6. RESULTS AND DISCUSSION.....	85
6.1 The Densification and Sintering Behaviours of Boron Carbide Ceramic Composites	85
6.1.1 The densification and sintering behaviors of cylindrical boron carbide samples.....	85
6.1.2 The densification and sintering behaviors of hexagonal samples.....	88
6.1.2.1 Densification behaviors of spark plasma sintered hexagonal monolithic boron carbide ceramics	88
6.1.2.2 Densification behaviors of spark plasma sintered hexagonal boron carbide ceramics with different C additions.....	90
6.1.2.3 Densification behaviors of spark plasma sintered hexagonal boron carbide composites with light metallic additions	93
6.1.2.4 Densification behaviors of spark plasma sintered hexagonal boron carbide composites with Ti and TiO ₂ additions	97
6.2 Phase Analysis of Boron Carbide Ceramic Composites	105
6.2.1 Phase analysis of monolithic boron carbide.....	105
6.2.2 Phase analysis of boron carbide ceramics with different carbon sources.....	105
6.2.3 Phase analysis of boron carbide ceramics with light weight metallic additives	106
6.2.4 Phase analysis of boron carbide ceramics with Ti or TiO ₂ additives.....	108
6.3 Mechanical Properties of Boron Carbide Ceramic Composites.....	113
6.3.1 Hardness and fracture toughness of cylindrical boron carbide ceramics	113
6.3.2 Hardness and fracture toughness of hexagonal boron carbide ceramic composites.....	114
6.3.2.1 Hardness and fracture toughness of hexagonal monolithic boron carbide ceramics	114
6.3.2.2 Hardness and fracture toughness of hexagonal boron carbide ceramics with different carbon sources	116
6.3.2.3 Hardness and fracture toughness of hexagonal boron carbide ceramic composites with light-weight metallic additions.....	120
6.3.2.4 Hardness and fracture toughness of hexagonal boron carbide ceramic composites with Ti and TiO ₂ additions	125
6.4 Microstructural Investigations of Boron Carbide Ceramic Composites	135
6.4.1 Microstructural investigations of cylindrical boron carbide ceramics ..	135
6.4.2 Microstructural investigations of hexagonal boron carbide ceramic composites.....	138

6.4.2.1 Microstructural investigations of hexagonal monolithic boron carbide ceramics.....	138
6.4.2.2 Microstructural investigations of hexagonal boron carbide ceramic composites with different C sources	140
6.4.2.3 Microstructural investigations of hexagonal boron carbide ceramic composites with light weight metallic additives	141
6.4.2.4 Microstructural investigations of hexagonal boron carbide ceramic composites with Ti and TiO ₂ additives	145
6.5 Ballistic Behaviors of Boron Carbide Ceramic Composites	158
6.6 Phase Analysis of Boron Carbide Ceramic Composites After Ballistic Tests	174
6.6.1 XRD analysis of hexagonal monolithic boron carbide ceramics	174
6.6.2 XRD analysis of hexagonal boron carbide ceramics with different C additions	175
6.6.3 XRD analysis of hexagonal boron carbide ceramics with light-weight metallic additions	177
6.6.4 XRD analysis of hexagonal boron carbide ceramics with Ti or TiO ₂ additions	180
7. CONCLUSIONS	185
REFERENCES.....	195
CURRICULUM VITAE.....	211



ABBREVIATIONS

AP	: Armor piercing
DEF	: Differential Efficiency Factor
DOP	: Depth of penetration
EDS	: Energy Dispersion Spektrometry
FAST	: Field Assisted Sintering Technique
HIP	: Hot Isostatic Pressing
HP	: Hot Pressing
HR-TEM	: High Resolution Transmission Electron Microscopy
SEM	: Scanning Electron Microscope
SPS	: Spark Plasma Sintering
TEM	: Transmission Electron Microscopy
XRD	: X-Ray Diffraction



SYMBOLS

B₄C	: Boron carbide
B	: Boron
Al	: Aluminium
Si	: Silicon
Ti	: Titanium
C	: Carbon
CNT	: Carbon nanotube
CO	: Carbon monoxide
CO₂	: Carbon dioxide
B₂O₃	: Boron oxide
Mg	: Magnesium
ρ	: Relative density
L	: Length
P	: Porosity
V	: Volume
t	: Time
Ni	: Nickel
Cr	: Chromium
J	: Flux
E	: Electric field
T	: Temperature
σ	: Stress
D	: Diffusion
δ_{gb}	: Grain boundary thickness
k	: Boltzman's constant
Ω	: Atomic Volume
Z	: Valance
e_q	: Electron charge
G	: Average grain size
r_p	: Average pore size
γ_{sv}	: Surface Energy
φ	: Stress intensity factor



LIST OF TABLES

	<u>Page</u>
Table 2.1 : The summary of general characteristics and properties of boron carbide...8	8
Table 2.2 : General properties of monolithic armor ceramics.....10	10
Table 4.1 : Binary and ternary compounds reported in the Al – B – C system 61	61
Table 5.1 : Impurities seen in powders used in experiments. 70	70
Table 5.2 : Average particle size and surface areas of powders used in this study... 71	71
Table 5.3 : The amounts of different powders used in the experiments 74	74
Table 5.4 : Metallographic sample steps used for microstructural observations 79	79
Table 5.5 : Some properties and materials of 7.62 mm bullets..... 80	80
Table 6.1 : Relative density values of cylindrical samples. 86	86
Table 6.2 : Comparison of phases expected from the simulated Al and Si containing composites performed with the thermochemical program and phases obtained from X-ray diffractograms..... 108	108
Table 6.3 : Comparison of phases expected from the simulated Ti and TiO ₂ containing composites performed with the thermochemical program and phases obtained from X-ray diffractograms..... 113	113
Table 6.4 : The hardness, and fracture toughness of spark plasma sintered cylindrical boron carbide ceramics..... 113	113
Table 6.5 : The relative density, hardness and fracture toughness values of spark plasma sintered hexagonal B ₄ C ceramics according to their measurement regions. 116	116
Table 6.6 : The relative density, hardness and fracture toughness values of 2 vol. % C and CNT added hexagonal B ₄ C ceramics according to their measurement regions. 118	118
Table 6.7 : The relative density, hardness and fracture toughness values of 5 vol. % Al added hexagonal B ₄ C ceramics according to their measurement regions. 121	121
Table 6.8 : The relative density, hardness and fracture toughness values of 5 vol. % Si added hexagonal B ₄ C ceramics spark plasma sintered under 40 or 60 MPa pressure according to their measurement regions..... 123	123
Table 6.9 : The relative density, hardness and fracture toughness values of 5, 10, 15 and 20 vol. % Ti-LP added hexagonal B ₄ C ceramics spark plasma sintered at 1550 °C under 40 MPa pressure according to their measurement regions. 127	127
Table 6.10 : The relative density, hardness and fracture toughness values of 5 and 10 vol. % Ti-SP added hexagonal B ₄ C ceramics spark plasma sintered at 1550 °C for 4 or 6 min under 40 MPa pressure according to their measurement regions. 130	130
Table 6.11 : The relative density, hardness and fracture toughness values of 5 and 10 vol. % TiO ₂ added hexagonal B ₄ C ceramics spark plasma sintered at 1550 °C for 4 or 6 min under 40 MPa pressure according to their measurement regions. 133	133

Table 6.12 : EDS elemental analysis results of 5 vol. % Ti-SP containing sample which was spark plasma sintered at 1550 °C for 4 min under a pressure of 40 MPa.....	151
Table 6.13 : EDS elemental analysis results of 5 vol. % TiO ₂ containing sample which was spark plasma sintered at 1550 °C for 4 min under a pressure of 40 MPa.....	155
Table 6.14 : The parameters seen during reference shots.	158
Table 6.15 : Some critical parameters considered during ballistic test.....	161
Table 6.16 : The projectile velocities obtained during ballistic tests.....	162
Table 6.17 : The comparison of center relative density values of hexagonal spark plasma sintered ceramics with velocity and DOP values.	169
Table 6.18 : Differential efficiency factors of spark plasma sintered hexagonal boron carbide ceramics and composites.....	172
Table 6.19 : Particle size distribution of the impact fractured powder for spark plasma sintered hexagonal boron carbide tiles according to sieve sizes (BSS No.).	173



LIST OF FIGURES

	<u>Page</u>
Figure 2.1 : Boron-carbon binary phase diagram.	5
Figure 2.2 : The crystal structure of boron carbide.....	6
Figure 3.1 : Two sphere sintering model.	19
Figure 3.2 : Sintering stage illustration.....	20
Figure 3.3 : Migrating pore and boundary.	22
Figure 3.4 : Illustration of the sintering mechanisms in a three particles array.....	24
Figure 3.5 : Angles and grains	25
Figure 3.6 : Scheme of the densification process under the presence of a wetting liquid	26
Figure 3.7 : A schematic plot of the various pressure-assisted sintering techniques versus the relative temperature.	28
Figure 3.8 : A sketch of hot pressing	30
Figure 3.9 : Schematic of a hot isostatic pressing apparatus	33
Figure 3.10 : Schematic of sintering process: (a) current-activated, pressure-assisted sintering apparatus (b) Hot pressing.....	35
Figure 3.11 : Schematic of sintering process: (a) hot pressing and (b) SPS.....	36
Figure 3.12 : A schematic of a typical experiment illustrating the six main user- defined process parameters: (1) heating rate, (2) maximum temperature, (3) cooling rate, (4) load application rate, (5) maximum load hold, (6) load removal rate	37
Figure 3.13 : Comparison between apparatuses.....	40
Figure 3.14 : Discharge occurred at the interface between the second and third punch on the die at different sintering stage: (a) $t = 60$ s, $T = 337$ °C; (b) $t = 120$ s, $T = 586$ °C; (c) $t = 240$ s, $T = 992$ °C	42
Figure 3.15 : Simulation of current distribution in a copper sphere between two copper plates: (a) Current density distribution, (b) current density profile, and (c) temperature profile	44
Figure 3.16 : Current distributions in the SPS die for alumina and copper samples under an applied voltage of 5 V.....	45
Figure 3.17 : Joule heat in the punch/die/specimen assembly	46
Figure 3.18 : Temperature in the punch/specimen/die assembly for (a) $T_{\text{surface}} = 56$ °C; (b) $T_{\text{surface}} = 983$ °C; (b) $T_{\text{surface}} = 1309$ °C.....	47
Figure 3.19 : Heat loss mechanism depending on the temperature.	48
Figure 3.20 : Temperature distribution inside the ZrO_2 (a) and TiN (b) specimen during the dwell at 1500 °C.....	48
Figure 3.21 : FEM simulation results of a complex shaped sample showing the temperature gradients.	49
Figure 3.22 : Temperature distribution in compact with round and sharp edges.....	50
Figure 3.23 : Complex shaping by Spark Plasma Sintering: (a) sintered part, (b) and (c) finite elements simulations, (d–f) microstructures at different locations.	50
Figure 4.1 : The B - C - Al system at 1400 °C.	60

Figure 4.2 : Isothermal section of B - C - Si system at 2000 K.	63
Figure 4.3: Isothermal sections of B - C - Ti system (a) at 1400 °C (b) 2100 °C.....	66
Figure 5.1: SEM images of (a) B ₄ C, (b) Al, (c) Si, (d) Ti-LP, (e) Ti- SP, (f) TiO ₂ and (g) C-black powders.....	72
Figure 5.2 : Process flowchart of the experiments	73
Figure 5.3 : SPS system used in experimental studies	75
Figure 5.4 : The dies used in SPS system	76
Figure 5.5 : Spark plasma sintered final product (a) showing 62 mm diagonal (b) having graphite in the surface and (c) after sand- blasting	77
Figure 5.6 : Crack formation by Vickers indentation.	78
Figure 5.7 : (a) Schematic view of the 7.62 mm AP projectile and (b) cross-sectional view of the core of the projectile.	79
Figure 5.8 : The photo of the 7.62 × 51-mm NATO bullet with and without full metal jacket.....	80
Figure 5.9 : A schematic view of the experimental setup used for the ballistic testing. Dimensions were given in meters.....	81
Figure 5.10 : The photo of the experimental setup showing (a) the velocity probes; (b) distance between target and shooting gun.	82
Figure 5.11: Schematic view of shooting weapon (1) main body and subframe compartment; (2) upper carrier section; (3) crib; (4) incremental adjustment; (5) side adjustment wheel.....	82
Figure 5.12 : (1) target platform; (2) target binding table; (3) target binding elements; (4) target table inclination angle adjustment lever; (5) target adjustment lever; (6) fixing feet to the target.....	83
Figure 5.13 : 5083 aluminum alloy backing material before the reference shots in the target chamber.....	84
Figure 6.1 : Temperature and displacement curves versus time during SPS process.	86
Figure 6.2 : The areas subjected to density measurement in the samples with hexagonal geometry.....	88
Figure 6.3 : Relative density values of hexagonal monolithic boron carbide ceramics spark plasma sintered at 1550 °C for 4 min under an applied pressure of 40 MPa.....	89
Figure 6.4 : Relative density values of 2 vol. % C and CNT added hexagonal boron carbide ceramics which were spark plasma sintered at 1550 °C for 4 min under an applied pressure of 40 MPa.....	91
Figure 6.5 : Temperature, displacement and displacement rate curves of (a). 2 vol. % C (b). 2 vol % CNT added boron carbide samples versus time during SPS process.	92
Figure 6.6 : Relative density values of 5 vol. % Al and Si added hexagonal boron carbide ceramics	94
Figure 6.7 : Temperature, displacement and displacement rate curves of 5 vol. % Al added boron carbide samples spark plasma sintered at 1450 °C for 4 min versus time during SPS process.	95
Figure 6.8 : Temperature, displacement and displacement rate curves of 5 vol. % Si added boron carbide samples spark plasma sintered at 1500 °C for 4 min under an applied pressure of (a). 40 MPa (b). 60 MPa versus time during SPS process.....	96

Figure 6.9 : Relative density values of 5, 10, 15 and 20 vol. % Ti-LP added hexagonal boron carbide ceramics which were spark plasma sintered at 1550 °C for 4 min under an applied pressure of 40 MPa.	98
Figure 6.10 : Relative density values of 5 vol. % Ti-SP added hexagonal boron carbide ceramics which were spark plasma sintered at 1550 °C for 4 and 6 min under an applied pressure of 40 MPa and 10 vol. % Ti-SP added hexagonal boron carbide ceramics produced in same conditions but only with 4 minute soaking time.....	100
Figure 6.11 : Relative density values of 5 vol. % TiO ₂ added hexagonal boron carbide ceramics which were spark plasma sintered at 1550 °C for 4 and 6 min under an applied pressure of 40 MPa and 10 vol. % TiO ₂ added hexagonal boron carbide ceramics produced in same conditions but only with 4 minute soaking time.....	101
Figure 6.12 : Temperature and displacement curves of 5, 10, 15 and 20 vol. % Ti-LP added boron carbide samples spark plasma sintered at 1550 °C for 4 min under an applied pressure of 40 MPa versus time during SPS process.	103
Figure 6.13 : Temperature and displacement curves of 10 vol. % Ti-SP or TiO ₂ added boron carbide samples spark plasma sintered at 1550 °C for 4 min under an applied pressure of 40 MPa versus time during SPS process.	103
Figure 6.14 : Phase change according to increased temperature in monolithic boron carbide obtained from Factsage 6 thermochemical simulation program.	105
Figure 6.15 : Phase change according to increased temperature in 2 vol. % C added boron carbide obtained from Factsage 6 thermochemical simulation program.....	106
Figure 6.16 : Phase change according to increased temperature in 5 vol. % Al added boron carbide obtained from Factsage 6 thermochemical simulation program.....	107
Figure 6.17 : Phase change according to increased temperature in 5 vol. % Si added boron carbide obtained from Factsage 6 thermochemical simulation program.....	107
Figure 6.18 : Phase change according to increased temperature in (a) 5 vol. % (b) 10 vol. % Ti added boron carbide obtained from Factsage 6 thermochemical simulation program.....	109
Figure 6.19 : Phase change according to increased temperature in (a) 5 vol. % (b) 10 vol. % TiO ₂ added boron carbide obtained from Factsage 6 thermochemical simulation programme.	110
Figure 6.20 : XRD analysis of spark plasma sintered hexagonal B ₄ C with 5 vol. % (a) Ti-SP and (b) TiO ₂ which were spark plasma sintered at 1550 °C for 4 min under a pressure of 40 MPa.	111
Figure 6.21 : XRD analysis of spark plasma sintered hexagonal B ₄ C with 5 vol. % (a) Ti-SP and (b) TiO ₂ which were spark plasma sintered at 1550 °C for 6 min under a pressure of 40 MPa.	111
Figure 6.22 : XRD analysis of spark plasma sintered hexagonal B ₄ C with 10 vol. % (a) Ti-SP and (b) TiO ₂ which were spark plasma sintered at 1550 °C for 4 min under a pressure of 40 MPa.	112
Figure 6.23 : The Vickers hardness and fracture toughness values of edges, edge average and center of hexagonal boron carbide ceramics which was spark plasma sintered at 1550 °C for 4 min under a pressure of 40 MPa in vacuum.....	115

Figure 6.24 : Vickers hardness values of 2 vol. % C-black and CNT added hexagonal boron carbide ceramics which were spark plasma sintered at 1550 °C for 4 min under an applied pressure of 40 MPa.	117
Figure 6.25 : Fracture toughness values of 2 vol. % C- black and CNT added hexagonal boron carbide ceramics which were spark plasma sintered at 1550 °C for 4 min under an applied pressure of 40 MPa.	119
Figure 6.26 : Relative density values of 5 vol. % Al added hexagonal boron carbide ceramic which was spark plasma sintered at 1450 °C for 4 min under an applied pressure of 40 MPa.	120
Figure 6.27 : Vickers hardness values of 5 vol. % Si added hexagonal boron carbide ceramics which were spark plasma sintered at 1500 °C for 4 min under an applied pressure of 40 MPa or 60 MPa.....	122
Figure 6.28 : Fracture toughness values of 5 vol. % Si added hexagonal boron carbide ceramics which were spark plasma sintered at 1500 °C for 4 min under an applied pressure of 40 MPa or 60 MPa.....	124
Figure 6.29 : Vickers hardness values of 5, 10, 15 and 20 vol. % Ti-LP added hexagonal boron carbide ceramics which were spark plasma sintered at 1550 °C for 4 min under an applied pressure of 40 MPa.	125
Figure 6.30 : Fracture toughness values of 5, 10, 15 and 20 vol. % Ti-LP added hexagonal boron carbide ceramics which were spark plasma sintered at 1550 °C for 4 min under an applied pressure of 40 MPa.	128
Figure 6.31 : Vickers hardness values of 5 and 10 vol. % Ti-SP added hexagonal boron carbide ceramics which were spark plasma sintered at 1550 °C for 4 or 6 min under an applied pressure of 40 MPa.	129
Figure 6.32 : Fracture toughness values of 5 and 10 vol. % Ti-SP added hexagonal boron carbide ceramics which were spark plasma sintered at 1550 °C for 4 or 6 min under an applied pressure of 40 MPa.	131
Figure 6.33 : Vickers hardness values of 5 and 10 vol. % TiO ₂ added hexagonal boron carbide ceramics which were spark plasma sintered at 1550 °C for 4 or 6 min under an applied pressure of 40 MPa.	132
Figure 6.34 : Fracture toughness values of 5 and 10 vol. % TiO ₂ added hexagonal boron carbide ceramics which were spark plasma sintered at 1550 °C for 4 or 6 min under an applied pressure of 40 MPa.	134
Figure 6.35 : SEM micrographs of fracture surfaces of monolithic boron carbide ceramics spark plasma sintered at: (a) 1650 °C; (b) 1725 °C for 5 min under a pressure of 40 MPa in vacuum atmosphere.	135
Figure 6.36 : SEM micrographs of fracture surfaces of boron carbide with 2 vol. % C-black spark plasma sintered at: (a) 1650 °C; (b) 1725 °C for 5 min under a pressure of 40 MPa in vacuum atmosphere.	136
Figure 6.37 : SEM micrographs of fracture surfaces of boron carbide with 2 vol. % CNT spark plasma sintered at: (a) 1650 °C; (b) 1725 °C for 5 min under a pressure of 40 MPa in vacuum atmosphere.	137
Figure 6.38: SEM fracture surface micrographs of (a) center (b) edge region of hexagonal monolithic boron carbide spark plasma sintered at 1550 °C for 4 min under a pressure of 40 MPa in vacuum atmosphere.	138
Figure 6.39 : SEM fracture surface micrographs of (a) center (b) edge region of hexagonal boron carbide with 2 vol. % C-black spark plasma sintered at 1550 °C for 4 min under a pressure of 40 MPa in vacuum atmosphere.	140

- Figure 6.40** : SEM fracture surface micrographs of (a) center (b) edge region of hexagonal boron carbide with 2 vol. % CNT spark plasma sintered at 1550 °C for 4 min under a pressure of 40 MPa in vacuum atmosphere..... **141**
- Figure 6.41** : SEM fracture surface micrographs of (a) edge (b) center region of hexagonal boron carbide with 5 vol. % Al spark plasma sintered at 1450 °C for 4 min under a pressure of 40 MPa in vacuum atmosphere..... **142**
- Figure 6.42** : SEM fracture surface micrographs of (a) center (b) edge region of hexagonal boron carbide with 5 vol. % Si spark plasma sintered at 1500 °C for 4 min under a pressure of 40 MPa in vacuum atmosphere..... **143**
- Figure 6.43** : SEM fracture surface micrographs of (a) center (b) edge region of hexagonal boron carbide with 5 vol. % Si spark plasma sintered at 1500 °C for 4 min under a pressure of 60 MPa in vacuum atmosphere..... **144**
- Figure 6.44** : The schematic demonstration of microstructural development occurred between Ti and B₄C during spark plasma sintering **145**
- Figure 6.45** : (a) center, SEI; (b) edge, SEI; (c) center, COMPO; (d) edge, COMPO SEM fracture surface micrographs of hexagonal boron carbide with 5 vol. % Ti-LP spark plasma sintered at 1550 °C for 4 min under a pressure of 40 MPa..... **146**
- Figure 6.46** : (a) center, SEI; (b) edge, SEI; (c) center, COMPO; (d) edge, COMPO SEM fracture surface micrographs of hexagonal boron carbide with 10 vol. % Ti-LP spark plasma sintered at 1550 °C for 4 min under a pressure of 40 MPa. **147**
- Figure 6.47** : (a) center, SEI; (b) edge, SEI; (c) center, COMPO; (d) edge, COMPO SEM fracture surface micrographs of hexagonal boron carbide with 5 vol. % Ti-SP spark plasma sintered at 1550 °C for 4 min under a pressure of 40 MPa..... **148**
- Figure 6.48** : (a) center, SEI; (b) edge, SEI; (c) center, COMPO; (d) edge, COMPO SEM fracture surface micrographs of hexagonal boron carbide with 5 vol. % Ti-SP spark plasma sintered at 1550 °C for 4 min under a pressure of 40 MPa..... **149**
- Figure 6.49** : The (a) SEM micrograph and (b) Region 1; (c) Region 2 and (d) Region 3 EDS analysis of 5 vol. % Ti-SP containing sample which was spark plasma sintered at 1550 °C for 4 min under a pressure of 40 MPa pressure. **151**
- Figure 6.50** : SEM fracture surface micrographs of (a) center (b) edge region of hexagonal boron carbide with 5 vol. % Ti-SP spark plasma sintered at 1550 °C for 6 min under a pressure of 40 MPa in vacuum atmosphere. **152**
- Figure 6.51** : SEM fracture surface micrographs of (a) center (b) edge region of hexagonal boron carbide with 10 vol. % Ti-SP spark plasma sintered at 1550 °C for 4 min under a pressure of 40 MPa in vacuum atmosphere. **152**
- Figure 6.52** : (a) center, SEI; (b) edge, SEI; (c) center, COMPO; (d) edge, COMPO SEM fracture surface micrographs of hexagonal boron carbide with 5 vol. % TiO₂ spark plasma sintered at 1550 °C for 4 min under a pressure of 40 MPa..... **153**
- Figure 6.53** : The (a) SEM micrograph and (b) Region 1 and (c) Region 2 EDS analysis of 5 vol. % TiO₂ containing sample which was spark plasma sintered at 1550 °C for 4 min under a pressure of 40 MPa pressure. ... **154**

Figure 6.54 : (a) center, SEI; (b) edge, SEI; (c) center, COMPO; (d) edge, COMPO SEM fracture surface micrographs of hexagonal boron carbide with 5 vol. % TiO ₂ spark plasma sintered at 1550 °C for 6 min under a pressure of 40 MPa.....	155
Figure 6.55 : (a) center, SEI; (b) edge, SEI; (c) center, COMPO; (d) edge, COMPO SEM fracture surface micrographs of hexagonal boron carbide with 10 vol. % TiO ₂ spark plasma sintered at 1550 °C for 4 min under a pressure of 40 MPa.....	156
Figure 6.56 : SEM micrographs of fracture surfaces of (a,b,c) monolithic, (d,e) 5 vol. % Ti containing and (f,g,h) 5 vol. % TiO ₂ added B ₄ C.	157
Figure 6.57 : View of the target plate after ballistic impact: (a) Front face and (b) Rear face of 5083 Al alloy plate with a thickness of 25.5 mm; (c) front face of second plate welded first block with 38.5 mm thickness.	159
Figure 6.58 : View of hexagonal tile on aluminium backing alloy.....	159
Figure 6.59 : High speed photographs of boron carbide ceramic tile subjected to ballistic test.	160
Figure 6.60 : The damage occurred on the Al backing alloy surface after the hit with the protection of monolithic boron carbide ceramic tile which was spark plasma sintered at 1550 °C for 4 min under a pressure of 40 MPa in vacuum atmosphere.	162
Figure 6.61 : The damage occurred on the Al backing alloy surface after the hit with the protection of 2 vol. % C-black added boron carbide tile which was spark plasma sintered at 1550 °C for 4 min under a pressure of 40 MPa in vacuum atmosphere.	163
Figure 6.62 : The damages occurred on the Al backing alloy surface after the (a) first (b) second hit with the protection of 2 vol. % CNT added boron carbide tile which was spark plasma sintered at 1550 °C for 4 min under a pressure of 40 MPa in vacuum atmosphere.	164
Figure 6.63 : The damages occurred on the Al backing alloy surface after the (a) first (b) second (c) third hit with the protection of 5 vol. % Al added boron carbide tile which was spark plasma sintered at 1450 °C for 4 min under a pressure of 40 MPa in vacuum atmosphere.	165
Figure 6.64 : The damages occurred on the Al backing alloy surface after the protection of 5 vol. % Al added boron carbide tile which were spark plasma sintered at 1450 °C for 4 min under a pressure of (a) 40 MPa; (b) 60 MPa in vacuum.....	165
Figure 6.65 : The damage occurred on the Al backing alloy surface after the hit with the protection of 5 vol. Ti-LP added boron carbide composite tile which was spark plasma sintered at 1550 °C for 4 min under a pressure of 40 MPa in vacuum.	166
Figure 6.66 : The damages occurred on the Al backing alloy surface after (a) first and (b) second hit with the protection of 10 vol. Ti-LP added boron carbide composite tile which was spark plasma sintered at 1550 °C for 4 min under a pressure of 40 MPa in vacuum.....	167
Figure 6.67 : The damage occurred on the Al backing alloy surface after the hit with the protection of 15 vol. Ti-LP added boron carbide composite tile which was spark plasma sintered at 1550 °C for 4 min under a pressure of 40 MPa in vacuum.	167

Figure 6.68 : The damage occurred on the Al backing alloy surface after the hit with the protection of 20 vol. Ti-LP added boron carbide composite tile which was spark plasma sintered at 1550 °C for 4 min under a pressure of 40 MPa in vacuum.	168
Figure 6.69 : The pieces of the broken shots of the projectile	168
Figure 6.70 : Particle size distribution of the impact fractured powder for spark plasma sintered hexagonal boron carbide tiles according to sieve sizes (BSS No.).	173
Figure 6.71 : XRD analysis of spark plasma sintered monolithic hexagonal B ₄ C before and after ballistic test.	174
Figure 6.72 : XRD analysis of spark plasma sintered hexagonal B ₄ C with 2vol. % C-black before and after ballistic test.	176
Figure 6.73 : XRD analysis of spark plasma sintered hexagonal B ₄ C with 2 vol. % CNT before and after ballistic test.	177
Figure 6.74 : XRD analysis of spark plasma sintered hexagonal B ₄ C with 5 vol. % Al before and after ballistic test.	178
Figure 6.75 : XRD analysis of spark plasma sintered hexagonal B ₄ C with 5 vol. % Si before and after ballistic test.	179
Figure 6.76 : XRD analysis of spark plasma sintered hexagonal B ₄ C with 5 vol. % Ti-LP before and after ballistic test.	181
Figure 6.77 : XRD analysis of spark plasma sintered hexagonal B ₄ C with 10 vol. % Ti-LP before and after ballistic test.	182
Figure 6.78 : XRD analysis of spark plasma sintered hexagonal B ₄ C with 20 vol. % Ti-LP before and after ballistic test.	183



PRODUCTION AND CHARACTERIZATION OF SPARK PLASMA SINTERED BORON CARBIDE CERAMIC COMPOSITES SUITABLE FOR BALLISTIC USE

SUMMARY

Boron carbide (B_4C) synthetic ceramics with the highest known hardness after diamond and cubic boron nitride are characterized by their ultra-hardness properties, high melting point, low density, high wear resistance, remarkable chemical stability and high neutron absorbing capacity. Besides nuclear applications, it has been widely used in ballistic applications for many years, especially due to the advantage of being lightweight material. However, because of its high covalent bond character, very high melting temperature and low self-diffusing properties, sinterability of B_4C is very difficult. B_4C ceramics intended to be sintered to high relative densities requires high temperature and pressure values during sintering. Moreover, even after a successful sintering process, fracture toughness of B_4C ceramics remains at very low levels.

The ultimate goal of this doctoral work is to produce B_4C armor prototypes with hexagonal geometry, with appropriate dimensions. Armor materials with hexagonal geometry have a higher ballistic strength in multiple shots if laid like mosaics. To this end, the spark plasma sintering system, which has proven its success in the sintering of highly covalent bonded ceramics to high densities, has been used. B_4C armor materials have been produced in sizes suitable for the final product. In the literature, this sintering system is generally used for very small size specimens, and in this work this can be regarded as an advantage to obtain final product dimensions. The ceramics and ceramic composites produced by spark plasma sintering system were subjected to various characterization processes to determine ballistic usability.

B_4C ceramics are particularly suitable for use as lightweight body armor or vehicle protection armor due to their low density. However, high fracture toughness as well as a high hardness, is a must for high ballistic performance. High hardness is inherent in B_4C and is an easy feature to achieve, if good sinterability is achieved. But the same is not the case for fracture toughness. In the literature, fracture toughness of B_4C has been tried to be increased by various additions to the structure. In this thesis, the most common and most effective additive materials have been added to the boron carbide to increase its fracture toughness and ballistic performance. These additives were selected as carbon black, carbon nanotube (CNT), aluminum (Al), silicon (Si), titanium (Ti) and titanium oxide (TiO_2). Another factor in selecting these additives is that low density, in order to keep the weight of final product low.

The ceramic and ceramic composites with desired compositions were mixed using ball milling for 24 hours in ethanol medium. In order to remove the ethanol, the mixtures were dried and sieved for granulation. B_4C ceramics and ceramic composites, without any pretreatment or binder or lubricant use, are directly sintered at SPS 7.40 MKVII, SPS Syntex Inc. apparatus in Spark Plasma Sintering Laboratory, Istanbul Technical

University, Metallurgical and Materials Engineering Department. In this thesis study, two product lines with different geometry and sizes have been realized. In the first stage, the experiments have been carried out using molds which are always used with the aim of being a preliminary study for understanding the character of the powder. As a result of these experiments, B₄C ceramics and ceramic composites of 50 mm in diameter and 5 mm in thickness were produced. In the second stage, hexagonal ceramic and ceramic composite materials with a 62 mm diagonal and 31.5 mm a side length and 10 mm thickness were produced. A sample with these dimensions and geometry is first used by spark plasma sintering system.

The density, hardness, fracture toughness, microstructure and ballistic properties of spark plasma sintered specimens were characterized and their phases were determined by XRD method. The graphite on the surfaces of the B₄C specimens removed by sand blasting and cut to the appropriate dimensions with a diamond disk to be subjected to physical and mechanical characterization processes. For the density, hardness and fracture toughness characteristics, each edge and center areas of the samples were examined and the average of the edge properties for each material was calculated and compared with each other. The density of the samples was measured using the Archimedes principle. The samples were carefully polished using various diamond solutions and the hardness and fracture toughness were measured by the Vickers indentation technique. Phase transformation in all samples was followed by X-ray diffractometry. Field-emission SEM was used for microstructure studies.

The ballistics tests of the samples were carried out in accordance with NIJ Standard 0101.06 Level IV in ROKETSAN Inc. Ballistic Protection Center Test Laboratories. Armor penetrating bullets with a diameter of 7,62 mm were used in the tests. According to this standard, the necessity of having a rate of 868 ± 15 m/s at the time of contact of the sample with the sample was taken into account during the test, and the hives were prepared using gunpowder to provide this rate. In order to investigate the effects of additives used in this project on B₄C ceramics, instead of RHA steel or 5083 aluminum alloy, a more ductile material was chosen as the backing material. Since the use of hard materials will lead to the formation of smaller penetration marks and the effect of the additive material can not be clearly understood. Accordingly, a more ductile backing material has been used.

Monolithic boron carbide materials and boron carbide samples with C-black and CNT were sintered at temperatures of 1650 and 1725 ° C, which were low compared to hot pressing or non-pressurized pressing but high for the spark plasma sintering system in studies on cylindrical sample production. As a result of the experiments, a density of 98.80 % was obtained in the center of the sample containing 2 vol. % CNT and the fracture toughness value reached to 4.50 MPa·m^{1/2} while the hardness value was 36.30 GPa. It has been determined that the microstructures of the examined specimens increased densification significantly with C-black and CNT addition.

Hexagonal monolithic boron carbide ceramics were sintered by a spark plasma sintering at 1550 ° C for 4 minutes under 40 MPa pressure in vacuum and reached a density of 95.34 % in the centre of the sample. The hardness value of the monolithic boron carbide ceramic measured to be 28.71 GPa and the fracture toughness was calculated to be 3.23 MPa · m^{1/2}. When the center and edge microstructures are compared, higher porosity is seen in edges. The depth of penetration (DOP) left on the Al surface after B₄C ceramics subjected to the ballistic test was measured as 3.87 mm and the ballistic efficiency factor was found as 4.88.

2 vol. % C-black or CNT added B₄C were produced with the spark plasma sintering system under the same conditions as mentioned above. The relative density values of the C-added boron carbide were found out to be 96.75 % in the center and 95.89 % in the average edge. CNT addition resulted in a more efficient sintering, resulting in a density of 97.26 % in the central region and 96.17 % in the edge. The addition of C-black to B₄C results in 32.81 GPa and CNT addition results in 33.66 GPa hardness. The fracture toughness increased to 3.69 and 4.46 MPa·m^{1/2}, respectively. Ballistic tests showed that C-black provided a more effective ballistic protection. The depth of 6.86 mm was obtained in the C added sample, whereas the depth increased to 9.50 mm in CNT containing sample.

With the addition of 5 vol. % Al to the B₄C structure, the spark plasma sintering temperature was reduced to 1450 °C and the other process parameters remained the same. As a result of the experiments, Al, which caused the liquid phase sintering at the B₄C structure due to the low melting temperature, caused the density in the central region to increase to 98.16%. The hardness of 31.96 GPa was obtained at the central zone and the fracture toughness value increased to 5.87 MPa·m^{1/2}. After the ballistic test, Al-added B₄C armor composites caused the trace depth to decrease to 3.10 mm. The ballistic effect factor increased to 4.93 despite the average material weight is increased with the Al addition.

5 vol. % Si addition was performed on the structure and Si, which has a lower melting point than B₄C, reduced the spark plasma sintering temperature to 1500 °C. When sintering is carried out at higher temperatures, a serious sticking problem occurred. As a result of the spark plasma sintering experiments, the density of Si-added boron carbide samples was found to be low, so another sintering enhancing mechanism, pressure increment was realized. The experiments carried out with increasing pressure to 60 MPa resulted in a density of 97.54 % in the centre of the sample. The hardness value in the same zone of the sample is 32.32 GPa and the fracture toughness is 5.41 MPa·m^{1/2}. XRD and EDS studies have shown that all the Si in the structure is converted to SiC by taking C from the B₄C and the graphite molds used during the process.

The Ti addition to the B₄C material was made in two different powder sizes. The experiments with coarse Ti powder have been carried out with 5, 10,15 and 20 vol. % Ti and only 5 and 10 vol. %Ti in the fine powder. It is discovered that Ti addition is a very effective additive to B₄C structure in terms of density, hardness and fracture toughness as well as ballistic performance. B₄C containing 20 vol.% Ti-LP and 5 vol. % Ti-SP addition have reached the theoretical density at center and one of the edge. Regardless of the amount of Ti added to the structure, it has been found to be converted to TiB₂ in all cases. When the microstructures were examined, TiB₂ agglomerates were formed in the center of the boron carbide matrix, irregularly distributed in the center. The ballistic effect factor of the boron carbide sample containing 5 vol % Ti-LP is calculated to be 5.00. The effect of TiO₂ addition on the boron carbide material was also investigated, and it was found that TiO₂, which was added in 5 and 10 vol. % resulted in TiB₂ and CO₂ formation. However, when microstructures were examined, homogeneously dispersed small TiB₂ grains, were obtained instead of agglomerates, as obtained in Ti addition. However, TiO₂ addition, when compared to Ti, contributed less to sintering. The highest density as 98.25 % is attained in the sample with 5 vol. % TiO₂. The center hardness value of the same specimen was measured as 30.98 GPa, while the fracture toughness value was calculated as 6.07 MPa·m^{1/2}.



BALİSTİK KULLANIMA UYGUN BOR KARBÜR SERAMİK KOMPOZİTLERİNİN SPARK PLAZMA SİNERLEME YÖNTEMİ İLE ÜRETİMİ VE KARAKTERİZASYONU

ÖZET

Elmas ve kübik bor nitrürden sonra bilinen en yüksek sertlik değerine sahip bor karbür (B_4C) sentetik seramikleri, ultra-sertlik özelliğinin yanı sıra yüksek ergime sıcaklığı, düşük yoğunluk, yüksek aşınma direnci, dikkat çekici kimyasal kararlılık ve yüksek nötron absorblama kapasitesi özellikleri ile öne çıkan önemli bir malzemedir. Nükleer uygulamalar yanında uzun yıllardır, özellikle hafif malzeme olma avantajından dolayı balistik uygulamalarda oldukça yaygın olarak kullanılmaktadır. Fakat B_4C seramikleri, yüksek kovalent bağ karakteri, çok yüksek ergime sıcaklığı ve düşük self difüzyon hızı özelliklerinden dolayı sinterlenebilmesi çok zor bir malzemedir. Yüksek rölatif yoğunluklara sinterlenmesi hedeflenen bir B_4C seramiği, sinterleme esnasında yüksek sıcaklık ve basınç değerlerine ihtiyaç duyar. Ayrıca, başarılı bir sinterleme sürecinin ardından bile B_4C seramiklerinin kırılma tokluğu çok düşük seviyelerde kalmaktadır.

Bu doktora çalışmasının nihai hedefi balistik kullanıma uygun boyutlarda, hekzagonal geometriye sahip B_4C zırh plakalar üretmektir. Hekzagonal geometriye sahip zırh malzemeleri, mozaik gibi döşendiği takdirde çoklu atışlarda daha yüksek dayanım sağlamaktadır. Bunun için, özellikle kovalent bağlı seramiklerin yüksek yoğunluğa sinterlenmesinde başarısını kanıtlamış spark plazma sistemi kullanılmış olup, son ürüne uygun boyutlarda B_4C zırh malzemeleri üretilebilmiştir. Literatürde genellikle bu sinterleme sistemi çok küçük boyutlu numuneler için kullanılmakta olup, bu çalışmada son ürün boyutlarının elde edilmesi bir ilktir. Spark plazma sinterleme sistemi ile üretilen seramik ve seramik kompozitler, daha sonra çeşitli karakterizasyon işlemlerine tabi tutularak balistik kullanıma uygunlukları belirlenmiştir.

B_4C seramikleri, özellikle düşük yoğunluklarından dolayı hafif beden zırhları olarak veya araç koruma zırhları olarak kullanıma uygundur. Fakat balistik performansı yüksek bir malzeme üretmenin ön koşulu, yüksek sertlik yanında yüksek kırılma tokluğudur. Yüksek sertlik, B_4C 'ün doğasında olup, B_4C 'de iyi sinterlenebilirlik sağlandığı takdirde elde edilebilmesi kolay bir özelliktir. Fakat kırılma tokluğu için aynı durum söz konusu değildir. Literatürde B_4C 'ün kırılma tokluğu, yapıya katılan çeşitli ilavelerle artırılmaya çalışılmıştır. Bunlardan en yaygın ve en etkili olduğu düşünülen katkı malzemeleri, bu tez çalışması kapsamında, hem bor karbürün kırılma tokluğunu hem de balistik performansını artırmak için yapıya katılmıştır. Bu katkılar karbon karası, karbon nanotüp (CNT), alüminyum (Al), silisyum (Si), titanyum (Ti) ve titanyum oksit (TiO_2) olarak seçilmiştir. Bu katkıların seçilmesinde göz önüne alınan bir diğer faktör, katkıların düşük yoğunluklu olması ve son ürünün ağırlığını belirgin şekilde artırmamasıdır. B_4C 'ün $2,52 \text{ g/cm}^3$ olan düşük yoğunluğu yapıya katılan katkılar ile korunmaya çalışılmıştır. C ve CNT 2.20 g/cm^3 ; Al 2.70 g/cm^3 ; Si 2.33 g/cm^3 ; Ti 4.50 g/cm^3 ; TiO_2 4.23 g/cm^3 yoğunluğa sahiptir.

Üretilmesi hedeflenen seramik ve seramik kompozitler uygun kompozisyonlarda, etanol ortamında 24 saat süre ile bilyalı değirmen kullanılarak karıştırılmıştır. Etüvde etanolü uzaklaştırılan karışımlar elekten geçirilerek granüle edilmiştir. Herhangi bir ön-işlem veya bağlayıcı, yağlayıcı kullanımı gerekmeksizin B₄C seramiklerinin ve seramik kompozitlerinin üretimi, İstanbul Teknik Üniversitesi, Metalurji ve Malzeme Mühendisliği Bölümü, Spark Plazma Sinterleme laboratuvarında SPS 7.40 MKVII, SPS Syntex Inc. cihazı kullanılarak gerçekleştirilmiştir. Bu tez çalışmasında iki farklı boyut ve geometride ürün eldesi gerçekleştirilmiştir. İlk aşamada gerçekleştirilen deneyler, toz karakteristiğini anlamak ve hegzagonal geometri için bir ön çalışma olması amacı ile her zaman kullanılan dairesel kesitli kalıplar kullanılarak yapılmıştır. Bu deneyler sonucunda 50 mm çapında 5 mm kalınlığında silindir geometride B₄C seramik ve seramik kompozitleri üretilmiştir. İkinci aşamada ise 62 mm köşegen, 31,5 mm kenar uzunluğuna sahip 10 mm kalınlığında hegzagonal seramik ve seramik kompozit malzemeler üretilmiştir. Bu boyutlarda bir numunenin, söz konusu geometride spark plazma sinterleme sistemi kullanılarak ilk defa üretimi gerçekleştirilmiştir.

Spark plazma sinterlenmiş numunelerin yoğunluk, sertlik, kırılma tokluğu, mikroyapı ve balistik özellikleri karakterize edilmiş olup, yapısında bulundurduğu fazlar XRD yöntemi ile belirlenmiştir. Spark plazma sinterleme sisteminde kullanılan grafit kalıplardan çıkarılan B₄C numunelerinin yüzeyleri, kumlama işlemi ile grafitinden arındırılmış ve fiziksel ve mekanik karakterizasyon işlemlerine tabi tutulabilmek için uygun boyutlara elmas disk yardımıyla kesilmiştir. Yoğunluk, sertlik ve kırılma tokluğu özellikleri için numunelerin her bir köşe ve merkez bölgeleri incelenmiş olup, her malzeme için köşe özelliklerinin ortalamaları hesaplanmış ve birbirleri ile kıyaslanmıştır. Numunelerin yoğunluğu Archimed prensibi kullanılarak ölçülmüştür. Numuneler, çeşitli elmas çözeltiler kullanılarak dikkatlice zımparalanmış ve parlatılmış sertlik ve kırılma toklukları Vickers indentasyon tekniği ile ölçülmüştür. Tüm numunelerde faz dönüşümü, X-ışınları difraktometresi ile takip edilmiştir. Mikro yapı çalışmalarında alan emisyonlu taramalı elektron mikroskobu kullanılmıştır.

Elde edilen numunelerin balistik testleri ROKETSAN A.Ş.'nin Balistik Koruma Merkezi Test Laboratuvarlarında NIJ Standart 0101.06 Seviye IV standartlarına uygun olarak gerçekleştirilmiştir. Testlerde 7,62 mm çaplı zırh delici mermiler kullanılmıştır. Bu standarda göre merminin numuneye temas ettiği sırada 868 ± 15 m/s hıza sahip olması gerekliliği test süresince dikkate alınmış, kovanlar bu hızı sağlayacak miktarda barut kullanılarak hazırlanmıştır. Bu çalışmada kullanılan katkıların B₄C seramiğine olan etkilerinin daha iyi incelenebilmesi için altlık malzemesi olarak RHA çeliği ya da normal çelik levhalara kıyasla daha sünek bir malzeme olan 5083 alüminyum alaşımı seçilmiştir. Sert altlık malzemelerinin kullanımı daha küçük derinliklerde penetrasyon izlerinin oluşumuna neden olacağı için, katkı malzemesinin etkisinin net olarak anlaşılamayacağı, farkların küçük olacağı ve sonuçların net olmayacağı düşünülerek daha sünek bir altlık malzemesi kullanılmıştır.

Silindirik numune üretimi hedeflenerek yapılan çalışmalarda, monolitik bor karbür malzemesi ve C-karası ve CNT ilaveli bor karbür numuneleri 1650 ve 1725 °C gibi, sıcak pres veya basınçsız preslemeye oranla düşük fakat spark plazma sinterleme sistemi için yüksek olan sıcaklıklarda sinterlenmiştir. Deneylerin sonucunda hacimce % 2 CNT içeren numunede % 98,80 yoğunluk elde edilmiştir. Bu numunelerin sertlik değeri 36,30 GPa iken kırılma tokluğu değeri 4,50 MPa·m^{1/2} mertebesine ulaşmıştır. Mikroyapıları da incelenen numunelerin, C-karası ve CNT eklentisi ile densifikasyonlarının belirgin derecede arttığı belirlenmiştir.

Hegzagonal monolitik bor karbür seramikleri ise 100 °C/dk ısıtma hızı ile ısıtılarak 1550 °C’de 4 dakika süre ile 40 MPa basınç altında vakum atmosferinde spark plazma sistemi ile sinterlenmiş olup, merkez bölgede % 95,34 yoğunluğa ulaşmıştır. Sertlik değeri merkezde 28,71 GPa olarak ölçülen monolitik bor karbür seramiğinin kırılma tokluğu değeri 3,23 MPa·m^{1/2} olarak hesaplanmıştır. Mikroyapıları kıyaslanan bor karbür seramiklerinin, köşe bölgelerde merkez bölgeye kıyasla daha yüksek oranda poroziteli bir yapı oluşturduğu görülmüştür. Balistik teste tabi tutulan B₄C seramiğinin Al yüzeyinde bıraktığı iz derinliği 3,87 mm olarak ölçülmüş olup, balistik etki faktörü 4,88 olarak bulunmuştur.

Yapıya eklenen hacimce % 2 C-karası veya CNT sonrası bor karbür malzemesi yine yukarıda belirtilen şartlarda spark plazma sinterleme sistemi ile üretilmiştir. Deneyler sonucu C- karası ilaveli bor karbürün rölatif yoğunluk değerleri merkezde % 96,75 iken ortalama kenar yoğunluğu % 95.89 olarak saptanmıştır. CNT ilavesi ise C-karasına göre daha etkin bir sinterlemeye neden olarak, merkez bölgede % 97.26, kenarda ise ortalama % 96.17 yoğunluk elde edilmesini sağlamıştır. Sertlikler kıyaslandığında ise, B₄C seramiklerine C-karası ilavesinin yine merkez bölgede 32,81 GPa, CNT ilavesinin ise 33,66 GPa sertlik özelliği göstermesine neden olduğu belirlenmiştir. Kırılma toklukları da yine sırası ile 3,69 ve 4,46 MPa·m^{1/2} değerine yükselmiştir. Balistik testler sonucunda ise C- karası, aynı oranda CNT ilavesine kıyasla daha efektif bir balistik koruma sağlamıştır. C-karası eklentili numunede 6,86 mm iz derinliği elde edilirken, CNT ilaveli bor karbürde iz derinliği 9.50 mm olarak ölçülmüştür. Her iki katkı da monolitik bor karbüre kıyasla daha düşük balistik dirençli malzeme oluşmasına neden olmuştur.

Alüminyumun hacimce % 5 oranında B₄C yapısına ilavesi ile spark plazma sinterleme sıcaklığı 1450 °C’ye düşürülmüş olup, diğer proses parametreleri aynı bırakılmıştır. Deneyler sonucunda, düşük ergime sıcaklığı sebebi ile B₄C yapısında sıvı faz sinterlemesine neden olan Al, merkez bölgede yoğunluğun % 98,16’ya yükselmesine neden olmuştur. Yine merkez bölgede 31,96 GPa sertlik elde edilmiş olup, kırılma tokluğu değeri 5,87 MPa·m^{1/2} değerine yükselmiştir. Yapılan balistik test sonucunda, monolitik bor karbüre kıyasla, Al ilaveli B₄C zırh kompoziti iz derinliğinin 3,10 mm’ye düşmesine neden olmuş, balistik etki faktörü ise Al katkısı ile artan ortalama malzeme yoğunluğuna rağmen 4,93 değerine yükselmiştir.

% 5 Si ilavesi ile gerçekleştirilen çalışmalarda, B₄C’ye kıyasla daha düşük ergime noktasına sahip olan Si, spark plazma sinterleme sıcaklığının 1500 °C’ye düşmesine neden olmuştur. Bu sıcaklığın üstündeki sıcaklıklarda sinterleme yapıldığı durumda ise numunelerin kalıba ciddi şekilde yapışarak, tek parça çıkarılamaması söz konusu olmuştur. Spark plazma sinterleme deneyleri sonucunda elde edilen Si ilaveli bor karbür numunelerin yoğunlukları düşük kalmış, sinterleme sıcaklığı artırılmadığı için bir diğer sinterleme artırıcı mekanizma olan basınç artırımı gerçekleştirilmiştir. 60 MPa’a yükseltile basınca yapılan deneyler sonucu merkez bölgede % 97,54 yoğunluk elde edilmiştir. Numunenin aynı bölgesindeki sertlik değeri 32,32 GPa iken kırılma tokluğu 5,41 MPa·m^{1/2} değerindedir. XRD ve EDS çalışmaları uygulanan numunede, yapıdaki tüm Si’un B₄C ve proses esnasında kullanılan grafit kalıplardan C olarak, SiC’ e dönüştüğü görülmüştür. Balistik test sonucu 8,52 mm iz derinliği elde edilen hacimce % 5 Si içeren numunede, balistik etki faktörü 4,43 olarak hesaplanmıştır.

Ti ilaveli B₄C çalışmalarında iki farklı toz boyutuna sahip Ti tozları kullanılmıştır. İlk grup deneylerde 26,46 µm ortalama tane boyutlu kaba taneli Ti tozu kullanılırken, ikinci grup deneylerde 5,12 µm ortalama tane boyutlu Ti tozları kullanılmıştır. Kaba taneli Ti tozu ile yapılan deneyler, karışımda hacimce % 5, 10, 15 ve 20 Ti içerecek şekilde hazırlanmış, ince taneli tozlarda ise sadece hacimce % 5 ve 10 Ti ilavesi gerçekleştirilmiştir. Deneyler sonucunda Ti ilavesinin B₄C yapısında yoğunluk, sertlik, kırılma tokluğu ve balistik performans açısından çok efektif bir katkı olduğu sonucuna ulaşılmıştır. Hacimce % 20 kaba taneli Ti ilavesi içeren bor karbürün hem merkez hem de köşe bölgelerinden birinde teorik yoğunluğa ulaşılmıştır. Ayrıca, % 5 ince taneli Ti ilaveli bor karbürün 1550 °C’de 6 dakika süre ile 40 MPa basınç altında spark plazma sinterlenmesi sonucu da yine hem bir köşe hem de merkez bölgede teorik yoğunluk elde edilmiştir. Yapıya katılan Ti’nin ilave miktarından bağımsız olarak, her durumda TiB₂’e dönüştüğü görülmüştür. Mikroyapılar incelendiğinde, bor karbür matrisi içerisinde düzensiz olarak dağılmış merkezinde C içeren TiB₂ aglomereleri elde edilmiştir. Balistik test sonucunda, hacimce % 5, 10, 15 veya 20 Ti içeren tüm bor karbür numunelerinin balistik performansının belirgin bir şekilde arttığı görülmüş ve 0,80 gibi çok düşük iz derinlik değerleri elde edilmiştir. Hacimce % 5 kaba taneli Ti içeren bor karbür numunesinin balistik etki faktörü 5,00 olarak hesaplanmıştır.

Ti katkısının B₄C matriste TiB₂’e dönüşerek hem mekanik özelliklerin iyileşmesine hem de efektif balistik artışa sebep olmaları nedeni ile B₄C içerisinde TiB₂ oluşumuna sebep olacak TiO₂ katkısının özelliklere etkisi de ayrıca incelenmiştir. Hacimce % 5 ve 10 oranında yapılan TiO₂ ilavesi sonucu yapıda bulunan tüm TiO₂’nin B₄C ile reaksiyona girerek TiB₂ ve CO₂ oluşumuna neden olduğu görülmüştür. Bu mikroyapılar incelendiğinde Ti ilavesinde elde edildiği gibi aglomereler yerine, homojen disperse olmuş küçük TiB₂ taneleri elde edilmiştir. Fakat Ti ile kıyaslandığında TiO₂ ilavesi sinterlemeye daha az katkı sağlamış olup, son ürünün merkez yoğunluğu en yüksek % 98,25 değeri ile 1550°C’de 6 dakika süre ile 40 MPa basınç altında üretilen ve hacimce % 5 TiO₂ içeren bor karbür numunesinde görülmüştür. Aynı numunenin merkez sertlik değeri 30,98 GPa ölçülürken, kırılma tokluğu değeri ise 6.07 MPa·m^{1/2} olarak hesaplanmıştır.

1. INTRODUCTION

Boron carbide (B₄C) ceramic is a covalently bonded carbide. In B₄C, carbon atoms bond to boron atoms by sharing a pair of electrons and, like all covalent bonds, these atoms form definite bond angles. The bonding is achieved by the hybridization of the valence electrons of the respective atoms [1]. B₄C is a very important industrial material with many current and potential applications. The structural characteristics of boron carbide can be reviewed as; high melting temperature, thermal and chemical stability, low density, low atomic weight, useful semiconductor properties, extremely high hardness, and high neutron absorption cross-section [1,2].

Boron carbide is the hardest material after diamond and cubic boron nitride, and it maintains its hardness to 1800 °C [2,3]. Hardness is a complex mechanical property of materials which involves elastic and plastic deformation, crack initiation, and the development of new surfaces. It can be defined in terms of bonding energy, covalency level, atomic spacing, and by the parameters of fracture and deformation characteristics. Hardness is dependent on the fabrication process, composition and the presence of impurities [2,4,5].

Boron carbide is characterized by flexure strength values on the order of 350 MPa [1,6]. Density of boron carbide varies with carbon concentration as $\rho = 2.422 \text{ g/cm}^3 + 0.0048 [\text{at.}\% \text{ C}]$, with a commonly reported value of 2.52 g/cm^3 corresponding to the B₄C stoichiometry. This combination of high strength and low density makes boron carbide one of the most attractive structural materials known. As expected of both a ceramic and a strong material, boron carbide has relatively low fracture toughness. Values of K_{IC} for boron carbide are given at $\sim 1.3 \text{ MPa}\cdot\text{m}^{1/2}$. [1,6,7]

There is considerable interest in the application of boron carbide as lightweight armor material due to its exceptional hardness, outstanding elastic properties and low theoretical density. From the ballistic viewpoint, of particular interest is the response of boron carbide to shock loading [6]. Military and civilian ballistic protection is divided into flexible lightweight protection and massive, stiff armor. For personnel

protection as well as protection of aircrafts and cars only light and flexible materials can be used [8]. Lightweight engineering in advanced product development is mainly based on composite technologies [9]. While high hardness is one of the very important requisite indicators for a material's ballistic potential, toughness might play an equally important role. Only materials with both high hardness and high fracture toughness are expected to yield the desired high ballistic performance [10]. Majority of the material scientists are in the same opinion that in 10-15 years, almost all the light and medium vehicle armor will be ceramic and it may eventually supplant the metal armors on the heavy vehicles [11]. In the light of these, boron carbide matrixed composites are very good candidates for ballistic protection and the new development and research is essential for boron carbide as an armor material.

The most common way of producing ceramic armor tiles is sintering the powder material. Pressureless sintering, hot pressing and hot isostatic pressing are the traditional manufacturing methods for ceramic tiles. However, sintering of covalently bonded pure boron carbide has proven difficult [12,13]. Sintering of covalently bonded materials is generally much more difficult than densification of oxide ceramics or metals. This is not only due to the low self-diffusion (poor tendency towards grain boundary and volume diffusion), high ratio of grain boundary to surface energies and high vapor pressure of particular constituents (strong tendency towards surface diffusion and evaporation/recondensation), but also due to their extreme sensitivity to environmental factors such as sintering atmosphere, traces of contaminants, particle size and distribution, temperature gradients etc. The sintering of boron carbide requires (i) oxygen removing additives such as graphite, carbon black or organic deoxidation agents such as formaldehyde resin, (ii) very fine powders of high surface area and therefore high driving force, (iii) high temperatures to enable grain boundary and volume diffusion, and if everything fails, (iv) high pressures [13].

On the other hand, spark plasma sintering (SPS), also known as the field-activated sintering technique and pulsed electric current sintering, is a comparatively novel sintering process that allows fabrication of bulk materials from powders using a fast heating rate (up to $1000\text{ }^{\circ}\text{C min}^{-1}$) and short holding times (in most cases 0–10 min) at low sintering temperatures ($200\text{--}300\text{ }^{\circ}\text{C}$ lower than most of the conventional sintering techniques). Because of its great advantages, SPS is by far the most popular of the ultrarapid sintering techniques, and is used to process nanostructured materials,

amorphous materials, intermetallic compound, metal matrix and ceramic matrix composites, highly refractory metals and ceramics, etc., which are difficult to sinter by common methods [14]. That is why, densification of boron carbide by using spark plasma sintering technique is one of the prominent research topics in materials science.

In this study, boron carbide powders were first directly spark plasma sintered and the properties of boron carbide mixed with various amounts of C-black, CNT, Al, Si and Ti additives are compared. All the mixtures are mixed by ball milling in ethanol medium by using proper balls. Then the dried powders were directly loaded into graphite dies and spark plasma sintering procedure were carried out. Various sintering temperatures differing from (1450 to 1725 °C), different pressure values (40 to 50 MPa), 100 °C/min heating rate, 4 to 6 min holding times at sintering temperatures, vacuum and argon atmospheres were the different parameters changed during spark plasma sintering temperatures. The uniqueness of this study can be regarded as the geometry and the dimensions of the final product. Because the aim of the study was to produce a final product which can be directly used as an armor material, the geometry has chosen to be hexagonal and the final hexagonal prism had 31.5 mm side and 62 mm diagonal length, whereas the thickness was at least 10 mm depending on the densification rates.

After spark plasma sintering procedure, the densification of ceramics and composites were measured by using Archimedes method. The mechanical characterization of materials were done by measuring the Vickers microhardness and fracture toughness of the samples. The microstructures of all the samples were observed by using SEM (Scanning Electron Microscopy). Also, the depth of penetration (DOP) values which shows the ballistic performances of the ceramic and composite tiles were obtained in ROKETSAN A.Ş., Ankara, according to NIJ 0101.04 standards. In the experiments, 7.62x50 mm NATO armour piercing bullets were used. Although, steel is generally used as backing block in such systems, a more ductile material, aluminum 5083 alloy has been chosen this time, in order to see and be able to make the comparison of the occurred depths more clearly.



2. BORON CARBIDE

As mentioned in the introduction section, B_4C is the third hardest material after diamond and cubic boron nitride, thanks to its very strong covalent bonds between boron and carbon atoms.

A boron carbide compound was discovered in 1858, then Joly in 1883 and Moissan in 1894 prepared and identified the compounds B_3C and B_6C , respectively. The 'stoichiometric formula' B_4C was only assigned in 1934 [1]. It was not until the end of World War II that the first major applications were developed particularly in the nuclear industry [2]. After 1950, numerous and various studies were made on structure and properties of boron carbide [1,2].

In the boron-carbon phase diagram, which can be seen in Figure 2.1, the rhombohedral boron carbide phase exists in the homogeneity range $B_{4.0}C$ (20 at % C) to $B_{10.4}C$ (8.8 at % C) [15] ; this phase is a complex solid solution [1,15,16]. Since B_4C is in equilibrium with free carbon and is only boundary between B_nC and B_nC_2C (where $4 < n < 10$) synthesis of B_4C without free carbon is a great challenge [17]. Carbon content of boron carbide greatly influences the structure and the properties of the compound and hence the exact knowledge of B/C ratio of the phase is very important [1,17].

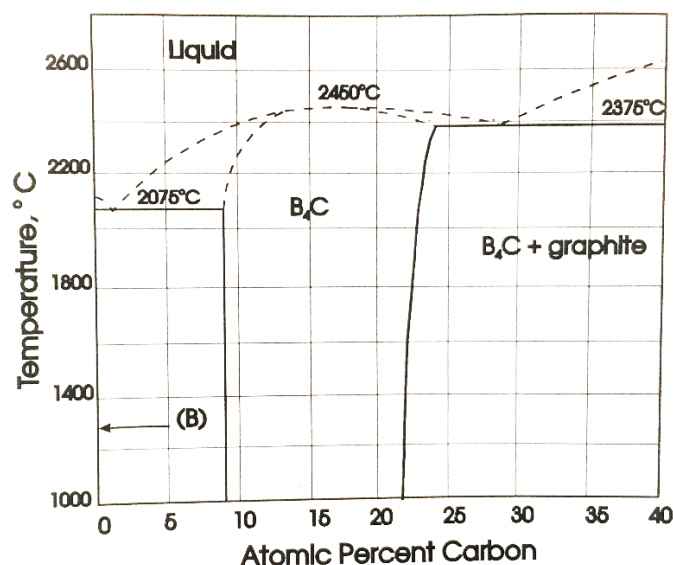


Figure 2.1 : Boron-carbon binary phase diagram [2].

2.1 Crystal Structure of Boron Carbide

The most widely accepted crystal structure of boron carbide is rhombohedral, consisting of 12-atom icosahedra located at the corners of the unit cell [17]. Schematic diagram of the structure of boron carbide can be found in Figure 2.2.

The atoms B and C can interchange within both the icosahedral and inter-icosahedral atomic chains. This forms the basis for a wide homogeneity range for the boron and carbon system. Three carbon atoms commonly studied, such as in $B_{12}C_3$ along the intericosahedral chain, can be completely or partially substituted by vacancies or a number of different atoms, so that stoichiometry can form boron-rich and carbon-rich enantiomers [18].

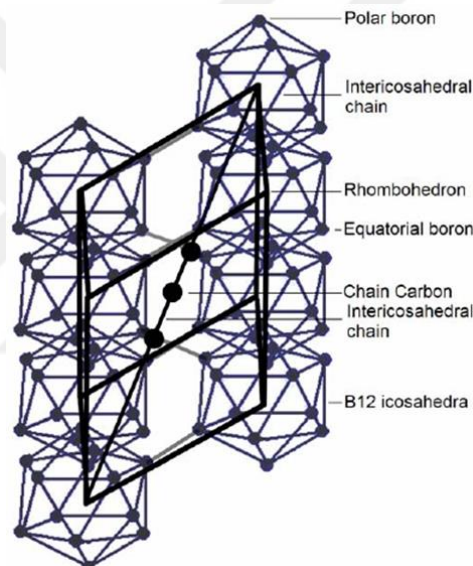


Figure 2.2 : The crystal structure of boron carbide [18].

Three atom linear chain (C-B-C) is seen in the longest diagonal of the rhombohedral unit cell. Each end element of the chain is covalently bonded to an atom of three different icosahedra. In general, icosahedra consist of 11 boron atoms and one carbon atom. The locations of carbon atoms within different icosahedra are not ordered relative to one another. The icosahedral configuration is the result of a tendency to form three-centre covalent bonds due to the lack of valence electrons of boron. Two crystallographically inequivalent sites exist in the icosahedron. Six atoms occupy in two polar triangles at the opposite ends of the icosahedron and the remaining six atoms reside equatorial sites. The atoms in the polar sites are directly bonded to neighbouring icosahedra via strong two-centre bonds along the cell edges. The atoms in equatorial

sites either bond directly to other icosahedra through threecentre bonds or to chain structures [17-18].

The bonds between the carbon and boron atoms as well as the boron atoms themselves in the icosahedra are strongly covalent. However, the difference between the atomic spacing of boron carbide and the sum of their ionic radii results in some ionicity. The calculated covalent bond energy E_0 is 9.42 eV, while the ionic bond energy E_p of boron carbide is 1.41 eV [2].

The lattice parameter values referring to hexagonal structure of boron carbide having the formula of $(B_{11}C)CBC$ are $a_0=0.55991$ nm and $c_0=1.20740$ nm, and the unit cell volume is 3.27809 nm³ [2]. Crystal lattice parameters lie within the intervals: $0.5594 \leq a \leq 0.5672$ nm, $1.1977 \leq c \leq 1.2314$ nm [19]. The change in lattice parameters may be the cause of several factors. Both lattice parameters decrease with decreasing carbon content [2]; small impurity concentrations can have a very large effect on the lattice parameter; and internal stresses may affect lattice parameters values [1,17].

2.2 Characteristics and Properties of Boron Carbide

The high refractoriness of boron carbide due to its high melting point allows it to be used for high-temperature applications. On the other hand, it is one of the hardest solid after synthetic diamond and cubic boron nitride. Actually under high temperatures above 1300 °C, its hardness exceeds that of diamond and cubic boron nitride. The Poisson ratio of boron carbide indicates its high anisotropy. It has a high compressive strength that may vary according to its density and percentage purity. It has a very low thermal conductivity. With such a strength-to-density ratio and low thermal conductivity, boron carbide looks promising and ideal for a wide variety of applications. Because of its high hardness, boron carbide succeeded in replacing diamond as a lapping material. Boron carbide is a material with excellent properties. It has a list of important properties such as ultimate strength to weight (density) ratio, exceptionally high hardness, and high melting and oxidation temperatures. In addition, it has a very low thermal expansion coefficient. However, owing to its high Young's modulus, it possesses less thermal shock resistance. Boron carbide is stable toward dilute and concentrated acids and alkalis and inert to most organic compounds. It is slowly attacked by mixtures of hydrofluoric-sulfuric acids or hydrofluoric-nitric acids. It resists attack by water vapor at 200 to 300°C. However, it is attacked rapidly

when put in contact with molten alkali and acidic salts to form borates [20]. The general characteristics and properties of boron carbide are listed in Table 2.1.

Table 2.1 : The summary of general characteristics and properties of boron carbide [2].

Characteristic or Property	Value
Composition	(B ¹¹ C)CBC
Molecular Weight (g/mol)	55.26
Color	Black (pure crystal is transparent and colorless)
X-Ray Density (g/cm ³)	2.52
Melting Point	2400°C (does not decompose)
Specific Heat (J/mole.K)	50.88
Heat of Formation (-ΔH) (kJ/mol.K)	57.8 ± 11.3
Thermal Conductivity (W/m.°C)	30
Thermal Expansion (10 ⁻⁶ /°C)	4.3
Electrical Resistivity (Ω.cm)	0.1-10
Seeback Coefficient (μV/K)	200 - 300
Vickers Hardness (GPa)	27.4 - 34.3
Modulus of Elasticity (GPa)	290 - 450
Shear Modulus (GPa)	165 - 200
Bulk Modulus (GPa)	190 - 250
Poisson's Ratio	0.18
Flexural Strength (MPa)	323 - 430
Compressive Strength (MPa)	2750
Oxidation Resistance	In air up to 600°C.

Elastic and mechanical properties of boron carbide are derivative of such characteristics of atomic bonding as localization and delocalization, ionicity and covalence of the bonds and electron density in inter-atomic regions. In particular, higher stiffness and hardness is associated with more localized covalent bonds and higher inter-atomic electron density [6].

2.3 Applications of Boron Carbide

Due to these outstanding properties, boron carbide finds lots of application areas. The major industrial use of boron carbide is as abrasive grit or powder. Particle sizes are available from 1 μm to 10 mm, used as polishing, lapping and grinding media for hard materials such as cemented carbides, technical ceramics, etc. Boron carbide can be regarded as an economic technical ceramic because it is far less expensive than

diamond which is the perfect grinding media. A second category is wear-resistance components made of hot-pressed sintered pieces. Boron carbide sand-blasting nozzles are characterized by minimum wear, even with silicon carbide or corundum grit [1].

Boron carbide is a high-temperature semiconductor and is used as a material for thermocouple electrodes utilized at elevated temperatures in inimical environments where metallic electrodes decay rapidly [19].

In nuclear reactors, boron carbide is used as a material for rods that controls the kinetics of nuclear fusion [19]. The main part (95%) of nuclear power is now produced in reactors controlled by two kinds of absorbing materials: boron carbide (B_4C) or a ternary alloy (Ag-In-Cd). Boron carbide is a neutron absorber widely used because of its high B content, its good chemical inertness and high refractoriness [1]. Absorption capacity of boron carbide can be increased by enriching B^{10} isotope. Composite material containing boron carbide with good thermal conductivity and thermal shock resistance are found suitable as first wall material of nuclear fusion reactors [17, 21, 22]. Boron carbide based composites are potential inert matrix for actinide burning [23]. Boron carbide is also used for treatment of cancer by neutron capture therapy [17, 24]. Boron carbide is highly stable chemically in various aggressive environments [19].

2.3.1 Boron carbide as an armour material

Ballistic protection is required for personal use, vehicles and permanent structures which are subject to ballistic threats [8]. The development of lightweight and inexpensive ceramic armor is under ongoing consideration by both ceramic armor manufacturers and armor users [25].

Ceramic armor systems consist, in general, of a monolithic ceramic body bonded with a soft but high tensile strength backing material such as special fiber lining (e.g. KevlarTM, SpectraTM or fiberglass) and sometimes, with soft metals (e.g. aluminum). Upon impact of the bullet with a high velocity (700-900 m/sec or greater), and kinetic energy of 2-4 kJ, the hard-faced ceramic is cracked and broken, and the residual energy is absorbed by the soft reinforced backing material. This backing material also supports post-impact fracturing of the ceramic body caused by the bullet and the bullet itself. Structure and properties of ceramic facing material and its manufacturing

features are the significant factors affecting ballistic energy dissipation and, hence, performance of ballistic protection systems [25].

Among different structural ceramics, some types of oxide ceramics (mostly alumina ceramics) and non-oxide ceramics (mostly carbides, nitrides, borides) are commonly used for ballistic protection systems. General properties of some armor ceramics can be found in Table 2.2.

Table 2.2 : General properties of monolithic armor ceramics [25].

Ceramics	Density (g/cm ³)	Vickers Hardness (GPa)	Fracture Toughness (MPa.m ^{1/2})	Young's Modulus (GPa)	Sonic Velocity (km/sec)	Flexural Strength (MPa)
Al ₂ O ₃	3.60-3.95	12-18	3.0-4.5	300-450	9.5-11.6	200-400
Al ₂ O ₃ -ZrO ₂	4.05-4.40	15-20	3.8-4.5	300-340	9.8-10.2	350-550
SiC-Sintered	3.10-3.20	22-23	3.0-4.0	400-420	11.0-11.4	300-340
SiC-Hot Pressed	3.25-3.28	20	5.0-5.5	440-450	11.2-12.0	500-730
Si ₃ N ₄ -Hot Pressed	3.20-3.45	16-19	6.3-9.0	-	-	690-830
B ₄ C-Hot Pressed	2.45-2.52	29-35	2.0-4.7	440-460	13.0-13.7	200-500
TiB ₂	4.55	21-23	8.0	550	-	350
TiB ₂ -Hot Pressed	4.48-4.51	22-25	6.7-6.95	550	11.0-11.3	270-700
AlN-Hot Pressed	3.20-3.26	12	2.5	280-330	-	300-400

Oxide ceramics, in particular alumina ceramics, have specific physical properties that are suited for armor applications. Although alumina ceramics have an elevated density (up to 3.95 g/cm³), they are of low cost and may be manufactured by a variety of methods, i.e. slip casting, pressing and some others, without any use of expensive equipment. However, in general, non-oxide armour ceramics such as boron carbide, silicon carbide, silicon nitride, titanium diboride and some others, including the materials based on their binary systems, have high physical properties and relatively low density that are more beneficial for ballistic applications than alumina ceramics [25].

Kaufmann et al. studied ballistic performance of modified alumina, boron carbide and silicon carbide tiles with similar relative density and thickness properties by measuring the depth of penetration values when impacted by a 12.7 mm (0.50 Caliber) AP

projectile. They concluded that at an impact velocity of 850 and 910 m/s, the silicon carbide and boron carbide ceramics had similar DOPs, approximately five times less than the DOP for the alumina and modified alumina ceramic materials. When they calculated the ballistic efficiencies of tested materials, they found out that alumina and modified alumina display lower ballistic efficiencies than silicon carbide and boron carbide. The ballistic efficiency of modified alumina is slightly better than standard alumina [26]. The development and selection of ceramic armor is often based on a traditional approach, i.e. it is assumed that ceramic armor should be denser, harder and stronger (like ceramic cutting tools). This approach is correct in many cases, especially for the single-hit ballistic applications, when a ceramic tile has only to stop one projectile [25].

While high hardness is one of the very important requisite indicators for a material's ballistic potential, toughness might play an equally important role. Only materials with both high hardness and fracture toughness are expected to yield the desired high ballistic performance. Therefore, a significant increase in fracture toughness of boron carbide based composites has the potential for realization of significantly improved armor material systems [10]. Porosity in B_4C , as in all ceramics, decreases its fracture strength. Upon impact from a projectile, microstructural inhomogeneities such as porosity and weak second phases can lead to local tensile fracture during passage of the initial shock wave, significantly lowering ballistic performance. Thus, ceramic armor must be sintered as closely as feasible to its theoretical density, particularly in the hypovelocity (velocity of the projectile is lower than the speed of sound through the armor material) ballistic impact regime [27].

Ballistic test results showed that some dense carbide based ceramics including silicon carbide and boron carbide may demonstrate elevated ballistic shattering. Although these materials stop bullets thanks to their very high hardness, the damaged zone is characterized by many small ceramic microcrack features and a comminuted powder. The surrounding zone with long cracks is not very strong and usually these armors exhibit limited capabilities for multi hit ballistic applications [25]. The boron carbide ceramic tiles should be evaluated for single hit ballistic materials.

2.4 Production of Boron Carbide

There are various ways of boron carbide production. The methods of boron carbide synthesis can be listed as; carbothermic reduction, magnesiothermic reduction, synthesis from elements, vapour phase reactions, synthesis from polymer precursors, liquid phase reactions, ion beam synthesis and VLS growth [17].

The first three common production methods for boron carbide powders will be explained deeply in next subtitles. However, subsequent five production techniques in the above list will not be explained because they are generally used for boron carbide coating. This thesis is interested with production of ballistic boron carbide from high purity micron sized starting powder; so the extensive explanations for boron carbide coating techniques is found to be irrelevant with the concern of this thesis.

When the first three production techniques are compared, one can conclude that although, boron carbide powder can be synthesized from elemental boron and carbon directly, the high cost of these elements has made this method economically unattractive [28]. Metallothermic and carbothermic processes which are inexpensive, have been widely used to produce boron carbide powder. Boric acid (H_3BO_3) and boron oxide (B_2O_3) are inexpensive starting materials, which can be reduced by using carbon to produce boron carbide. The powder prepared by this method has morphology and surface characteristics suitable for hot pressing and hot isostatic pressing [28,29].

On the other hand, the strong covalent bonds and low self-diffusion coefficient of B_4C result in the poor sustainability and densification, which leads to the generation of B_4C in the tens of micrometer range. The obtained B_4C has to be ground to a desirable smaller particle size for further application. In addition, the residual free carbon in final powder is a serious problem that should be taken into consideration. Therefore, for business interests, an important challenge is to develop an approach that can synthesize pure finegrained B_4C powder at lower temperature [29].

2.4.1 Carbothermal reduction of boron oxide

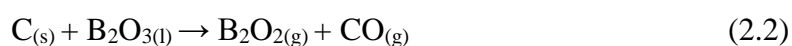
B_4C powder is commercially synthesized by carbothermal reduction of boron oxide (B_2O_3) and carbon powder at high temperature (usually above $1750\text{ }^\circ\text{C}$), and the whole synthesis process can be divided into two main steps: (i) pyrolysis of boric acid (BA)

and the formation of B₂O₃; (ii) reduction and carbonization between B₂O₃ and carbon to form B₄C [28,29].

Boron carbide is produced by the carbothermal reduction of boron oxide via the equation 2.1:



This reaction is highly endothermic, possessing a ΔH of 1812 kJ/mol, and is typically performed in an electric furnace [1]. For a CO pressure equal to 1 atm, the above reaction exhibits a ΔG that is zero at 1561 °C and negative at higher temperatures. However, temperatures in excess of 2000 °C are required for the reaction to proceed at an acceptable rate [30]. It is important to note that certain gas-solid reactions may occur during boron carbide synthesis. At the high temperatures required for the production of boron carbide, B₂O₃ transitions into a liquid at ~452 °C and boils at ~1860 °C [31]. As a result, boron oxide has a significant vapor pressure at the reaction temperature, so the loss of boron via evaporation may be a production concern. The reduction of liquid B₂O₃ with carbon produces the volatile suboxide B₂O₂ starting at 1227 °C. The reaction of B₂O_{2(g)} with excess carbon results in a gas-solid reaction mechanism for the production of boron carbide as can be seen as below equations 2.2 and 2.3:



After these reactions, large pieces of boron carbide are removed from the reactor and crushed and milled to produce a fine powder. The powder is then cleaned with HCl to remove any metal impurities imparted to the powder during mechanical processing [1,31].

2.4.2 Magnesiothermic reduction of boron oxide

The magnesiothermic reduction is a self-propagating high temperature synthesis (SHS), which is the way for preparation of various materials. In this method, reaction starts by external heating and continues with energy supplied by the reaction. Anyway, it is difficult to control the SHS reaction process because of the high exothermic effect in a few seconds. In this technique, final products have many types of impurities such

as $Mg_xB_2O_{(x+1)}$ ($x = 2, 3$), B_xO , MgB_x ($x = 2, 4, 6$), and leached final powders have low purity about 88 wt % and product has a large particle size distribution like 0.5–5 μm [32].

As the vapour pressure of magnesium is high at the reaction temperature of $>1000^\circ C$, a cover gas such as argon or hydrogen is used and also the system pressure maintained high. The products of the reaction are processed by aqueous methods to remove magnesium oxide from boron carbide. The carbide is still contaminated with magnesium borides formed as stable compounds. This reduction technique yields very fine amorphous powder, which is well suited for use in the fabrication of sintered products. One method of controlling the temperature and the particle size of the product is by choosing the right size of the reactants. Post reductive sintering at temperatures 200–300 $^\circ C$ higher than the reaction temperature increases the particle size of the product. Seeding of the charge with a small quantity (1–2%) of boron carbide has been found to increase the growth of B_4C particles and the yield significantly [17, 33].

Exothermic magnesiothermic reduction of boron oxide in the presence of carbon is a convenient method for producing boron carbide of small particle size:



The reaction seen in equation 2.4 occurs in two stages equations 2.5 and 2.6:



This reduction synthesis produces fine powders which are very useful to synthesize ceramic bodies. The amount and grain size of the reactants, particularly the carbon, influences the reaction temperature and particle size of the nano sized product. Porous materials can be used as templates to produce reactive mesoporous carbons with high surface areas and large massive pores [34].

2.4.3 Synthesis from elements

Synthesis of boron carbide from its elements is considered uneconomical due to the high cost of elemental boron and hence employed for specialised applications only,

i.e. nuclear applications where B¹⁰ enriched or very pure boron carbide powder is needed. To synthesize enriched boron carbide, carbothermic reduction is not preferred due to loss of boron as well as boron hold-up in the furnace and hence “synthesis from elements” is the only suitable economical method.

Even though boron carbide formation from its elements is thermodynamically possible at room temperature, the heat of reaction (239 kJ/mol) is not sufficient to carry out in a self-sustaining style [30]. Formation of boron carbide layer slows down further reaction, due to slow diffusion of reacting species through this layer, thus necessitating high temperature and longer duration for complete conversion of the elements into the compound. For synthesis from elements, boron and carbon are thoroughly mixed to form uniform powder mixture, which is then pelletised and reacted at high temperatures like 1500°C in vacuum or inert atmosphere. The partially sintered pellet of boron carbide is then crushed and ground to get fine B₄C powder. To achieve a high purity product of B₄C, high purity elemental boron powder produced by fused salt electrolytic process is often used [17, 35].

Shock wave method have also been tried for boron carbide formation from amorphous boron and graphite powder by using trimethyl enetrinitramine as detonator [36]. Various morphologies, such as filaments, distorted ellipsoid, plates and polyhedron particles of nanosize are obtained. In this method, reactants are kept inside a steel container which is placed in plastic tube, and the detonator is set between container and the plastic tube. Initiation of explosive detonation was carried out by an electric detonator. After the shock treatments, samples were recovered by shaving off the container with a lathe. In this procedure, very high heating and cooling rates are achieved along with high pressure. The chemical reaction is very fast and completed in micro to milliseconds. Consequently, shock wave method is suitable for the preparation of crystals of various morphology and non-equilibrium phases which are hard to be produced in thermal equilibrium conditions [17].



3. SINTERING

Almost all ceramic bodies must be sintered to produce a microstructure with the required properties. This widespread use of the sintering process has led to a variety of approaches to the subject. In practice, the ceramist, wishing to prepare a material with a particular set of properties, identifies the required microstructure and tries to design processing conditions that will produce this required microstructure. The key objective of sintering studies is therefore to understand how the processing variables influence the microstructural evolution [37]. Sintering is the process of transforming a powder into a solid body using heat [38].

In order to understand sintering of ceramics, both experimental studies (measuring the sintering behavior empirically under a set of controlled conditions) or database and modelling studies have still been conducted. The theoretical analyses and experimental studies performed over the last 50 years have produced an excellent qualitative understanding of sintering in terms of the driving forces, the mechanisms, and the influence of the principal processing variables such as particle size, temperature, and applied pressure. However, the database and models are far less successful at providing a quantitative description of sintering for most systems of interest [37].

Some parameters, such as the sintering temperature, applied pressure, average particle size, and gaseous atmosphere, can be controlled with sufficient accuracy. Others, such as the powder characteristics and particle packing, are more difficult to control but have a significant effect on sintering. While partial information exists in the other areas of behavior, characterization measurements, and the data base, much critically needed information is severely lacking. This lack of information coupled with the complexity of practical ceramic systems makes quantitative predictions of the sintering behavior very difficult even for the simplest systems [37].

For sintering to occur, there must be a decrease in the free energy of the system. The curvature of the free surfaces and, when used, the applied pressure provide the main motivation or driving force for sintering to occur. However, to accomplish the process within a reasonable time, the kinetics of matter transport should also be considered.

In crystalline ceramics, matter transport occurs predominantly by diffusion of atoms, ions, or other charged species. Solid-state diffusion can occur by several paths that define the mechanisms of diffusion and, hence, the mechanisms of sintering. The rate of diffusion depends on the type and concentration of defects in the solid, so an understanding of the defect structure and the changes in the defect concentration (the defect chemistry) is important. Also one should understand how the defect chemistry is controlled by key variables in the sintering process such as temperature, gaseous atmosphere, and solutes (dopants) [37].

In order to predict how the rate of sintering depends on the primary processing variables, equations for the flux of matter must be formulated and solved subject to the appropriate boundary conditions. Matter transport can be viewed in terms of the flux of atoms (ions) or, equivalently, in terms of the counterflow of vacancies. Following Fick's laws of diffusion, the flux can be analyzed in terms of the concentration gradient of the diffusing species, but the equations take a more generalized form when expressed in terms of the chemical potential (the molar Gibbs free energy). In this view, the matter transport occurs in the direction from the regions of higher chemical potential to lower chemical potential. In inorganic solids, these various ions or charged species diffuse at different rates, however the matter transport has to take place in such a way that the stoichiometry and electroneutrality of the solid are preserved. The diffusion of the ions is therefore coupled and this is referred to as the ambipolar diffusion [37].

3.1 The Sintering Process

Sintering is fundamentally a one-way event. Once sintering starts, surface energy is consumed through particle bonding, resulting in increased compact strength and often a dimensional change [39]. Accordingly, the definition of sintering is as follows:

“Sintering is a thermal treatment for bonding particles into a coherent, predominantly solid structure via mass transport events that often occur on the atomic scale. The bonding leads to improved strength and lower system energy” [40].

Necks grow between the contacting spheres, providing strength and rigidity. Longer sintering gives a larger neck and usually more strength. The emergence of the necks between is driven by the system thermodynamics, while the rate of sintering depends

mostly on the temperature. At room temperature, the atoms in a material are not noticeably mobile, so the particles do not sinter. However, when heated to a temperature near the melting range, the atoms are very mobile. Atomic motion increases with temperature and eventually this motion induces bonding that reduces the overall system energy [39].

Early models for sintering realized that, since the sphere particles has much more surface area compared to flat plates, they have more surface energy. So that, early studies concerning sintering measured the neck size between spheres and plates, and subsequently between contacting spheres. The two-sphere model considers two equal-sized spheres in point contact that subsequently form a single larger sphere with a diameter 1.26 times the starting sphere diameter [39]. The sketch of model is given in Figure 3.1.

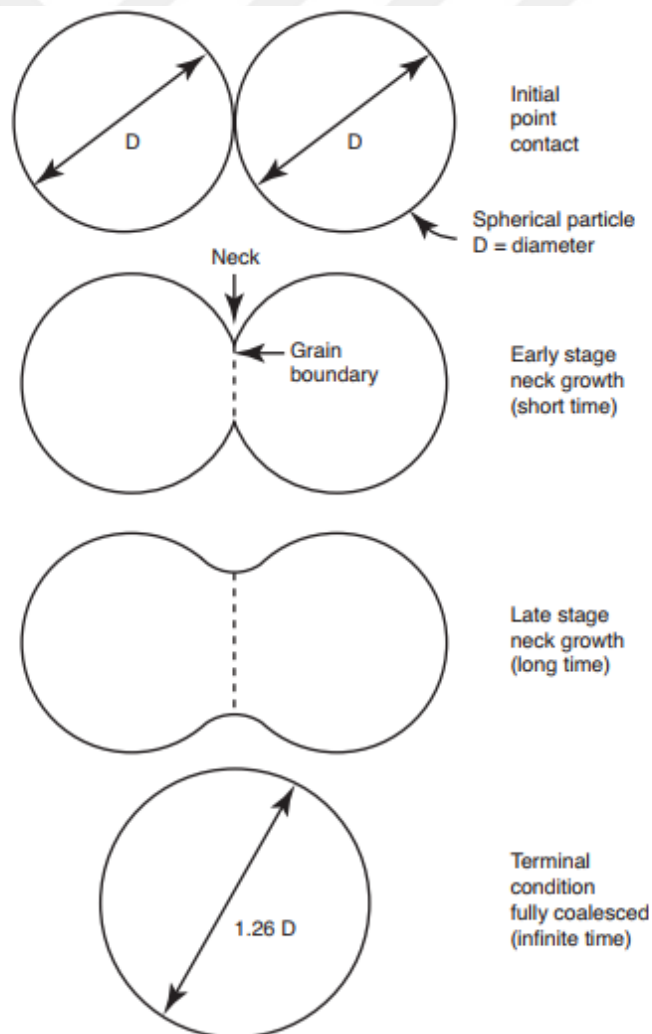


Figure 3.1 : Two sphere sintering model [39].

3.2 Thermodynamics and Stages of Sintering

Sintering occurs in stages, as shown in Figure 3.2. In dense random packages, a packing density of 64% is observed. At the first sintering stage, the neck grows up between particles whose neck size is less than one third of the particle size. There are usually small size changes, so 3% linear shrinkage is seen at the beginning. For loose spheres this generally corresponds to a density below 70 % of theoretical. In the intermediate stage, sintering shows that the necks are larger than one-third of the particle size, but less than half of the particle size. For a system that densifies, this corresponds to a density range from 70 % to 92 % for spheres. During the intermediate stage, the pores are tubular in character and connected (open) to the outer surface. The sintering body is not hermetic so the gas can pass in or out during the process. The final sintering stage corresponds to the elimination of the last 8% porosity, where the pores are no longer open to the external surface. Isolated pores, associated with the final stage sintering, are filled with the atmosphere of the process [39].

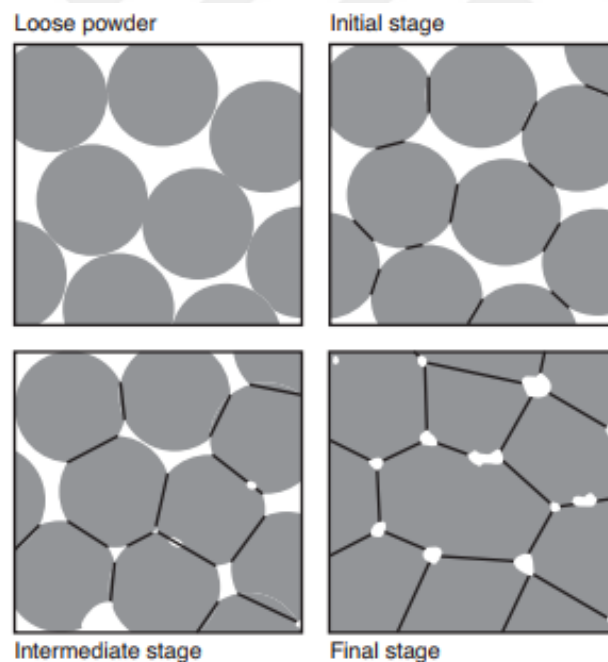


Figure 3.2 : Sintering stage illustration [39].

Transport mechanisms describe how mass flows in order to lower the system energy during sintering. There are two classes of sintering mechanisms: surface transport and bulk transport. Each one consists of several atomistic events that contribute to bonding. The pores are large deposits of vacancies, so the sintering mechanisms define the vacancy motion and annihilation during heating. Vacancies and atoms move along

particle surfaces (surface diffusion), across pores (evaporation-condensation), along grain boundaries (grain boundary diffusion), and through the lattice (viscous flow or volume diffusion). Moreover, vacancies mate with dislocations through plastic flow and dislocation climb [39].

Surface transport processes allow neck growth without any change in particle spacing (no shrinkage or densification) because the mass flow originates and ends up at the particle surface. The atoms are rearranged, however no annihilation of vacancies occurs. For surface transport controlled sintering, surface diffusion and evaporation-condensation are two contributors. Surface diffusion dominates the sintering of many metals and ceramics at low temperatures, while evaporation condensation is effective when the vapor pressure is high. Bulk transport processes results to improve the neck growth and shrinkage during sintering. In order to have better densification, the mass must be sourced from the particle interior with deposition at the neck. The vacancy annihilation occurs on the grain boundary by particle rotation and rearrangement [39].

Volume diffusion, grain boundary diffusion, dislocation climb, plastic flow and viscous flow are the basic bulk mass transport mechanism instruments. Plastic flow is essential during the heating time frame, especially for compacted powders where the initial dislocation density is high. Without fast heating, surface tension stresses are generally deficient to produce new dislocations and the dislocations are annihilated once they intersect a grain boundary or free surface. In this way, the role of plastic flow reduces as the dislocations are annealed out at increased temperatures. Interestingly, amorphous materials, such as glasses and polymers, sinter by viscous flow, where the particles are mixed at a rate that depends on the particle size and material viscosity. A type of viscous flow is also possible for metals with liquid phases on the grain boundaries. Grain boundary diffusion is sufficiently important for densification of most crystalline materials, and appears to dominate the densification of many common systems. Volume diffusion is most active when it is in cooperation with dislocation climb. In respect to the melting temperature, bulk transport processes are dominant at higher temperatures and surface transport processes are dominant at lower temperatures [39]. The sinter bond between the contacting particles is the critical region. It is the point where atoms are deposited to reduce the surface energy. Generally all of the key sintering measures relate to the mass transport rates and how they influence neck growth and change the pores and grains [39].

Regardless of what the transport mechanism, once the neck size achieves a thermodynamic equilibrium directed by the solid–vapor dihedral angle, additional neck growth happens if there is grain growth. Neck growth happens until the surface energy, dihedral angle and grain boundary energy accomplish a balance. Starting here on, neck growth takes after grain growth and generally both increase with the cube-root of time [39].

During the last stage of sintering, the pores are blocked by the pore structure as they attempt to continue to move at the grain boundaries. As shown in Figure 3.3, a migrating pore boundary combination leads to differential curvature between the front and the remaining faces. The corresponding vapor pressure gradient allows the pores to move with grain boundaries. The mass evaporates from the lower curvature surface and collapses onto the higher curvature surface. Densification in the final stage is critically dependent on minimized grain growth and pore bonding to grain boundaries. Vapor transfer provides one of the means for this process [39].

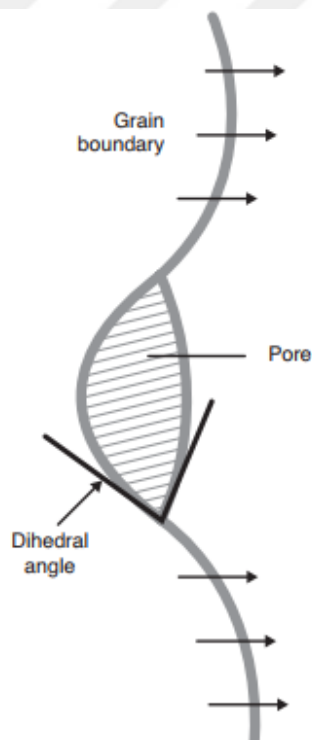


Figure 3.3 : Migrating pore and boundary [39].

Surface diffusion is active during heating to the sintering temperature. The activation energy for surface diffusion is less than that for other mass transport processes. Subsequently, it starts at a low temperature. Surface diffusion moderates as the surface defect structure is expended or as the available surface area is lost to sintering bonds.

It does not produce shrinkage. Therefore surface diffusion conflicts with densification. Surface diffusion is an initial contributor to the sintering of almost all materials. Boron and a few covalent ceramics exhibit surface diffusion dominance. Covalent ceramics show surface diffusion controlled sintering so it is common to add grain boundary dopants to actuate liquid phase sintering to achieve sintering densification. Surface transport processes are associated with pore smoothing and migration during the latter stages of sintering densification. [39].

3.3 Kinetics and Mechanisms of Sintering

The kinetics of sintering will clarify how quick sintering occurs, what is the path the atoms go for, and thus what is the final microstructure. Unquestionably thermodynamics is firmly related to the kinetics, and both will control the final microstructure of the sintered body [41].

The kinetics of densification are ordinarily defined in terms of the density or shrinkage of the material as a function of time or temperature. The bulk density, described as the mass divided by the volume of the body, or normally, the relative density (ρ) defined as the bulk density divided by the theoretical density of the solid, is used as density parameter. Relative density and the total porosity P of a solid are related by the equation 3.1 [39]:

$$\rho = 1 - P \quad (3.1)$$

In equation 3.2, the linear shrinkage is defined as $\Delta L/L_0$, where L_0 is the original length, L is the length at a given time or temperature, and $\Delta L = L - L_0$ (a negative quantity). If the shrinkage is isotropic, then:

$$\rho = \frac{\rho_0}{\left(1 + \frac{\Delta L}{L_0}\right)^3} \quad (3.2)$$

where ρ_0 is the initial relative density. Measurement of ρ or $\Delta L/L_0$ is easy to perform and provides substantial information about the rate of sintering. The densification rate, defined as $(1/\rho)(d\rho/dt)$, where t is the time, is equivalent to a volumetric strain rate [39].

In a general categorization of sintering techniques, pressure is one of the primary consideration. Most sintering is performed without an external pressure (pressureless sintering). For many high-performance applications, high densities are attained using external pressure sources. Such techniques as hot pressing, hot isostatic pressing, hot forging, and hot extrusion use a combination of temperature, stress, and strain rate to densify powder compacts. The major distinction among pressureless sintering techniques is between solid state and liquid phase processes. Single-phase, solid state sintering has received the greatest consideration from a theoretical standpoint [42].

3.3.1 Solid state sintering

The driving force (surface energy decrease) gives a motivation for sintering, but sintering requires transport of matter to occur. In crystalline solids, matter transport happens by diffusion of atoms, ions, or molecules along definite paths that describe the mechanisms of sintering [39]. Figure 3.4 demonstrates the solid state sintering mechanisms as an illustration.

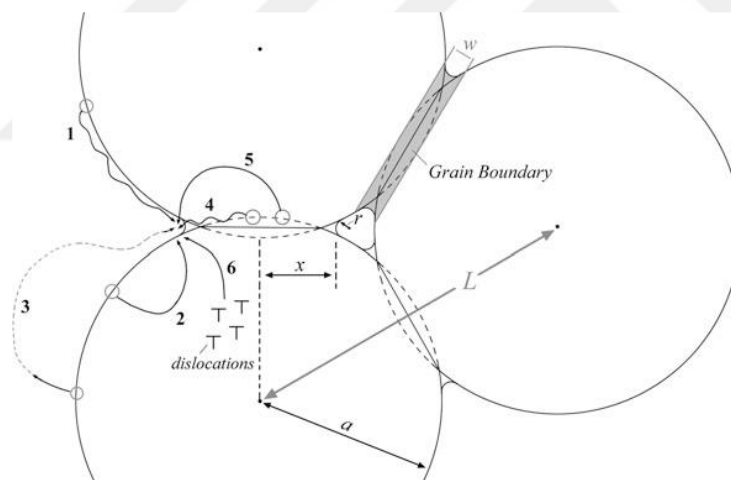


Figure 3.4 : Illustration of the sintering mechanisms in a three particles array [41].

The numbers in above figure, Figure 3.4 represent the different mechanisms and sources of material. In the initial stages of sintering the neck is considered to be the sink for the atoms. Therefore, atoms from the surface, from the grain boundary, or from the bulk, can move using different paths towards the neck. The following transport mechanisms can be seen: (1) Lattice diffusion; (2) Grain boundary diffusion; (3) Surface diffusion; (4) Gas phase transport by evaporation/condensation or gas diffusion; and (5) Viscous flow. The atoms' source can be the surface of the grain, the grain boundary, and the bulk [41].

The theory builds up a reasonable connection between the source of material and the density of the compact straightforwardly. If material is moving from the grain boundary or bulk to the neck, one should see high densification during sintering (pore elimination). In the event that, material is moving from the surface to the neck, densification will be restricted. The clarification is given in the light of the distance between the particles' center. If two particles touching each other is imagined, material is being expelled from the area in between the particles, they are expected to become closer by increasing neck area (with consequent centers approach). On the other hand, if material is being removed from the surface of the particle to the neck, the neck area increases, but can lead solely to a particle elongation and not to centers approach, resulting in low densification [41].

The surface tensions must adjust at every junction between the grain boundaries for a grain structure to be in metastable equilibrium. It is theoretically conceivable to construct a three-dimensional polycrystal in which the boundary tension forces balance at all faces and junctions, however in a real random polycrystalline aggregate there are always going to be boundaries with a net curvature in one direction and thus curved triple junctions. Therefore, a random grain structure is inherently unstable and, when heating at high temperatures, the unbalanced forces will cause the boundaries to migrate toward their center of curvature [38]. The effect of grain-boundary curvatures in two dimensions is shown in Figure 3.5.

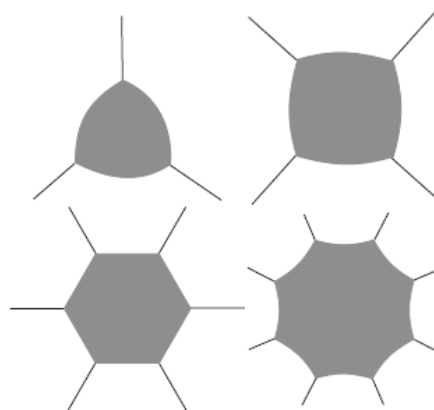


Figure 3.5 : Angles and grains [38].

It has been expected that the equilibrium at each grain boundary intersection results in angles of 120° . In this manner, if a grain has six boundaries, they can be planar (i.e., flat) and the structure is metastable. However, in case the total number of boundaries around a grain is less than six, each boundary must concave internally. These grains

will hence shrink and eventually vanish during sintering. Large grains, on the other hand, will have more than six boundaries and will grow. The change in free-energy gives rise to grain growth and a decrease in the surface area between the fine-grained material and the larger-grain-sized product and the corresponding lowering of the grain-boundary energy are observed [38].

3.3.2 Liquid phase sintering

Liquid phase sintering reveals sufficient internal force via liquid capillary action on the particulate solid that external forces are not required. The magnitude of the capillary pressure is equal to very large external pressures [42]. A large number of authors agree that for complete densification to take place it is crucial to have (1) an appreciable amount of liquid, (2) an appreciable solubility of the solid, and (3) complete wetting of the solid by the liquid [43]. Three steps that arise coincidentally in the densification process are observed: the rearrangement process, the solution-precipitation process, and the coalescence process.

When liquid phase is formed, there is a rearrangement of particles to produce a more effective packing and a minimum of resultant pore surface. This process can lead to complete densification if the volume of liquid present is sufficient to completely fill the vacancies between the solid particles as shown in Figure 3.6; however, in practice, trapped gases may prevent this from being achieved [43].

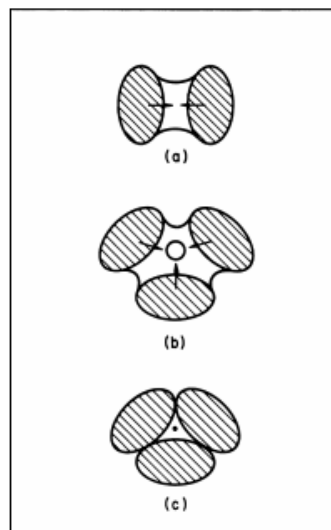


Figure 3.6 : Scheme of the densification process under the presence of a wetting liquid [43].

When the volume of liquid is insufficient to fill the voids, this stage will finish when the contact between the solid particles is established. The initial step in this rearrangement corresponds to a viscous flow process since in this stage of the process the capillary pore size decreases but does not change in order of magnitude; therefore the rate of densification corresponds approximately to the viscous flow and follows a relation seen in equation 3.3:

$$\Delta L/L_0 = 1/3 (\Delta V/V_0) \sim t^{1+y} \quad (3.3)$$

where the exponent $1 + y$ is somewhat larger than unity due to the fact that the pore size decreases and the driving force increases during the process while, at the same time, resistance to rearrangement increases from the initial pure viscous flow [43].

As densification by rearrangement slows, solubility and diffusivity effects become dominant. This second stage of classic liquid phase sintering is termed solution-precipitation. A general attribute of solution-precipitation processes is microstructural coarsening. The coarsening is due to a distribution in grain sizes. The solubility of a grain in its surrounding liquid varies inversely with the grain size; small grains have a higher solubility than coarse grains. The difference in solubilities establishes a concentration gradient in the liquid. Material is transported from the small grains to the large grains by diffusion. Solution-precipitation not only contributes to grain coarsening, but also to densification [42].

Coalescence process is predominant if the liquid does not completely penetrate between the solid grains; thus recrystallization and grain growth sufficient to form a solid skeleton occur, and the densification process is slowed down and stopped. When there is not a complete wetting along a line between grain centers, the material will be solid, and for densification to take place, material must be transferred within the solid phase. Consequently, rapid densification corresponding to the liquid phase processes is stopped, and the densification rate should decrease to that observed for solid particles under similar conditions [43].

Several factors are simultaneously changing during liquid phase sintering. The porosity is usually decreasing, while the grain size is increasing. Furthermore, the dihedral angle and contiguity will vary during the initial portion of liquid phase sintering. These microstructural changes provide a monitor on both the thermodynamics and kinetics during sintering [42].

An important component of liquid phase sintering is the interfacial energy. The contact angle will depend on the solid-liquid, liquid-vapor, and solid-vapor energies. The dihedral angle is strongly dependent on the solid-solid and solid-liquid interfacial energies. These energies also are dependent on solubility, surface contamination, and temperature, and they can change during liquid phase sintering as reactions occur. Therefore, the microstructural parameters which depend on these energies will be shifting with time during initial liquid phase sintering [42].

3.4 Sintering Techniques

Sintering materials that naturally resist high temperatures is difficult. Normally the sintering driving force comes from the surface energy associated with small particles. An external pressure increases the driving force, giving faster densification. Thus, pressure-assisted sintering is beneficial for densify materials which are normally resistant to sintering [44]. In general, application of pressure allows the sintering temperature to be lowered by up to 500 °C. For many materials, sintering with pressure is the only practicable route to obtain a dense compact [45]. Pressure-assisted sintering techniques employ combinations of temperature and pressure to eliminate pores. Net-shaping is used to imply fabrication to the final size and shape to eliminate machining [44]. A schematic map of the processes is given in Figure 3.7.

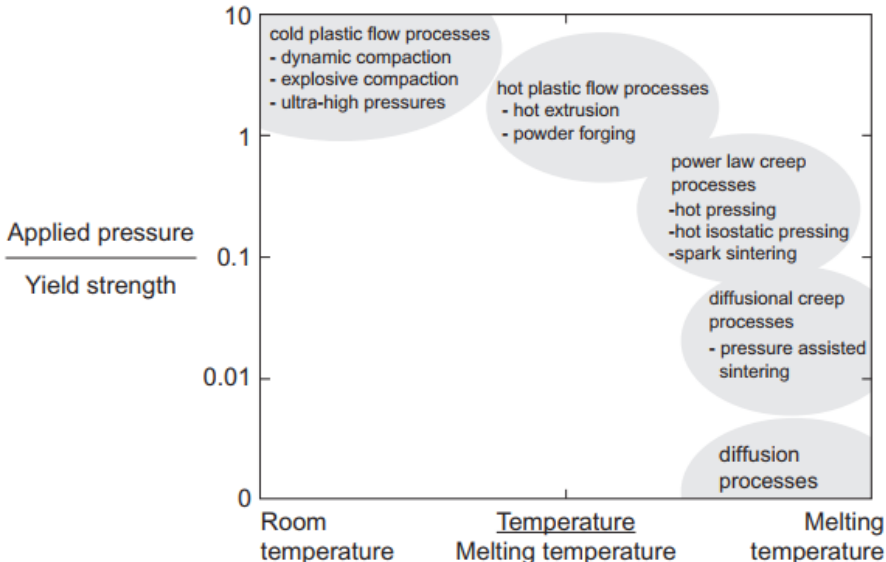


Figure 3.7 : A schematic plot of the various pressure-assisted sintering techniques versus the relative temperature [44].

The axes seen in Figure 3.7 are temperature relative to the melting temperature and pressure relative to the yield strength (at that temperature). The high temperature processes rely on less pressure, while the high pressure processes rely on lower temperatures. In terms of process variables, smaller particle sizes, high pressures, and high temperatures contribute to rapid densification. There are many combinations that produce full density [44].

3.4.1 Hot pressing

The hot pressing is a traditional compaction process that uses simultaneous utilization of high uniaxial pressure, while a powder compact in a graphite die-punch assembly is heated to elevated temperatures (up to $\sim 2500^{\circ}\text{C}$) for adequate holding time. The temperature is usually above the recrystallization temperature that is enough to induce the sintering and creep processes to consolidate the green compact into partially or fully dense component. The use of pressure expands the driving force required for densification, thereby bringing down the processing temperature, when compared with pressureless sintering [46].

The majority of hot pressing utilizes a basic uniaxial (linear) arrangement comprising of a punch and die assembly and furnace (induction or resistance) mounted in a press frame. Typical operating pressures range from about 10 MPa to about 70 MPa. For moderate pressures (~ 40 MPa) graphite dies can be used, however for higher pressures (like 120 MPa) more expensive and special refractory metal (Mo(TZM), W) and ceramic (Al_2O_3 , SiC) dies can be used. Graphite is normally preferred because of its low cost, ease of machining and superb creep resistance at high temperatures. Furthermore, the low expansion coefficient of graphite helps to prevent thermal expansion differences from producing stresses on cooling, therefore simplifying the removal of the sample from the die. The fundamental disadvantage of graphite is its high reactivity with other ceramic systems. In order to limit this problem, the die can be coated with a thin protective layer of boron nitride [47].

Figure 3.8 shows a schematic diagram of the hot pressing technique. Loading is along the vertical axis on punches pressurized from a hydraulic system which is located on the outside of the system. Despite the fact that the pressure is applied along the vertical axis, there is a radial pressure against the die wall. The differential stress between the axial and radial directions creates shear that makes particle bonding possible. This

shear stress is proportional to the applied stress. In initial densification stages, particle rearrangement and plastic flow occurs. As densification progresses, creep by grain boundary diffusion and volume diffusion becomes noticeably controlling [44].

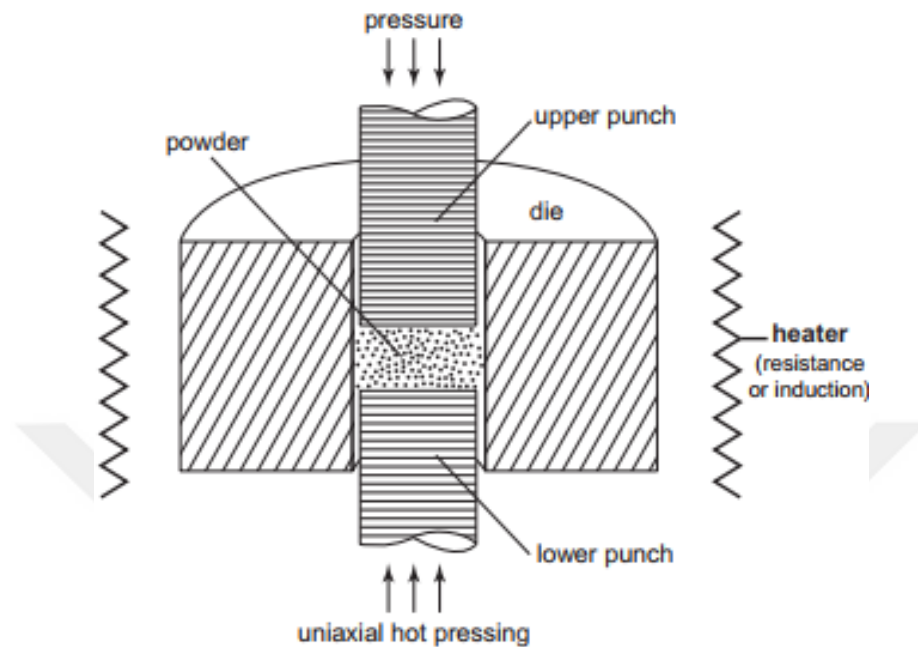


Figure 3.8 : A sketch of hot pressing [44].

The most obvious advantage of hot pressing lies in the improvement in the densification kinetics of the ceramic powder. This usually means that the densification cycle is much shorter than in the case of pressureless sintering and that the temperature of operation is significantly lower (by several hundred kelvin) [45].

When compared to pressureless sintering, the improvement of hot pressing can be regarded as the minimization of grain growth and pore growth which can happen in many ceramics during prolonged sintering treatments. Submicrometer powders, for instance, often show strong grain growth, producing a final average grain size of several micrometers. In addition, hot pressing avoids the disadvantages associated with inhomogeneous grain growth. Ceramic materials containing volatile species such as lead oxide, zinc oxide and some nitrides are more promptly densified in the relatively rapid hot-pressing process, compared to pressureless sintering. A further advantage is that direct pressing to shapes with good dimensional accuracy is conceivable. The requirements for grinding and polishing of the finished part are thereby minimized [45]. The heating of the ceramic compact can be attained by three different heating mechanisms:

Inductive heating: In this technique, with the help of induction coil, which produces heat within the die high-frequency electromagnetic field is generated. Uniaxial pressure is applied by using two punches. The independent use of pressure and inductive power permits the achievement of liquid phase at lower pressures. It should be remembered that uniform heating will not occur if the air gap between the die and induction coil is not same all through the die profile, which can cause nonuniform heating of the ceramic and hence nonuniform material properties [46].

Indirect resistive heating: The die containing the ceramic powder is put inside the sintering chamber. Electric current is used to heat the heating elements in this technique, and the heat is transferred to the die by convection. Since the heat flows to the die in a secondary manner, the process is known as indirect resistive heating. The advantage incorporates the achievement of high temperatures, independent to the conductivity of the die, heat, and pressure. However, longer processing times are needed for heat transferring to the die in order to reach the desired temperatures [46].

Direct heating: The die is directly connected to the electric power. The resistance of the die and powder generates the heat, which brings the advantages of higher heating rates. This permits accomplishing higher and uniform densities (close values to the theoretical densities) in shorter cycle times with precision near-net shape of the component. This additionally brings down the threshold sintering temperature and pressure compared with that required in the conventional sintering process. Hence, direct heating provides a reduction in processing cost by lowering the processing time, temperature, and pressure [46].

Besides these advantages, uniaxial hot pressing is usually slow because of the thermal mass associated with the tooling. Overall hot pressing is expensive and restricted to diameters smaller than 400 mm. Compact contamination from the die is a perpetual problem. Even so, hot pressing is widely used to fabricate unique materials; especially brittle materials [44]. However die wear is a significant problem in the hot pressing of harder ceramic powders [45].

Special powders - very fine and homogeneous grain size – is required in order to take advantage of the rapid sintering kinetics. All low-temperature volatile constituents such as adsorbed water must be carefully removed from the powders before

processing. Also, dimension and shape limitations of the parts produced are additional important constraints on the widespread use of the process [45].

A most important use for uniaxial hot pressing is in the consolidation of diamond metal cutting tools. A typical composite consists of 1.5 μm particles of cobalt that form a matrix containing about 10 vol.% diamond. This composite is hot pressed in graphite tooling at 35 MPa with a peak temperature of 900 °C using a hold time of 2 min to avoid diamond decomposition [44].

3.4.2 Hot isostatic pressing

Hot isostatic pressing (HIP) can be defined as an simultaneous application of temperature and isostatic pressure. Unlike hot pressing, the pressure is applied uniformly in all directions in HIP process. HIP is generally used for fabricating ceramics and metals, including components with complex shapes, high- density ceramics and composites, and it is usually used for the solid phase bonding of similar or dissimilar materials. The specimen is surrounded by a gaseous medium and undergoes thermal treatment at high pressure to consolidate it [48].

In HIP, the main advantage is the obtaining very flexible sample shapes. The sintering process simultaneously densifies and bonds the powders. This process can improve the mechanical properties and workability of the sintered materials [48]. Since densification takes place by the use of isotropic hydrostatic pressure, little amounts of shear stress occurs along the particle surfaces. When this is properly controlled, HIP allows near-net-shaped compact with full density and minimal microstructural defects, making the process ideal especially for the large and complex components for high-performance applications [46].

The common difficulty of HIP is to isolate the interface from the gaseous pressure medium used to obtain the isostatic pressure. If an interacting surface or interconnected porosity exists, the isostatic pressure is not available. There are three main types of encapsulation for isolation the pressure medium and the powder [48].

The first method is the direct sealing of the circumference of the contact area between two parts. The second is the placement of a sleeve of material around the contact area between two parts. And the third is the full or partial encapsulation of the entire component. The applied pressure can be up to 310 MPa and soaking temperature can be increased up to 2000 °C [48]. Figure 3.9 shows a schematic of hot isostatic pressing.

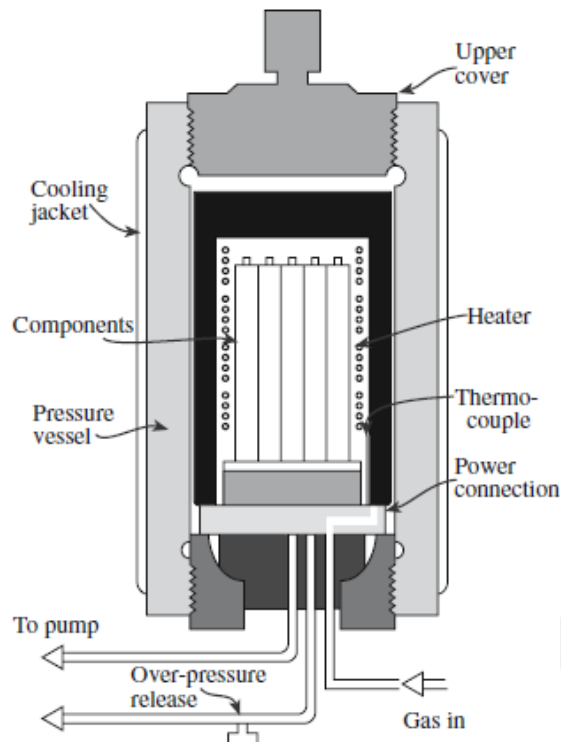


Figure 3.9 : Schematic of a hot isostatic pressing apparatus [38].

Argon is the most common pressurizing medium. As the argon density in the 100-200 MPa regime approaches that of the lubricating oil, special designs with double diaphragms, a double-acting hydraulic cylinder with an isolation chamber, replacement seals and associated leak-detection devices, and an oil-free liquid-argon pumping unit have been developed to prevent oil carryover into the autoclave [45].

In the HIP system, the resistance-heating element is the most complex unit. They are made of Fe-Cr-Al alloy, molybdenum or fiber-reinforced graphite for use in the temperature ranges of 25-1252 °C, 1200-1300 °C and 1500-2000 °C, respectively. The HIP system may contain single or multiple elements and heating zones [45].

Now HIP is used for a wide variety of ceramic (and metallic) components such as alumina based tool parts and silicon nitride nozzles used by the public sector in flue gas desulfurization plants. As interest in structural ceramics such as Si_3N_4 increases, the advantages of HIP processing become even more important [38].

Nonoxide ceramics can be HIPed to full density without the use of additives by keeping the grain size small. When very high densities (due to relatively low temperatures) are combined with small particle sizes, products with special mechanical properties appear. HIPing has also been applied to the formation of piezoelectric

ceramics such as BaTiO₃, SrTiO₃ and lead zirconate titanate (PZT) for use in acoustic wave filters and oscillators [38].

3.4.3 Spark plasma sintering

For powder condensation, the benefits of using electric current and mechanical pressure have been realized for decades. A recent worldwide interest in current-activated, pressure-assisted densification driven primarily by two distinct factors: the efficiency of the process and the unique materials that can be manufactured by it. First, with the help of high electric currents, it is possible to densify the powders to full density much faster and at lower temperatures compared to the traditional methods such as pressureless sintering and hot pressing [49].

For instance, a normal spark plasma sintering system takes approximately 20 min from start to finish, as opposed to processing times on the order of hours required for traditional methods. The second and perhaps more attention-taking and spurring factor is that the advantages go beyond efficiency and offer a stage for producing materials that are extremely difficult. This last factor makes this technique a successful production tool for dense and nanocrystalline materials [49].

As the years passed, current-activated powder densification methods have been commonly classified as spark plasma sintering (SPS), field-assisted sintering technique (FAST), and pulsed electric-current sintering (PECS), among others. Regardless of the name, the regular purpose of both is that very large electric currents and applied loads are employed simultaneously [49].

These systems are fabricated primarily by companies such as Sumitomo / SPS Syntex (Japan, since 1991); FCT Systeme (Germany, since 2003); Thermal Technology LLC (USA, since 2008); Izumi Technology (Japan, since 2010); Eltek Co. (Korea, 2010). In addition to these companies, there are universities and institutes that have custom-made these machines successfully [50].

Essentially, the same punch/die system concept as the more familiar hot pressing process is used in basic current-activated, pressure-assisted densification method as can be seen in Figure 3.10. A powder or green compact is placed in the mold and subsequently pressed between two counter-sliding punches. The mechanical loading is normally uniaxial. In the hot pressing process, the powder mainly densifies owing to a combination of thermal and pressure effects [51].

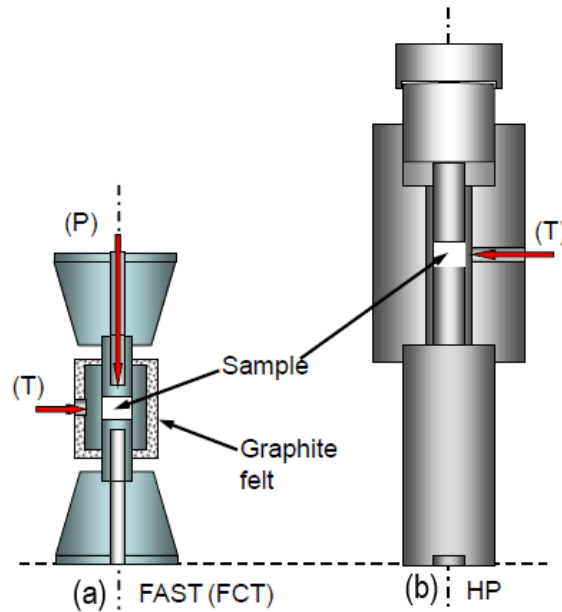


Figure 3.10 : Schematic of sintering process: (a) current-activated, pressure-assisted sintering apparatus (b) Hot pressing [50].

However, hot pressing and electric current activated pressure assisted sintering apparatus or in other name, SPS, differ significantly in the heating mode as can be seen from Figure 3.11. Specifically, in hot pressing an array of heating elements indirectly heats the punch/powder/die assembly by radiation and eventually by convection and/or conduction which is shown in Figure 3.11 (a). The powder heating rate is controlled by the rate of radiation and/or convection and conduction. Conversely, in SPS (Figure 3.11 (b)), the punches transfer the electricity and Joule heat directly to the powder. As the supplied current density can be very large, the heating rate in the powder can approach $106 \text{ K}\cdot\text{s}^{-1}$. This heating rate is much higher than $80 \text{ }^\circ\text{C}\cdot\text{min}^{-1}$ for the hot pressing process. Therefore, the SPS time can be lowered and the production rate increased [51]. However, in addition to providing heat, the current (typically pulsed DC current) has been assigned another role by influencing the sintering kinetics and result in a plasma. The plasma is mentioned to be the reason of a cleansing effect on the surface of the particles leading to sintering increment and TEM observations proved the clean grain boundaries down to atomic scale level [52].

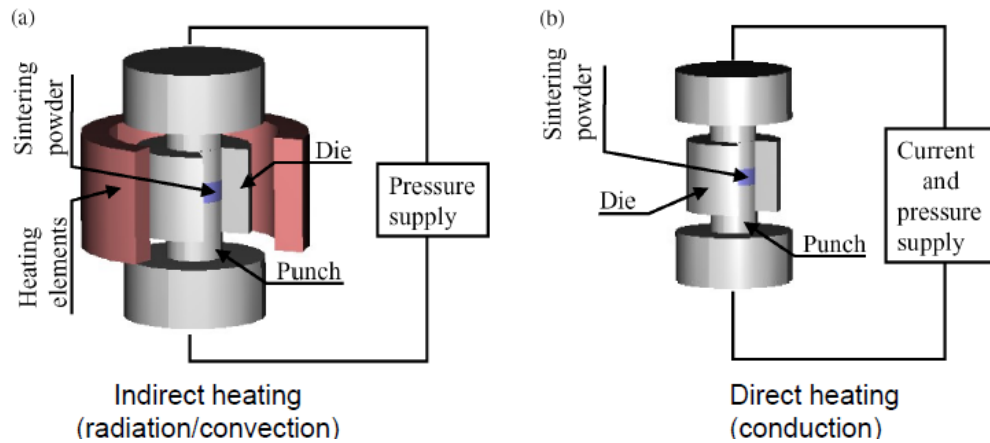


Figure 3.11 : Schematic of sintering process: (a) hot pressing and (b) SPS [51].

Yang and Qian stated in their study that the major difference seen amongst SPS and HP is their capability in realizing solute homogenization [53]. They sintered Ti-6Al-4V by using SPS and hot pressing sintering techniques and found out that SPS is much more effective than HP in producing a homogenous Ti-6Al-4V microstructure. A homogeneous microstructure is characteristic of a generally homogenous solute distribution, which relies upon the diffusion rate. It creates that the intensive Joule heating effect may have raised the local temperature and in this manner upgraded the diffusion rate. This may be the motivation behind why SPS is substantially more powerful in accomplishing microstructure homogeneity than hot pressing [53].

Also, less power consumption opportunity is one of the main advantage of spark plasma sintering technique, compared to hot pressing. When two samples having the precisely same final dimensions as $\text{Ø}42 \times 67$ mm is sintered at 1700°C , hot pressing takes 3 hours whereas spark plasma sintering procedure finalizes at 1 hour including the cooling times. This prompts to ~ 60 kW/h power consumption per a sample in hot pressing while the power consumed in spark plasma sintering technique is ~ 18 kW/h per one sample [50].

In SPS systems, a standard tool material is chosen as graphite because of the requirement for conductive material. The main advantages of graphite can be listed as: ease to machine; resistance to high temperature ($>2200^\circ\text{C}$) in inert atmospheres; and low cost [50]. In addition, Tuan and his coworkers mentioned that the temperature variation can be significantly reduced by inserting a carbon paper in between graphite punches and graphite mold [54]. Graphite foils between sample, die and punches minimize contact resistance between constitutive parts (accomodation layer), lead to

achieve better thermal homogeneity in the sample, prevent possible reaction between punch and powder, facilitate sample extraction and extend tool life by reducing the possibility of damage [50].

3.4.3.1 Processing parameters of SPS

The range and controllability of processing parameters make SPS extremely versatile and are among largest advantages of SPS. Figure 3.12 schematically shows a typical parameters that can be controlled during experiments.

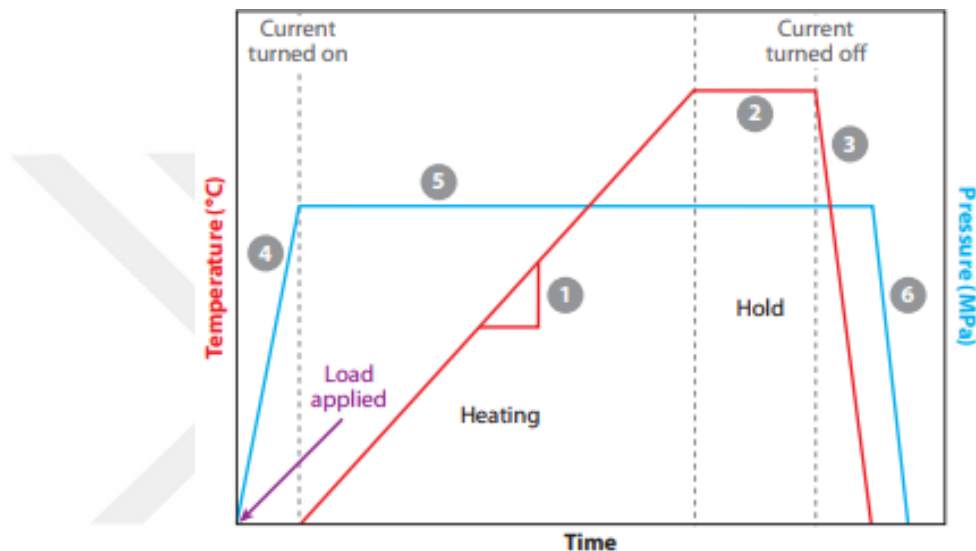


Figure 3.12 : A schematic of a typical experiment illustrating the six main user-defined process parameters: (1) heating rate, (2) maximum temperature, (3) cooling rate, (4) load application rate, (5) maximum load hold, (6) load removal rate [49].

The process parameters which can be easily changed are heating rate, maximum (holding) temperature, cooling rate, load application rate, maximum load hold, and load removal rate. Typical values of heating rate are $100 - 600 \text{ }^\circ\text{C min}^{-1}$, and those for pressure are $30 - 150 \text{ MPa}$. Much higher (and lower) heating rates and pressures are possible and have been demonstrated, but these ranges are considered typical. Alternatively, the process can be used in current-control mode, in which a particular maximum current is set and the system relaxes to a steady-state temperature [49].

Pressure

The practical limits on the amount of pressure which can be applied to the powder are directly linked to the failure strength of the die materials. The upper limits of high-quality graphite (the most common die material) is $\sim 140 \text{ MPa}$ [49]. Other tool

materials also can be conducted which has high fracture toughness, high fracture strength and electrical conductivity.

There are studies in the literature which produced their own dies with combining the graphite and ceramic in order to increase the strength for the higher pressures while retaining conductivity. Anselmi Tamburini et al used discs produced from nanometric WC powders and internal, smaller die also has a graphite body, but with plungers made out of silicon carbide [55]. They spark plasma sintered nano oxide powders through the use of high pressures (up to 1 GPa), high heating rates (200 °C/min) and short sintering times (4 min) successfully. They concluded that the high pressure may play a role in the initial stages through particle re-arrangement and the destruction of agglomerates as well as in the late stages of the densification through plastic or superplastic deformation [55]. Also, the main drawback of increasing the stress applied to the material is the requirement of reducing the cross-section of final material due to the capacity of hydraulic press of SPS.

Electrical Current

There are current-activated, pressure-assisted sintering techniques which uses electric source from pulsed, DC or AC currents. Bernard et al. investigated the effects of role of the electric stimulation on the sintering conditions and on the microstructure of the end products by comparing the initiation results of the FAPAS (field activation by an AC current) and SPS (field activation by pulsed DC current) processes, however they could not make a distinct conclusion [56]. The capacity of SPS currents, depending on the machine model, ranges between 1,000-10,000 A, the voltage is between 5-15 V; and the current density should be smaller than 1 kA/cm² [50].

Temperature

In spark plasma sintering system, depending on the capacity and size of the SPS device, the standard temperature range is up to 2400 °C. Typically, the heating rates are chosen to be 75, 100, 150 °C/min up to 400 °C/min however >1000°C/min heating rate application is even possible. The temperatures can be measured either with pyrometer or thermocouple. Pyrometer is a contactless device measuring thermal radiation which enables to measure very high temperatures, however it usually cannot measure the temperatures lower than 600 °C. On the other hand, thermocouples are the

measurement devices occurred by junction between two different metals producing a (non-linear) voltage and allow the measurement of intermediate temperatures [50].

The features that should be considered in pyrometers can be listed as; operating temperature range (from 400-600°C to 2400°C), spot size, focus distance, emissivity of sample (graphite lies between 0.75 and 1-black body and depends on temperature) and response time (less than 1 sec.) related to a temperature difference. It is strongly recommended to SPS operators to drill a hole into the die surface to create a black body radiator and the transparent window between the dies and pyrometer should be checked and cleaned regularly [50].

Table 3.1 shows the general properties of usually used thermocouples in SPS. SPS operators should be careful when using thermocouples. They should carefully insulate the thermocouple from conductive pathways and reactive materials (with alumina sleeves). There is no necessity to shield from electromagnetic fields when using thermocouples as a temperature measurer [50].

Table 3.1 : Thermocouples used in SPS [50].

Type	Composition	Temperature Range	Environment (bare wire)	Accuracy	Notes
K	+lead -lead Ni-Cr Ni-Al	0 to 1250 °C	Oxidizing, inert, limited in vacuum or reducing	2.2°C or 0.75% whichever is greater 1.5°C or	Low cost
R (S)	Pt-13% (10%) Rh Pt	0 to 1600 °C	Oxidizing, inert	0.25% whichever is greater	Expensive

Atmosphere

It is well known that SPS can be operated under various atmospheres such as vacuum, inert gas or nitrogen. Inadequate atmospheres or operating conditions may facilitate sparking whereas in ultrafast SPS reduced chamber pressure may induce a glow discharge between particle. The atmosphere may significantly affect the final properties of the sintered products. Sintering can be operated under an oxidizing, inert or reducing atmosphere and even in liquid media. In the latter case a dielectric is preferred to prevent sparking [51]. Also, one should also note that reducing nature of the environment (due to carbon) can lead to oxygen vacancies and sintering in air

atmosphere is only possible at low temperature (<600°C) again due to the carbon oxidizing [50].

3.4.3.2 Comparison of SPS with hot pressing

The schematic diagrams given in Figure 3.13 shows the difference in measuring the temperature by pyrometer.

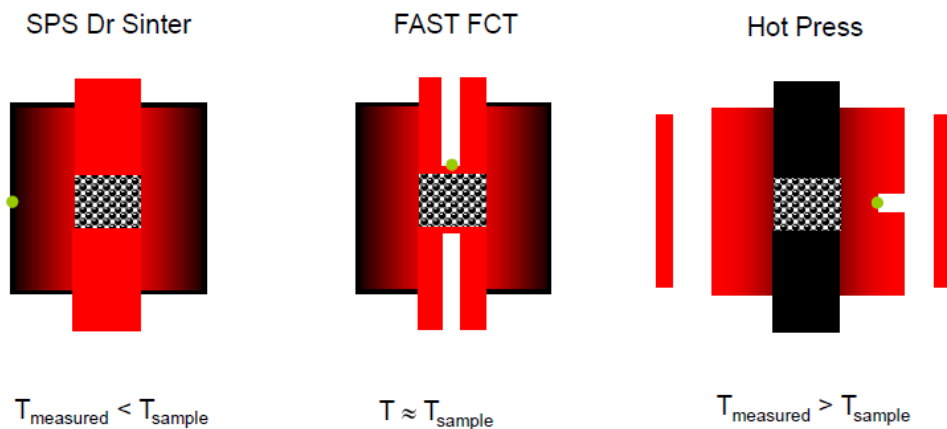


Figure 3.13 : Comparison between apparatuses [50].

In FAST, the pyrometer with a measurement scope of 450–2200 °C was centered on the bottom of the upper punch at a distance of 5 mm from the sample. However during the SPS process, a pyrometer (measurement range: 600–2200 °C) was focused on the black hole drilled on the die surface with a distance of 10 mm from the sample. Accordingly, lower temperature control in FAST is more accurate compared to SPS.

Langer et al sintered alumina and zinc oxide by SPS and FAST by arranging the parameters as much close to each other [57]. They used same heating rates at 10 °C/min; 25:5 ms ON/OFF pulse sequence in the FAST and a pulse pattern of 8:2 (corresponding to a ratio of 26.4:6.6 ms ON/OFF) in SPS process. As a result, they reached higher density values in the samples produced by SPS compared to that processed in FAST with the same apparent processing parameters. Furthermore, they observed an enhancement in grain growth in the samples produced by SPS. Also, they applied a calibration by copper melting and the results demonstrated that the radial temperature control in SPS process measures the real temperature of the sample at least 100 °C below. These results show that the underestimation of the actual temperature within the sintering specimen in SPS may partially contribute to the apparent lower sintering temperatures often reported with this apparatus. Although FAST and SPS

works in the same principle, direct comparisons may lead to problems. The problem appears to be less severe when the starting powder has poor thermal conductivity [57].

3.4.3.3 Basic mechanisms involved in spark plasma sintering

Spark plasma sintering involves experimental conditions more complex than in conventional sintering, so more mass transfer mechanisms might be involved. It should be noted that rapid densification by SPS cannot be corresponded to the kinetically slow diffusion mechanisms such as grain boundary and volume diffusion, but rather to mechanisms with faster kinetics, such as surface diffusion, diffusion through the melt, or time-independent processes such as plastic deformation. The number of included mechanisms and their relative significance is still an important debate topic. It is extremely dependent on the material physical and chemical properties and on the experimental conditions. Although, a few different mechanisms such as vaporization condensation, plastic deformation, surface, grain boundary, and volume diffusions were accepted for the sintering and densification during the SPS process [58].

Arc and spark discharge

Particularly early materials science researchers, ascribed the advantages of processing with SPS to the creation of a current arc between the powders encouraging neck development or the formation of a plasma around the powders during processing. For example, aluminum is difficult to sinter by traditional methods because of the coherent oxide layer which forms around the powder. However, aluminum sinters very well with SPS, which scientists have attributed to the presence of plasma which evacuates, or at least disrupts, the oxide layer and enables diffusion to proceed. While some earlier techniques may have indeed produced sparks due to high potentials, the conductive pathway through the die and low voltages make the formation of a current arc or plasma unlikely. The authors suggest that the low potentials employed during SPS are insufficient to produce an arc [59].

Most researchers stated that during the SPS process due to the a high electric-pulsed current applied on the electrodes, and the microscopic electrical discharges in the gaps between the powder particles generate plasma, and results in sintering [60,61]. According to them, the spark discharge can eliminate the adsorptive gas and any impurities that are present on the surface of the powder particles, and can easily destroy the oxide films on the particle surface [60,62,63], leading to an enhancement of the

thermal diffusion ability of the sintered material [61]. Furthermore, Joule heating and plastic deformation affects the densification of the powders. The high current, low voltage, momentary pulsed plasma discharge generates highly localized Joule's heating up to a few thousand degrees Celsius between particles in few minutes [64].

In their study, Zhang et al. tried to provide direct evidence for the occurrence of spark discharge and the existence of plasma in the SPS process, using typical SPS experiments, including sintering of ceramic powders, metal powders and metal–ceramic composite powders [60]. They observed several spark discharges and could get the photo of them. They found out a huge temperature difference such as at the centre of the discharge position reached 2088 °C, while the sintering temperature of the die was only 992 °C. They concluded that the experimental results indicates that spark discharge really occurs in the SPS process [60]. The photos related to their study are given in Figure 3.14.

Also, Omori argues that there are gaps between the two electrodes in the electric discharge machine, and high-energy plasma is generated there [65]. According to Omori, the effect of the plasma is remarkable at the initial stage of sintering, because there are many gaps in the powder. The plasma sites are gradually reduced with decreasing porosity on the middle stage of sintering, and are not generated when the gaps disappear. Samples shrink until the densification is achieved. After the shrinkage stops at a certain temperature, the sample starts to melt simultaneously in the small area between the sample and the graphite punch. Gaps appear in the melt, and the spark plasma is regenerated there. As the site of plasma generation is limited, the plasma is concentrated only on the melted area [65].

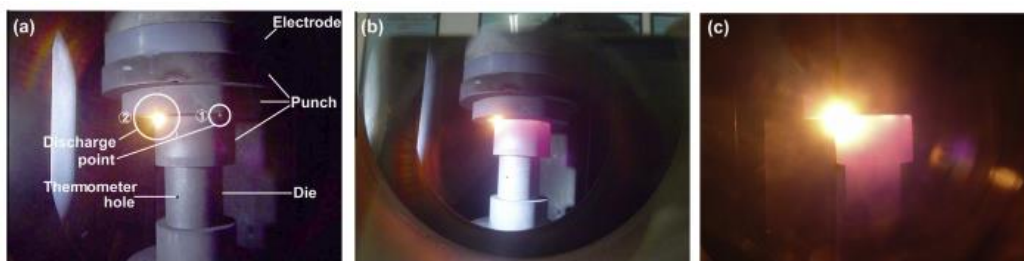


Figure 3.14 : Discharge occurred at the interface between the second and third punch on the die at different sintering stage: (a) $t = 60$ s, $T = 337$ °C; (b) $t = 120$ s, $T = 586$ °C; (c) $t = 240$ s, $T = 992$ °C [60].

On the other hand, Hulbert et al. insists the absence of momentary plasma generated between particles during SPS and they mentioned that based on the physics of plasma,

the formation of plasma in the environment produced by SPS apparatus is unlikely [39, 66]. They advocated their considerations by utilizing in situ atomic emission spectroscopy, direct visual observation and ultrafast in situ voltage measurements. They concluded that no evidence of plasma could be found across a wide variety of SPS conditions using several different powders. Beside the formation of plasma, other and more substantiated effects can be associated with the presence of high currents. For instance, in the case of electronically conductive materials high currents can produce electromigration and enhancement of solid state reactivity [66]. In addition, they believe that rapid heating rate is responsible for the enhanced sintering capabilities of the SPS. According to them, the fundamental underpinnings of the SPS method involve a rapid heating rate accompanied by moderate uniaxial pressures and high currents [66,67].

Electromigration

Two major components of densification-contributing mass transfer is considered during SPS: (i) grain-boundary diffusion and (ii) power-law creep. The driving sources for these material transport mechanisms are: (i) externally applied load, (ii) sintering stress (surface tension), and (iii) steady-state electromigration (electric field contribution to diffusion) [68,69].

The flux of matter J caused by the grain boundary diffusion is determined by Nernst-Einstein equation including the chemical potential gradient along the grain boundaries due to the normal stresses and the electromigration seen in equation 3.4:

$$J = C_E \dot{E} + C_\sigma \nabla \sigma \quad (3.4)$$

Here \dot{E} is the component of the electric field in the tangent plane of the grain boundary, $\nabla \sigma$ is the gradient of stresses normal to the grain boundary, $C_\sigma = \delta_{gb} D_{gb} / kT$, where D_{gb} is the coefficient of the grain boundary diffusion, δ_{gb} is the grain boundary thickness, k is the Boltzman's constant, T is the absolute temperature. Parameter C_E is determined by Blech's formula which can be seen in equation 3.5:

$$C_E = \frac{\delta_{gb} D_{gb}}{\Omega k T} Z^* e_q \quad (3.5)$$

where Ω is the atomic volume, Z^* is the valence of a migrating ion, and e_q is the electron charge (the product $Z^* e_q$ is called "the effective charge"). One can determine

the effective electromigration stress P_{em} contributing to sintering densification from equation 3.6:

$$P_{em} = \frac{Z^* e_q G^2 U}{3\Omega(G + r_p) l} \quad (3.6)$$

where u and l are the electric potential and the characteristic length along the electric field; G is the average grain size and r_p is the average pore radius [68].

Based on the influence of electromigration on the flux equation, the interaction between the electron wind and metal atoms can be considered as an additional driving force for matter transport. In a phenomenological sense the sintering of conductive powders in SPS can be driven by three factors: intrinsic surface curvature, applied pressure and electromigration [39].

Enhanced mass transport by electromigration contributes significantly to the marked increase in neck growth when sintering is carried out under the influence of a current. Because of geometric considerations, the density of the current is highest in the neck area, especially near the perimeter of the neck, as can be seen from the simulation results depicted in Figure 3.15.

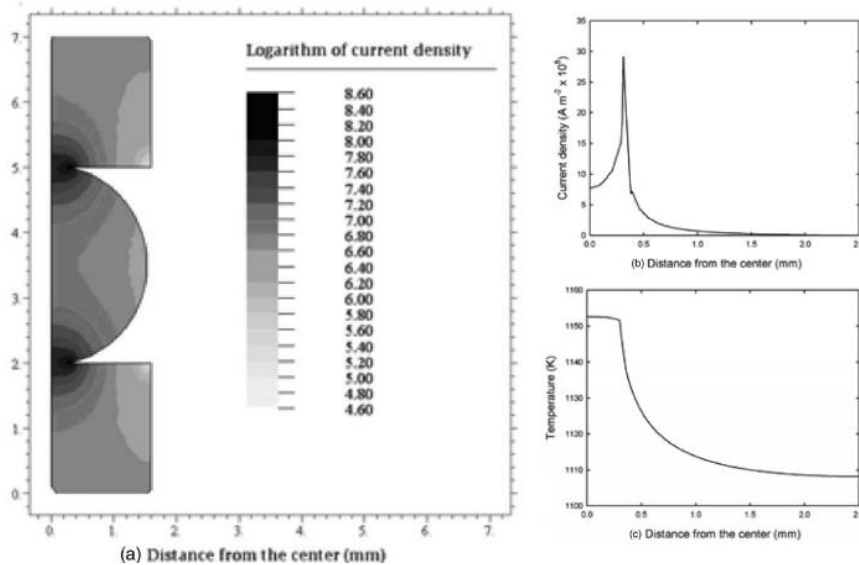


Figure 3.15 : Simulation of current distribution in a copper sphere between two copper plates: (a) Current density distribution, (b) current density profile, and (c) temperature profile [69].

The simulation results shown in Figure 3.15 demonstrates that the temperature inside the neck is constant but decreases very slightly beyond the perimeter of the neck. In

contrast, the current density distribution is uneven, showing a peak at the edge of the neck and decreasing to a zero value beyond the perimeter. The existence of high current density outside the perimeter of the neck appears to have an effect on evaporation and the development of corresponding surface morphology.

During sintering, the current is passed from the electrodes into the punches which are in contact with both the powder and the die. From there, the current pathway is different for non-conductive powders than for conductive powders [59]. For nonconductive powder, the current must pass through the die and heat the powder indirectly, while for conductive powder, the current can pass through the powder and heat it directly [70].

As can be seen from Figure 3.16, a remarkable difference exists in the current distribution, particularly through the sample. For example, a non-electrically conducting sample such as alumina, shows no Joule heating at this temperature, and the initial heating of the sample is not made by the current, but from the radiation. However, in the copper sample Joule heating is formed immediately. When compared, the highest current densities are in the exposed portions of the plungers [59,70].

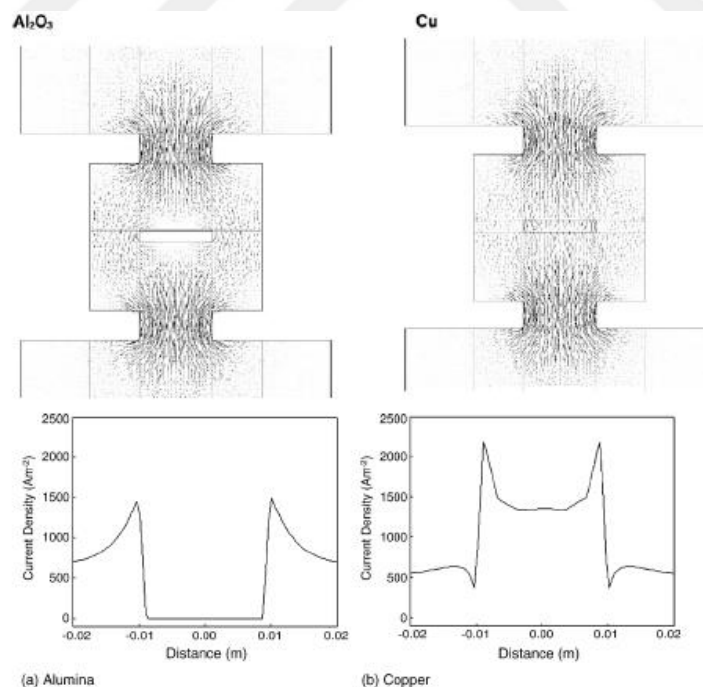


Figure 3.16 : Current distributions in the SPS die for alumina and copper samples under an applied voltage of 5 V [70].

If the current pathway is isolated by coating the die and punch walls with boron nitride, conductive powders will sinter but non-conductive powders will not as no sufficiently

conductive pathway exists for the current to create heat and sinter the powder [59,71]. Carney and Mah concluded that there is insufficient current through the Al_2O_3 to initiate heating in the compact when the punch walls were coated with boron nitride. The resistivity of Al_2O_3 sample with temperature and the fact that consolidation begins before current flow can be expected through the compact suggests that the current or pulses may play no role in the sintering of insulator materials. Conversely, conductive materials can be densified by internal Joule heating [71].

Figure 3.17 shows the overall distribution of Joule heat in the punch, die and specimen assembly for a graphite cylinder specimen with and without alumina powders. Joule heating is maximum at the end of punch end due to smallest cross section area in the system. Joule heating is almost zero for both alumina and graphite cylinder; however the reasons are different. For alumina containing condition, all current passes through die due to the conduction properties of alumina, whereas in graphite, low resistivity of specimen causes zero Joule heating [72].

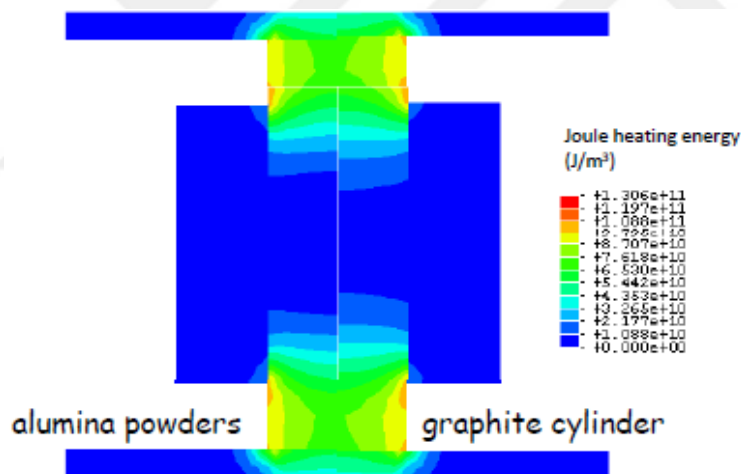


Figure 3.17 : Joule heat in the punch/die/specimen assembly.

Temperature gradients

The temperature distribution during an SPS experiment (both within the sample and in the die) is important, as it influences the sample homogeneity [70]. The different current pathways for conductive and non-conductive powders lead to different temperature distributions in the samples [59,72]. Since heating is resistive, the temperatures inside the sample and that on the surface depend on the conductivity of the sample, as well as that of the die. During SPS experiments using an optical pyrometer focused on the external surface of the die is common practice to measure

and control the temperature. While this may be adequate for very slow heating rates where thermal equilibrium can be attained, it is not satisfactory for high heating rates, whose feasibility is one of the most obvious advantages of the SPS process. While a difference in temperature (between the sample and the die surface) is often qualitatively acknowledged, the reported experimental results are based on the die temperature [70].

Figure 3.18 gives the detailed information for the evolution of temperature in the vicinity of the specimen. Initially the area of the punches outside the die is hottest as can clearly be seen from Figure 3.18(a); surface temperature: 56 °C, because of the Joule heat is generated at this location. As the temperature increases, the temperature maximum is still in the punch but shifts closer to the die as the specimen is heated up by heat conduction (Figure 3.18(b); surface temperature: 983 °C). With radiation from the die becoming significant at higher temperatures, a considerable radial temperature gradient develops (Figure 3.18(c); surface temperature: 1309 °C) [72].

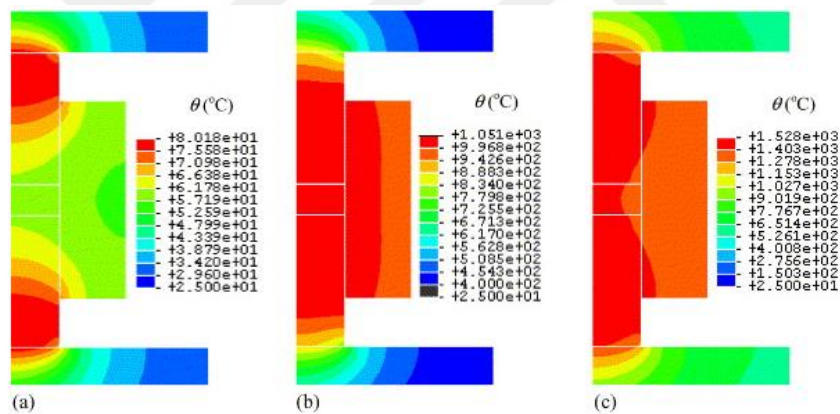


Figure 3.18 : Temperature in the punch/specimen/die assembly for (a) $T_{\text{surface}} = 56^{\circ}\text{C}$; (b) $T_{\text{surface}} = 983^{\circ}\text{C}$; (c) $T_{\text{surface}} = 1309^{\circ}\text{C}$ [72].

The generated heat is partially diffused into the specimen and partially lost into the machine (upper and lower graphite spacers), which is water cooled (a forced conduction situation). As the process progresses, the temperature in the specimen increases due to thermal conduction from the punches. In addition, the surface radiation causes a secondary heat loss for the specimen/die assembly. This pattern of heat flow results in a temperature differential between die surface and specimen center with the specimen center at a higher temperature than the control temperature on the surface of the die. [73]. As can be seen from Figure 3.19, at low temperature heat conduction through the loading train is dominant. Radiation becomes more important at higher temperatures.

One can conclude that spark plasma sintering of high melting point materials requires radiation shielding [74].

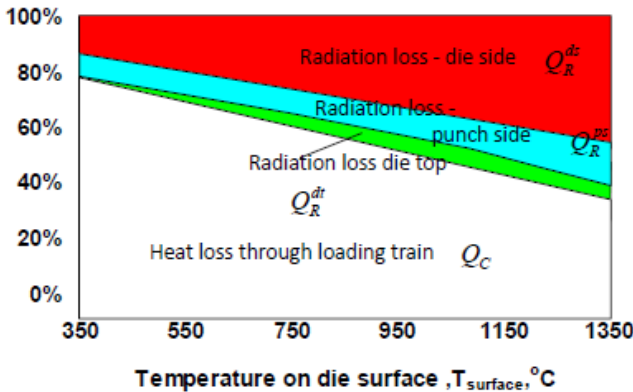


Figure 3.19 : Heat loss mechanism depending on the temperature [74].

A combination of current flow through the sample and radiative heat loss on the die wall gives rise to a radial temperature distribution in conductive samples [59,75]. Vanmeensel et al carried out the modelling studies based on two materials which show very different conduction properties [75]. Figure 3.20 shows the temperature distribution of mentioned materials according to their study.

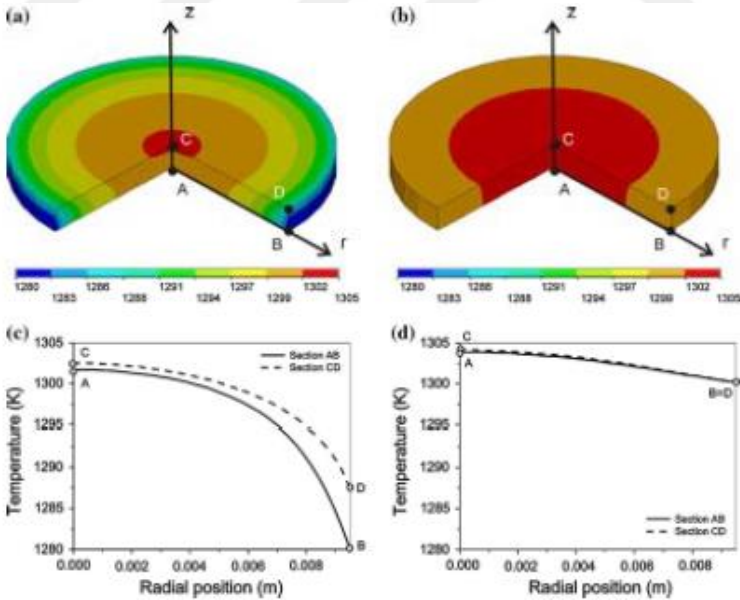


Figure 3.20 : Temperature distribution inside the ZrO₂ (a) and TiN (b) specimen during the dwell at 1500 °C [74].

TiN has been chosen to understand the temperature distribution behavior of electrically conductive materials whereas ZrO₂ has been chosen for electrical insulator. In the case of a TiN sample, the difference in case of temperature in the sample was smaller compared to the temperature gradient in an electrically insulating ZrO₂ sample. Much higher

thermal gradients were observed in insulating 3Y-ZrO₂ sample under identical SPS cycles. In the case of ZrO₂, the current only flows through the punches and die, in such a way compensating the heat losses due to the radiation from the exposed tool surfaces. When using a TiN sample, the current mainly flows through the specimen itself [75]. Nonconductive samples have a more uniform temperature distribution; the current passes around the sample and the powder is more evenly heated from the die. Temperature gradients can lead to sample inhomogeneity [59,74]. Gradients become more complex when processing complex shapes and/or larger specimens [74]. Minimum 150°C difference of compact edges is obtained as can be seen from Figure 3.21.

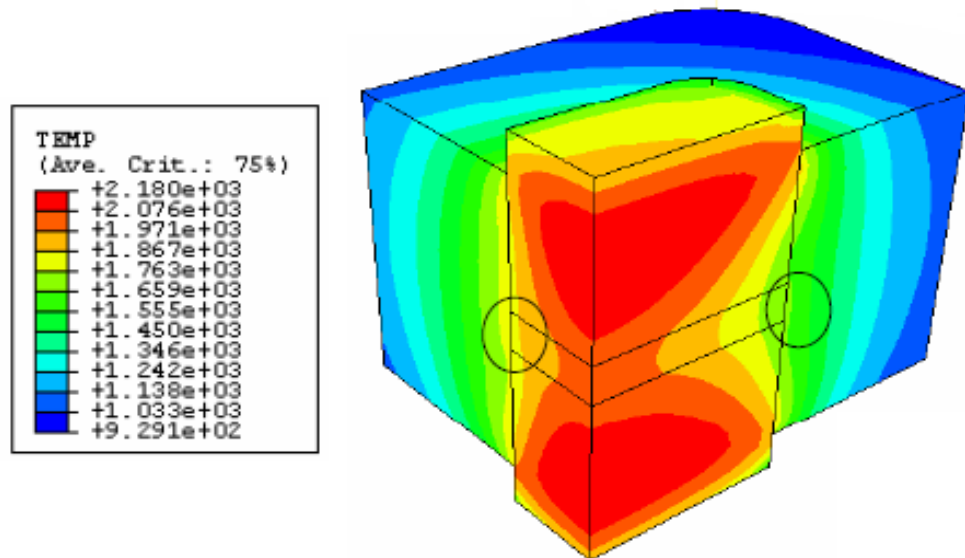


Figure 3.21 : FEM simulation results of a complex shaped sample showing the temperature gradients [74].

When Figure 3.22 is considered, distinct temperature difference is obtained in complex shaped samples. It has been determined that lower temperatures will occur in the rounded edges of the sample compared to the sharp angled edges. The sharp edges cause the current density to accumulate in a narrow area and increase in temperature in these regions. As the sample size increases, the temperature difference between the center of the sample and the nearest part of the mold increases. A more homogeneous thermal distribution can be obtained in production using cylindrical molds or cylindrical mold inner cavities [74,76].

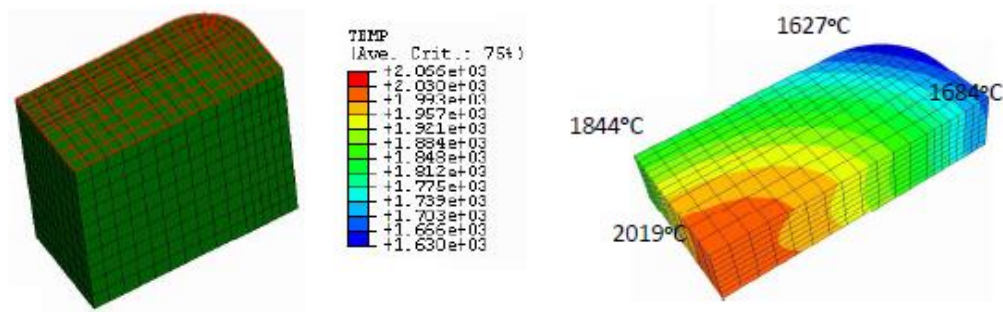


Figure 3.22 : Temperature distribution in compact with round and sharp edges [74].

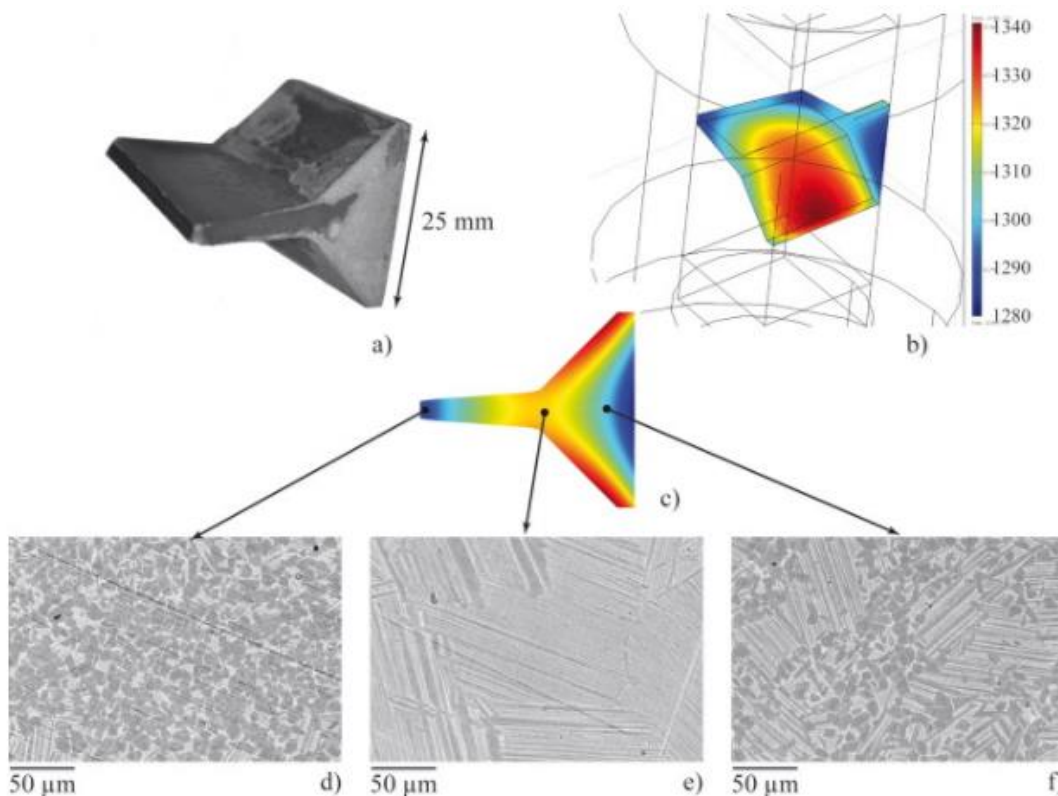


Figure 3.23 : Complex shaping by Spark Plasma Sintering: (a) sintered part, (b) and (c) finite elements simulations, (d–f) microstructures at different locations.

It should be noted that full densification is possible with using appropriate tools, no matter the size of the sample increases or the shape of the sample gets more complex. Voisin et al managed to sinter large samples and complex shaped samples satisfactorily, and they proved perfect densification of the samples with microstructural control [77]. With an assembly designed to reduce the thermal gradient, they could obtain more homogenous temperature gradients and microstructures in the sample as shown in Figure 3.23. With the help of the Finite Element Modeling simulations, they managed to design the ideal assembly, however they concluded that the ideal will change based on the thermal properties of graphite and sample [77].

Mechanical Pressure

The application of pressure during sintering has both mechanical and intrinsic roles. Mechanical pressure can help rearrange particles and break powder agglomerates. On the intrinsic side, the effect of applied pressure is described by below equation 3.7:

$$\frac{1}{1-\rho} \frac{d\rho}{dt} = B \left(\frac{\gamma_{sv}}{r} + \phi K P_a \right) \quad (3.7)$$

Where ρ is the fractional solid density, B represents a collection of kinetics parameters including temperature, diffusivity and grain size, r is a parameter representing microstructure scale (related to particle size), γ_{sv} is surface energy of the sintering particle, ϕ is stress intensity factor, K is a factor depending on sintering stage, and P_a is applied pressure [39].

As already seen, densification rate depends on both temperature (via B) and applied pressure (via P_a). In other words one can trade temperature for pressure and still achieve the same density. This concept is more important in sintering of nanoparticles because grain growth is more sensitive to sintering temperature than pressure in these kind of powders [39,55].

In SPS processing, it is found that the effects from applied pressure are similar to what is observed from hot pressing. At low to moderate temperatures, higher applied pressure yields better final density. Since pressure assists densification and changes pore configuration, it also indirectly affects grain growth. A higher density results in a higher packing coordination number, which leads to an early onset of grain growth [39,69].

3.4.3.4 Processing issues of spark plasma sintering

Temperature reporting must be carefully considered. The reported lower sintering temperatures may not always be real. The models and experiments showed that a sizable gradient exists between die surface and sample center. The usual measured surface temperature is lower than that of the center. Measurement type (pyrometer vs. thermocouple) and location, machine configuration must be taken into consideration [50,69,74].

Microstructural inhomogeneities in fully dense samples have been occasionally observed and mainly attributed to temperature gradients due to high heating rates and

short holding times. Generally the sample inhomogeneity increases with the size of the sample. However, there are studies in the literature advocating the more uniform densification obtained by using SPS apparatus compared to hot pressing [39,50,69,74].

Stoichiometry changes occur in oxide ceramics or in materials with high vapor pressure components (e.g. iodine losses). Darkening of light-colored oxide ceramics has often been observed and attributed to reducing atmosphere inside graphite tools or direct carbon contamination. A post sintering annealing generally restores the oxide chemistry [39,50,69,74].

Carbon contamination from the graphite die and punches inevitably occurs. For most materials, it is only on the surface and it is mechanically eliminated by grinding and polishing. Problems with residual surface carbon have been reported in carbon sensitive materials (e.g. Fe based alloys) or in transparent materials [39,50,69,74].

The manufacturing potential of spark plasma sintering is promising due to process simplicity. In SPS, fewer processing steps with no need for preshaping techniques and binders, simultaneous reaction and densification, high throughput (whole cycle ~ 30 min), capability of process control (monitoring the relative displacement) and process flexibility (simple changes in sintering temperature, time, pressure, sintering environment, but also on heating rates, timing, levels and rate of pressure application) in one/multiple sintering steps. All these potentials make SPS applicable in sintering novel, advanced engineering materials ranging from refractory, additive free, hard to sinter, nano or transparent materials and in reaction sintering [39,50,69,74].

4. BORON CARBIDE BASED MATERIALS IN LITERATURE

The sintering of boron carbide, with its high fraction of covalent bonding (>90%), is difficult due to low diffusion coefficients. Also, naturally occurring oxide layers on the surface of fine powder particles promote evaporation-condensation processes that do not contribute to densification but rather enhance grain growth. Extreme high vapor pressures of gaseous boron oxide compounds at temperatures exceeding 1500 °C lead to reactions such as in Equation 4.1. Thus, boron carbide is transported from regions of high curvature (convex) to regions of low curvature (concave); that is, the grains coarsen with no shrinkage at all [78].



Transport mechanisms such as volume and grain boundary diffusion which contribute to the overall shrinkage become effective temperatures above 2000 °C—that is close to the melting point (2450 °C) [78]. It is proved that the regime of predominant surface diffusion extends from 1500 to 1800 °C, whereas sublimation occurs above 1800 °C with boron being volatile species [79]. A high resistance to plastic deformation and grain boundary sliding, combined with low surface energies, constrains any considerable particle rearrangement and shape accommodation before densification by the transport of matter occurs. Therefore, for the densification of stoichiometric boron carbide, the use of very fine powders low in oxygen content is a prerequisite condition [78].

Activation of grain boundary and volume diffusion and thus densification at lower temperatures is possible by increasing the density of point defects or dislocations: (i) mechanically by high energy milling (attrition-milling); (ii) by doping with trivalent ions, which substitute for carbon and thus introduce electron deficiencies and vacancies, e.g. by adding boron and aluminum; (iii) by introducing sintering additives, which remove oxide layers on the surface of boron carbide particles and thus increase the surface energy, e.g. by adding carbon, aluminum carbide, silicon carbide or related compounds, which also inhibit grain growth [78,80].

Densification of boron carbide without deterioration of mechanical properties can be achieved either by using a suitable sintering aid and/or applying the external pressure (e.g. hot pressing, hot isostatic pressing). According to the application area of final product, the additive and the method of densification are determined according to the properties that are required. For example, an additive by itself or due to in situ reaction with boron carbide would result in a non volatile second phase which aids the consolidation and desired property enhancement. Hence, the selection of the additive should be made according to the formation of a suitable structure providing the desired properties in boron carbide. Advanced production techniques like microwave/spark plasma sintering, explosive compaction, etc. help to obtain dense products without microstructural coarsening [17].

4.1 Consolidation Techniques Used in Boron Carbide Sintering

4.1.1 Pressureless sintered boron carbide

Pressureless sintering is a simple and economic process to produce dense compacts. This operation is carried out in two steps. In the first step green compacts with sufficient handling strength are prepared by uniaxial die compaction. These green pellets are then fired at chosen high temperatures in controlled atmosphere [17]. Increase in particle surface area (9 to $17 \text{ m}^2 \cdot \text{g}^{-1}$) and sintering temperature (2100 to 2190°C) give higher densities (56 to 71% relative densities). Densities of 90% relative density values are achieved by sintering at a temperature of 2200°C with particles close to or $<1 \text{ }\mu\text{m}$ size. Grain coarsening is the common feature in compacts with high densities obtained by pressureless sintering [17,81,82]. Vickers hardness and flexural strength of the pressureless sintered boron carbide samples are in the range 18 – 24 GPa and 120 – 200 MPa respectively, which are lower than theoretical values. It can be concluded that, with pure B_4C , $>90\%$ densification is possible only at very high sintering temperatures of $\sim 2300^\circ\text{C}$. Such compacts have a coarse grained microstructure of $\sim 50 \text{ }\mu\text{m}$, high amount of intragranular porosity and poor flexural strength ($\sim 200 \text{ MPa}$). [17].

For successful pressureless sintering of boron carbide, sintering aid was regarded as a must until Speyer et al. developed a process for pressureless consolidation obtaining fine-grained boron carbide without the use of sintering aids [83]. The amount of boron oxide was aimed to decrease with an annealing step in vacuum or hydrogen

atmosphere, and powders are sintered at temperatures in the range of 2300-2400 °C, using very high heating rates of 100-150 °C/min. By rapid heating, the extraction rate of boron oxide was accelerated especially in temperatures about 1870-1950 °C. There was less time for oxide facilitated particle coarsening to take place due to rapid heating. Also, by high heating rates applied through the range of about 2010-2140 °C, the time over which coarsening could occur by evaporation and condensation of B₄C was aimed to be minimized. Densities of up to <97% were achieved in this way [83].

Schwetz and Grellner pressureless sintered boron carbide with 1–3 wt % C addition and they reached full densification (>99%) by a post HIP treatment at 2000 °C under argon atmosphere of 200 MPa [84]. In addition to carbon, other grain refinement aids used in pressureless sintering of B₄C which can be listed as Si and Al. Although the strength can be significantly improved by grain size reduction, the toughness may still remain low. Addition of carbides and borides is found to be beneficial for increasing the flexural strength and fracture toughness of B₄C by grain refinement and crack propagation by affecting mechanisms such as crack deflection, micro crack interaction and crack impediment [85]. Addition of various transition metal (Ti, Zr, Hf, V, Nb and Ta) carbides/borides for preparing dense boron carbide is again common in literature [86,87].

Also, in the literature oxides such as Al₂O₃, ZrO₂, Y₂O₃ are listed as the effective sintering aids used in pressureless sintering of boron carbide [17]. Baharvandi et al. studied the effects of yttria doped zirconia addition to boron carbide sintering [88]. Density values of 97 % were attained in samples with >15% ZrO₂ addition. Fracture toughness and flexural strength of the compacts increased from 2.1 to 3.1 MPa·m^{1/2} and 200 to 340 MPa respectively with the increase of ZrO₂ content from 0 to 30% [88]. Also, they studied talc, which is one of the traditional ceramic raw material, effects on the mechanical properties of boron carbide [89].

4.1.2 Hot pressed boron carbide

In order to obtain dense samples and fine microstructures, hot pressing of boron carbide is rather common technique compared to hot isostatic pressing. Hot pressing has been applied to induce grain boundary sliding, twinning, creep, and bulk diffusion accompanied by crystallization [1,17,78]. Still, in 2017 lots of studies related to hot pressing have being made [90-94].

The consolidation properties such as density, porosity and microstructure of hot pressed B₄C is very dependent on the hot pressing parameters, such as temperature, pressure, time, heating/cooling rate, etc. In order to achieve high densities without any sintering aids, the use of submicron powders (1-10 μm), sintering temperatures in the range of 2100-2200 °C, pressures of 25-40 MPa, a dwell time of 15-20 min, and a vacuum or argon atmosphere should be applied [78]. Also, slow cooling after densification resulted in reducing the final density due to the formation of pores while cooling. As boron carbide reacts with the die material, inner lining of the graphite die is essential to prevent this reaction. BN lining has been found to be most suitable [17].

In the literature B₄C ceramics produced by hot pressing generally have the best properties with the following values: hardness, 29–35 GPa; fracture toughness, 2.8–2.9 MPa·m^{1/2}; elastic modulus, 450–470 GPa; thermal conductivity, 30–42 Wm⁻¹ K⁻¹; coefficient of thermal expansion, 5610⁻⁶ K⁻¹; flexural strength, 350 MPa; compressive strength, 1400–3400 MPa [17].

One of the most common sintering aid can be regarded as boron which is one component of the compound [78,95,96]. It was found that boron additions up to 20 wt.%, decreased the average grain size and reduced the porosity of the boron carbide. A material with 60 wt.% boron exhibited very low porosity and supreme resistance to particle erosion [97]. The reaction of boron carbide with elemental boron was modeled as a eutectic at 0.2 at % C and 2073 °C [13].

The other most effective sintering aid is carbon which is the other component of the compound. Sintering is tried to be promoted by a carbon layer on the submicron boron carbide [83]. It is seen that residual carbon at grain boundaries is not consumed by reaction with boron oxide and as a result, C may control the surface diffusion, evaporation and grain boundary movement, thus limiting grain growth [17, 78].

Also, metals such as Mg, Al, Si, Ti, V, Cr, Fe and Cu have been used to promote densification and to decrease sintering temperature. Also, compounds such as alumina, sodium silicate with Mg(NO₃)₂, Fe₂O₃, MgF, AlF₃ or ethyl silicate have been added to lower the sintering temperature and improve mechanical properties and toughness [78].

Mikijelj et al. patented their study and fabricated dense boron carbides by hot pressing at temperatures as low as 1825 °C, using additive mixtures of the quasiternary system

$\text{Al}_2\text{O}_3\text{-AlN-Y}_2\text{O}_3$ [98]. Starting with a submicron boron carbide powder, bending strength values in the range of 700-820 MPa, a maximum fracture toughness of 3.9 $\text{MPa}\cdot\text{m}^{1/2}$, and a hardness of 25.1-26.8 GPa were obtained. They concluded that fine grained microstructure (1-2 μm average grain size) led to the high strength. All of these values were superior to those achieved with dense-hot pressed boron carbide with any sintering aid [98].

4.1.3 Hot isostatic pressed boron carbide

Hot isostatic pressing (HIP) is also applied to densify boron carbide, as well as various other difficult to sinter materials, in order to obtain near 100 % density. By using a diffusion barrier and a special boron oxide glass as a canning material, Larker et al. produced dense boron carbide ceramics without using any sintering aids [99]. They reported that no grain growth occurred and very high strength values such as 714 MPa could be obtained in a material with a 3 μm average grain size [78,99].

In the literature, boron carbide has been injection moulded and then pressureless sintered at 2175 °C. After that, post-HIPed at 200 MPa in argon atmosphere and B_4C doped with 4 wt-% carbon black is obtained fully dense and very fine grained [100]. A patented process explains the preparation of boron carbide samples containing metallic diborides (of Ti, Zr, Hf, V, Nb and Ta), sintered in the temperature 2100 to 2200 °C to give a density of 2.47 g/cm^3 , which on further hot isostatic pressing at 2100 °C under an argon pressure of 200 MPa to achieve a theoretical density of 2.56 g/cm^3 [78,87].

4.1.4 Spark plasma sintered boron carbide

Spark plasma sintering has attracted attention as a densification method for boron carbide, because the sintering temperatures can be lowered without using additives that would reduce grain growth and achieve enhanced mechanical properties compared to classical sintering techniques [78].

Ghosh et al. have consolidated submicrometre sized commercial boron carbide to near theoretical densities using spark plasma sintering as a compaction technique [101]. The densities obtained in the sample spark plasma sintered at 1750 °C under 88 MPa pressure in 2 and 4 min were 96 and 99.2% respectively. The average grain size of these compacts was 1.6 and 2 μm [101]. Kim et al. densified commercial submicron

powders at 1950 °C and obtained <99% density. A Vickers Hardness of 34.5 GPa and a toughness of 4.7 MPa·m^{1/2} have been reported [102]. Anselmi Tamburini et al. obtained 95% dense submicron structured samples at sintering temperatures as low as 1600 °C [103]. The rapid densification rates obtained in such low temperatures could be addressed to excessive crystallographic stacking faults in the grains formed below 1200 °C. A rapid densification is achieved by means of a disorder-order transformation [103]. Due to these benefits, the interest in spark plasma sintering of boron carbide is increasing. It is still one of the trendy research topics in literature and there are lots of on-going projects [104-111].

4.2 Sintering Additives Used in Boron Carbide Sintering

There are various sintering aids used in boron carbide sintering as mentioned above. Only the sintering aids used in experimental stage of this thesis will be extended and explained.

4.2.1 Carbon addition

Carbon has been found to be very effective sintering aid in boron carbide consolidation, primarily in reducing the oxide layer of the boron carbide powders, there by promoting sintering and hindering grain growth. Carbon, well distributed between the particles reacts with B₂O₃ coating according to the reaction in equation 4.2[17]:



Removal of oxide layer allows direct contact between B₄C particles, permitting sintering to initiate at significantly lower temperature (~1350 °C). In addition, carbon at the grain boundaries enhances diffusion, facilitating accelerated solid state sintering. Various types of carbon such as petroleum coke, carbon black, graphite, glucose and phenolic resin (e.g. phenolformaldehyde) can be used as sintering aid. If carbon in solid form such as coke, graphite or carbon black is chosen, it is mandatory that very fine size is used and the mixing carried out thoroughly. Any carbon which is not consumed by the reduction reaction is left in the compact as excess carbon [17].

It is possible to achieve a density over 98% as a result of the small amount of carbon being added to the submicron boron carbide powder, followed by sintering without

pressure by heating to a temperature of 2150 °C in an inert atmosphere. Another effect of carbon addition is on temperature. Condensation caused by grain boundaries or lattice diffusions can be seen at lower temperatures thanks to excess carbon on grain boundaries. In B₄C + C phase would inhibit grain growth during sintering [112]. Simultaneously, due to the presence of carbon on grain boundaries, the melting point of interface of B₄C-C phase at the grain boundaries would decrease to that of eutectic point, thereby materials transport was enhanced [113].

Besides the C addition, other C resources can also been used to enhance the densification of boron carbide. One of the new and trendy carbon source can be regarded as carbon nanotubes (CNT) due to their exceptional mechanical properties, such as elastic moduli of 1000GPa. Therefore, it is generally expected that CNTs can be used as additives to reinforce strengths of composite materials [114]. CNT improves the fracture toughness of the composites through the range of toughening mechanisms like CNT pull-out, crack bridging, and crack deflection [115,116]. Yavas et al. concluded in their study that the addition of CNT increased both Vickers hardness and fracture toughness. The highest hardness and fracture toughness values were 32.76 GPa and 5.94 MPa·m^{1/2}, respectively [116].

4.2.2 Metal addition

In ceramic-metal composites, the increase of the ceramic ratio in the composite increases the hardness, the wear resistance and the high temperature resistance, while the increase of the metal ratio causes the fracture toughness to increase; however the hardness, wear resistance and high temperature resistance to decrease. Ceramic-metal composites containing high-quality ceramics are usually produced by the unpressurized sintering of preformed porous ceramic structures and infiltrating the liquid metal with a temperature above the metal melting temperature. This method, known as metal infiltration technique, requires that the absorbed metal should wet the ceramic matrix, without any reaction between metal and ceramic at the infiltration temperature (in order to eliminate low-specific intermediate phases). Although this method is a suitable method for economical production of complex parts without applying pressure, the most important difficulties encountered are that the porosity can not be formed as a homogeneous in the structure of material, and that the metal can completely fill the ceramic homogeneously without any gap [117].

However the production principle of dense ceramic-metal composites is different. Ceramic-metal composites is also wanted to be sintered in full densification with small grain sizes. As discussed above, boron carbide tends to grow exaggeratedly at the temperatures required for high densities. According to theory of sintering, isolated inert particles dispersed in the boron carbide matrix would also inhibit the grain growth by pinning the grain boundaries. Metals such as Mg, Al, B, Fe, Co, Ni, Cu, Si, Fe and Ti are the most common metallic additive materials used in sintering process in order to provide the desired process control. With the addition of these metals to the system, the sintering temperature can be reduced to temperatures between 1600 °C and 1900 °C and grain growth can be avoided. The addition of metallic phases with low melting temperatures generally changes the physical and mechanical properties of hard ceramics [78]. Although various studies have been carried out on the sintering of SPS and B₄C ceramics, the literature on the production of B₄C-metal composites directly using this method is limited [118].

4.2.2.1 Al addition

Aluminum is an effective sintering aid for boron carbide. Although the binary boundary phase diagrams of the Al-B-C system are rather well established there is only limited data concerning the experimental information on the ternary equilibria [13]. The binary boundary phase diagrams of the Al-B-C system can be seen in Figure 4.1.

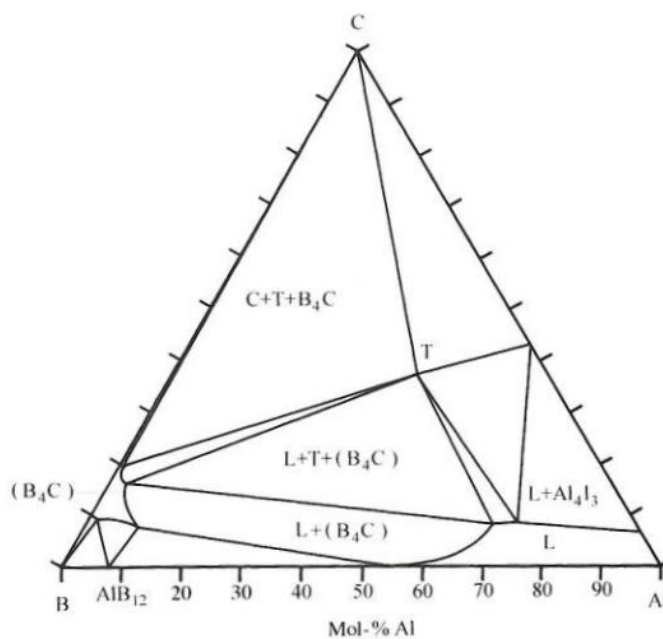


Figure 4.1 : The B - C - Al system at 1400°C [13].

According to Figure 4.1, six ternary phases have been discovered. $B_{40}AlC_4$ and $B_{48}Al_2C_8$, which have a B_4C structure and thus are probably $B_{12}(B,C,Al)_3$ solid solutions, orthorhombic $B_{51}Al_2C_8$, hexagonal and orthorhombic $B_{48}Al_3C_8$, and hexagonal B_4Al_8C , denoted T. The temperature stabilities of these phases are not known [13]. Viala et al. [119] mentioned in their study that many phases containing Al, B and C are reported in various compositions and different crystal structures and they listed these phases in a table as can be seen in Table 4.1.

Table 4.1 : Binary and ternary compounds reported in the Al - B - C system [119].

Formula	Thermal Stability (K) and homogeneity range (h.r.)	Symmetry	Unit cell parameters
Al_4C_3	Decomposes at 2429 narrow h.r.	Rhombohedral (R-3m)	a=0.33388 c=2.4996
B_4C	Decomposes at 2723 $8.8 < C < 20$ at%	Rhombohedral (R-3m)	$a_{8,8}=0.8672$ $c_{8,8}=1.225$ $a_{20}=0.5607$ $c_{20}=1.209$
AlB_{12}	Decomposes at 1165 narrow h.r.	Hexagonal (P ₆ /mmm)	a=0.30054 c=0.32528
AlB_{12}	High temperature α -variety decomposes at 2323 Low temperature γ -form	Tetragonal (P ₄ 12 ₁ 2 or P ₄ 32 ₁ 2) Orthorhombic (P2 ₁ 2 ₁ 2 ₁)	a=1.016 c=1.428 a=1.656 b=1.753 c=1.016
$Al_3B_{48}C_2$ (β - AlB_{12})	High temperature form, decomposes near 2300 Low temperature form A	Tetragonal (P ₄ /mmm) Orthorhombic	a=0.882 c=0.509 a=1.234 b=1.263 c=0.508
	Low temperature form B	Orthorhombic	a=0.617 b=1.263 c=1.016
$AlB_{24}C_4$ (AlB_{10})	Decomposes above 2000	Orthorhombic	a=0.8881 b=0.9100 c=0.5690
$Al_8B_4C_7$ ($Al_8B_xC_6$)	Decomposes at 2110 ($2 < x < 4$)	Hexagonal (P6 ₃ /mcm)	a=0.59118 c=1.5915
Al_3BC (x, Al_4BC)	Stable up to at least 1273	Hexagonal	a=0.6046 c=1.1541

In the literature, spark plasma sintered aluminum added boron carbide is studied limitedly. Hulbert et al. [120] produced B_4C preforms with a 70% of theoretical density with following the steps: mixing, drying, crushing, sieving and directly spark plasma sintering very fine and fluffy textured amorphous B and C powder mixture. Then, this porous structure was infiltrated with Al at 1180 °C and the relative density reached 90% of theoretical density. However, when the internal structure of these materials is examined, it has been determined that the microstructure shows differences in the

material cross section, and that the preforms formed by this show the pore structure. The B₄C-Al materials produced by this method are called FGM- (Functionally Graded Materials) because they contain Al at different ratios along the cross-section [120].

Arslan and Kalemantas [121] obtained a relative density of 98% in SiC-B₄C-Al systems by using an infiltration technique after spark plasma sintering. They concluded that the formation of Al₄C₃, which prevent the formation of dense compact structures, should be avoided by controlling the surface chemistry, the particle size of the starting powders, the process parameters used and by improving the the wetting properties of these systems [121].

When B₄C reacts with Al by adding Al in minimum amount, various compounds such as Al₃BC and AlB₂ can be obtained. Using the experimental data obtained, it was found that the Al addition increases the grain size while decreases the porosity. In addition, fully dense boron carbide structures can be obtained with Al addition at temperatures of 2050-2150 °C by pressureless sintering. 4 wt.% aluminum addition resulted in an increase in the bending strength, hardness and fracture toughness compared to monolithic pressureless sintered boron carbide. 1% to 3 wt.% Al addition by weight caused an increase in the modulus of elasticity. However, it has been observed that increasing Al addition, in general, is accompanied by a decrease in the mechanical strength due to the grain growth. [122].

Kang et al. [123] produced Al-B₄C composites containing 5, 10, 20 and 40 wt.% Al by using hot pressing method and studied the phases formed. The sintering procedure was carried out using the graphite molds at 1600 °C for 1h, under an applied pressure of 35 MPa, the results were compared with pure B₄C. X-ray diffraction (XRD), scanning electron microscope (SEM) and transmission electron microscopy (TEM) were used to identify the phase constituent of the powders and sintered samples. As a result of characterization investigations they found out that B₂O₃ is formed during the mixing stage of B₄C and Al powders, and the resulting B₂O₃ was reduced to B by reaction with Al due to high temperature during sintering. To prevent this, the sintering temperature has to be lowered. In addition, the reaction between Al and B₄C resulted in a ternary phase of Al₈B₄C₇ and the B₄C transformed to a rich boron phase (B_{6.5}C) because of the superfluous boron in the system [123].

Chen et al tried to increase the toughness by reinforcing boron carbide with 6061 Al for the use of neutron shielding with high strength and low density [124]. After hot pressing, they observed B_4C , Al, AlB_2 and Al_3BC phases. With the Al 6061 addition the yield strength and ultimate tensile strength of the $B_4C/6061Al$ neutron absorbers are enhanced while ductility to fracture is slightly decreased [124].

4.2.2.2 Si addition

Silicon is one of the other effective sintering aid of boron carbide due to its low density. Figure 4.2 shows the phase relations between B-C and Si. The experimental data indicated a ternary equilibrium between C, SiB_6 and SiC up to temperatures exceeding $1900^\circ C$ [13].

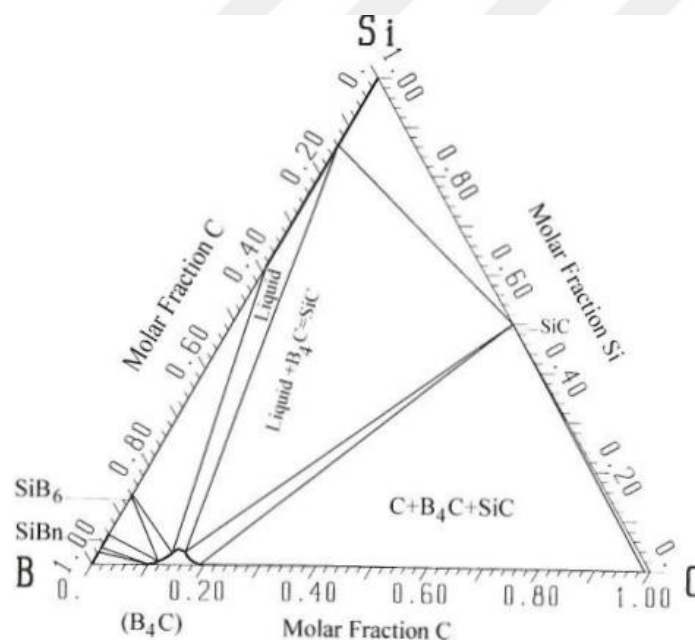


Figure 4.2 : Isothermal section of B - C - Si system at 2000 K [13].

Thermodynamic calculations showed the existence of a binary phase equilibrium of boron carbide and a Si- B- containing (SiB_n) which melt above $1560^\circ C$. The characteristics of the B-C-Si system comprise the stability of a $B_{12}(B,C,Si)_3$ solid solution with a maximum of 2.5at % Si being in a equilibrium with a boron saturated silicon melt [125]. The formation of $B_{12}(B,C,Si)_3$ is accompanied by the precipitation of β -SiC which melts eutectically with SiB_6 and residual Si above $1380^\circ C$. As a Si incorporation into the boron carbide lattice always results in the C or the simultaneous formation of SiC if Si is present in excess, it may be concluded that Si substitutes for C assuming that there is no carbon in boron carbide on interstitial sites [13].

Sahani et al. [126] conducted a comparative study and mixed B_4C , SiC with 5, 10, and 20 wt. % Si metal powders and investigated their sinterability and properties after two different sintering processes: conventional sintering at 1950 °C and spark plasma sintering (SPS) at 1350 °C. They did not obtain any glassy phases and reaction phases observed in the sintered products for SPS specimens with Si contents. Si turned into SiC and they achieved better mechanical and physical properties in 5 and 10 wt. % Si added samples; however residual Si is obtained in 20 wt. % Si containing sample. They concluded that with increasing Si content from 5 to 10 wt. %, the density and the hardness values increases, while further increase of Si to 20 wt. % affects the hardness negatively due to the existence of large amount of residual Si and increase of the SiC content in the composition. Also, they were successful in spark plasma sintering at such lower temperatures like 1350 °C [126].

Rehman et al [127] chose Si as a sintering aid in spark plasma sintering of boron carbide. They spark plasma sintered their powders with 4, 6, 8 and 10 wt. % Si at 1700 °C for 7 min with a heating rate of 100 °C/min in a vacuum under a uniaxial pressure of 60 MPa. The relative density, Vickers hardness and flexural strength of the B_4C/SiC composite prepared from 8 wt% Si reached $99.73\pm 0.07\%$, 36.72 ± 1.55 GPa, and 612 ± 10 MPa, respectively. By using Si, B_4C densification is assisted due to the formation of liquid Si during sintering. Also, the formation of SiC phase successfully restrained the growth of B_4C and improved its hardness and strength [127].

Ye et al. [128] examined the production of boron carbide with mixing 0 to 10 wt % Si and directly spark plasma sintered by using graphite molds which have 20 mm inner diameter. Spark plasma sintering procedure is carried out at 1800 °C for 4 min (100 °C/min heating rate is used) and under 50 MPa pressure. In this study, it was found that Si facilitated sintering by forming liquid phase and the relative density increased from 99.0 % to 99.93 %. At the same time, the hardness value obtained by sintering pure B_4C is found to be 24 GPa while it reaches 39.11 GPa in samples containing 8% Si and 41.83 GPa in 4 % Si containing samples. When the content of Si was increased to 10%, they observed a slight decrease in hardness due to the increased amount of Si [128].

Xu et al in investigated Al and Si additions to boron carbide both individually and together. For the sample with 5 wt.% Si added, the Si reacts with the B_4C leading to the formation of SiC . They showed the difference of phases occurred after infiltration

and sintering processes. Si reacts with B_4C to form $B_xC_{1-y}Si_y$, rather than the main secondary phase of SiC, at the B_4C grain boundaries in infiltration process. The disks were sintered at 2050–2250 °C for 1 h in a graphite furnace under flowing argon, with a heating rate of 50 °C/min. The phase difference is linked to process temperature difference. The infiltration processing of B_4C based composites with Si as an infiltrant is normally performed at a moderate temperature of around 1400–1500 °C, while the sintering process is carried out at elevated temperatures such as 2050–2250 °C. They concluded that the $B_xC_{1-y}Si_y$ phase formed during the infiltration processing might decompose into B_4C and SiC [122].

Another study concerning spark plasma sintered boron carbide with the additions of Si and “amorphous B was carried out at 1300 °C for 30 min in vacuum under an applied pressure of 50 MPa. The long soaking time was to remove the oxide impurities from the particle surfaces. The densification is enhanced by Si and B additions in comparison with pure B_4C sample. This densification improvement is attributed to the formation of a liquid phase during sintering, which promoted the mass transfer between the powder particles. They concluded that the Seebeck coefficient and electrical conductivity of the sample with 10 wt% Si is higher than that of the B_4C sample, the thermal conductivity is reduced for Si added samples [129].

4.2.2.3 Ti addition

Among above mentioned metallic additives, Ti is the most common used metal [130]. However, the researchers generally preferred to use Ti with B and C powders instead of B_4C [131-134]. Besides the usage of TiB_2 powders directly [135-142] lots of studies have been made by adding TiO_2 and C to boron carbide structure for obtaining TiB_2 [142-146].

The ternary B-C-Ti system was generally considered for cutting tool industry. No ternary phases have been found in this system. The ternary solid solubility of the particular binary compounds except $TiC_{0.81}B_{0.17}$ is generally less than 1 at. % TiB_2 coexists with TiC_{1-x} in a quasi binary eutectic equilibrium at 2620 °C and 57 mol % TiC_{1-x} . Also, TiB_2 forms a quasi-binary eutectic with B_4C at 2310 °C and 88 mol % B_4C ; as well as with C at 2507 °C and 33 mol % C. This means that TiC is not stable in the presence of B_4C but reacts to form $TiB_2 + C$. On the other hand, TiB_2 - B_4C

composites can be fabricated from TiC and B by reaction sintering. Isothermal section of B-C-Ti system is shown in Figure 4.3.

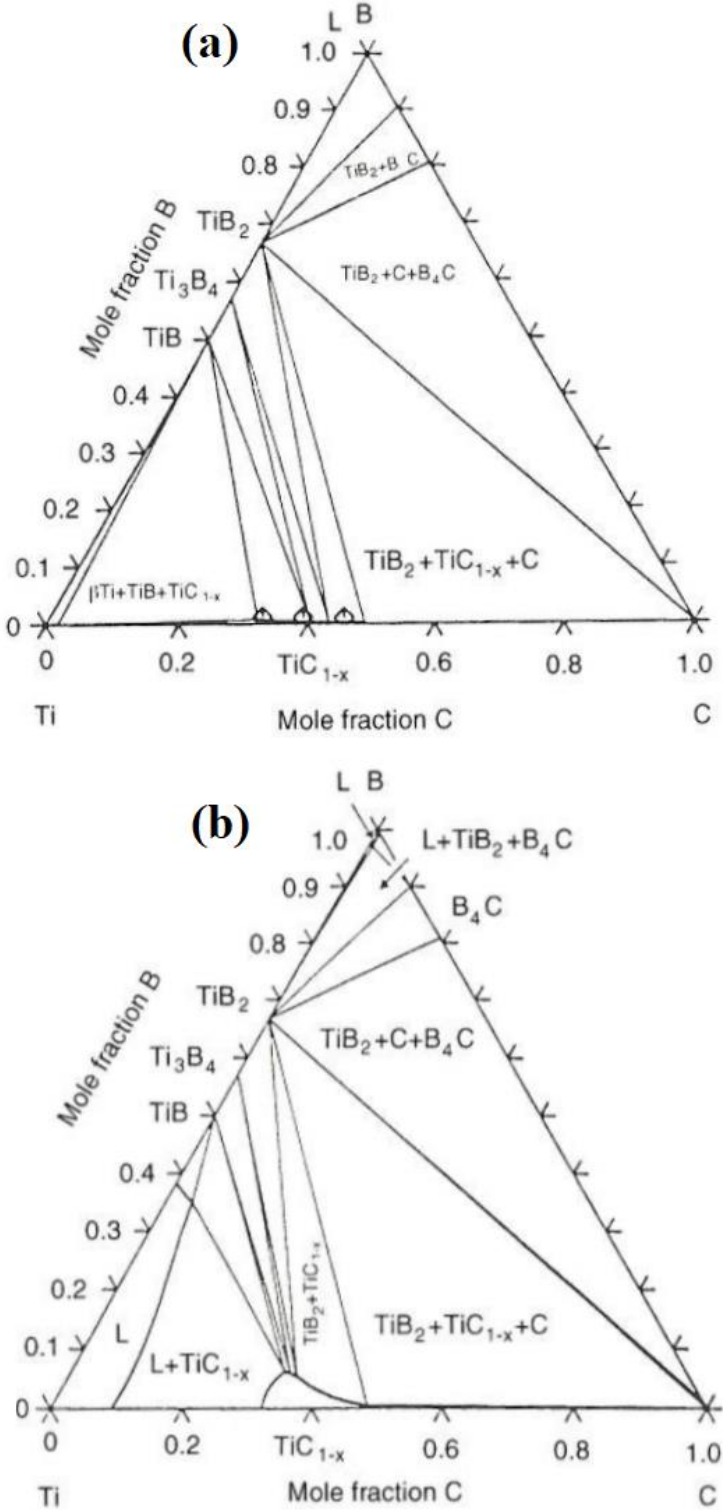


Figure 4.3 : Isothermal sections of B - C - Ti system (a) at 1400 °C (b) 2100 °C [13].

Nikzad et al. [131] studied the simultaneous synthesis and densification of B₄C/TiB₂ composite starting from ball milled Ti, B and graphite powders by using SPS

apparatus. They obtained the full conversion of powders to the TiB₂-B₄C composite at much lower temperatures such as 1200 °C. Also, when the process is held at relatively low heating rate conditions, the desired product is formed through relatively slow solid-solid reactions. However in rapid heated spark plasma sintered samples, a combustion synthesis process occurs, and the remarkable amounts of unreacted and intermediate phases are observed. A composite material with homogeneous phase distribution and fine-grained microstructure could be obtained when the heating procedure was slow [131].

Furthermore, when TiO₂ is used instead of Ti as a sintering aid in boron carbide sintering, again all addition phase transforms into TiB₂ phase. However this time, stoichiometric amount of C is required for the reaction to take place:



Conversion of TiO₂ to TiB₂ with the above reaction led to a significant reduction in sintering temperature and increase in toughness and strength. Skorokhod sintered boron carbide and titania powders at 2000 °C, under a pressure of 20 MPa in a static argon gas atmosphere by using hot pressing technique [146]. According to their phase characterizations, only B₄C and TiB₂ phases were identified, although the presence of a small amount of oxygen or carbon cannot be ruled out. They observed cracks and weakened interfaces between the TiB₂ particles and B₄C matrix according to microstructures and concluded that they are the result of a large difference in the linear thermal expansion between B₄C ($\alpha = 5.7 \times 10^{-6}/^\circ\text{C}$) and TiB₂ ($\alpha = 8.7 \times 10^{-6}/^\circ\text{C}$). The thermal expansion mismatch stress developed on cooling to room temperature places the TiB₂-B₄C boundary under the tensile stress and leads to partial or full fracture of the interface. Flexural strength of 621 MPa and fracture toughness of over 6.1 MPa·m^{1/2} is obtained and the reason of increase in mechanical properties linked to the changed fracture mechanisms with the TiB₂ formation. Almost all of the grains fractured transgranularly in boron carbide, creating very rough fracture surface, whereas TiB₂ particles forces the crack to propagate in a nonplanar fashion (both transgranular and intergranular) thus enhancing the energy dissipation at the crack tip [146].

Huang et al. used spark plasma sintering for consolidating boron carbide with in-situ reaction of TiO₂, carbon and B₄C at a temperature of 2000 °C in order to produce the

B₄C–TiB₂ composites. Full density has been achieved by adding 30 vol.% TiB₂, while the highest fracture toughness value has been obtained as 3 MPa·m^{1/2} [143].

One of the highest fracture toughness value belongs to Wang et al. with 8.2 MPa·m^{1/2}. % 40 at. TiB₂ containing boron carbide which was sintered at 1850 °C for 0.5 h, and then hot-pressed for 1 h at 2050 °C under a pressure of 35 MPa in a vacuum of 1.3x 10⁻³ Pa showed this value while its elastic modulus is found to be 562 MPa, but authors did not mention exact value of hardness. They concluded that the main toughening mechanisms are microcracks toughening and deflection toughening of propagating cracks caused by the thermal expansion mismatch between TiB₂ and B₄C [145].

The second highest fracture toughness belong to a study which is conducted in İstanbul Technical University laboratories by using same system in experimental section of this thesis. Uygun et al. reached 6.9 MPa.m^{1/2} fracture toughness and 32.5 GPa hardness in 10 vol. % TiB₂ containing boron carbide ceramics which showed 98.30 % relative density. The highest hardness was attained in 5 vol. % TiB₂ containing sample with 34.5 GPa value. They found out that with the increasing TiB₂ content the densification promotes, however the hardness and fracture toughness is affected negatively [135].

Heydari and Baharvandi concluded their comprehensive and comparative review as defining titanium diboride as an effective sintering aid and the B₄C–TiB₂ composites as a useful material for the designing of thermoelectric materials. TiB₂ addition generally improves the hardness, fracture toughness and strength of boron carbide. Also, the presence of TiB₂ prevents the growth of B₄C grains, reduces the sintering temperature, improves the mechanical properties and modifies the microstructure of the resulting composite [130].

5. EXPERIMENTAL PROCEDURE

5.1 Powders Used in Experiments

As mentioned above, to promote the densification of boron carbide, hinder the exaggerated grain growth and decrease the sintering temperature boron carbide generally requires some sintering additives. In this study, both carbon based and metal based additives were used for this purpose. Boron carbide powders were supplied from H.C. Stark company, Germany whose grade is HS and B:C ratio is 3.7 – 3.8 [147].

As a C source, both C-black and CNT powders were used. C-black was supplied from Mitsubishi Chemical, Tokyo, Japan with #30 grade, whereas multi-wall carbon nanotube (1020 MT-MW-010-020) which is chemically functionalizable and possesses high purity, good mechanical properties as well as controlled diameter and length was supplied from Carbon NT&F 21[®] company. The purity of the CNT is mentioned to be >95% and the amorphous carbon is <3%, whereas the ash in the content is given as <0.2% [148]. On the other hand, the purity of C-black is 98 % with an ash content <0.2%. Ash content can be defined as the remaining percentage by weight when carbon source is burned at 750°C [149]. The moisture content of the C-black powder is also <0.2%. Nowadays, the most important carbon black is the ‘furnace black’ in which hydrocarbons are partially combusted and immediately quenched with water. The primary particle consists of several graphene-like layers, which combine to form spherical or oval particles. The particle diameter can vary according to the processing conditions and generally lies between 5 and several 100 nm [150]. The average particle size of the C-black used in this study is 30 nm.

The metallic additives, Al, Si and Ti (all of them having 99.8% purity) were both supplied from Alfa Aesar company, USA. In further stages, more experiments were designed with Ti powder having smaller particle sizes and with TiO₂ powders in order to see the reactive spark plasma sintering effects on the final microstructure. Smaller particle sized Ti with 99.8% purity and TiO₂ powders with 99.90% purity were supplied from US Research Nanomaterials Inc, USA. Table 5.1 lists the impurities

seen in boron carbide powder and additives, Al, Si, Ti with large and small particles, TiO₂ and C-black powders.

Table 5. 1 : Impurities seen in powders used in experiments.

Impurities	B ₄ C	Al	Si	Ti-LP	Ti-SP	TiO ₂	C-black
Al	0.01	99.80	0.09	0.0022	<0.0005	≤0.003	-
B	-	-	-	<0.0005	-	-	-
Bi	-	-	-	<0.02	-	-	-
C	-	-	-	-	<0.02	-	98.0
Ca	-	-	0.008	0.0007	-	≤0.005	-
Cl	-	-	-	<0.01	-	-	-
Co	-	-	-	<0.01	-	≤0.01	-
Cr	-	0.001	-	0.006	-	≤0.005	-
Cu	-	<0.001	-	-	-	-	-
Fe	0.03	0.146	0.04	-	<0.05	≤0.005	0.08
K	-	-	-	-	-	≤0.005	-
Mg	-	<0.001	-	-	-	≤0.01	0.075
Mn	-	0.002	-	-	-	-	-
Mo	-	-	-	-	<0.0002	≤0.005	-
N	0.4	-	-	-	<0.02	-	-
Nb	-	-	-	<0.01	-	-	-
Ni	-	0.004	-	0.011	-	-	0.8
O	1.4	0.012	0.5956	0.3595	-	-	-
P	-	-	-	-	-	≤0.01	-
Pb	-	0.001	-	-	-	-	-
Pd	-	-	-	<0.005	-	-	-
S	-	-	-	-	-	≤0.005	-
Si	0.09	0.034	99.80	0.0059	<0.0003	≤0.003	-
Sn	-	-	-	<0.01	-	-	-
Ta	-	-	-	<0.005	-	-	-
Ti	-	0.004	-	99.80	99.80	-	-
V	-	-	-	<0.005	-	-	-
W	-	-	-	-	-	≤0.01	-
Zn	-	0.004	-	-	-	-	-
Zr	-	0.001	-	-	-	-	-

Ti-LP: Ti with large particles, Ti-SP: Ti with smaller particles

In order to define particle characteristics, the average particle size, particle size distribution and surface area should be considered and these key properties should be determined. Average particle size and particle size distribution of powders used in experimental studies was measured by Malvern Zetasizer Nano S Measurement System using dynamic light scattering and zeta potential [151]. In addition, Nova 2200e Surface Area & Pore Size Analyzer was used to calculate the surface area of powders. During the measurements, de-gassing temperature was set at 160 °C and the duration was 30 min. Surface areas and the average particle size (d₅₀) of the powders are given in Table 5.2.

Table 5.2 : Average particle size and surface areas of powders used in this study.

Powders	d_{50} (μm)	Surface area (m^2/g)
B_4C	1.78	13.6 ± 0.03
Al	9.48	5.09 ± 0.03
Si	4.29	6.71 ± 0.03
Ti-LP	26.46	0.38 ± 0.03
Ti-SP	5.12	6.38 ± 0.04
TiO_2	0.56	15.78 ± 0.04
C-black	0.033	101.08 ± 0.18

Ti-LP: Ti with large particles, Ti-SP: Ti with smaller particles

Due to unique structure of CNTs, the surface area and average particle size could not be measured using mentioned apparatuses. According to product catalogue, multiwalled CNT powders has 10-20 nm diameter and 5-15 μm length and $>200 \text{ m}^2/\text{g}$ surface area [148]. The average grain size values given in Table 5.2 are consistent with SEM images below. Also, the microstructures of the B_4C , Al, Si, Ti-LP, Ti-SP, TiO_2 and C-black powders used in the experimental studies were examined by scanning electron microscopy and the images of the powders are given in Figure 5.1, respectively. The average grain size values given in Table 5.2 and the SEM images in Figure 5.1 are consistent with each other.

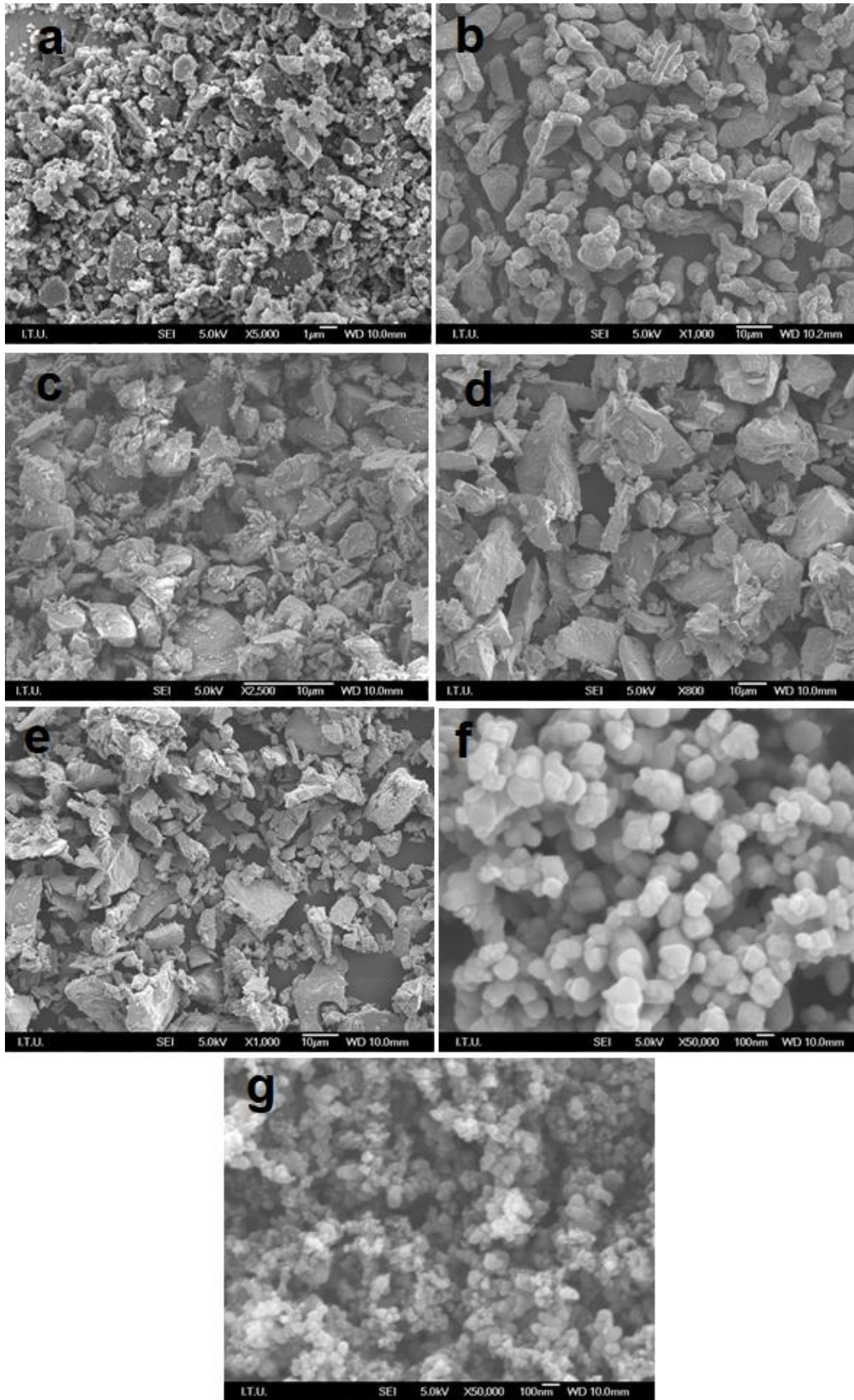


Figure 5.1 : SEM images of (a) B₄C, (b) Al, (c) Si, (d) Ti-LP, (e) Ti- SP, (f) TiO₂ and (g) C-black powders.

5.2 Production of Boron Carbide Based Composites

5.2.1 Powder preparation

The process flowchart followed in the experimental studies is given in Figure 5.2.

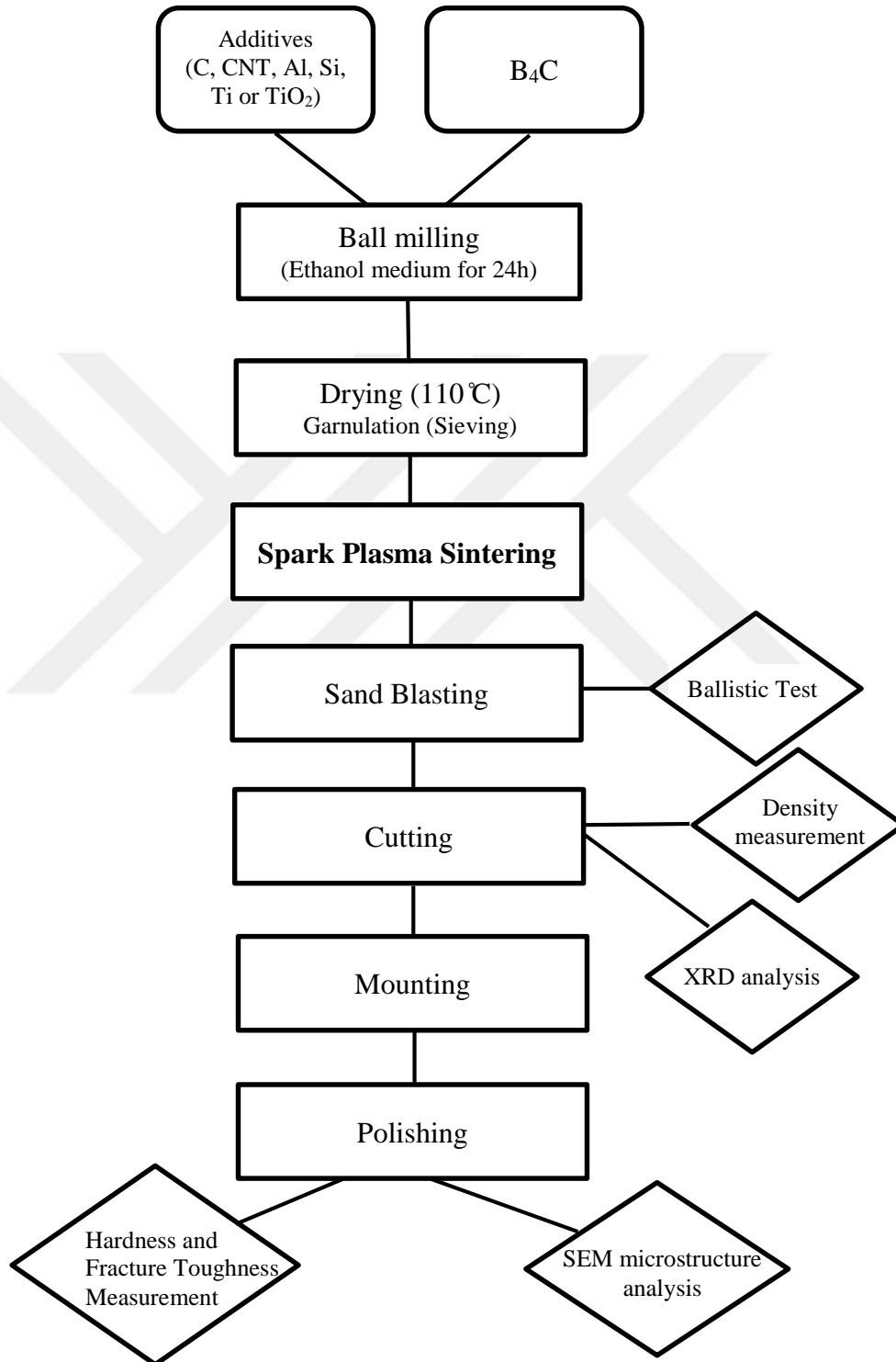


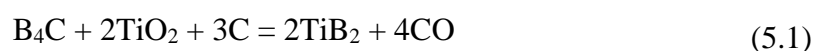
Figure 5.2 : Process flowchart of the experiments.

In the first stage of experiments, boron carbide powders were weighed with corresponding amounts of different additives. Due to the dimensions of used dies in experiments, the final product is formed in an hexagonal shape with 62 mm diagonal, 31.5 mm length and 10 mm thickness. Based on the final product volume, all the additive amounts are calculated. The amounts of additives used in the experiments are given in Table 5.3.

Table 5.3 : The amounts of different powders used in the experiments.

Powder Mixture	B ₄ C	Additive	Total Weight
B ₄ C	64.97 g	-	64.97 g
B ₄ C + 5 vol. % Al	61.72 g	3.48 g Al	65.20 g
B ₄ C + 5 vol. % Si	61.72 g	2.99 g Si	64.71 g
B ₄ C + 5 vol. % Ti	61.72 g	5.81 g Ti	67.53 g
B ₄ C + 10 vol. % Ti	58.47 g	11.62 g Ti	70.10 g
B ₄ C + 15 vol. % Ti	55.22 g	17.42 g Ti	72.64 g
B ₄ C + 20 vol. % Ti	51.97 g	23.23 g Ti	75.20 g
B ₄ C + 5 vol. % TiO ₂	64.03 g	6.69 g TiO ₂	72.23 g
B ₄ C + 10 vol. % TiO ₂	63.10 g	13.39 g TiO ₂ 1.51 g C	79.51 g
B ₄ C + 2 vol. % C	63.66 g	3.02 g C	64.74 g
B ₄ C + 2 vol. % CNT	63.66 g	1.08 g C 1.08 g CNT	64.74 g

All the metallic additives and C-black and CNT additives are mixed according to the direct volumetric ratio. However TiO₂ containing powder mixture was weighed such that the final composition will have 5 or 10 vol. % TiB₂. As a result of in-situ reaction of TiO₂, carbon and B₄C, all TiO₂ and C is transformed into TiB₂ and B₄C [146]. The amounts were calculated based on equation 5.1.



According to the stoichiometry of above reaction, 55.25 g B₄C will be used by 159.74 g TiO₂ and needs 36 g C to form 138.98 g TiB₂ (2 moles of TiB₂). However, according to volumetric calculations, final composite should contain 5.82 g TiB₂ to form boron carbide with 5 vol. % TiB₂ and 11.65 g TiB₂ to form boron carbide with 10 vol. % TiB₂. In the light of these calculations, needed amounts are given in Table 5.3.

All of the powders in corresponding quantities were weighed in Mettler Toledo PG503-S model scale. Then the powder mixtures were prepared in ethanol medium by using appropriate balls in ball milling for 24 hours. After ball milling, the batches were

dried at 110 °C for at least 48 hours by using Electromag M420 binder drying oven. Then the dried powder was granulated thanks to sieve with 150 µm openings. Only in C and CNT containing samples, due to the heterogenous mixing possibility due to CNT precipitation or agglomeration risk, carbon elements were introduced into boron carbide and mixed in ethanol medium first by using ultrasonic mixer. Then the batches were prepared by mixing B₄C and CNT or C-black by magnetic mixer and then ball milled at room temperature for 24 hours. The slurry was then dried and screened from 150 µm openings.

5.2.2 Spark plasma sintering stage

Experimental studies were carried out in SPS 7.40 MK VII, SPS Syntex Inc. apparatus in Spark Plasma Sintering Laboratory, ITU Metallurgical and Materials Engineering Department, shown in Figure 5.3.



Figure 5.3 : SPS system used in experimental studies.

The prepared powders were directly loaded into a graphite die for SPS without any binder addition or preshaping application. The graphite dies used in the experiments which enables to form hexagonal shaped final products with 62 mm diagonal, 31.5 mm length and 10 mm height can be seen in Figure 5.4.

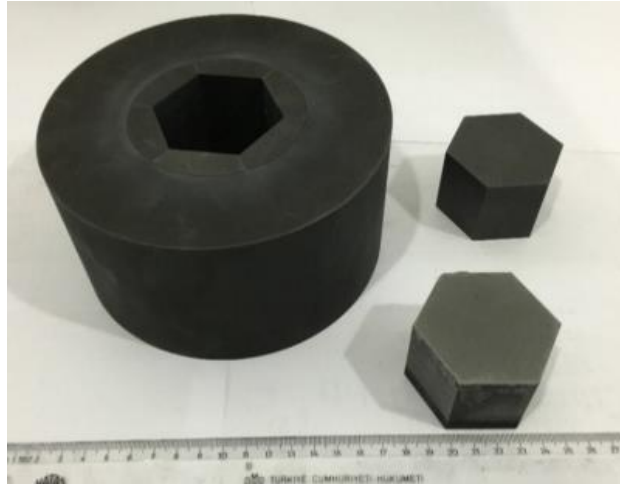


Figure 5.4 : The dies used in SPS system.

During sample preparation stage before SPS experiments, the bottom and upper punch mold surface is covered with two layers of graphite paper. Graphite papers were placed in order to avoid the possible contamination from graphite dies, and for better thermal homogeneity in the sample [50]. Also, possible reactions between boron carbide and graphite especially in samples containing additives which can possibly react with carbon or graphite is tried to be prevented. The powders were carefully flattened in order to obtain final samples with same thicknesses in every point of the sample. Bottom and upper punches both arranged as in equal length and then compressed with a hand press under 10 MPa. In order to lower the heat loss according to radiation, whole molding system was wrapped by a graphite blanket.

The temperature of the SPS process was measured with an optical pyrometer that was focused on the small hole at a depth of 1 mm from the graphite mold surface. The current was controlled manually. The direct current impulse frequency used is 12: 2 and the current is delivered to the powder sample 12 times for 3.3 ms and resting 2 times. During sintering, the parameters such as displacement, displacement rate, temperature, vacuum, current, voltage and pressure were monitored. The linear shrinkage of the specimens during the SPS process was continuously monitored by displacement of the punch rods. The effect of the thermal expansion of the graphite punch rods with increasing specimen temperature was negligible.

The composites were sintered in a vacuum environment and under the conditions required, using the Argon atmosphere. After the spark plasma sintering process, sand blasting is carried out to remove graphite papers from the surface of sintered compacts.

Figure 5.5 shows the photo of hexagonal shaped final product before and after sand blasting procedure.

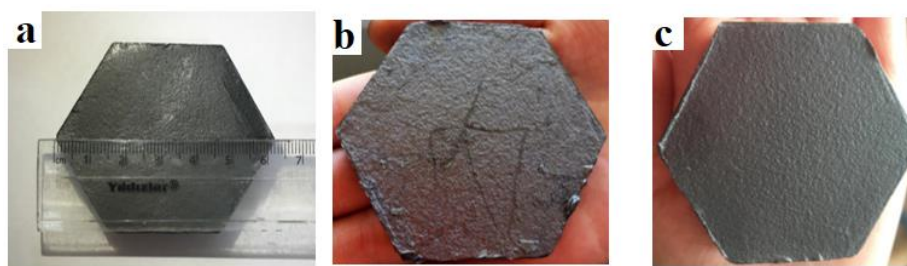


Figure 5.5 : Spark plasma sintered final product (a) showing 62 mm diagonal (b) having graphite in the surface and (c) after sand- blasting.

Samples were cut to the appropriate dimensions with the help of diamond wheel by using Struers Labotom-5 cutting device. After the mounting process, polishing processes were carried out using Struers Tegramin-25 polishing machine.

5.2.3 Characterization of boron carbide ceramic composites

5.2.3.1 Density

The density measurement of sintered samples was carried out by using AND-1653 model density measurement device according to the Archimedes principle. The bulk density of a complex shape is measured using Archimedes' principle, where the difference in the weight of the shape in air compared to the weight suspended in water permits calculation of the volume. As a result, the density of the sample can be found according to equation 5.2:

$$\rho = \rho_{\text{water}} * W_s / (W_s - W_{\text{sw}}) \quad (5.2)$$

where ρ is for density (g/cm^3); ρ_w is water density value (g/cm^3); W_s is the sintered sample weight in air (g) and W_{sw} means the weight of sintered sample suspended in water (g). The relative densities of sintered samples are calculated by equation 5.3:

$$\rho_{\text{relative}} = \frac{\rho_{\text{measured}}}{\rho_{\text{theoretical}}} \times 100 \quad (5.3)$$

5.2.3.2 XRD analysis

Phase analyzes of the starting powders and the resulting samples were carried out using $\text{Cu-K}\alpha$ radiation with a X-ray diffractometer (Rigaku Miniflex) at $2\theta:5-85^\circ$, $2^\circ/\text{min}$

scan rate. XRD analyzes were carried out to investigate whether any reaction occurred during sintering to form a different compound.

5.2.3.3 Hardness and fracture toughness measurements

In order to determine the effects of hexagonal geometry on the densification and mechanical properties, samples are cut from their centre and six different edges. Then the cut samples are mounted and carefully polished down to 1 μm diamond paste. The polished surfaces were subjected to Vickers microhardness measurement using a Leica VH-MOT Vickers microhardness tester with 12 seconds duration and a load of 9.8 N. The Vickers microhardness values were measured according to ASTM C132-08 (Standard Test Method for Vickers Indentation Hardness Advanced Ceramics) standard. For each sample, 15 measurements were taken and mean hardness values and standard deviations were calculated.

The fracture toughness values of the samples were calculated by the indentation method with the Palmqvist approach given in below equation. In brittle structures like boron carbide, the most appropriate method for fracture toughness is found to be Palmqvist equation [152]. The equation 5.4 used in fracture toughness calculation can be seen in below:

$$K_{1C} = 0.0264 \times (H_v \cdot a) \times \left(\frac{E}{H_v}\right)^{0.4} \times l^{-0.5} \quad (5.4)$$

where H_v represents the Vickers hardness, a represents the half of the diagonal length E represents modulus of elasticity of sample and l represents crack length. A schematic view of the Palmqvist crack type is given in Figure 5.6.

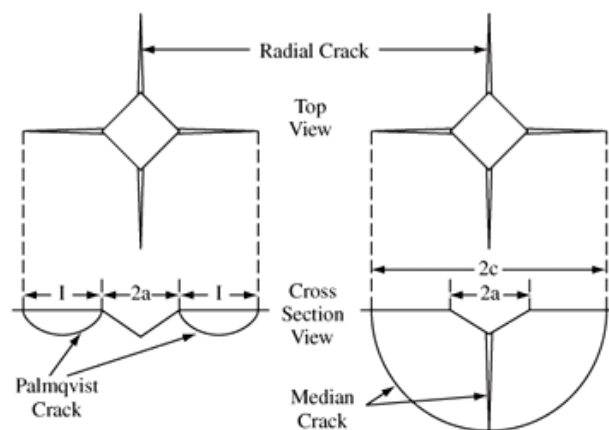


Figure 5.6 : Crack formation by Vickers indentation [153].

5.2.3.4 Microstructure observations

Microstructural analyzes of specimens which are produced with spark plasma sintering (SPS) technique were performed by using JEOL JSM 7000F field emission scanning electron microscope (FE-SEM).

Before microstructural characterization, some metallographic preparations have been applied to the samples. The samples were cut to the appropriate dimensions and "DuroFast", a thermosetting resin with solidification properties at high temperatures, was used as mounting resin. DuroFast epoxy resin was chosen due to its high amounts of mineral filler, which makes it ideal for surface smoothness and edge sharpness especially for hard materials. The grinding and polishing procedures were carried out using the steps given in Table 5.4 using Struers Tegramin 25 semi automatic grinding and polishing device.

Table 5.4 : Metallographic sample steps used for microstructural observations.

Disc	Abrasive	Speed	Force	Duration
MD-Piano 220	Water	300 rpm	210 N	1 min
MD-Piano 1200	Water	150 rpm	210 N	2 min
MD-Largo	DiaPro Allegro Largo 9 μ m diamond susp.	150 rpm	210 N	6 min
MD-Dac	DiaPro Dac 3 μ m diamond suspension	150 rpm	150 N	4 min
MD-Nap	DiaPro Nap 1 μ m diamond susp.	150 rpm	150 N	1 min

5.2.4 Ballistic test

The ballistic performances of the samples were tested in Ballistic Protection Center Test Laboratories, ROKETSAN Inc., Ankara, Turkey. NIJ Standard 0101.06 Level IV [154] using M61 type armor piercing 7.62 \times 51-mm NATO projectiles with full metal jacket (FMJ) is used in experiments. Figure 5.7 shows the schematic view of a 7.62 \times 51-mm NATO bullet and the cross-sectional view of the core of the projectile [155].

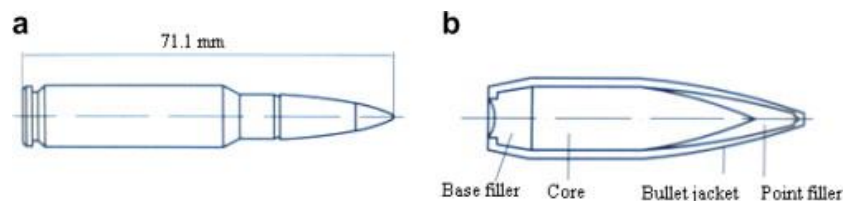


Figure 5.7 : (a) Schematic view of the 7.62 mm AP projectile and (b) cross-sectional view of the core of the projectile [155].

Table 5.5 demonstrates the general properties and used materials of M61 type AP projectiles which are manufactured by Makine Kimya Endüstrisi, Turkey.

Table 5.5 : Some properties and materials of 7.62 mm bullets [155].

Type	Property
Cartridge length	71.12 ± 0.76 mm
Cartridge weight	25.47 ± 1.75 g
Case material	7.62 × 51 mm Brass (CuZn30)
Core material	DIN 100Cr6 (HRC 61–62)
Bullet weight	9.75 ± 0.1 g
Length of bullet	32.95 mm
Nose type	Conical (cone half angle, $\alpha = 17^\circ$)

According to NIJ 0101.06 Level IV standard, the bullet should reach to 878 ± 15 m/s speed when it contacts the sample. During the tests, this regulation has been taken into account. The results of the shootings that did not provide this status were not taken into consideration. In order to achieve right speed in bullets, the gunpowder (base) amount is important. The hives were prepared in required amounts of gunpowders to achieve these speed rates. The photo of the bullet is given in Figure 5.8 and it demonstrates the bullet used in ballistic tests. The study of ballistic performance using actual military ammunition is important because fragmentation of the ceramics depends on actual conditions.



Figure 5.8 : The photo of the 7.62 × 51-mm NATO bullet with and without full metal jacket.

The experimental setup in ROKETSAN Ballistic Protection Center consists of a computer and software that have the ability to measure velocity, velocity probes equipped with laser diodes, timer for time and velocity calculations (multiplication

rate) located at different distances. The light gates are mounted in a fixed frame of 2000 mms as shown in Figure 5.9. The bullet generates a START signal when passing through the first velocity probe and a STOP signal when passing through the second velocity probe. The flight time of the bullet between the doors through the timer is measured. The bullet speed is calculated using a known road value and the measured time. The first velocity probe named as velocity probe I in Figure 5.9, is located 2.2 m far from the shooting gun, whereas the second velocity probe (velocity probe II) is located 10.4 m away from the shooting gun. The speed at which the target was hit was calculated by interpolation technique by using a software programm called BMS. Also, the obliquity and yawing of shots are determined in each test. The shots performed yawing angle higher than 3° are repeated and did not taken into consideration.

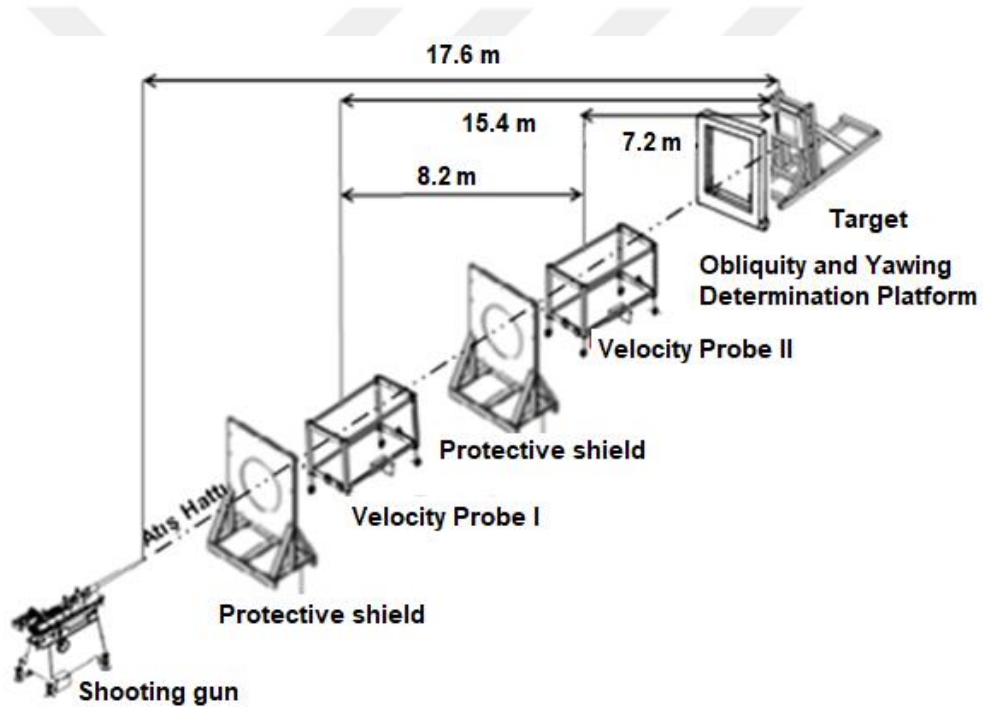


Figure 5.9 : A schematic view of experimental setup used for the ballistic testing.

In the test center, there are two of the velocity probe with laser diodes shown below. These systems are positioned on the firing line as shown in Figure 5.10. Also protective shields providing safe testing can be seen in this figure. The impact velocity on the target (17.6 m) is calculated by using the difference between the velocity values (velocity loss, ΔV) and the distance relation between the two velocity probes with laser diode systems. The accuracy of the speed measurement system is checked with periodic calibrations.

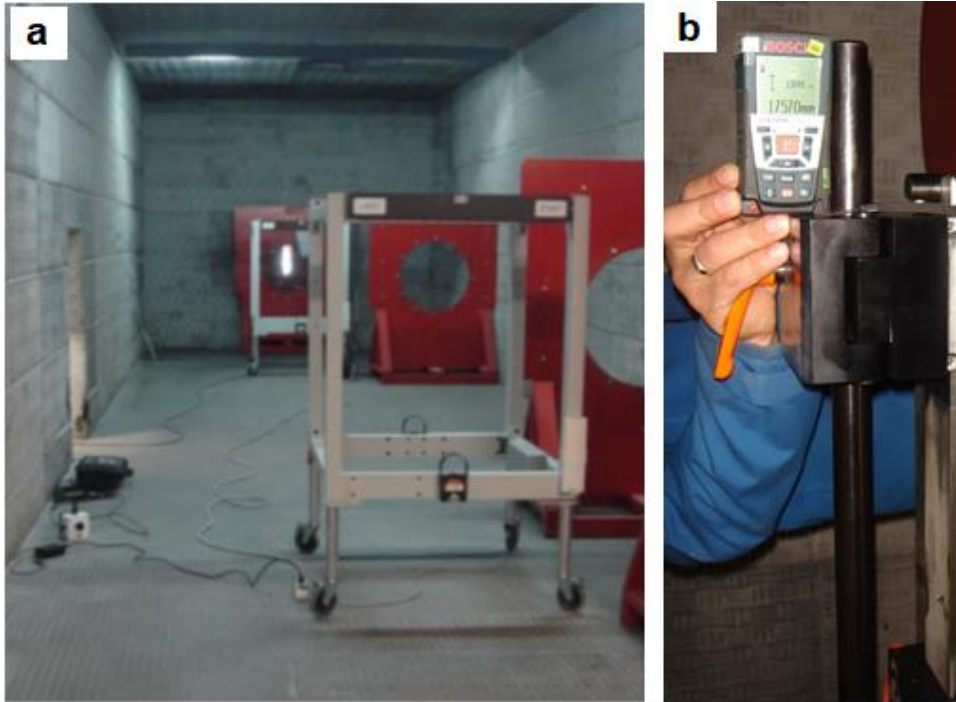


Figure 5.10 : The photo of the experimental setup showing (a) the velocity probes; (b) distance between target and shooting gun.

The weapon brand and model used in the experimental stage of the thesis has not been specified because ROKETSAN A.Ş. kept confidential as company policy. Figure 5.11 shows a schematic representation of the weapon cauldron and its pedestal.



Figure 5.11 : Schematic view of shooting weapon (1) main body and subframe compartment; (2) upper carrier section; (3) crib; (4) incremental adjustment; (5) side adjustment wheel.

The ballistic performance of the armor materials to be inspected is fixed on a standard backing material on a standard target platform as can be seen in Figure 5.12. The segments of the target platform are indicated by numbers in the figure.

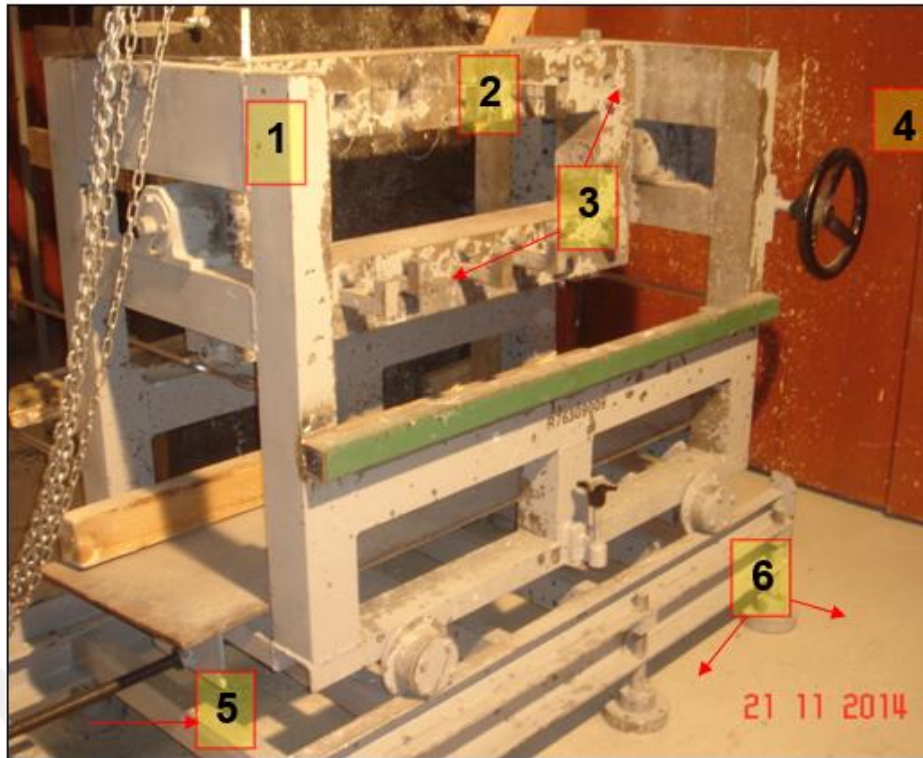


Figure 5.12 : (1) target platform; (2) target binding table; (3) target binding elements; (4) target table inclination angle adjustment lever; (5) target adjustment lever; (6) fixing feet to the target.

In order to better investigate the effects of additives on B₄C ceramics used in this project, 5083 aluminum alloy, a more ductile material compared to normal steel plates, was chosen as the backing material. Since the use of harder materials such as steel, would lead to penetration traces at smaller depths, it was thought that the effect of the additive material would not be clearly understood, the depth of penetration differences would be small, and the results would not be clear. So, more ductile material, aluminium alloy 5083 is found to be appropriate for this application.

Figure 5.13 shows the photo of 5083 aluminum alloys placed in the target chamber. The large holes in the lower left of the plate have previously been used in another study held in ROKETSAN and are not related to our work and do not affect the results of the study. Since there is no one-piece 5083 aluminum plate in appropriate thickness that can withstand the shot made without using any ceramic armor in ROKETSAN, reference shots were made by attaching it two thin plates with 25.5 mm and 38.5 mm thicknesses. Reference shots can also be called heating shots. Two reference shots were made in this study.

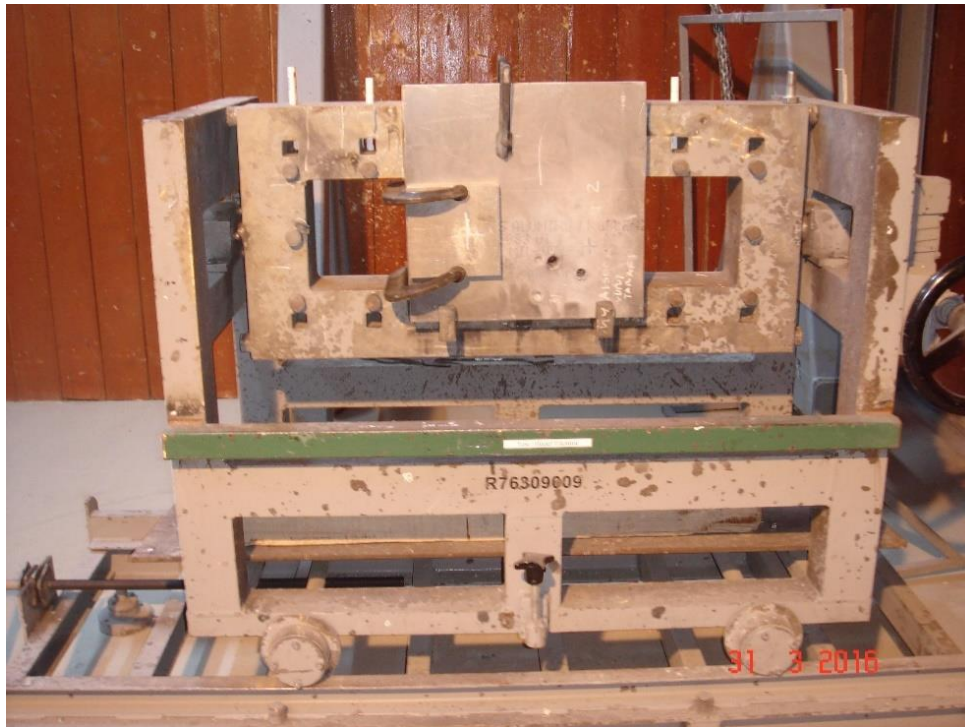


Figure 5.13 : 5083 aluminum alloy backing material before the reference shots in the target chamber.

6. RESULTS AND DISCUSSION

6.1 The Densification and Sintering Behaviours of Boron Carbide Ceramic Composites

6.1.1 The densification and sintering behaviors of cylindrical boron carbide samples

The densification of the specimens during SPS process was evaluated by the displacement of punch rods due to the shrinkage of the composites. The densification behaviors are monitored during the whole spark plasma sintering process. The effect of the thermal expansion of the graphite punch rods with increasing specimen temperature was negligible.

At the beginning of the experimental studies of the thesis, regular graphite dies with 50 mm diameter are used in order to see the densification behaviors of boron carbide ceramics with or without additives. Because regular graphite dies leads to produce cylindrical samples and the wall thickness of the cylindrical dies are smaller than that of hexagonal dies, the spark plasma sintering temperature for cylindrical samples were much higher when compared to the dies which leads to produce hexagonal samples. If the experiments are repeated exactly in the same temperature used in cylindrical dies, melting or serious sticking problems occur in hexagonal shaped dies. In other words, measured spark plasma sintering temperature and the actual temperature of the powders are different and the temperature difference increases with increased wall thicknesses of the dies as explained in detailed in Section 3.4.3.3.

Although the spark plasma sintering temperatures are different, the densification and sintering behaviors does not change according to the die thickness, but shows differences with additions. Figure 6.1 shows the displacement change of pure boron carbide powder, 2% C added B₄C and 2% CNT added B₄C powder mixtures that were spark plasma sintered at 1725 °C for 5 min. The sample which contains monolithic B₄C started to shrink at 1595°C, whereas the shrinking temperature was approximately same (1525 °C) in C and CNT containing samples. The addition of carbon to boron

carbide decreased and resulted in 70 °C temperature difference between the starting temperatures of shrinkage. Densification curves also showed that the addition of both carbon and carbon nanotube was clearly effective in enhancing the sintering process [156].

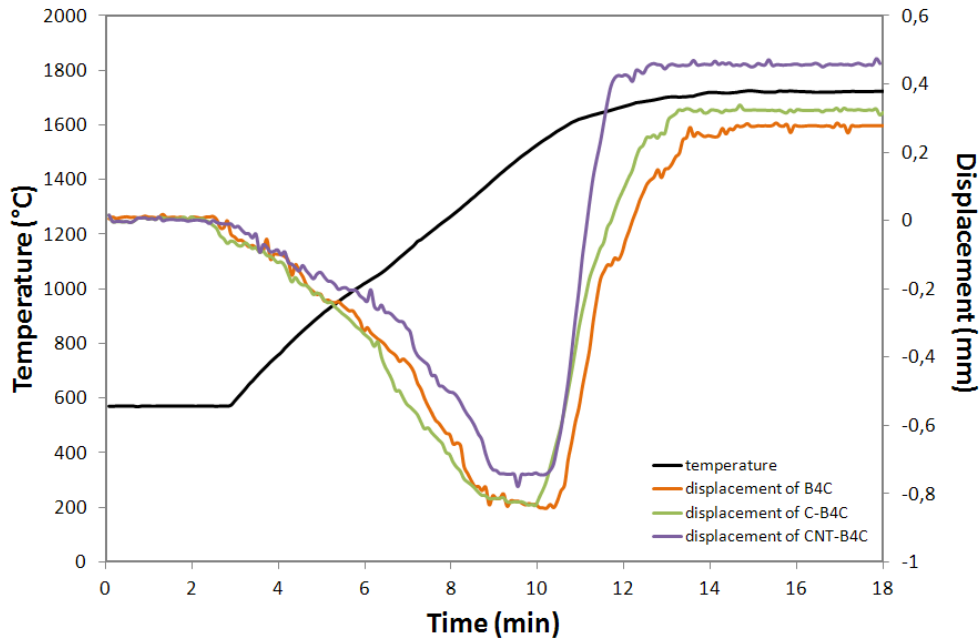


Figure 6.1 : Temperature and displacement curves versus time during SPS process.

The relative density values of cylindrical boron carbide samples without any addition or with 2 vol. % C-black and 2 vol. % multiwall CNT added are given in Table 6.1.

Table 6.1 : Relative density values of cylindrical samples.

Composition	SPS Temperature (°C)	Relative density (%)
Pure B ₄ C		88.5
B ₄ C + 2 % C- black	1650	94.4
B ₄ C + 2 % CNT		97.9
Pure B ₄ C		96.9
B ₄ C + 2 % C- black	1725	98.4
B ₄ C + 2 % CNT		98.8

The highest relative density, approximately 99 %, was obtained in 2 % CNT added boron carbide composites which were heated with 150 °C/min heating rates and spark plasma sintered at 1725°C for 5 min under an applied pressure of 40 MPa. Addition of both carbon and carbon nanotube resulted in higher density values especially in the samples which were spark plasma sintered at lower temperature (1650 °C). This is probably because adding carbon or carbon containing compounds to remove any boron

oxide layers from the boron carbide particle surface enhances the densification at especially lower temperatures. Sintering is promoted by a carbon layer on the submicron boron carbide powder. Residual carbon at grain boundaries not consumed by reaction with boron oxide may control the surface diffusion, evaporation and grain boundary movement, thus limiting excessive grain growth [17,78]. The relative densities were in agreement with the shrinkage results presented in Figure 6.1.

When these results are compared with the study of Yavas et al. [116]; one can see that they reached higher densification rates when lower amounts of CNT is added to the system. The highest relative density is found to be 99.50 % in 0.5 vol. % CNT added sample which heated with 150 °C/min and spark plasma sintered at 1620°C (lower than compared to temperatures used in this study) for 5 min under a pressure of 40 MPa. When they increased the CNT amount from 1 wt. % to 2 and 3 wt. % CNT and spark plasma sintered the samples in exactly same conditions, a slight decrease in relative density values is obtained, the relative densities were found to be 99.40, 98.24 and 96.58 % respectively. They explained the decrease in relative density for further CNT addition is caused from CNT aggregates remained in the composites [116]. Also, Yamamoto et al. have studied carbon nanotube/alumina composites and they have concluded that CNT aggregates reduced the relative density of the composite because of their porous rope-like structure [157].

In addition, the spark plasma sintering temperatures used in this study and study of Yavas et al. [116] showed the beneficial effect of increased temperature on improving the densification. They obtained 98.24 % relative density in 2 wt. % CNT added sample which was heated with 150 °C/min and spark plasma sintered at 1620°C under an applied pressure of 40MPa in vacuum atmosphere, whereas in this study 2 vol. % CNT is manufactured in the same conditions, but spark plasma sintered at 1725 °C showed the relative density as 98.80 %. Although, the sample which was spark plasma sintered at 1650°C in the same conditions with the study of Yavas et al. showed lower relative density value (97.9 %), the difference is thought to be caused from the volumetric and weight percentage additions. In this study, volumetric CNT addition is made to the boron carbide system which corresponds to the higher amounts of CNT addition compared to weight percentage addition. As described above, the increased amount of CNT addition results in decreasing the densification, the results are all in agreement with each other.

6.1.2 The densification and sintering behaviors of hexagonal samples

6.1.2.1 Densification behaviors of spark plasma sintered hexagonal monolithic boron carbide ceramics

In order to see the geometry effects on the densification of spark plasma sintered boron carbide ceramics, the density values are obtained from the center and all the edges of the spark plasma sintered samples. Figure 6.2 represents the areas cut for the density measurement in samples with hexagonal geometry schematically.

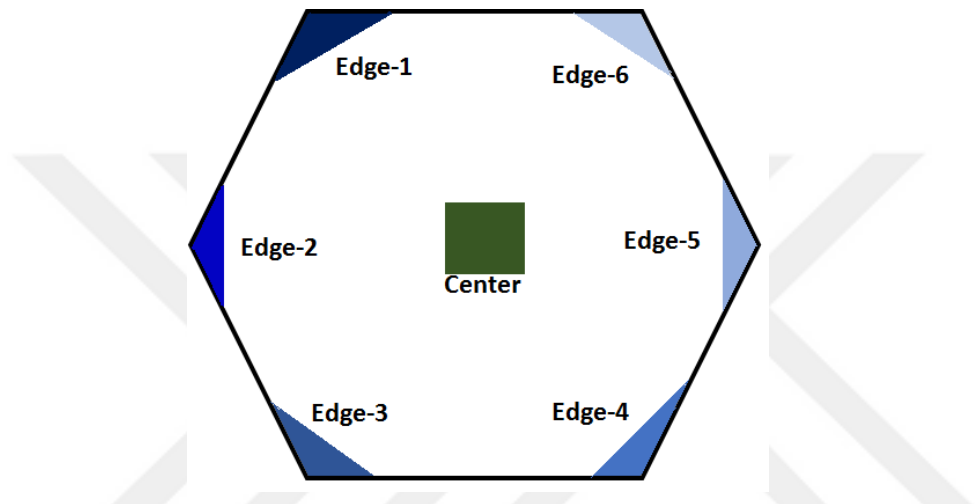


Figure 6.2 : The areas subjected to density measurement in the samples with hexagonal geometry.

Figure 6.3 shows the relative density values of pure boron carbide sample with hexagonal geometry which was heated with 100 °C/min and spark plasma sintered at 1550 °C for 4 min under an applied pressure of 40 MPa in vacuum atmosphere. All of the edges were cut carefully and measured for five times, the average density values of six edges were calculated concerning the results of all edges. Furthermore, the center of the sample is also measured and compared with edge values.

When the relative density values of both edges and center of the monolithic boron carbide sample are compared, it can clearly be seen that center relative density value is higher than the relative density value of all edges. The edge relative density values were found to be ranging between 95.2 and 93.9 with an average of 94.72 %.

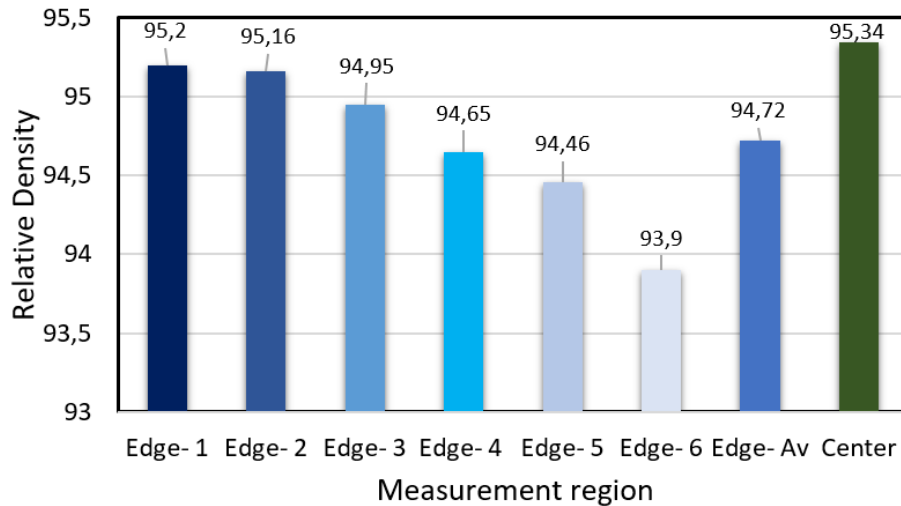


Figure 6.3 : Relative density values of hexagonal monolithic boron carbide ceramics spark plasma sintered at 1550 °C for 4 min under an applied pressure of 40 MPa.

In order to evaluate the densification differences seen in the sample, the thermal distribution occurred in spark plasma sintering due to heat radiation losses should be clearly mentioned. In the first stages of sintering, in other words at the low temperatures, the temperature gradient formed in the sample is directly dependent on current distribution, however with increasing temperature temperature gradient looks very different and usually independent from electrical conductivity of the sample powder. Due to the radiation heat losses from the outer die wall surface, the center of the sample is always hotter than the edges of the samples, the effect of electrical conduction properties of powder sample does not matter in high temperatures. The radiation heat losses is the dominant mechanism for thermal gradient formation. However, the amount of temperature difference between the center and the edges composed during high spark plasma sintering temperatures are directly related to electrical conductivity [73, 158].

Current distribution (together with radiation heat losses) is the main cause of the temperature gradient between the sample and the external surface of the die [70]. In electrically conductive samples, the main part of the current flows through the sample and the temperature of the sample center is modeled higher due to the current path. On the other hand, the current is forced to flow through the die in the case of a strong electrical insulator. However, since the sample is small compared to the tool and since the graphite has a good thermal conductivity, the heat is quickly transferred to insulator powders [73].

The electrical properties of boron carbide is rather complex. Experimentally, boron carbide was found to be a semiconductor, however there are various band gap values reported for boron carbide. Boron carbide was described as a p-type semiconductor with an estimated band gap of 1.64 eV [159]. However, this is much smaller than the band gap of other semiconductor ceramics. Werheit et al. reported two different band gap values as 0.48 eV and 2.09 eV, suggesting that a wide range of gaps could be identified in the boron carbide structure within the stoichiometric range of $B_{4.3}C$ – $B_{11}C$ [160]. Larger band gaps, typically exceeding 3 eV, confirm the semiconducting nature of boron carbide for the stoichiometric B_4C .

The direct current (dc) conductivity of boron carbide as a function of carbon content tends to increase till ~13 at.% C, then decreases [6]. Furthermore, the electrical resistivities of boron carbide decrease with increasing temperature, showing semiconducting characteristics [161]. In other words, boron carbide shows very different electrical conductivity properties depending on temperature and C content in the structure, also no certain values in the literature exists. So, to evaluate and to educe a conclusion for the electrical behavior of boron carbide during spark plasma sintering is very difficult. However, considering the relative density results, one can conclude that monolithic boron carbide ceramics reach higher temperatures in the center of the sample compared to the edges of the sample during spark plasma sintering.

6.1.2.2 Densification behaviors of spark plasma sintered hexagonal boron carbide ceramics with different C additions

Figure 6.4. gives the relative density values of center and six edges of hexagonal boron carbide samples with 2 vol. % C and 2 vol. % CNT addition which were heated with 100 °C/min and spark plasma sintered at 1550°C for 4 min under an applied pressure of 40 MPa in vacuum atmosphere.

When the relative density results obtained from 2 vol. % C and CNT additions are compared, one can clearly see that both center and average edge density results are higher in CNT added sample. The average edge density of 2 vol. % CNT added sample was higher than that of 2 vol. % C containing boron carbide. Same result is seen in center relative density values. So, it can be concluded that CNT is a more effective densification agent compared to C when the addition amounts and the process conditions are same in spark plasma sintered boron carbide ceramics.

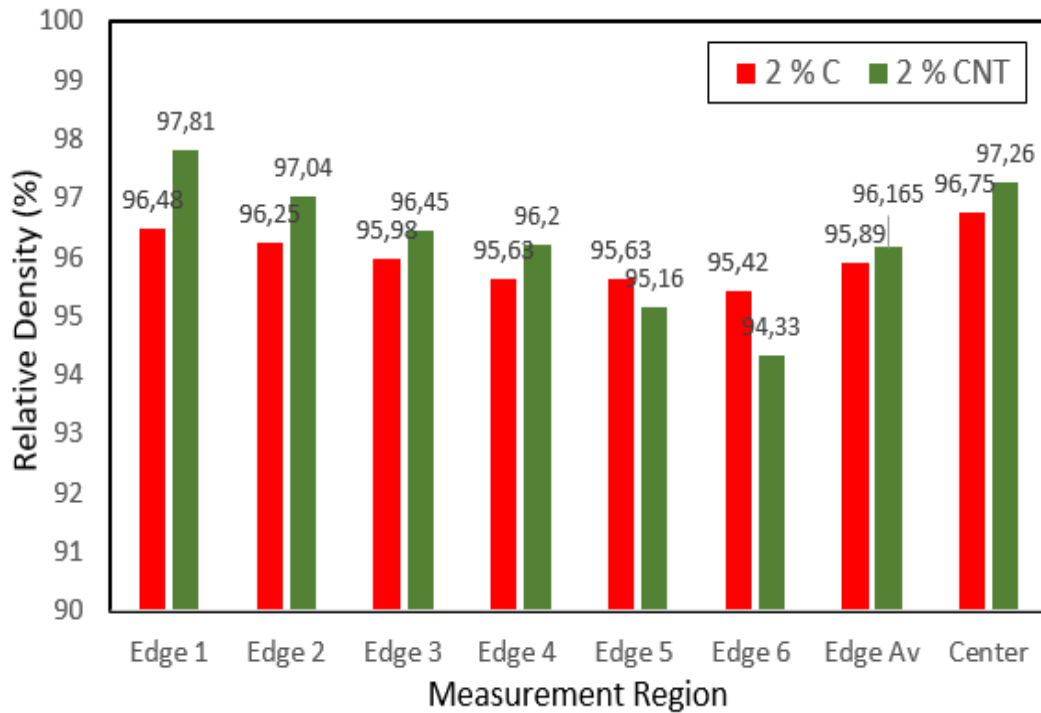


Figure 6.4 : Relative density values of 2 vol. % C and CNT added hexagonal boron carbide ceramics which were spark plasma sintered at 1550 °C for 4 min under an applied pressure of 40 MPa.

However, the point that needed to be given attention is the distribution of relative density values in edges of CNT added boron carbide. 2 vol. % CNT added sample which was spark plasma sintered at 1550 °C for 4 min under an applied pressure of 40 MPa showed the highest density value in one of the edges, as 97.81 % which is higher than the center value of this sample. To obtain highest relative density in an edge, but not in the center is probably because of the non-homogeneous distribution of CNT in the sample. CNT is defined as difficult to distribute homogeneously material in the literature many times [162-164]. To achieve more homogeneous sintering, Cha et al stated that the most promising process to obtain homogeneous dispersion of CNTs and strong interfacial strength is the molecular level mixing process, which was originally designed for CNT/metal nanocomposites [165]. Also, the lowest density value is obtained in one of the edges of 2 vol.% CNT added sample as 94.33 %, but not in C-black containing sample. When these two different carbon sources are compared, it can be mentioned that C-black addition to boron carbide results in lower but more homogeneous densification compared to CNT addition.

Figure 6.5 demonstrates the densification behaviors of 2 vol. % C and 2 vol. % CNT added boron carbide powders during whole spark plasma sintering process. When two

process are compared, one can clearly see that the displacement achieved during spark plasma sintering of CNT added sample is nearly twice of the displacement obtained in C added sample.

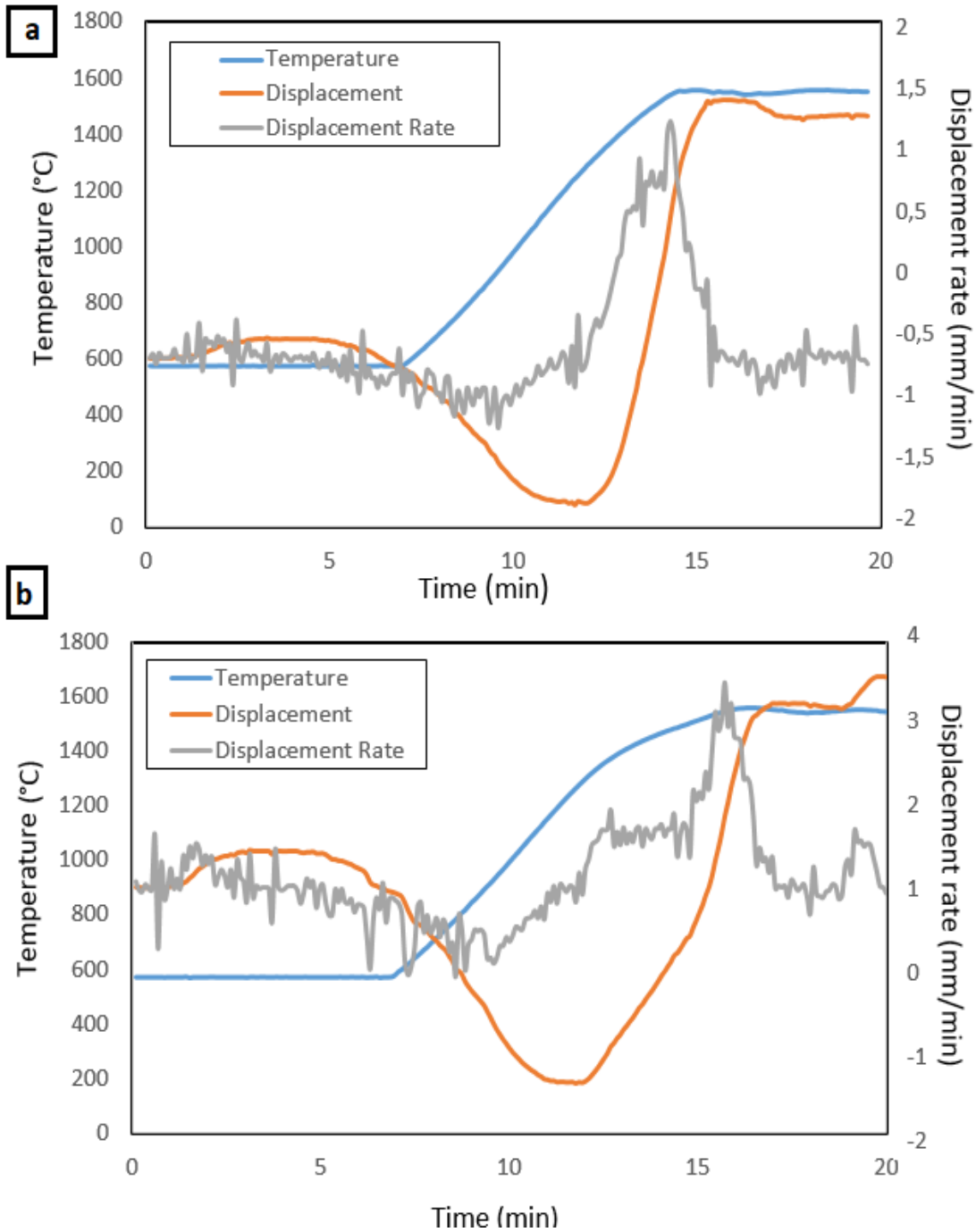


Figure 6.5 : Temperature, displacement and displacement rate curves of (a). 2 vol. % C (b). 2 vol % CNT added boron carbide samples versus time during SPS process.

When Figure 6.5 is analyzed in detail, it can be mentioned that the shrinkage starts at 1298 °C in C containing boron carbide, whereas the shrinkage starts at 1286 °C in CNT containing sample. The shrinkage starting temperatures are very close to each other.

When the displacement curves for cylindrical and hexagonal samples are compared, a huge shrinkage temperature difference can be seen in the samples. As can be seen from Figure 6.1, 2 vol. % C and CNT added boron carbide samples start to shrink 1525 °C in cylindrical molds, however the shrinkage temperature in hexagonal molds are nearly 250 °C lower.

In addition, CNT addition enhanced the densification more effectively compared to C addition. The displacement reached to 1.72 mm during spark plasma sintering of 2 vol. % C added sample, whereas 3.063 mm in 2 vol. % CNT containing boron carbide. These results make an agreement with the relative density values.

6.1.2.3 Densification behaviors of spark plasma sintered hexagonal boron carbide composites with light metallic additions

In order to protect the lightness advantage of boron carbide but increasing the mechanical and ballistic performances of the material, some light metallic additions such as Al and Si have been made. Because these two metals have lower melting temperatures compared to boron carbide, the sintering temperatures are limited and needed to be lowered due to sticking and melting problems occurred during spark plasma sintering processes.

The spark plasma sintering temperature is determined as 1450 °C in 5 vol. % Al containing boron carbide sample. The heating rate was 100 °C/min, applying pressure was 40 MPa, holding time was 4 minutes and the atmosphere was chosen to be vacuum. On the other hand, 5 vol. % Si containing boron carbide sample was spark plasma sintered at 1500 °C and heated with 100 °C/min under an applied pressure of 40 MPa for 4 min in vacuum. In this conditions, the densification could not reach to satisfactory values and higher spark plasma sintering temperatures are tried. However, a serious sticking problem has been observed in higher sintering temperatures, and neither of the samples can be removed from the molds as monoblocks, so all process parameters are fixed but another densification promoting parameter, pressure, is increased to 60 MPa. The densification and sintering behaviors are enhanced. Figure 6.6 gives the relative density values of both six edges, average edge and the center of 5 vol. % Al and Si containing hexagonal boron carbide samples which were produced as mentioned conditions.

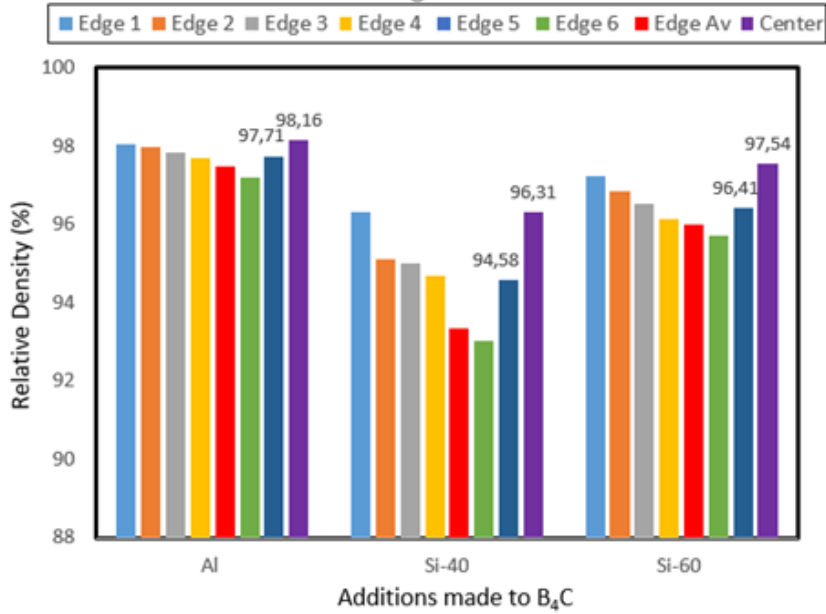


Figure 6.6 : Relative density values of 5 vol. % Al and Si added hexagonal boron carbide ceramics.

The edge relative density values of 5 vol. % Al containing boron carbide sample which was spark plasma sintered at 1450 °C for 4 min under a pressure of 40 MPa in vacuum were ranged between 97.20 % and 98.06 % with an average value of 97.71 %. The homogeneity in terms of densification is distinct in Al containing sample. Al addition to boron carbide leads to liquid phase sintering and as German et al. mentioned that once the liquid forms, liquid phase sintering tends to homogenize the microstructure, eventually removing the inhomogeneities and results in homogen densification [166]. Also, the average edge relative density value is found to be close to the center relative density value. Accordingly, one can conclude that the higher homogeneity densification degrees can be reached in Al containing sample.

Furthermore, the relative edge density values of 5 vol. % Si added boron carbide which was spark plasma sintered at 1500 °C for 4 min under a pressure of 40 MPa in vacuum were ranged between 93.03 % and 96.30 %, with an average value of 94.58 %. When the applied pressure increased to 60 MPa, the edge relative density values were ranged between 95.72 % and 97.22 %, with an average density value of 96.41 %. Also increment of pressure resulted in an increase of center relative density values from 96.31% to 97.54%. As Frage et al stated in their study that increasing the applied pressure generally results in promoting the densification of spark plasma sintered boron carbide with Fe addition [167]. Same results have been obtained in this study.

Figure 6.7 shows the temperature increase during spark plasma sintering procedure as well as the obtained displacement and calculated displacement rate. As can be seen clearly, the highest displacement change occurs at minute 10.33 which corresponds to 1188 °C. Al addition decreased the shrinkage starting temperature very remarkably.

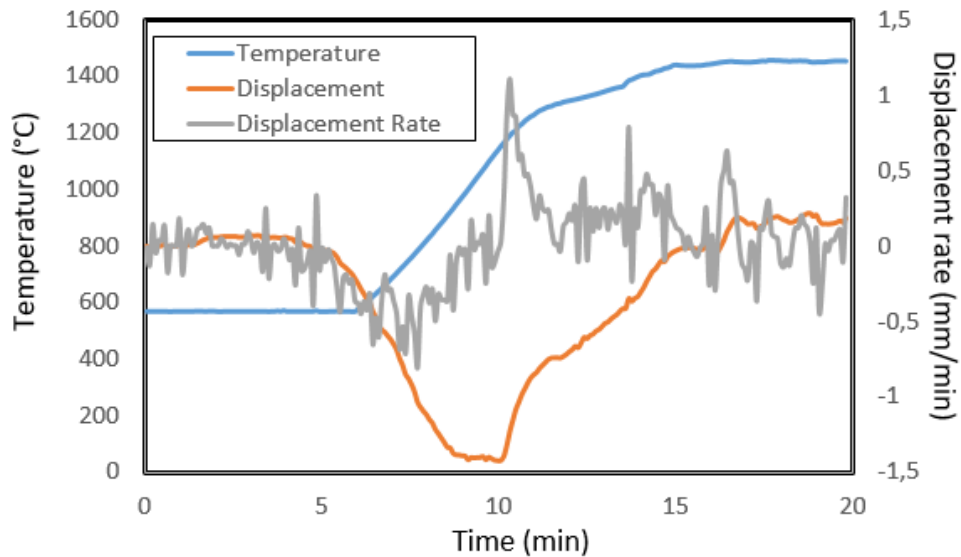


Figure 6.7 : Temperature, displacement and displacement rate curves of 5 vol. % Al added boron carbide samples spark plasma sintered at 1450 °C for 4 min versus time during SPS process.

In addition, the calculated displacement rate curve shows dramatic changes during the whole process which have not been seen neither monolithic boron carbide nor C or CNT added sample. The radical displacement changes starting from the very low temperatures may indicate the liquid Al formation. According to Panasyuk et al liquid aluminium spread over the boron carbide particles in the temperatures of 1100 – 1200 °C with an angle of 92° and the contact angle decreases to 28° in two- three minutes [168]. Slow spreading of aluminum was linked with the formation of new compounds in the contact zone. The kinetics of B₄C – Al system is rather complex and results in radical displacement curves [168].

The temperature, displacement and displacement rate curves obtained during the spark plasma sintering process of 5 vol. % Si containing boron carbide powder heated with 100 °C/min and spark plasma sintered at 1500 °C for 4 min under 40 or 60 MPa pressures in vacuum atmosphere can be seen in Figure 6.8.

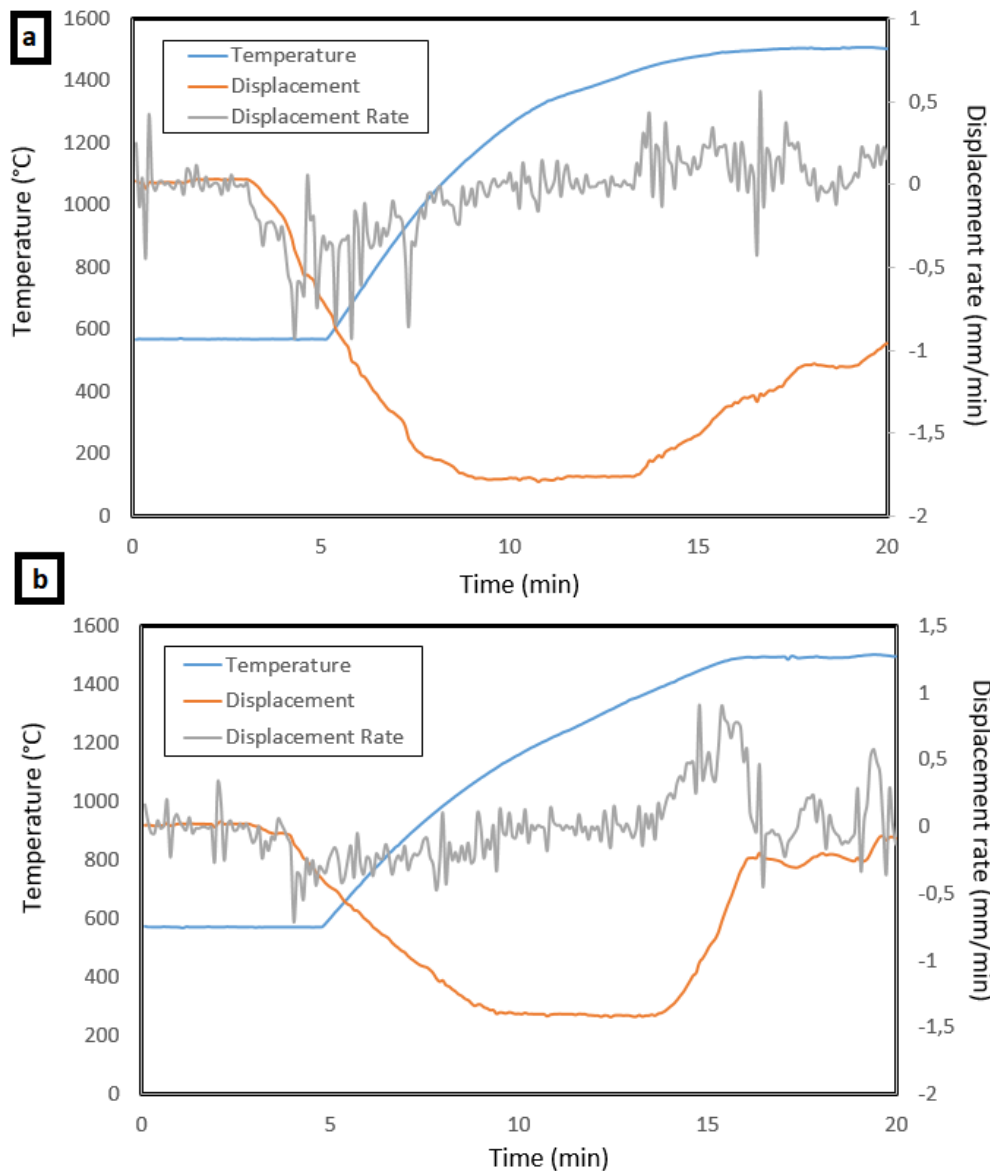


Figure 6.8 : Temperature, displacement and displacement rate curves of 5 vol. % Si added boron carbide samples spark plasma sintered at 1500 °C for 4 min under an applied pressure of (a). 40 MPa (b). 60 MPa versus time during SPS process.

When Figure 6.8 is analyzed, a different displacement curves can be seen. First, with the increasing temperature, the displacement is regressed which corresponds to the expansion of the powders and die due to the temperature increase. However, the displacement curve remains stable, neither the sample expands nor shrinks, between the temperatures 1134 °C and 1435 °C in the sample which was spark plasma sintered under a pressure of 40 MPa. After that, the sample started to shrink at 1435 °C. In the sample which was spark plasma sintered under a pressure of 60 MPa, displacement remains constant between the temperatures 1125 °C and 1384 °C. Increment of applied pressure from 40 to 60 MPa lead to lower the shrinkage temperature from 1435 °C to

1384 °C. Also, the displacement occurred during the whole process was higher in the sample which was spark plasma sintered under a pressure of 60 MPa.

6.1.2.4 Densification behaviors of spark plasma sintered hexagonal boron carbide composites with Ti and TiO₂ additions

As the aim of this thesis study is to produce a boron carbide based ceramic composite which is suitable for ballistic applications and TiB₂ is also defined as an effective armour material in the literature [169-172], Ti and TiO₂ additions were made to boron carbide ceramics in order to increase the desired ballistic properties. In addition, the presence of titanium diboride prevents the growth of boron carbide grains [132]. Existence of TiB₂ in B₄C reduces the sintering temperature and modifies the microstructure of resulting structure [130]. B₄C-TiB₂ composites possess the outstanding hardness of boron carbide and the high fracture toughness and strength of titanium diboride [141]. Furthermore, the difference between the thermal expansion coefficients of boron carbide and titanium diboride particles have led to the improvement of fracture toughness [173,174].

After some trials and following the displacement curves during the experiments, spark plasma sintering temperature as 1550 °C is found to be suitable due to sticking problems in higher temperatures and all the experiments with Ti and TiO₂ additions, independent from the addition amount, were made at 1550 °C. The powders were heated with 100 °C/min and the soaking time was 4 minutes. However, later on, only for the 5 vol. % Ti containing sample, the experiments were also held for 6 minutes in order to see the soaking time effect on the densification properties. Two different powders with different particle sizes were used as Ti source. First, Ti with an average particle size of 26.46 µm is used and coded as Ti-LP (large particle) in this thesis. Then Ti with an average particle size of 5.12 µm is chosen and coded as Ti-SP (small particle). Ti-LP addition were made 5, 10, 15 and 20 vol. % to boron carbide whereas only 5 and 10 vol. % Ti-SP were added to boron carbide.

In order to see the densification homogeneity in the samples, the relative densities of all the edges and center is measured. Figure 6.9 shows the relative density values of six edges, edge average and center of 5, 10, 15 and 20 vol. % Ti-LP added hexagonal boron carbide samples.

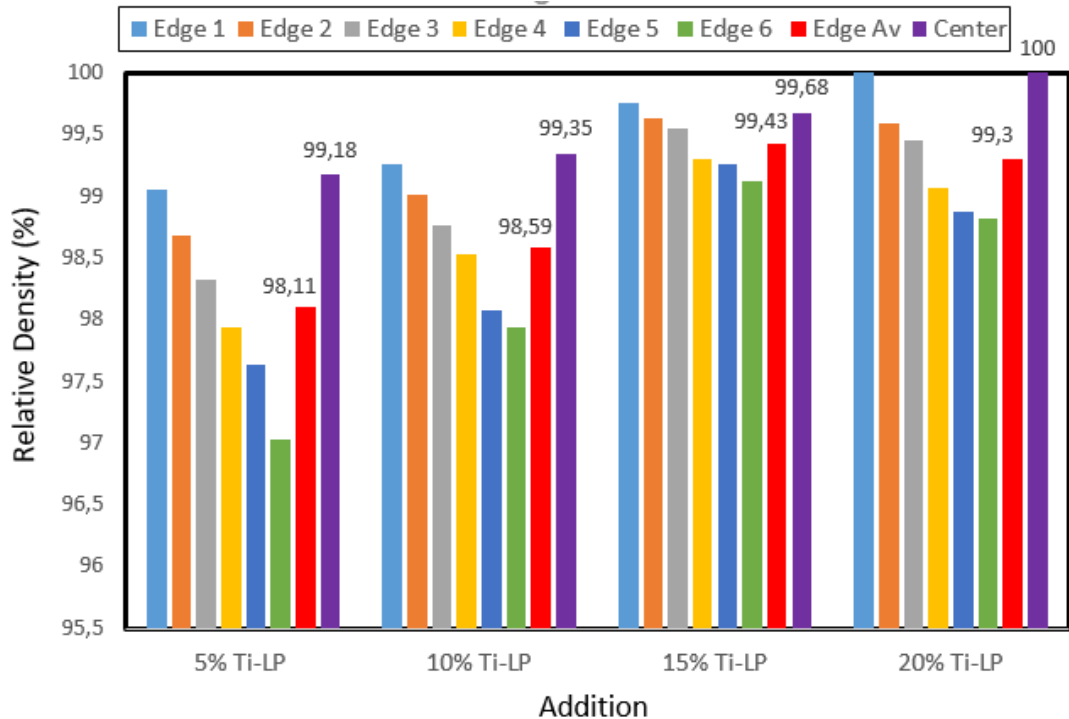


Figure 6.9 : Relative density values of 5, 10, 15 and 20 vol. % Ti-LP added hexagonal boron carbide ceramics which were spark plasma sintered at 1550 °C for 4 min under an applied pressure of 40 MPa.

As can be seen from the variation of relative density as a function of Ti addition in Figure 6.9, Ti is a very effective sintering aid for boron carbide and result in increasing the relative density values of boron carbide. Among all the additions (C, CNT, Al or Si) made to the boron carbide system, Ti is the most beneficial one for promoting the densification. When the amount of Ti added to boron carbide is increased, the obtained relative density values are increased in the samples which were heated with 100 °C/min and spark plasma sintered at 1550 °C under 40 MPa pressure in vacuum.

Again in all the samples, center relative density values were measured to be higher than the edge relative density values. Theoretical density was achieved in both center and one edge of 20 vol. % Ti containing sample. The most homogenous sample in terms of relative density values can be termed as 15 vol. % Ti added sample because the closest edge density values were attained in this sample. The relative density values seen in the edges of 15 vol. % Ti added sample were ranged between 99.12 and 99.75, with the average of 99.43%. Because all of the Ti in the boron carbide is transformed into TiB₂, these results overlap with the study of Baharvandi and Haidan [175]. They also found out that with the increase of TiB₂ addition from 5 to 30 vol. %, the density

results of boron carbide are increased. According to them, the better sinterability results in increasing density by increasing the amount of TiB_2 .

In the B_4C -Ti powder mixture, the increase in the amount of Ti also affects the homogenization positively. Since the melting temperature of the Ti metal is lower than the melting temperature of the boron carbide, in other words main matrix phase, during the spark plasma sintering, melted Ti reacts with the B_4C , takes B in its structure and forms TiB_2 . As mentioned before, the path of current followed in the spark plasma sintering system is highly dependent on the electrical properties of the sintered powder. When the electrical conductivity of the sample is high, the current prefers to pass from both powder and die, and when the electrical conductivity of powder is low, the current passes through the die.

With the addition of TiB_2 , especially in 20 vol. % Ti containing sample, the electrical properties of boron carbide have been changed a lot. When the conductivities of the TiB_2 phase and the B_4C phase are compared, it has been observed that the electrical conductivity of the TiB_2 phase is high, the B_4C matrix allows the conduction of the TiB_2 phase to increase by increasing the amount of Ti added, thereby increasing the conductivity of the mixtures, thereby activating the centering direction of the heating direction. This mechanism explains why 20 vol. % Ti containing sample showed lower homogeneity compared to 15 vol. % Ti added sample. From one point, changed electrical properties affects the obtained homogeneity of densification, center and one edge of the sample is densified better, whereas lower density values are attained in the other edges of the 20 vol. % Ti containing sample.

In order to see the effect of starting powder particle size on the densification, 5 and 10 vol. % Ti added are repeated in the same conditions. Also, sintering homogenization (minimization of density differences between edge and mid region) can also be achieved by extending the soaking times. However, one should consider the possibility of very fast grain growth and reduced mechanical properties originated from prolonged soaking times, just 6 minutes soaking time is tried in this study. Figure 6.10 shows the edge and center relative density values of 5 and 10 vol. % Ti-SP containing hexagonal boron carbide samples which were heated with $100\text{ }^\circ\text{C}/\text{min}$ and spark plasma sintered at $1550\text{ }^\circ\text{C}$ for 4 minutes under 40 MPa pressure in vacuum atmosphere.

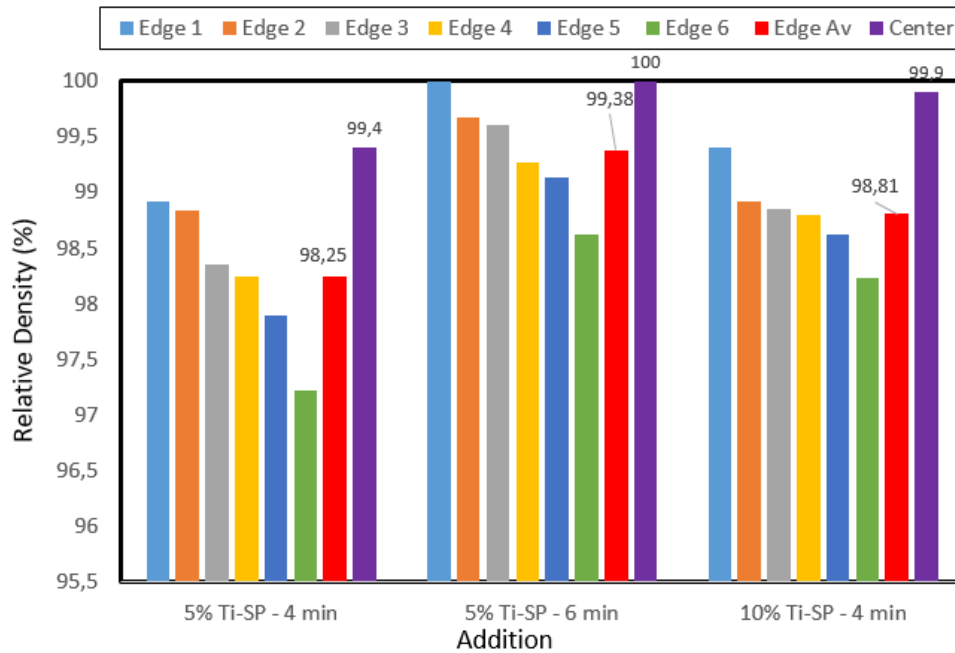


Figure 6.10 : Relative density values of 5 vol. % Ti-SP added hexagonal boron carbide ceramics which were spark plasma sintered at 1550 °C for 4 and 6 min under an applied pressure of 40 MPa and 10 vol. % Ti-SP added hexagonal boron carbide ceramics produced in same conditions but only with 4 minute soaking time.

When Ti with small particle size is used as a sintering aid, again Ti addition is found to be beneficial for promoting the densification. For example, when 5 vol. % Ti-LP and Ti-SP which were heated with 100 °C/min and spark plasma sintered at 1550 °C for 4 min under a pressure of 40 MPa in vacuum are considered, both center and average edge value is higher in Ti with smaller particle size. The relative density value attained in the center of Ti-LP was found to be 99.18 % whereas the relative density of Ti-SP center was 99.40 %. Furthermore, same results are obtained in 10 vol. % Ti containing samples. In like manner, 10 vol. % Ti-SP containing boron carbide showed 99.90 % relative density value in the center, while the center relative density of the Ti-LP added boron carbide has the relative density of 99.35 %.

If the relative density values obtained from different soaking times (4 or 6 minutes) of 5 vol. % Ti-SP added boron carbide samples are examined, it can be seen that by extending the soaking times, both sintering homogenization and an increase in the relative densities can be achieved. The difference between edge average and center of the sample with 4 min soaking time was 1.15 %, in the sample with 6 min soaking time the difference is reduced to 0.62 %. Theoretical density is reached by increasing the soaking time to 6 minutes in 5 vol. % Ti-SP containing sample which was spark plasma sintered at 1550 °C for 4 minutes under a pressure of 40 MPa in vacuum

atmosphere. Figure 6.11 shows six edges, edge average and center relative density values of 5 and 10 vol. % TiO₂ added hexagonal boron carbide samples according to their soaking times.

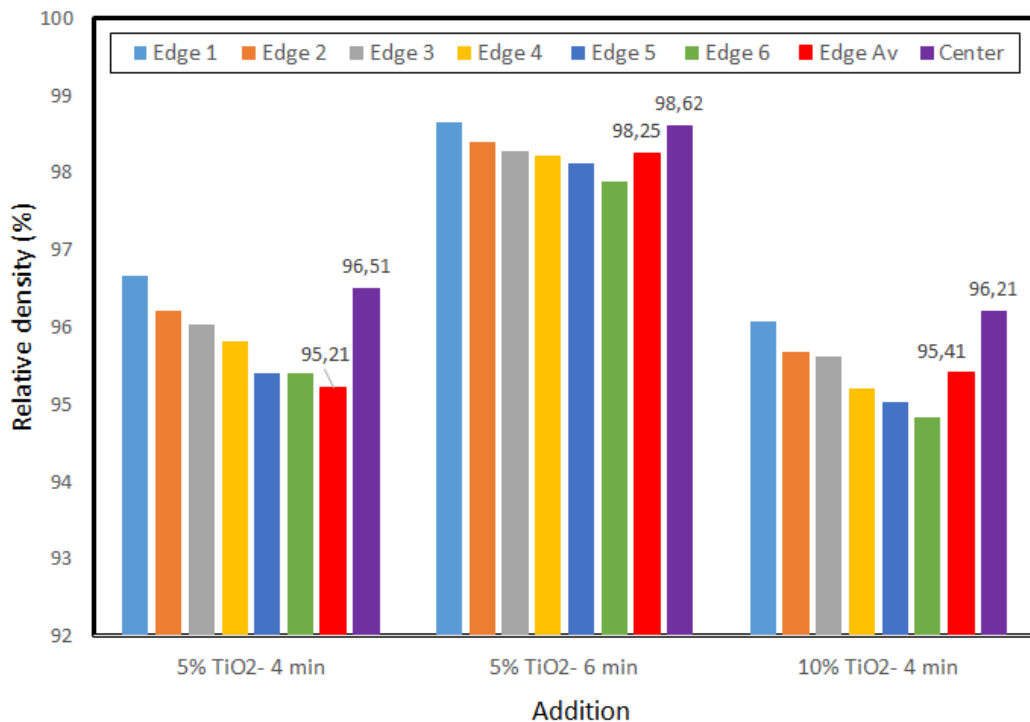


Figure 6.11 : Relative density values of 5 vol. % TiO₂ added hexagonal boron carbide ceramics which were spark plasma sintered at 1550 °C for 4 and 6 min under an applied pressure of 40 MPa and 10 vol. % TiO₂ added hexagonal boron carbide ceramics produced in same conditions but only with 4 minute soaking time.

When the relative density values of TiO₂ added boron carbide composites are examined, one can conclude that with the increasing TiO₂ amount, the relative density values does not affected remarkably. However, increasing the soaking time from 4 to 6 minutes resulted in higher relative density values both in edges and center of the sample. Also, the sintering is observed to be more homogenous in the sample with 6 minute soaking time. The highest relative density value is attained in the center of hexagonal boron carbide sample with 5 vol. % TiO₂ which was heated with 100 °C/min and spark plasma sintered at 1550 °C for 6 min under an applied pressure of 40 MPa in vacuum atmosphere. The relative density values of edges were ranged between 97.88 and 98.66 % with an average of 98.25 %. Accordingly, increasing the soaking time is found to be more effective in densification of spark plasma sintered boron carbide with TiO₂ addition.

When the studies in the literature are examined, 1550 °C can be regarded as a very low sintering temperature for B₄C-TiB₂ composites in the literature. However, as

mentioned before, to measure the real sintering temperature of powders during spark plasma sintering is impossible, and is dependent to a lot of factors such as electrical properties of the sample, die and mold size etc. In this study, when Ti and TiO₂ additions made to boron carbide are compared, Ti addition can be stated as a more beneficial addition in terms of densification of boron carbide. In the literature, there are limited studies comparing the addition of Ti and TiO₂ [176], but a lot of studies can be confronted for sintering of boron carbide with TiO₂ or TiB₂ additions [142,177,178]. These studies found TiO₂ more effective than Ti or direct TiB₂ additions. Levin et al. expressed the reason for qualification TiO₂ as a better densifier is because of the formation of substoichiometric B and C [176]. In principle, a substoichiometric compound with a significantly higher structural defect concentration may display improved mobility of its constituents, leading to higher diffusivities and therefore to higher sinterability [176]. However, pressureless sintering is carried out in the mentioned study, spark plasma sintering is a process which increases the concentration of the point defects and charge carriers, and enhance their interaction with the electric field [58].

Furthermore, a very recent study carried out by Zhang et al [104] explained two distinct regimes corresponding to two different mechanisms were involved in the SPS process on the basis of the different effective stress exponents. At low temperatures (1700 - 2000 °C) and low effective stress regime, suggesting that the creep deformation which was controlled by grain-boundary sliding or by interface reaction is responsible for the densification [104]. Ti, which melts and then forms TiB₂ in the structure may be a more effective sintering aid for this reason. However, at higher temperatures (more than 2000 °C) and high stress regime, the dominant mechanism is described as the dislocation climb. Accordingly, high temperature sintered boron carbide samples, TiO₂ may be found more effective addition because it forms a substoichiometric compound with a significantly higher structural defect concentration [104, 176].

In Figure 6.12, the temperature and displacement curves of 5, 10, 15 and 20 vol. % Ti-LP added boron carbide sample obtained during spark plasma sintering procedure is given. When Figure 6.12 is examined, one can see that 5, 10 and 15 vol. % Ti added sample started to shrink approximately at same temperatures, at 1157 °C, 1115 °C and 1101 °C respectively. However the shrinkage starting temperature of 20 vol. % Ti

containing sample was lower and observed to be at 865 °C. In other words, Ti addition results in lowering the sintering temperature of boron carbide samples and the displacement is proportional to shrinkage of the sample in the densification process during SPS.

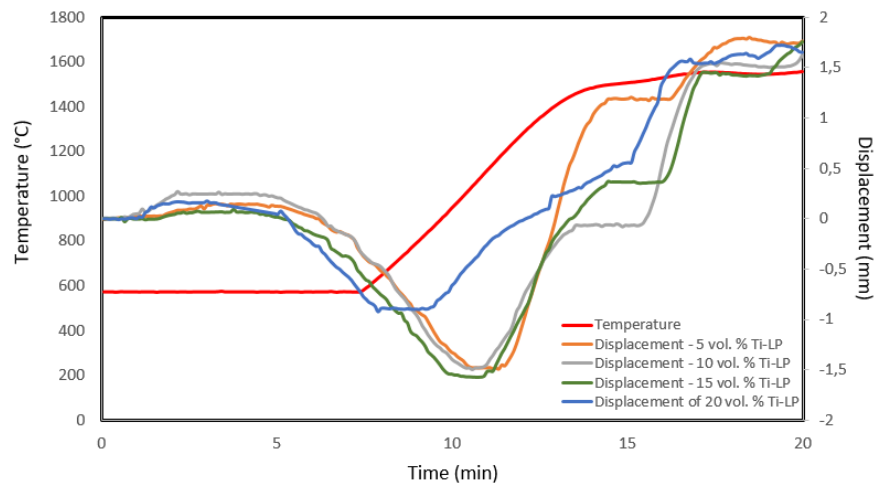


Figure 6.12 : Temperature and displacement curves of 5, 10, 15 and 20 vol. % Ti-LP added boron carbide samples spark plasma sintered at 1550 °C for 4 min under an applied pressure of 40 MPa versus time during SPS process.

Also, Figure 6.13 gives the comparison of displacement curves 10 vol. % Ti-SP and TiO₂ containing samples.

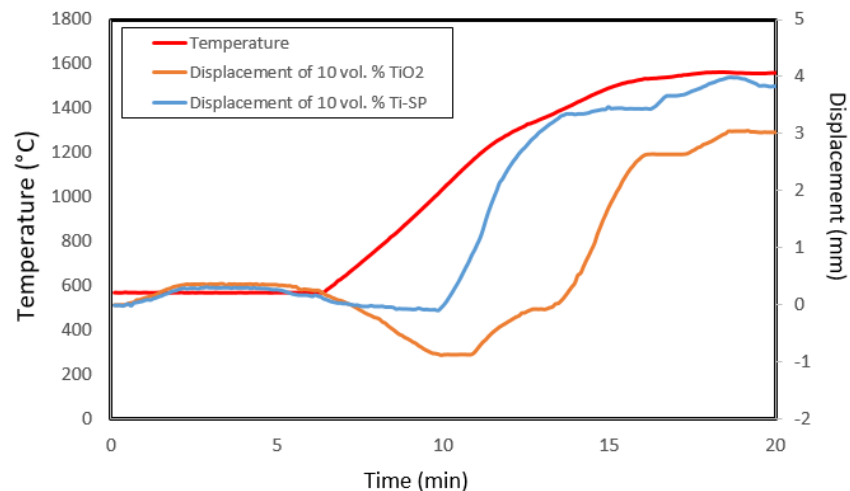


Figure 6.13 : Temperature and displacement curves of 10 vol. % Ti-SP or TiO₂ added boron carbide samples spark plasma sintered at 1550 °C for 4 min under an applied pressure of 40 MPa versus time during SPS process.

10 vol. % Ti-SP containing sample started to shrink 1017 °C, whereas the shrinkage starting temperature is observed to be 1151 °C for 10 vol. % TiO₂ containing hexagonal boron carbide sample. As mentioned before, the shrinkage starting

temperature of 10 vol. % Ti-LP added sample have been found to be 1115 °C. When the shrinkage starting temperatures are considered, it can be said that in boron carbide samples which contains Ti with smaller particle size, the shrinkage starts earlier. Also, Ti leads the shrinkage start before compared to same amount of TiO₂.

In the spark plasma sintering system, depending on the electrical resistance of the powder material and the geometry of the part to be produced, homogeneity may occur from the center to the edges in terms of density, since the heat is formed directly by transferring the energy onto the powder material and mold. The density differences of the edge and center regions of the compacts obtained from B₄C-Ti powders can be minimized by going to high temperatures such as 1550 °C. In the B₄C-Ti powder mixture, the increase in the amount of Ti also affects the sintering homogenization positively. Since the melting temperature of the Ti metal is lower than the melting temperature of the boron carbide main matrix phase, during the spark plasma sintering, Ti reacts with the B₄C passing through the space between the boron carbide grains and melts and forms TiB₂ by taking B in its structure. In the spark plasma sintering system, the heating of the sample takes place due to the electrical resistance of the sample and the mold surrounding the sample, by passing the pulsed electrical current through the sample and the electrically conductive pattern (graphite). When the electrical resistance of the sample is high, the heating is from the sample center to the edges of the mold, whereas when the electrical resistance of the sample is low, the heating is centered from the mold surface. In other words, when the electrical conductivity of the sample is high, the heating effect of the sample remains at the edges of the sample near the mold surface, so that the edge is heated more efficiently by the mold. When the conductivities of the TiB₂ phase and the B₄C phase are compared, it has been observed that the electrical conductivity of the TiB₂ phase is high, the B₄C matrix allows the conduction of the TiB₂ phase to increase by increasing the amount of Ti added, thereby increasing the conductivity of the mixtures.

Sintering homogenization (minimization of density differences between edge and mid region) in the sintering order of the samples can also be achieved by extending the sintering times. However, the use of long sintering times in the SPS system is not recommended, as the prolongation of sintering times can lead to very rapid grain growth and mechanical degradation especially at high temperatures in the SPS system.

6.2 Phase Analysis of Boron Carbide Ceramic Composites

6.2.1 Phase analysis of monolithic boron carbide

In order to produce a hexagonal monolithic boron carbide ceramic armor tiles, 64.97 g boron carbide powders were spark plasma sintered at 1550 °C for 4 min, under a pressure of 40 MPa in vacuum. Spark plasma sintering process under these condition does not result in any phase change and it can be seen that all B₄C in the structure remained as B₄C. Factsage 6 thermochemical simulation programme is used in order to investigate any possible phase change with increasing temperature. However, no phase change is observed in pure B₄C as shown in Figure 6.14. Also, when XRD analysis is applied, only boron carbide phase is obtained.

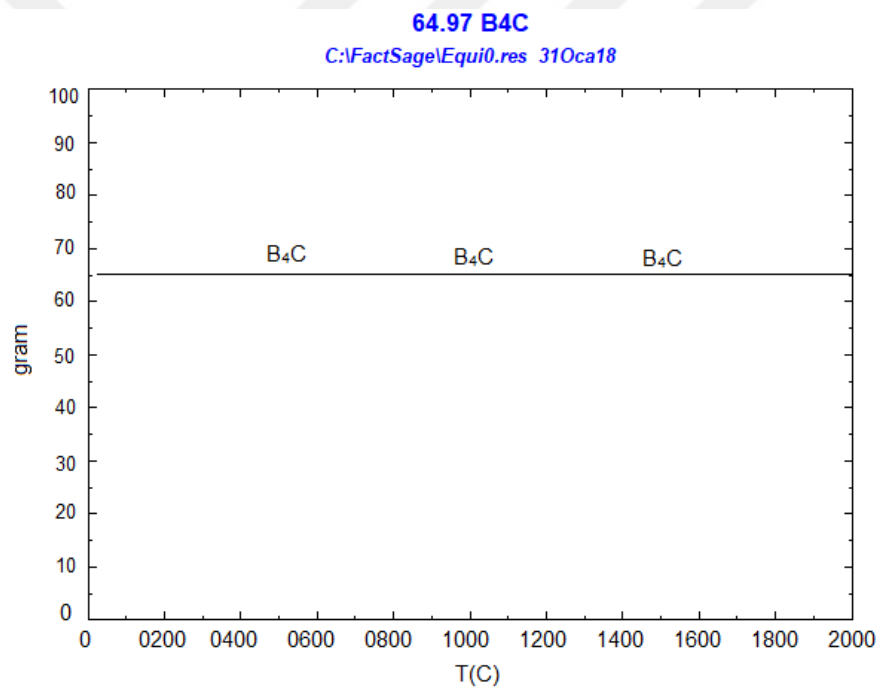


Figure 6.14 : Phase change according to increased temperature in monolithic boron carbide obtained from Factsage 6 thermochemical simulation program.

6.2.2 Phase analysis of boron carbide ceramics with different carbon sources

To increase the sinterability and mechanical behaviors of monolithic boron carbide, 2 vol. % C and CNT is added to the boron carbide structure. The powder mixtures are spark plasma sintered at 1550 °C for 4 min under a pressure of 40 MPa. As a result, no phase changes occurred and it is demonstrated in Figure 6.15. In addition, XRD analysis also showed that after spark plasma sintering at 1550 °C, only B₄C and C phases are existed in the structure.

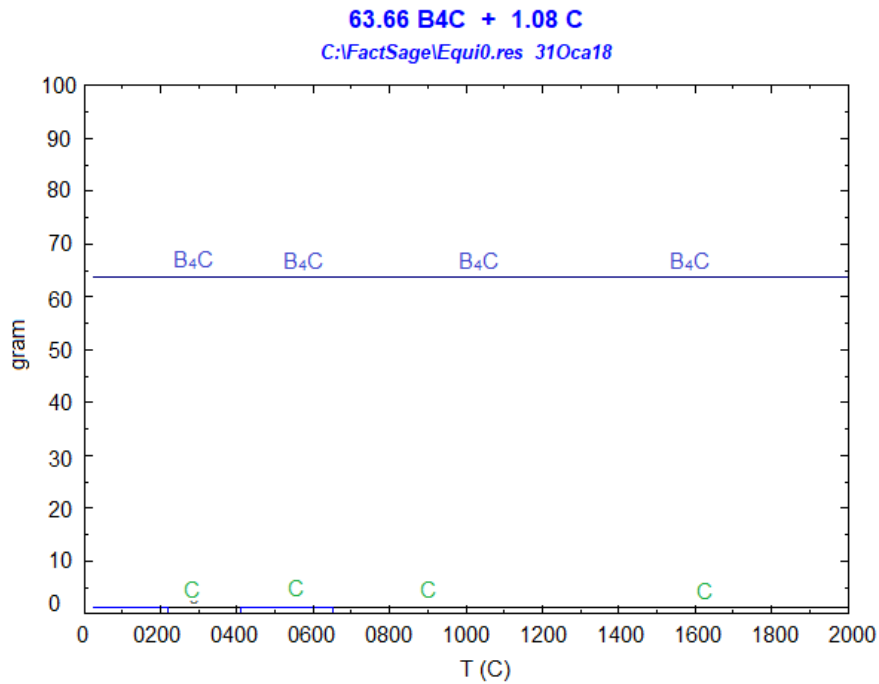


Figure 6.15 : Phase change according to increased temperature in 2 vol. % C added boron carbide obtained from Factsage 6 thermochemical simulation program.

6.2.3 Phase analysis of boron carbide ceramics with light weight metallic additives

For increasing the densification, hardness, fracture toughness and ballistic strength properties of boron carbide, 5 vol. % Al and 5 vol. % Si is added to the structure. These two metallic additives did not remain in metallic form under boron carbide existence and spark plasma sintering procedure conditions.

5 vol. % Al added boron carbide is spark plasma sintered at 1450 °C for 4 min under a pressure of 40 MPa in vacuum and XRD results showed that Al₈B₄C₇ and Al₂OC intermetallic phases are occurred. The oxide phase comes from aluminium and thought that it is originated from starting powders. When no oxide phase in the starting powders is considered, the expected phases according to Factsage thermochemical programme can be seen in Figure 6.16.

In Figure 6.16, one can see that a portion of B₄C reacted with Al to form some Al₄C₃ and AlB₁₂ starting from low temperatures. With increasing temperature, from 1100 °C, Al₄C₃ decomposed to aluminum and carbon. Also, Al reacted with B₄C and amount of AlB₁₂ in the structure is increased and this reaction caused to form a free carbon. Above 1890 °C, AlB₁₂ began to decompose causing the reaction to free carbon to increase the

amount of B_4C . When the sintering temperature used in this study (1550 °C) is considered, 5 vol. % Al is expected to form only AlB_{12} in the structure.

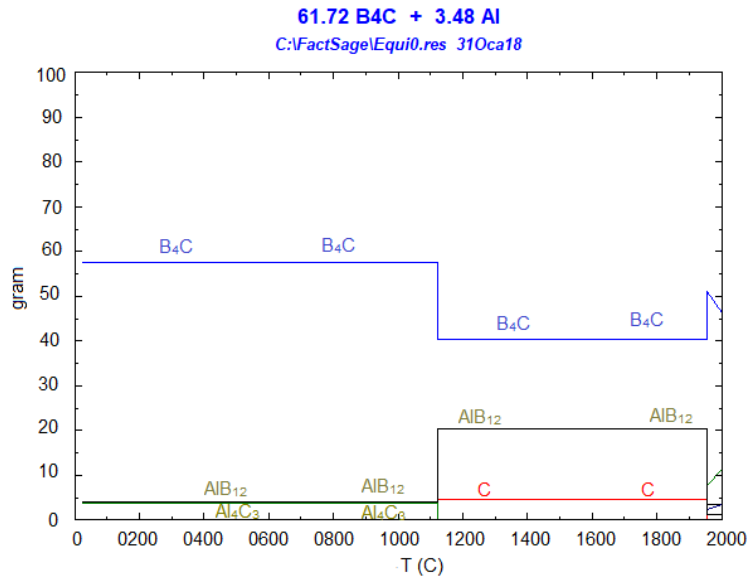


Figure 6.16 : Phase change according to increased temperature in 5 vol. % Al added boron carbide obtained from Factsage 6 thermochemical simulation program.

When 5 vol. % Si is added to the boron carbide structure, some phase changes occur with increased temperature. Figure 6.17 demonstrates the possible phases formed with increasing temperature in boron carbide structure with 5 vol. % Si addition.

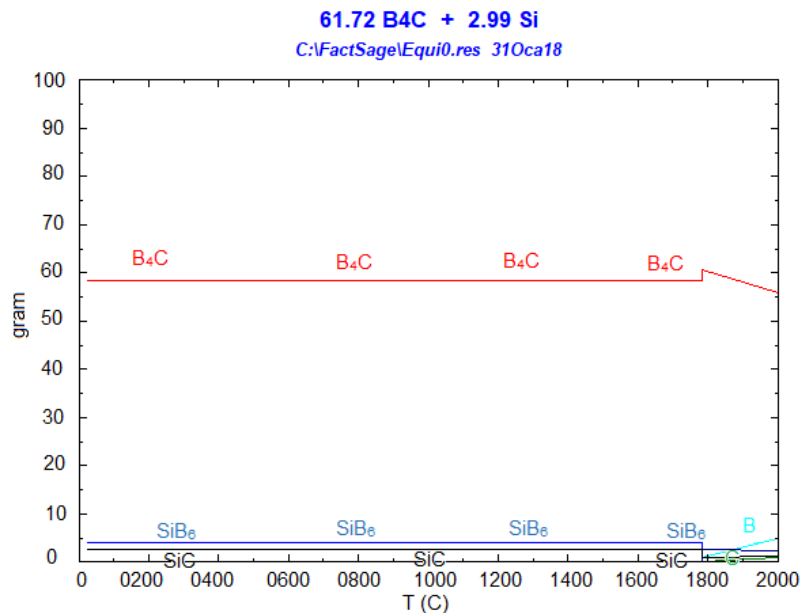


Figure 6.17 : Phase change according to increased temperature in 5 vol. % Al added boron carbide obtained from Factsage 6 thermochemical simulation program.

As can be seen from Figure 6.17, Si reacts with B_4C starting from very low temperatures and results in a formation of SiB_6 and B_4C phases. However,

approximately at 1800 °C, SiB₆ is decomposed and the amount of B₄C is increased. Then at higher temperatures, B₄C is decomposed into B and C. At high temperatures, only B₄C and SiC is remained in the system. In the literature, it is known that the phases exists in the B-C-Si system are only B₄C and SiC, according to the C % in the process environment [13]. If spark plasma sintering is considered, Si in the system takes the C not only from B₄C, but also from the graphite walls. After the experiments, a significant wear on the graphite mold surfaces where the powders interact with the molds, can be observed. As a result, only B₄C and SiC are obtained in the XRD analysis of 5 vol. % Si containing B₄C, instead of expected SiB₆ phase.

Table 6.2 shows the comparison of the expected phases according to Factsage thermochemical simulation programme and XRD analysis when 5 vol. % Al or Si is added to the boron carbide structure.

Table 6.2 : Comparison of phases expected from the simulated Al and Si containing composites performed with the thermochemical program and phases obtained from X-ray diffractograms.

Addition	SPS Process Parameters	Expected phases according to Factsage	Obtained phases from XRD
5 vol. % Al	1450 °C, 4 min, 40 MPa	B ₄ C, AlB ₁₂ , Al ₄ C ₃ , C	B ₄ C, Al ₈ B ₄ C ₇ , Al ₂ OC, C
5 vol. % Si	1500 °C, 4 min, 40 MPa	B ₄ C, SiB ₆ , SiC	B ₄ C, SiC
5 vol. % Si	1500 °C, 4 min, 60 MPa	B ₄ C, SiB ₆ , SiC	B ₄ C, SiC

6.2.4 Phase analysis of boron carbide ceramics with Ti or TiO₂ additives

In order to promote the densification, mechanical properties and ballistic strength of boron carbide, 5, 10, 15 and 20 vol. % Ti-LP additions were made to boron carbide. When B₄C with different amounts of Ti were spark plasma sintered at 1550 °C for 4 min under a pressure of 40 MPa in vacuum atmosphere, Ti is transformed into TiB₂ and resulted in a formation of free carbon in the structure. TiC is not stable in the presence of boron carbide [13]. XRD analysis proved that only TiB₂, B₄C and C peaks can be observed after spark plasma sintering procedure. In addition, the Factsage thermochemical simulation of 5 and 10 vol. % Ti added boron carbide is investigated and the results are shown in Figure 6.18.

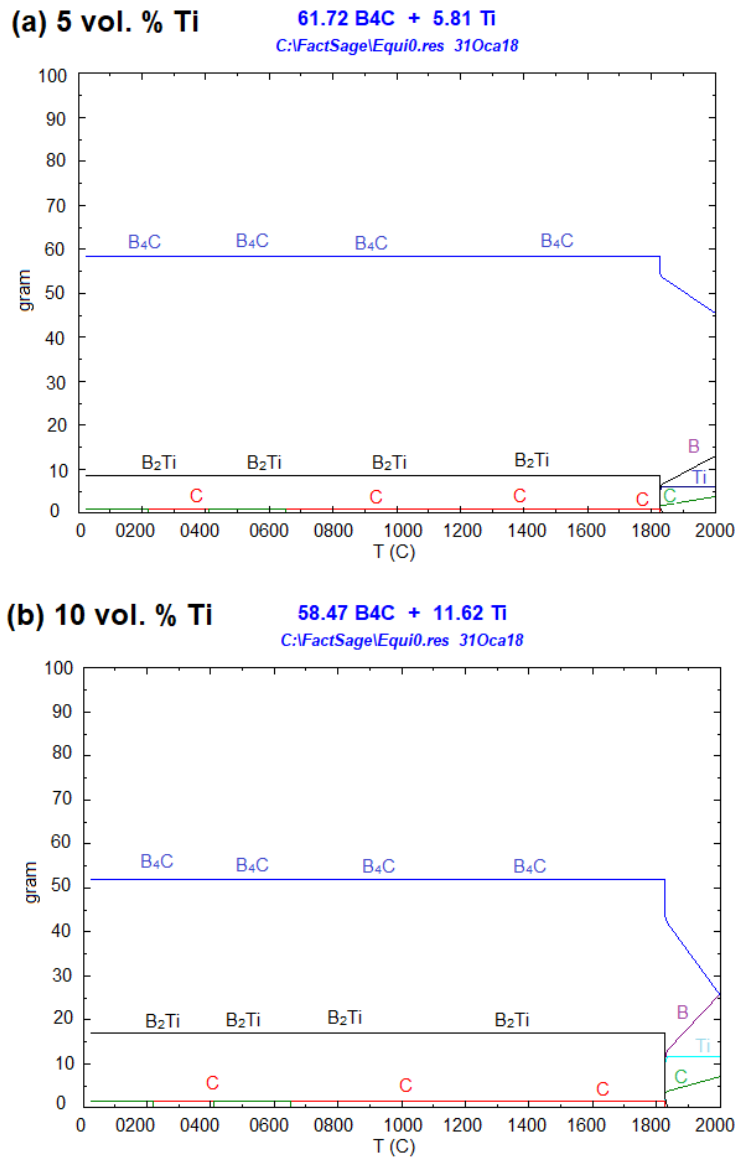


Figure 6.18 : Phase change according to increased temperature in (a) 5 vol. % (b) 10 vol. % Ti added boron carbide obtained from Factsage 6 thermochemical simulation program.

On the other hand, TiO₂ additions were also made in order to see the effect on densification and some mechanical properties of boron carbide. Figure 6.19 the Factsage thermochemical simulation of 5 and 10 vol. % TiO₂ added boron carbide. As can be seen from Figure 6.19, all TiO₂ is transformed into TiB₂ starting from very low temperatures and the amount of formed TiB₂ increased with the increased TiO₂ addition. In 10 vol. % TiO₂ containing B₄C sample, the increase in oxide addition resulted in a formation of B₂O₃ phase. However approximately at 1500°C, B₂O₃ decomposes and the amount of B₄C increases, then at higher temperatures B₄C is seem to be decomposed to B and C.

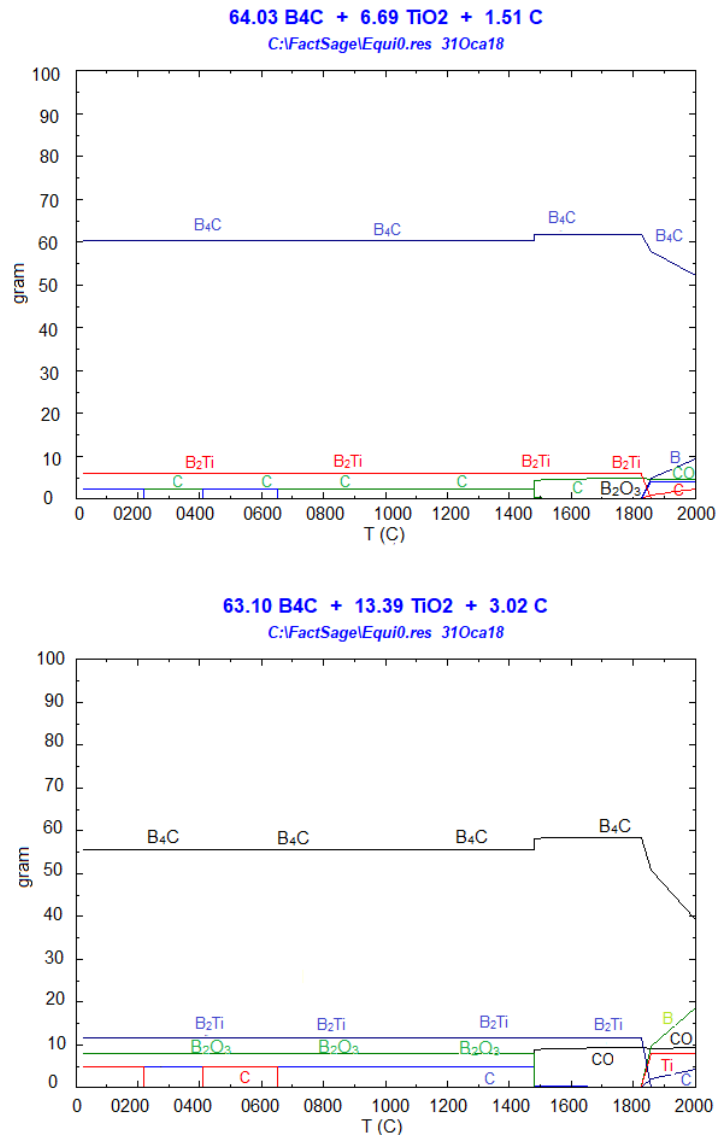


Figure 6.19 : Phase change according to increased temperature in (a) 5 vol. % (b) 10 vol. % TiO₂ added boron carbide obtained from Factsage 6 thermochemical simulation programme.

Figure 6.20 shows 5 vol. % Ti-SP or TiO₂ containing boron carbide samples which was spark plasma sintered at 1550 °C for 4 min under a pressure of 40 MPa in vacuum. When Figure 6.20 is considered, it can be seen that Ti-SP caused to form TiB₂ peaks, but no C in the structure. Also all TiO₂ is transformed into TiB₂ and no oxide phase could be obtained after the XRD evaluation. When TiB₂ peaks caused by Ti and TiO₂ are compared, it can clearly be seen that the peak intensities is higher in 5 vol. % TiO₂ containing sample. Apart from the starting powder particle size difference between Ti and TiO₂, this could also be related to final grain sizes of TiB₂. Ti causes TiB₂ agglomerates in boron carbide structure, whereas TiO₂ results in formation of homogenous distributed small TiB₂ grains in boron carbide matrix. After the spark

plasma sintering of 5 vol. % TiO₂ added boron carbide, very distinct C peak is also observed. Because of the reaction, C is expected to react with O₂ and form CO/CO₂. However, the existence of C in final product may be due to the inclusion coming from starting powder or the sintering conditions.

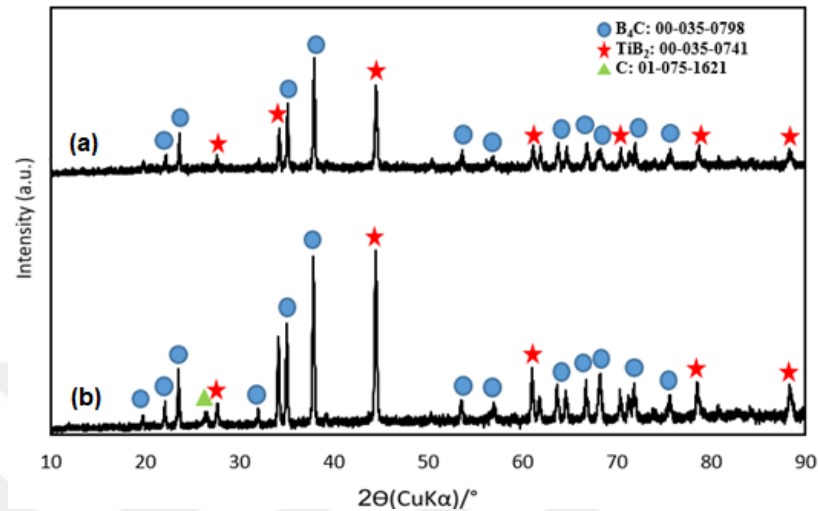


Figure 6.20 : XRD analysis of spark plasma sintered hexagonal B₄C with 5 vol. % (a) Ti-SP and (b) TiO₂ which were spark plasma sintered at 1550 °C for 4 min under a pressure of 40 MPa.

Furthermore, to increase the densification rate and give time for reactions to take place, the soaking time is increased to 6 min and the experiments are repeated. The XRD results of B₄C samples with 5 vol. % Ti or TiO₂ spark plasma sintered at 1550 °C for 6 min under a pressure of 40 MPa in vacuum atmosphere are given in Figure 6.21.

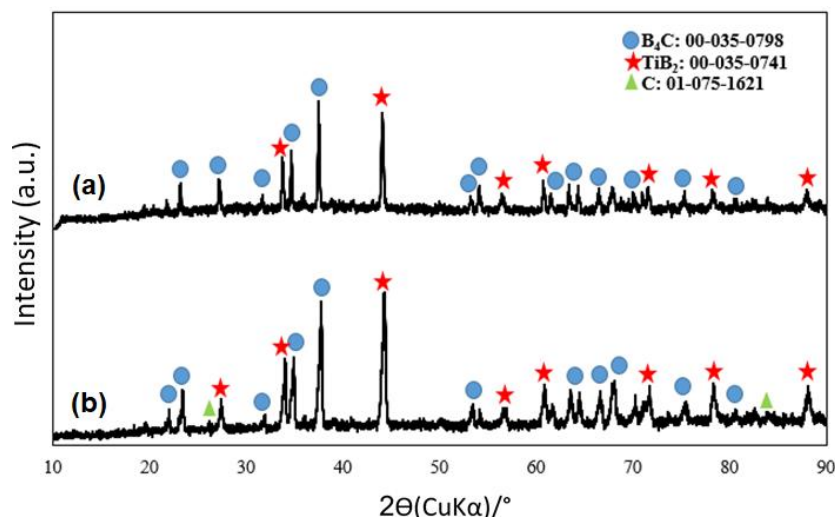


Figure 6.21 : XRD analysis of spark plasma sintered hexagonal B₄C with 5 vol. % (a) Ti-SP and (b) TiO₂ which were spark plasma sintered at 1550 °C for 6 min under a pressure of 40 MPa.

When Figure 6.20 (a) and Figure 6.21 (a) are compared, one can see that with increasing soaking time, the intensity of TiB_2 peaks are increased. The same trend is also obtained in TiO_2 included boron carbide samples which was given in Figure 6.20 (b) and Figure 6.21 (b). Moreover, again TiO_2 addition resulted in higher peak intensities compared to Ti-SP addition and C peak is observed in TiO_2 containing sample but not in Ti-SP added boron carbide.

Further experiments were carried out with 10 vol. % Ti-SP or TiO_2 containing boron carbide in order to see the increasing addition effects on boron carbide properties and structure. Figure 6.22 shows the XRD evaluation of 10 vol. % Ti-SP or TiO_2 added samples. It can clearly be seen that with increasing Ti or TiO_2 amount, the peak intensities tend to increase, as expected. Also, with increased Ti content, C peak could also be observed in Ti-SP added boron carbide sample.

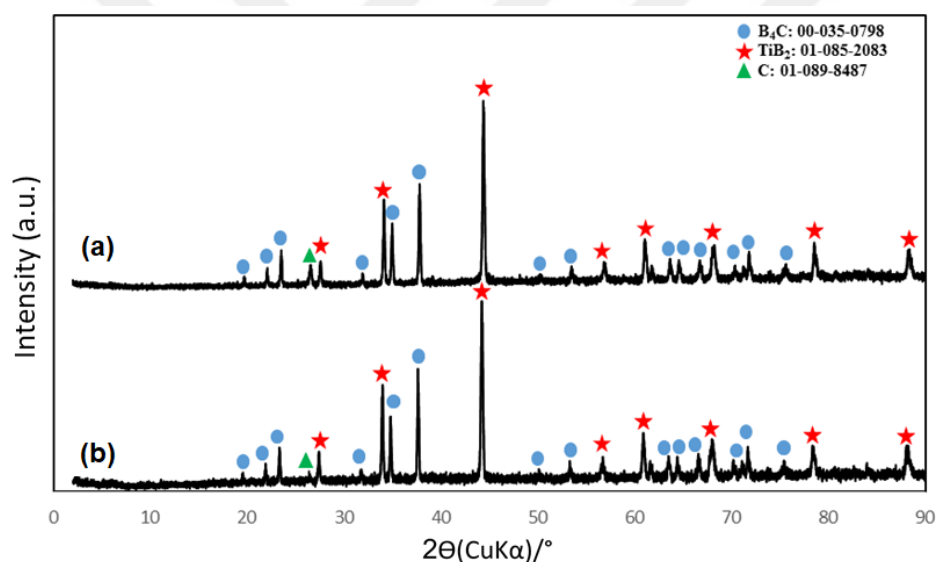


Figure 6.22 : XRD analysis of spark plasma sintered hexagonal B_4C with 10 vol. % (a) Ti-SP and (b) TiO_2 which were spark plasma sintered at $1550^\circ C$ for 4 min under a pressure of 40 MPa.

Table 6.3 gives the comparison of the expected phases according to Factsage thermochemical simulation programme and XRD analysis when 5, 10, 15 and 20 vol. % Ti and 5 and 10 vol. % TiO_2 is added to the boron carbide structure. B_4C , TiB_2 and C phases were expected according to the simulation program and XRD results corresponded with the expectations. Because C amount is very low, XRD may not be able to detect carbon phase. It is very clear that during spark plasma sintering process, Ti did not remain in metallic form, and take B from B_4C to form TiB_2 intermetallic phase. Neither of the X-ray diffractograms of the obtained samples showed Ti metallic

phase. Only in 10 vol. % TiO₂ containing B₄C expected to form B₂O₃ however it does not exist in temperatures higher than 1400 °C.

Table 6.3 : Comparison of phases expected from the simulated Ti and TiO₂ containing composites performed with the thermochemical program and phases obtained from X-ray diffractograms.

Addition	SPS Process Parameters	Expected phases according to Factsage	Obtained phases from XRD
5 vol. % Ti-LP	1550 °C, 4 min, 40 MPa	B ₄ C, TiB ₂ , C	B ₄ C, TiB ₂
5 vol. % Ti-SP	1550 °C, 4 min, 40 MPa	B ₄ C, TiB ₂ , C	B ₄ C, TiB ₂
5 vol. % Ti-SP	1550 °C, 6 min, 40 MPa	B ₄ C, TiB ₂ , C	B ₄ C, TiB ₂
10 vol. % Ti-LP	1550 °C, 4 min, 40 MPa	B ₄ C, TiB ₂ , C	B ₄ C, TiB ₂
10 vol. % Ti-SP	1550 °C, 4 min, 40 MPa	B ₄ C, TiB ₂ , C	B ₄ C, TiB ₂ , C
15 vol. % Ti-LP	1550 °C, 4 min, 40 MPa	B ₄ C, TiB ₂ , C	B ₄ C, TiB ₂
20 vol. % Ti-LP	1550 °C, 4 min, 40 MPa	B ₄ C, TiB ₂ , C	B ₄ C, TiB ₂
5 vol. % TiO ₂	1550 °C, 4 min, 40 MPa	B ₄ C, TiB ₂ , C	B ₄ C, TiB ₂ , C
5 vol. % TiO ₂	1550 °C, 6 min, 40 MPa	B ₄ C, TiB ₂ , C	B ₄ C, TiB ₂ , C
10 vol. % TiO ₂	1550 °C, 4 min, 40 MPa	B ₄ C, TiB ₂ , C	B ₄ C, TiB ₂ , C

6.3 Mechanical Properties of Boron Carbide Ceramic Composites

6.3.1 Hardness and fracture toughness of cylindrical boron carbide ceramics

The Vickers hardness and fracture toughness values of cylindrical B₄C, B₄C with 2 % C and 2 % CNT composites which was spark plasma sintered at 1650 and 1725 °C for 5 minutes under a pressure of 40 MPa in vacuum atmosphere is measured by indentation method at a load of 9.8 N and the obtained results are given in Table 6.4.

Table 6.4 : The hardness, and fracture toughness of spark plasma sintered cylindrical boron carbide ceramics.

Composition	SPS Temperature (°C)	Hardness (GPa)	Fracture Toughness (MPa·m ^{1/2})
Pure B ₄ C		24.6±0.21	3.8±0.06
B ₄ C + 2 % C- black	1650	34.2±0.17	4.0±0.04
B ₄ C + 2 % CNT		34.6±0.24	4.2±0.06
Pure B ₄ C		34.0±0.20	3.5±0.02
B ₄ C + 2 % C- black	1725	35.8±0.31	4.2±0.05
B ₄ C + 2 % CNT		36.3±0.19	4.5±0.07

Both carbon black and CNT added composites showed higher hardness values than monolithic B₄C sintered body. The highest hardness is attained in the boron carbide with 2 vol. % CNT sample showing the highest density. Vicker hardness of 36.3 is attained in the boron carbide sample containing 2 vol. % CNT which was spark plasma

sintered at 1725 °C for 5 min under a pressure of 40 MPa in vacuum atmosphere. The relative density of mentioned specimen have been found to be 98.8 %. Accordingly, increased density resulted in higher hardness values. The hardness values are found to be higher than the study held by Yavas et al. [116]. They obtained hardness values ranging between 32.23 and 32.76 GPa in 1 and 3 wt. % CNT added boron carbide, respectively. They also concluded that there is no significant change between the hardness values of CNT added boron carbide samples [116].

On the other hand, with the addition of carbon to boron carbide body, fracture toughness values were also tended to increase as can be seen from Table 6.2. The highest fracture toughness, 4.5 MPa·m^{1/2}, was achieved with the addition of 2 vol. % CNT to boron carbide. The increase in fracture toughness of composites with carbon addition is in agreement with study of Hirota et al [179]. This could be related to homogeneous distribution of carbon nanotubes in the structure, higher relative densities, crack inclination and bridging effects introduced by carbon nanotubes [179].

In addition, Yavas et al. measured the fracture toughness values of 1, 2 and 3 wt. % CNT added boron carbide samples and found higher fracture toughness values compared to experimental studies of this thesis. According to their study, the fracture toughness of boron carbide samples with CNT addition, was between 5.23 to 5.94 MPa·m^{1/2}, and the highest fracture toughness value is attained in 3 wt. % CNT added sample which was heated with 150 °C/min and spark plasma sintered at 1650 °C for 5 min under a pressure of 40 MPa in vacuum [116, 180].

6.3.2 Hardness and fracture toughness of hexagonal boron carbide ceramic composites

6.3.2.1 Hardness and fracture toughness of hexagonal monolithic boron carbide ceramics

In order to determine the geometry effect on spark plasma sintered boron carbide ceramics, both of the edges and the center of the boron carbide sample is subjected to Vickers hardness test and the hardness and fracture toughness of each edges and center are investigated. Figure 6.23 represents the hardness and fracture toughness values of hexagonal boron carbide ceramics heated with 100 °C/min and spark plasma sintered at 1550 °C for 4 min under a pressure of 40 MPa in vacuum atmosphere. The hardness

and fracture toughness values are both obtained under a 9.8 N load by Vickers indendation technique.

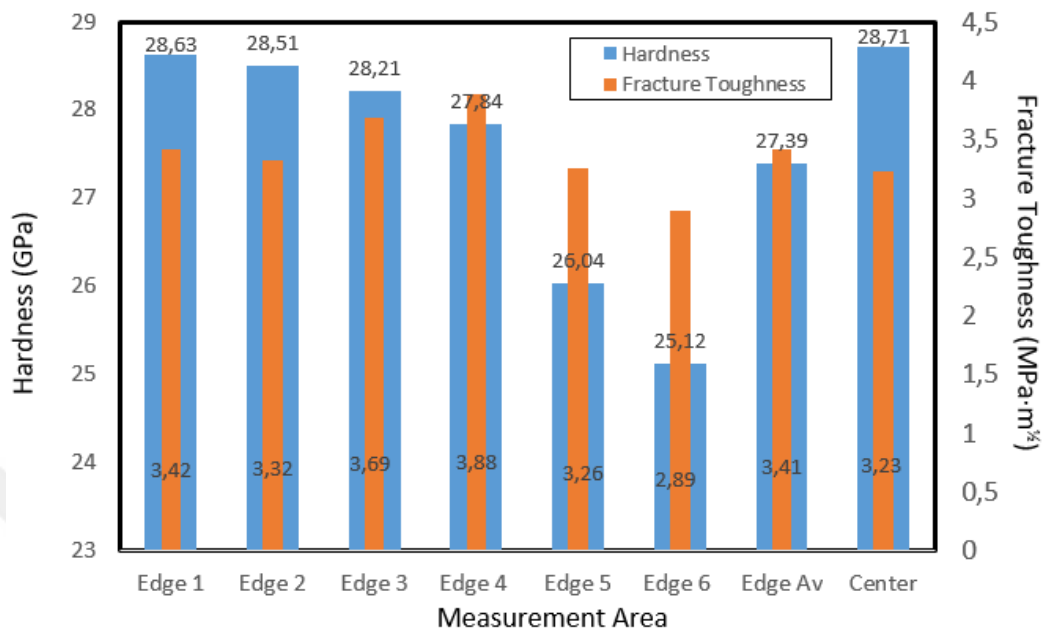


Figure 6.23 : The Vickers hardness and fracture toughness values of edges, edge avenge and center of hexagonal boron carbide ceramics which was spark plasma sintered at 1550 °C for 4 min under a pressure of 40 MPa in vacuum.

Domnich et al [6] reported in their study that mechanical properties such as hardness, strength, fracture toughness, etc., strongly depend on such external factors as quality and size of the sample, grain size, porosity, presence of defects and flaws, conditions of loading. That is why one can find various hardness results regarding to boron carbide [6]. The center of hexagonal monolithic boron carbide ceramic has been found to have 28.71 GPa. The edge hardness values were ranged between 25.12 and 28.63 GPa, with an average of 27.39 GPa. The hardness of hexagonal monolithic boron carbide showed higher values in measurement regions where the relative density values are found to be higher, the hardness is prominently dependent to density, with increasing density the hardness values increased.

When the fracture toughness values of spark plasma sintered hexagonal boron carbide ceramics are considered, it is difficult to mention a prominent conclusion. However, it can be mentioned that with increasing relative density and hardness, fracture toughness values tend to decrease. The average fracture toughness value for edges is measured as 3.41 MPa·m^{1/2} which is higher than the more densified region, center of the sample, as 3.23 MPa·m^{1/2}. Lee and Speyer also provided the similar results and they reported

that the fracture toughness of the undoped boron carbide samples which was produced by pressureless sintering increased as hardness decreased [7]. To compare the relation between density, hardness and fracture toughness, Table 6.5 is given.

Table 6.5 : The relative density, hardness and fracture toughness values of spark plasma sintered hexagonal B₄C ceramics according to their measurement regions.

Measurement Area	Relative Density (%)	Hardness (GPa)	Fracture Toughness (MPa·m ^{1/2})
Edge 1	95.20	28.63±0.21	3.42±0.07
Edge 2	95.16	28.51±0.26	3.32±0.07
Edge 3	94.95	28.21±0.20	3.69±0.09
Edge 4	94.65	27.84±0.33	3.88±0.06
Edge 5	94.46	26.04±0.39	3.26±0.11
Edge 6	93.90	25.12±0.49	2.89±0.17
Edge Av	94.72	27.39	3.41
Center	95.34	28.71±0.27	3.23±0.09

On the other hand, the lowest fracture toughness is obtained in the region with the lowest relative density and hardness value. The lowest density showing part, coded as Edge 6, in this study may probably have the smallest grain because of the insufficient densification. According to Lee and Speyer, the fracture toughness of the monolithic boron carbide decreased for smaller grains, because dislocation pileups more rapidly accumulate at the grain boundaries of smaller grains, which fosters more immediate strainhardening. Thus, the solid displays a greater propensity to crack, rather than plastically deform, under the load of an indenter and higher fracture toughness values are obtained in boron carbide with larger grains [7].

6.3.2.2 Hardness and fracture toughness of hexagonal boron carbide ceramics with different carbon sources

In order to see the C-black and CNT addition on the mechanical properties of boron carbide samples, 2 vol. % C-black or CNT addition have been made to boron carbide samples and the hexagonal geometry effect on these samples are investigated. Each edges and the center of the both samples are subjected to 10 Vickers hardness measurements under a load of 9.8 N and the fracture toughness values are calculated by Palmqvist method. Figure 6.24 gives the hardness values of 2 vol. % C-black and CNT containing hexagonal boron carbide samples which were heated with 100 °C/min

and spark plasma sintered at 1550 °C for 4 min under an applied pressure of 40 MPa in vacuum atmosphere according to edges, edge average and center of the samples.

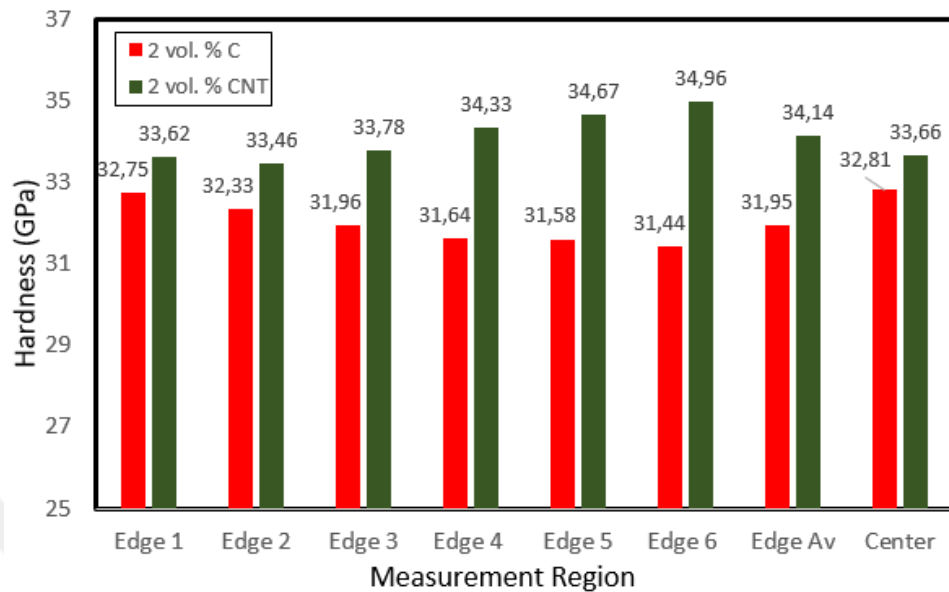


Figure 6.24 : Vickers hardness values of 2 vol. % C-black and CNT added hexagonal boron carbide ceramics which were spark plasma sintered at 1550 °C for 4 min under an applied pressure of 40 MPa.

When the hardness values of hexagonal boron carbide samples containing 2 vol. % C or CNT, CNT can be regarded as more beneficial addition for increasing the hardness values. In order to find out the relation between the relative density values and mechanical properties of C-black and CNT added boron carbide, Table 6.6 can be viewed.

When the hardness values of 2 vol. % C-black and CNT containing samples are compared with that of pure boron carbide, it can be stated that both C additions resulted in higher hardness values. Also, Lee and Speyer have obtained similar results in their study [7]. They concluded that carbon containing specimens sintered to 97 and higher % of theoretical density demonstrated no statistically significant trend, and higher hardness values than those of undoped samples have been attained [7].

The highest hardness of C-black containing sample is obtained in the center region as 32.81 GPa, which can be regarded as the most densified part of the hexagonal boron carbide. The hardness results obtained in different regions of C-black added sample is expected as hardness increased as sintered density increased. Also, the lowest hardness value was found out to be 31.44 GPa in one of the edges with the lowest relative density.

Table 6.6 : The relative density, hardness and fracture toughness values of 2 vol. % C and CNT added hexagonal B₄C ceramics according to their measurement regions.

Addition made to B ₄ C	Measurement Area	Relative Density (%)	Hardness (GPa)	Fracture Toughness (MPa·m ^{1/2})
C-black	Edge 1	96.48	32.75±0.32	3.71±0.06
	Edge 2	96.25	32.33±0.21	3.75±0.08
	Edge 3	95.98	31.96±0.27	3.82±0.04
	Edge 4	95.63	31.64±0.20	3.91±0.09
	Edge 5	95.63	31.58±0.33	4.01±0.06
	Edge 6	95.42	31.44±0.17	4.09±0.06
	Edge Av	95.89	31.95	3.88
	Center	96.75	32.81±0.39	3.69±0.07
	CNT	Edge 1	97.81	33.62±0.21
Edge 2		97.04	33.46±0.28	4.16±0.09
Edge 3		96.45	33.78±0.31	3.97±0.04
Edge 4		96.20	34.33±0.20	3.73±0.10
Edge 5		95.16	34.67±0.43	4.08±0.13
Edge 6		94.33	34.96±0.41	3.32±0.11
Edge Av		96.17	34.14	3.93
Center		97.26	33.66±0.16	4.46±0.07

On the other hand, CNT showed a rather complex trend on the hardness. The hardness of edges were observed higher than the center of the sample although the densification was higher in center region of 2 vol. % CNT added boron carbide sample. However when the study held by Yavas [180] is analyzed, it can be seen that they also could not find out a prominent trend for hardness change in terms of CNT addition. All of the hardness values were very close to each other and the average of the edge hardness is identified to be 34.14 GPa, whereas 33.66 GPa is obtained in the center of 2 vol. % CNT added boron carbide which was heated with 100 °C/min and spark plasma sintered at 1550 °C under a pressure of 40 MPa in vacuum atmosphere.

As mentioned before, the highest relative density values in case of monolithic boron carbide and 2 vol. % C-black and CNT added samples are both attained in center region. If the center fracture toughness values of these samples are examined, both C-black and CNT addition can be remarked as beneficial in increasing fracture toughness of boron carbide. The center of the monolithic boron carbide ceramic showed 3.23 MPa·m^{1/2}, whereas the fracture toughness is found to be 3.69 MPa·m^{1/2} in C- black containing sample and 4.46 MPa·m^{1/2} in CNT containing boron carbide. These increases corresponds to approximately 15 % and 38 % increase in fracture toughness values of 2 vol. % C and CNT added boron carbide samples compared to monolithic

boron carbide, respectively. Similar with the study of Lee and Speyer, hardness increased as sintered density increased, whereas the fracture toughness showed the reversed trend [7]. The hardness and fracture toughness results of C-black containing boron carbide made a very good agreement with this finding.

Figure 6.25 shows the fracture toughness values of 2 vol. % C-black and CNT containing hexagonal boron carbide samples which were heated with 100 °C/min and spark plasma sintered at 1550 °C for 4 min under an applied pressure of 40 MPa in vacuum atmosphere according to edges, edge average and center of the samples.

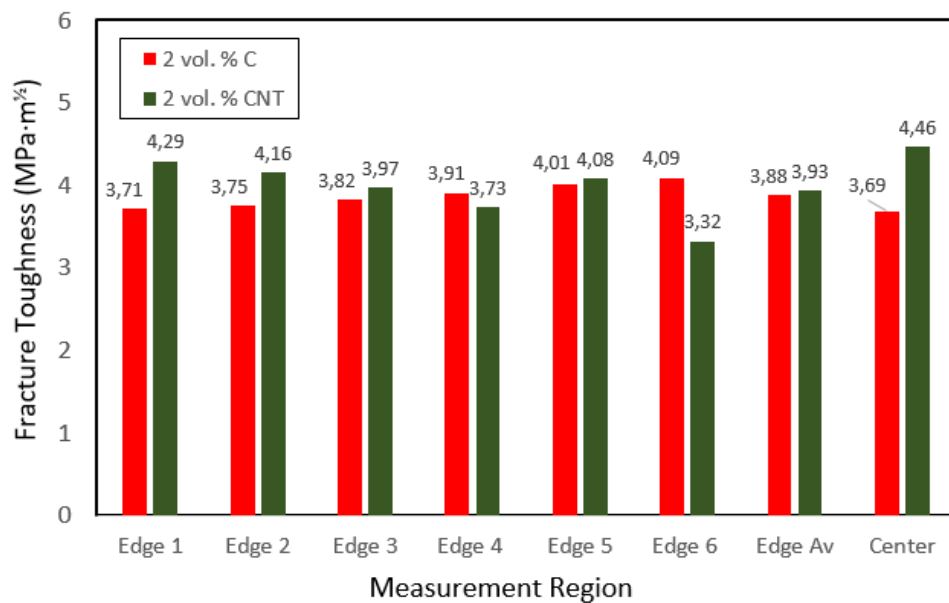


Figure 6.25 : Fracture toughness values of 2 vol. % C- black and CNT added hexagonal boron carbide ceramics which were spark plasma sintered at 1550 °C for 4 min under an applied pressure of 40 MPa.

The highest fracture toughness value is observed in the center region of 2 vol. % CNT added sample. Also, the lowest fracture toughness value is attained in one of the edges of 2 vol. % CNT added boron carbide which showed 94.33 % relative density. To make greater use of ceramic materials such as boron carbide with their exceptional high- temperature capability and wear resistance, tougher microstructures which are less sensitive to the presence of defects are needed to be developed. However because of the ceramic nature, intrinsic toughness remains low and the researchers must concentrate on extrinsic toughening mechanisms. There are several crack-tip shielding mechanisms that contribute greatly to the toughening of ceramics and their composites. These are distinguished by those mechanisms that occur in the frontal zone (ahead of the advancing crack front) and those that act in the crack wake (bridging

mechanisms). CNT supplies and forms a bridging mechanism in boron carbide structure and works for increasing the fracture toughness of the ceramic.

6.3.2.3 Hardness and fracture toughness of hexagonal boron carbide ceramic composites with light-weight metallic additions

Al addition

The edge, edge average and center hardness and fracture toughness values of 5 vol. % Al containing hexagonal boron samples which was heated with 100 °C/min and spark plasma sintered at 1450 °C for 4 min under an applied pressure of 40 MPa in vacuum is demonstrated in Figure 6.26.

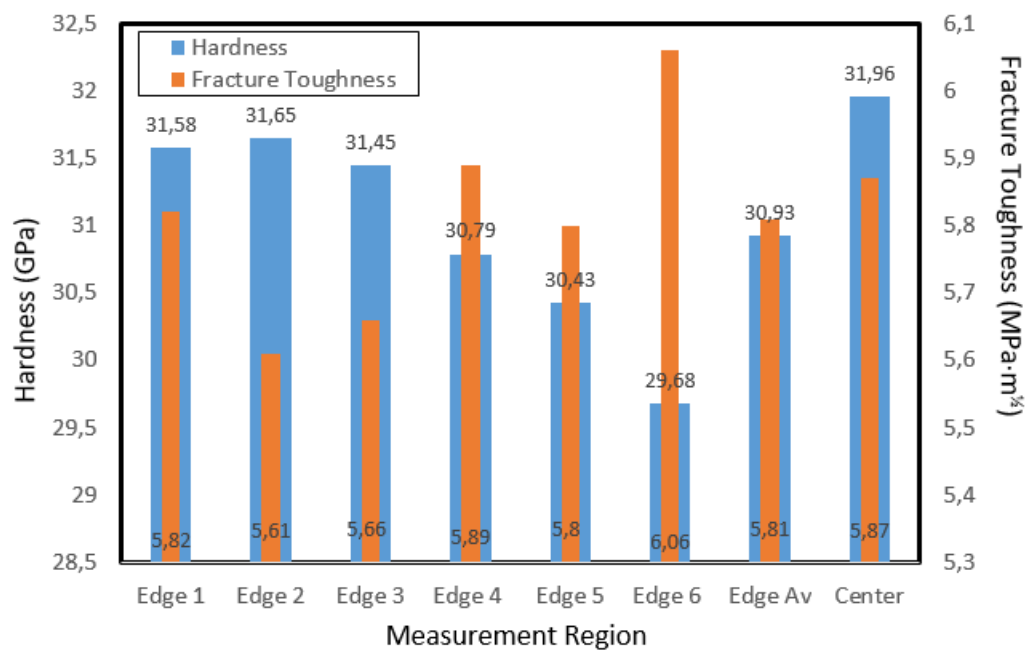


Figure 6.26 : Hardness and fracture toughness values of 5 vol. % Al added hexagonal boron carbide ceramic which was spark plasma sintered at 1450 °C for 4 min under an applied pressure of 40 MPa.

As can clearly be seen from Figure 6.26, the hardness and fracture toughness values attained in edge regions of hexagonal boron carbide sample with 5 vol. % Al is inversely proportional. However the hardness values are observed to be directly proportional with the relative density values. The highest hardness is obtained in the center region of the 5 vol. % Al containing hexagonal boron carbide which is also the most densified part of the sample. Also, the lowest hardness value was seen in Edge 6, which can be regarded as the part with lowest density. The edge hardness values of

5 vol. % Al containing boron carbide were ranged between 29.68 to 31.65 GPa, with an average of 30.93 GPa, whereas the center hardness was found out to be 31.96 GPa. When all these hardness values of 5 vol. % Al containing sample and monolithic boron carbide are considered, the elevated hardness in the Al containing specimen can occurred due to the reinforcing effect the aluminum has on preventing pore collapse as similar with Hulbert et al [120]. The relative density, hardness and fracture toughness values of 5 vol. % Al added boron carbide which was heated with 100 °C/min and spark plasma sintered at 1450 °C for 4 min under a pressure of 40 MPa in vacuum can also be followed from Table 6.7.

Table 6.7 : The relative density, hardness and fracture toughness values of 5 vol. % Al added hexagonal B₄C ceramics according to their measurement regions.

Measurement Area	Relative Density (%)	Hardness (GPa)	Fracture Toughness (MPa·m ^{1/2})
Edge 1	98.06	31.58±0.29	5.82±0.06
Edge 2	97.99	31.65±0.17	5.61±0.07
Edge 3	97.84	31.45±0.19	5.66±0.06
Edge 4	97.69	30.79±0.12	5.89±0.09
Edge 5	97.49	30.43±0.12	5.80±0.11
Edge 6	97.20	29.68±0.18	6.06±0.06
Edge Av	97.71	30.93	5.81
Center	98.16	31.96±0.21	5.87±0.08

The highest fracture toughness was seen in the Edge 6 as 6.06 MPa·m^{1/2} whereas this edge showed the lowest hardness value of whole sample, also the relative density was lowest in this part of the sample. In addition the lowest fracture toughness was attained as 5.61 MPa·m^{1/2} in Edge 2 which was the edge with highest hardness and relative density value. Although the highest fracture toughness value was attained in an edge, the fracture toughness value in the center was higher. Accordingly, one can conclude that the fracture toughness values are found out to be very close to each other.

Aluminium addition increased the fracture toughness of monolithic boron carbide remarkably. Aluminium inclusions in boron carbide body can increase fracture toughness by two mechanisms: (i) toughening due to crack bridging and plastic deformation of aluminium particles; (ii) toughening due to thermal residual stress [181]. Mashadi et al [182] stated that crack interacts with tougher Al phase in the structure or crack deflects by microcracks around Al compounds phases. In this study, all Al is transformed into Al₈B₄C₇ and Al₂O_C, which brought the higher fracture

toughness values. Due to thermal expansion mismatch between Al and B₄C, microcracking can be supposed around Al phase [182]. Furthermore, higher relative density values, in other words less porosity is observed in the samples sintered with 5 vol. % Al compared to monolithic boron carbide.

In addition, one other reason for lower fracture toughness in center compared to some edge regions can be linked to the increase of the grain size [182]. The grain size of the center is found to be generally higher than that of edge values in this study. Since increasing grain size decreases the grain boundary, the effect of grain boundary in toughening of sintered B₄C containing Al additive, decreases. Increasing the grain size decreases the bridging length and in conclusion, toughness decreases [182].

Si addition

The edge, edge average and center hardness values of hexagonal boron carbide with 5 vol. % Si addition is given in Figure 6.18. 5 vol. % Si added boron carbide samples were heated with 100 °C/min and spark plasma sintered at 1500 °C for 4 min under 40 or 60 MPa pressures in vacuum.

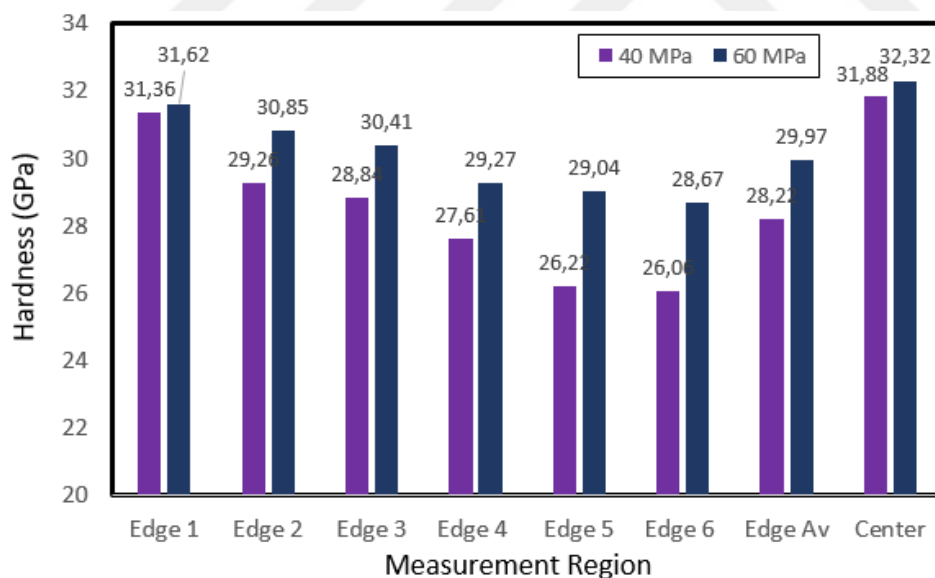


Figure 6.27 : Vickers hardness values of 5 vol. % Si added hexagonal boron carbide ceramics which were spark plasma sintered at 1500 °C for 4 min under an applied pressure of 40 MPa or 60 MPa.

According to Figure 6.27, center of hexagonal boron carbide with 5 vol. % Si showed higher hardness compared to edge values. These results are found to be parallel with the study of Cengiz [118]. Also, with the increasing applied pressure, the hardness values increased. 40 MPa pressure resulted in 31.88 GPa hardness in center of 5 vol.

% Si containing sample and 28.22 GPa is attained as average edge hardness. However, the highest hardness is attained in the center of 5 vol. % Si containing sample which was spark plasma sintered under 60 MPa pressure as 32.32 GPa, and the average edge hardness was found out to be 29.97 GPa.

In the literature, Ye et al. [128] used Si as a sintering aid and spark plasma sintered boron carbide with 4, 8 and 10 vol. % Si and they reported 41.83 GPa hardness value in 8 wt% Si containing sample. They concluded that the addition of Si could further facilitate the densification of boron carbide due to the formation of Si liquid phase during spark plasma sintering. Also, the formation of SiC through the reaction between B₄C and Si during sintering effectively inhibited the growth of B₄C grains and significantly improved hardness and strength [128]. The hardness values was directly proportional with the density values and with increased relative density, the hardness tend to increase. The relative density, hardness and fracture toughness values of 5 vol. % Si added B₄C which was heated with 100 °C/min and spark plasma sintered at 1500 °C for 4 min under a pressure of 40 MPa in vacuum can also be seen in Table 6.8.

Table 6.8 : The relative denisty, hardness and fracture toughness values of 5 vol. % Si added hexagonal B₄C ceramics spark plasma sintered under 40 or 60 MPa pressure according to their measurement regions.

Pressure applied	Measurement Area	Relative Density (%)	Hardness (GPa)	Fracture Toughness (MPa·m ^{1/2})
40 MPa	Edge 1	96.30	31.36±0.28	5.32±0.09
	Edge 2	95.10	29.26±0.22	5.32±0.07
	Edge 3	95.02	28.84±0.29	5.44±0.09
	Edge 4	94.69	27.61±0.22	5.55±0.09
	Edge 5	93.33	26.22±0.19	5.67±0.07
	Edge 6	93.03	26.06±0.21	5.76±0.06
	Edge Av	94.5	28.22	5.51
60 MPa	Center	96.31	31.88±0.24	5.37±0.07
	Edge 1	97.22	31.62±0.28	5.38±0.09
	Edge 2	96.86	30.85±0.20	5.59±0.06
	Edge 3	96.54	30.41±0.20	5.69±0.04
	Edge 4	96.13	29.27±0.26	5.75±0.05
	Edge 5	96.01	29.04±0.29	5.88±0.05
	Edge 6	95.72	28.67±0.28	5.97±0.09
Edge Av	96.41	29.97	5.71	
	Center	97.54	32.32±0.26	5.41±0.05

The fracture toughness values of the edge, edge average and center of hexagonal boron carbide with 5 vol. % Si addition which were heated with 100 °C/min and spark plasma

sintered at 1500 °C for 4 min under applied pressures of 40 or 60 MPa in vacuum atmosphere is given in Figure 6.28.

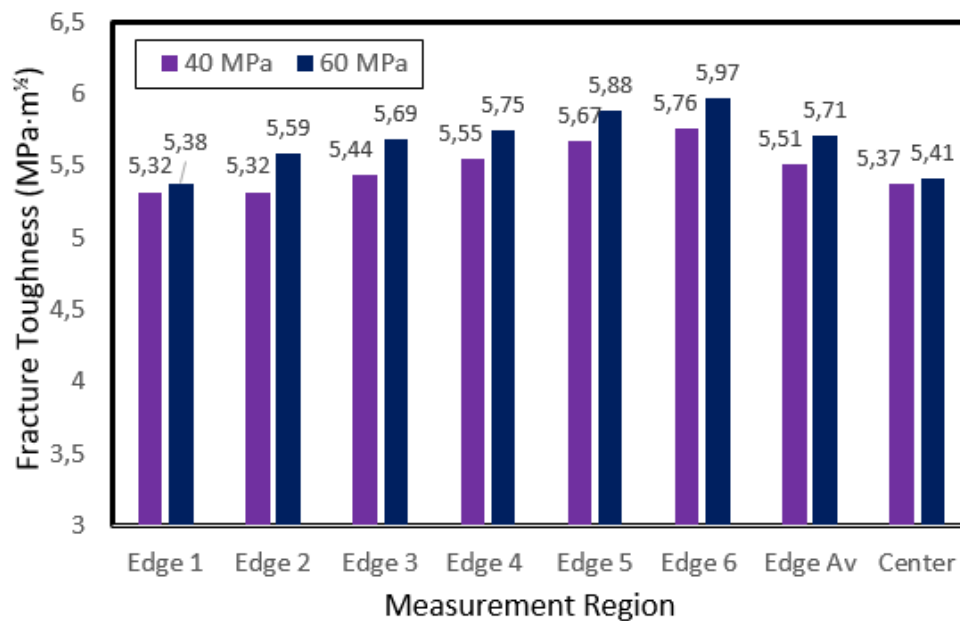


Figure 6.28 : Fracture toughness values of 5 vol. % Si added hexagonal boron carbide ceramics which were spark plasma sintered at 1500 °C for 4 min under an applied pressure of 40 MPa or 60 MPa.

When Figure 6.28 is analyzed, it can be concluded that with the increased applied pressure during spark plasma sintering, the fracture toughness of 5 vol. % Si added boron carbide composites are also increased. In addition, the hexagonal geometry effect is very clear in 5 vol. % Si containing boron carbide composites. The highest fracture toughness values are attained in edge regions with lowest density and the average edge fracture toughness is found to be higher than the center fracture toughness values. The center edge value is obtained as 5.37 MPa·m^½ and the edge average is found out to be 5.51 MPa·m^½ in the sample which was produced by spark plasma sintering under 40 MPa, whereas the center edge value is 5.41 MPa·m^½ and edge average fracture toughness is attained as 5.71 MPa·m^½ in 5 vol. % Si containing sample heated with 100 °C/min and spark plasma sintered at 1500 °C for 4 min under a pressure of 60 MPa in vacuum atmosphere.

If the fracture toughness results obtained from 5 vol. % Si containing composites are compared with that of the monolithic boron carbide ceramics, one can see that fracture toughness values are improved remarkably. Ye et al [128] explained this situation as the residual thermal stress due to the thermal expansion mismatch between the B₄C and SiC promoted the crack deflection. They supported their finding with fracture

surface microstructures of the samples. According to them, Si changes the fracture mode of B₄C from a predominantly transgranular mode in pure B₄C specimen to the intergranular mode due to the crack deflection [128].

6.3.2.4 Hardness and fracture toughness of hexagonal boron carbide ceramic composites with Ti and TiO₂ additions

Ti-LP addition

The edge, edge average and center hardness values of hexagonal boron carbide with 5, 10, 15 and 20 vol. % Ti addition is given in Figure 6.29. Boron carbide samples with different amounts of metallic Ti additive were heated with 100 °C/min and spark plasma sintered at 1550 °C for 4 min under 40 MPa pressures in vacuum atmosphere.

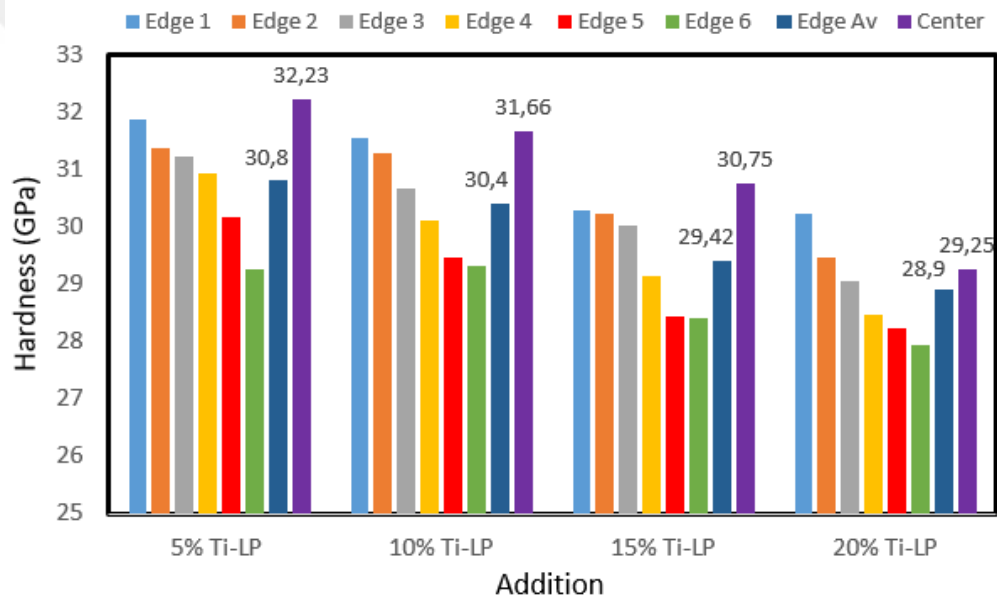


Figure 6.29 : Vickers hardness values of 5, 10, 15 and 20 vol. % Ti-LP added hexagonal boron carbide ceramics which were spark plasma sintered at 1550 °C for 4 min under an applied pressure of 40 MPa.

When Figure 6.29 is analyzed, one can see that with increasing Ti content in the boron carbide structure, the hardness is lowered although the densification is promoted with increasing Ti content. As mentioned before, all Ti added to boron carbide turns into TiB₂, resulting a free C in the structure. Accordingly, it is possible to evaluate these results with the existing studies in the literature concerning the boron carbide with Ti, TiO₂-C or direct TiB₂ additions. These results are both parallel to the results existed in the studies of Uygun et al [135], Huang et al [136, 143], Wang et al [145], Çakır et

al. [139]. In both studies, hardness is observed to be increased compared to monolithic boron carbide and after adding 15 and 20 vol.% TiB₂, it diminishes.

In this study, by increasing the amount of Ti in the B₄C-Ti powder mixtures, the amount of liquid phase formed around the granules increased and the amount of TiB₂ was increased by facilitating the formation of TiB₂ phase. Since the hardness of TiB₂ (24-29 GPa) is lower than the hardness of B₄C (32-36 GPa), the increase in the amount of TiB₂ in the boron carbide structure causes the hardness of the composite to decrease. Although, TiB₂ is softer than B₄C, TiB₂ addition avoids the grain growth in the microstructure and results in an increase in hardness. However with increasing Ti addition, increase in soft phase amount in a matrix, hardness values starts to fall down. Wang et al explained this situation as soft phase dispersed in the hard matrix reduces the hardness of the composite [145].

Furthermore, in this study the coarse-grained Ti metal, was first converted to liquid with increasing temperature. Then Ti reacts with boron carbide and the recrystallization of small (3-5 μm) TiB₂ grains via B₄C grains occurs. After that, these small TiB₂ grains agglomerate in the same region until the liquid Ti is consumed, resulting in new small TiB₂ grains and the free carbon result in lower hardness values in the composites with higher Ti content.

The highest hardness is attained in the center region of 5 vol. % Ti-LP containing sample which was heated with 100 °C/min and spark plasma sintered at 1550 °C for 4 min under a pressure of 40 MPa as 32.23 GPa while the average edge hardness is found to be 30.80 GPa. With increasing Ti content to 10, 15 and 20 vol. %, the center hardness values decreased to 31.66, 30.75 and 29.25, respectively while the average edge values were 30.40, 29.42 and 28.90, respectively. Again in both Ti containing samples, the edge hardness values were always lower than that of the center of the sample. Hexagonal Ti-LP containing boron carbide showed higher hardness values in center regions where the densification was higher.

The relative density values of 5, 10, 15 and 20 vol. % Ti-LP containing samples which were heated with 100 °C/min and spark plasma sintered at 1550 °C for 4 min under a pressure of 40 MPa in vacuum atmosphere was compared with hardness and fracture toughness in Table 6.9.

Table 6.9 : The relative density, hardness and fracture toughness values of 5, 10, 15 and 20 vol. % Ti-LP added hexagonal B₄C ceramics spark plasma sintered at 1550 °C under 40 MPa pressure according to their measurement regions.

Ti Content	Measurement Area	Relative Density (%)	Hardness (GPa)	Fracture Toughness (MPa·m ^{1/2})
5 vol. %	Edge 1	99.05	31.86±0.25	4.75±0.06
	Edge 2	98.68	31.37±0.23	4.85±0.04
	Edge 3	98.32	31.24±0.28	5.23±0.09
	Edge 4	97.94	30.94±0.24	5.41±0.09
	Edge 5	97.63	30.16±0.16	5.69±0.07
	Edge 6	97.03	29.25±0.20	6.06±0.11
	Edge Av	98.10	30.80	5.33
	Center	99.18	32.23±0.20	4.86±0.09
10 vol. %	Edge 1	99.26	31.56±0.28	6.01±0.16
	Edge 2	99.01	31.28±0.20	6.15±0.12
	Edge 3	98.76	30.67±0.29	6.48±0.11
	Edge 4	98.53	30.12±0.18	6.79±0.14
	Edge 5	98.08	29.45±0.22	7.12±0.16
	Edge 6	97.94	29.33±0.20	6.51±0.14
	Edge Av	98.60	30.40	6.51
	Center	99.35	31.66±0.21	6.25±0.16
15 vol. %	Edge 1	99.75	30.30±0.28	5.06±0.08
	Edge 2	99.63	30.24±0.25	5.35±0.09
	Edge 3	99.55	30.03±0.24	6.42±0.12
	Edge 4	99.30	29.14±0.26	6.65±0.13
	Edge 5	99.26	28.45±0.22	6.72±0.10
	Edge 6	99.12	28.40±0.24	6.68±0.09
	Edge Av	99.44	29.42	6.15
	Center	99.68	30.75±0.16	5.51±0.13
20 vol. %	Edge 1	100	30.24±0.18	4.35±0.12
	Edge 2	99.59	29.45±0.20	5.15±0.16
	Edge 3	99.45	29.05±0.16	5.25±0.13
	Edge 4	99.07	28.48±0.18	5.75±0.11
	Edge 5	98.87	28.24±0.22	6.25±0.10
	Edge 6	98.82	27.95±0.28	6.52±0.15
	Edge Av	99.3	28.90	5.55
	Center	100	29.25±0.20	4.95±0.09

When Table 6.9 is considered, to make a generalization for spark plasma sintering of Ti containing boron carbide with a hexagonal geometry is possible. When all the hardness and fracture toughness values of one sample is considered particularly, hardness can be defined as higher in the regions where relative density is higher whereas fracture toughness is generally lower in the regions where densification is higher. Figure 6.30 demonstrates the fracture toughness values of 5, 10, 15 and 20 vol. % Ti-LP containing boron carbide samples which were heated with 100 °C/min and

spark plasma sintered at 1550 °C for 4 min under an applied pressure of 40 MPa in vacuum atmosphere.

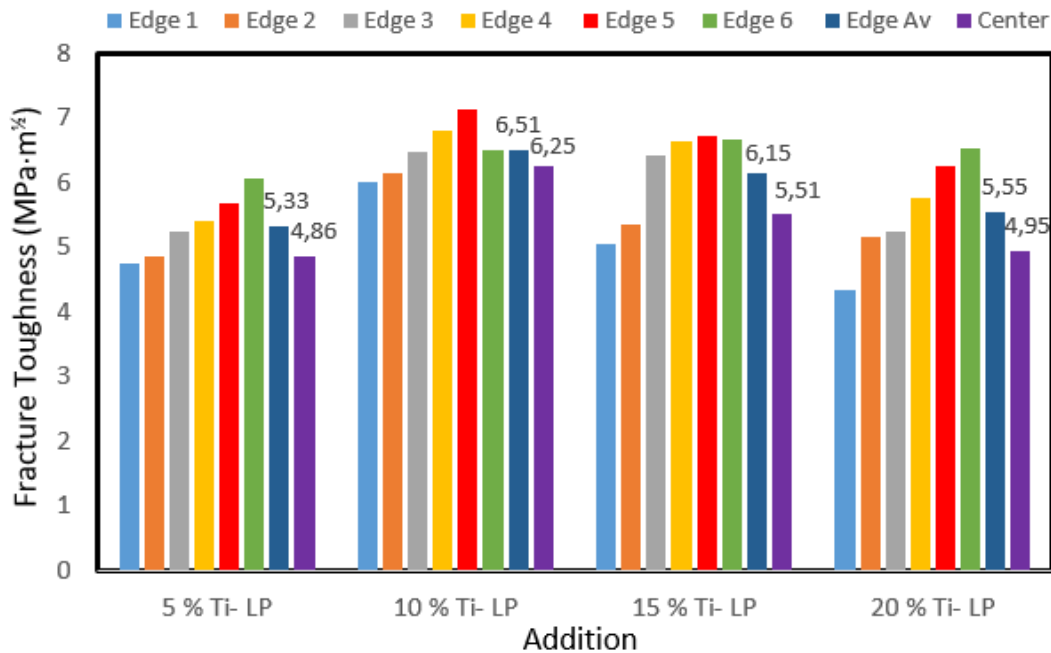


Figure 6.30 : Fracture toughness values of 5, 10, 15 and 20 vol. % Ti-LP added hexagonal boron carbide ceramics which were spark plasma sintered at 1550 °C for 4 min under an applied pressure of 40 MPa.

When the fracture toughness values of hexagonal boron carbide samples with different Ti content is examined, it can be concluded that the highest fracture toughness is attained in 10 vol. % Ti-LP added sample as 6.25 MPa·m^{1/2} in the center and 6.51 MPa·m^{1/2} as an edge average. All Ti additions with different contents resulted in higher fracture toughness values compared to monolithic boron carbide ceramics. The main reason for the increase in toughness is linked to the different thermal expansion coefficients between B₄C and TiB₂ (TiB₂: 8.7x10⁻⁶ K⁻¹; B₄C: 5.7x10⁻⁶ K⁻¹) by Skorokhod et al [140,146]. During the cooling stage from sintering temperature to room temperature, TiB₂ particles shrink more than boron carbide matrix, resulting in a tensile stress at the interface. As a result of these stresses, the microfractures formed at the interface provide the increase of toughness by stopping the crack progression in the matrix or by changing the direction of the crack.

The reason for the decrease in the samples with higher Ti contents, like 15 and 20 vol. % Ti-LP, is again described in the same studies of Skorokhod [140,146]. TiB₂ reaches to critical grain size and when TiB₂ particles exceeds the critical grain sizes, the positive effect of TiB₂ addition on the fracture toughness is also disappears. This is

also evidenced by the decrease of fracture toughness in the samples with 15 and 20 vol. % Ti-LP content.

Ti-SP addition

The edge, edge average and center hardness values of hexagonal boron carbide with 5, and 10 vol. % Ti-SP addition is shown in Figure 6.31. Boron carbide samples with different amounts of metallic Ti-SP additive were heated with 100 °C/min and spark plasma sintered at 1550 °C for 4 or 6 min under 40 MPa pressures in vacuum atmosphere.

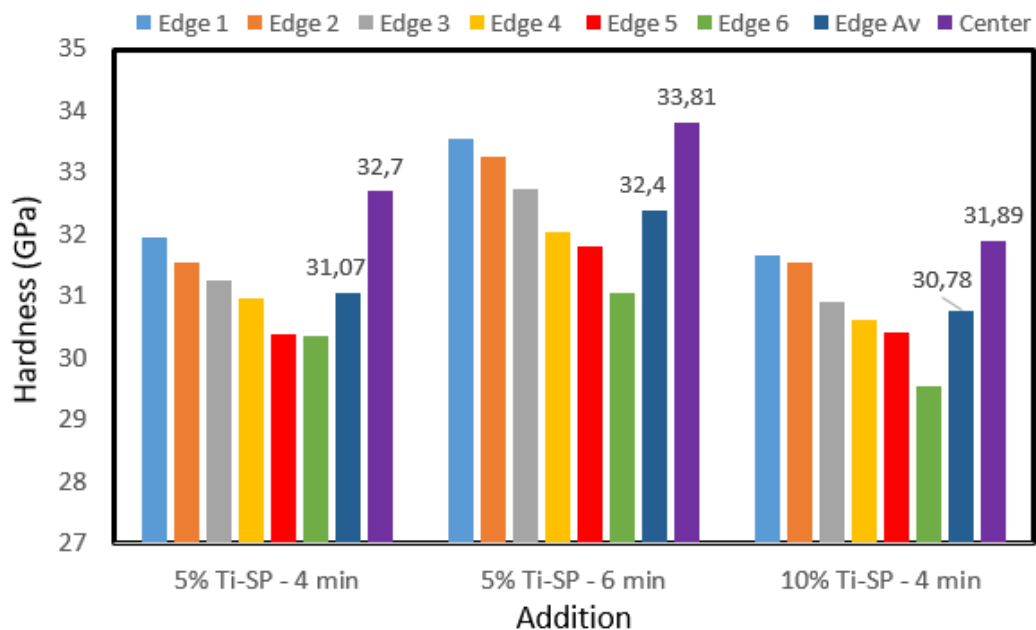


Figure 6.31 : Vickers hardness values of 5 and 10 vol. % Ti-SP added hexagonal boron carbide ceramics which were spark plasma sintered at 1550 °C for 4 or 6 min under an applied pressure of 40 MPa.

It can clearly be observed from Figure 6.31 that with increasing Ti-SP amount from 5 to 10 vol. %, the hardness value for both center and edges are decreased. For instance, the center hardness value of 5 vol. % Ti-SP is found out to be 32.7 GPa and the average edge hardness is measured 31.07 GPa, whereas the center hardness of 10 vol. % Ti-SP were 31.89 and the average hardness was measured 30.78 GPa. Furthermore, in all samples with different Ti-SP contents, hardness values are higher than the edge hardness and edge regions exhibited lower hardness values compared to center of the sample.

Furthermore, in order to overcome the different density values in edge and center, soaking time is enhanced from 4 min to 6 min and sintering homogenization is tried to

be achieved. It is seen that the homogenization in sintering did not reflect to hardness values and the edges and center of the sample which was spark plasma sintered for 6 min showed higher differences in hardness values. However, it can be concluded that with increasing soaking time, hardness values of both center and the edges tend to increase. The relative density values of 5 and 10 vol. % Ti-SP containing samples which were heated with 100 °C/min and spark plasma sintered at 1550 °C for 4 min under a pressure of 40 MPa in vacuum atmosphere was compared with hardness and fracture toughness in Table 6.10.

Table 6.10 : The relative density, hardness and fracture toughness values of 5 and 10 vol. % Ti-SP added hexagonal B₄C ceramics spark plasma sintered at 1550 °C for 4 or 6 min under 40 MPa pressure according to their measurement regions.

Process Variables	Measurement Area	Relative Density (%)	Hardness (GPa)	Fracture Toughness (MPa·m ^{1/2})
5 vol. % Ti- SP 4 min	Edge 1	98.92	31.95±0.20	6.05±0.04
	Edge 2	98.84	31.55±0.25	6.35±0.08
	Edge 3	98.36	31.26±0.18	6.55±0.09
	Edge 4	98.25	30.96±0.20	6.72±0.07
	Edge 5	97.90	30.40±0.26	6.99±0.12
	Edge 6	97.23	30.35±0.24	6.99±0.17
	Edge Av	98.25	31.07	6.60
5 vol. % Ti- SP 6 min	Center	99.40	32.70±0.22	6.31±0.13
	Edge 1	100	33.54±0.20	4.65±0.08
	Edge 2	99.67	33.26±0.19	5.24±0.09
	Edge 3	99.61	32.75±0.27	4.85±0.16
	Edge 4	99.27	32.05±0.25	5.21±0.12
	Edge 5	99.13	31.80±0.16	5.32±0.10
	Edge 6	98.62	31.05±0.24	5.75±0.04
10 vol. % Ti- SP 4 min	Edge Av	99.38	32.40	5.17
	Center	100	33.81±0.21	5.27±0.10
	Edge 1	99.4	31.68±0.25	5.75±0.05
	Edge 2	98.92	31.55±0.26	5.28±0.08
	Edge 3	98.86	30.91±0.20	6.13±0.08
	Edge 4	98.80	30.62±0.18	6.46±0.12
	Edge 5	98.63	30.41±0.20	6.74±0.13
10 vol. % Ti- SP 4 min	Edge 6	98.23	29.56±0.26	6.42±0.10
	Edge Av	98.80	30.78	6.13
	Center	99.90	31.89±0.24	6.54±0.09

When Ti-LP and Ti-SP containing hexagonal boron carbide samples are considered, a slight increase in hardness can take attention in the sample with small Ti particles. However, the fracture toughness change was more remarkable. The boron carbide sample with 5 vol. % Ti-LP showed 4.86 MPa·m^{1/2} in the center region, whereas 5 vol.

% Ti-SP containing sample which was manufactured in the same conditions showed $6.31 \text{ MPa}\cdot\text{m}^{1/2}$ fracture toughness. Same situation is observed in 10 vol. % Ti containing samples as well. The boron carbide sample with 10 vol. % Ti-LP resulted in $6.25 \text{ MPa}\cdot\text{m}^{1/2}$ in the center region, whereas 10 vol. % Ti-SP containing sample which was manufactured in the same conditions showed $6.54 \text{ MPa}\cdot\text{m}^{1/2}$ fracture toughness. Between all fracture toughness values in this thesis, the highest fracture toughness belongs to this sample with $6.54 \text{ MPa}\cdot\text{m}^{1/2}$ value.

Figure 6.32 demonstrates the fracture toughness values of 5 and 10 vol. % Ti-SP containing boron carbide samples which were heated with $100 \text{ }^\circ\text{C}/\text{min}$ and spark plasma sintered at $1550 \text{ }^\circ\text{C}$ for 4 or 6 min under an applied pressure of 40 MPa in vacuum atmosphere.

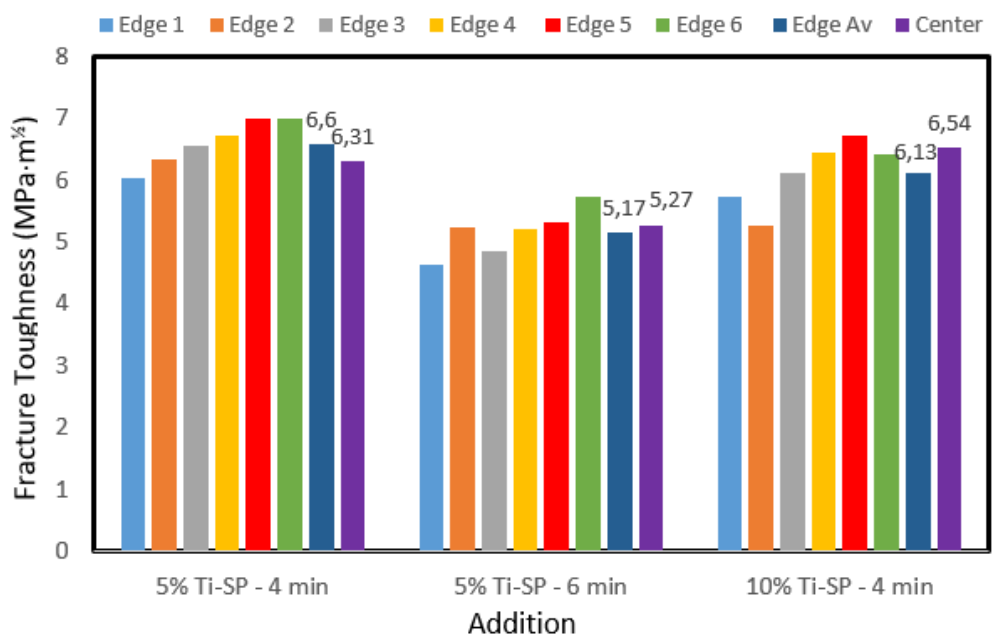


Figure 6.32 : Fracture toughness values of 5 and 10 vol. % Ti-SP added hexagonal boron carbide ceramics which were spark plasma sintered at $1550 \text{ }^\circ\text{C}$ for 4 or 6 min under an applied pressure of 40 MPa.

As can be seen from Figure 6.23, increase in soaking time of 5 vol. % Ti-SP containing sample resulted in a decrease in fracture toughness values and found out to be inversely proportional to hardness and relative density. Although in Ti-LP containing samples, a generalization can be done, Ti-SP added hexagonal boron carbide samples cannot be generalized in terms of edge and center fracture toughness values. In general, the edge values tend to be higher than the center values, however in 10 vol. % Ti-SP containing sample showed higher fracture toughness value in center compared to its edge average.

This is probably related to the critical grain size in center and the edge, as above explained by benefiting the study of Skorokhod et al [140,146].

TiO₂ addition

The edge, edge average and center hardness values of hexagonal boron carbide with 5 and 10 vol. % TiO₂ addition can be seen in Figure 6.33. Boron carbide samples with different amounts of TiO₂ additive were heated with 100 °C/min and spark plasma sintered at 1550 °C for 4 or 6 min under 40 MPa pressures in vacuum atmosphere.

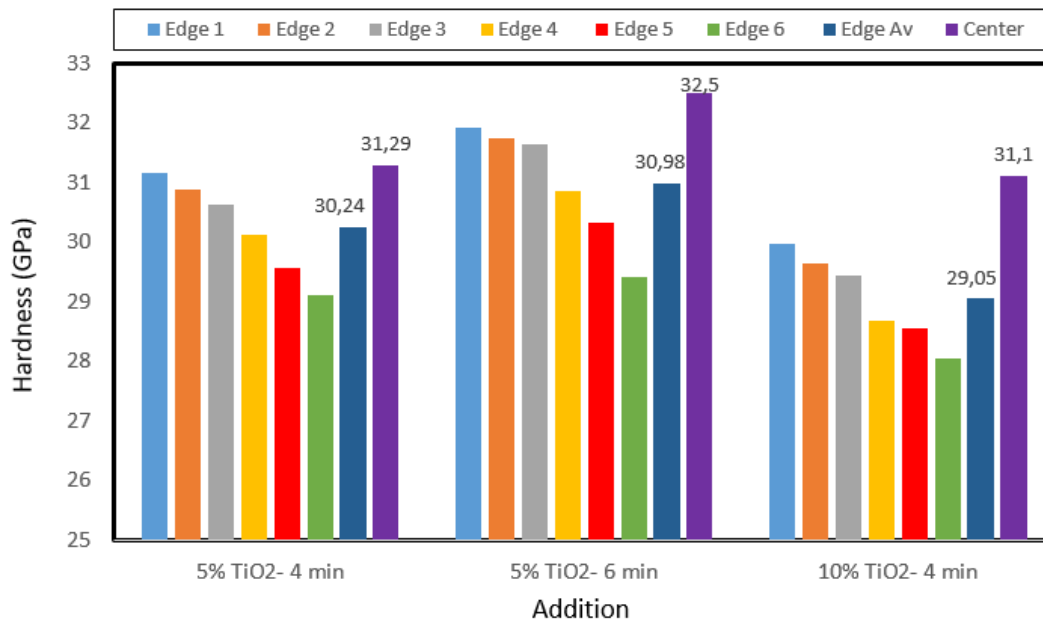


Figure 6.33 : Vickers hardness values of 5 and 10 vol. % TiO₂ added hexagonal boron carbide ceramics which were spark plasma sintered at 1550 °C for 4 or 6 min under an applied pressure of 40 MPa.

Figure 6.33 shows that with increasing TiO₂ amount in hexagonal boron carbide structure, the hardness values in both center and edge is decreased. This situation is also explained by Wang et al [145] as the increase of TiO₂ content results in a decrease in Hv due to the lower hardness of the reaction product, TiB₂, than that of B₄C and the rule of mixtures. Again in a sample, hardness values in center were found out to be higher than that of edge values. With increasing TiO₂ content, the difference between the edges and center is rised in terms of hardness.

If the hardness values attained in 5 vol. % Ti-LP, Ti-SP and TiO₂ which were spark plasma sintered at 1550 °C for 4 min under a pressure of 40 MPa are compared, Ti can be regarded as more beneficial for increasing the hardness of boron carbide. In all samples, the center hardness values are found out to be higher that of the edges. The

hardness values increased to 32.70 GPa from 32.23 GPa by using Ti powders with smaller particle size. However reaction sintering of TiO₂ and C remained low and 5 vol. % TiO₂ added boron carbide possessed 31.29 GPa hardness in its center region.

The relationship between relative density, hardness and fracture toughness obtained in TiO₂ added hexagonal boron carbide composites can be seen in Table 6.11.

Table 6.11 : The relative density, hardness and fracture toughness values of 5 and 10 vol. % TiO₂ added hexagonal B₄C ceramics spark plasma sintered at 1550 °C for 4 or 6 min under 40 MPa pressure according to their measurement regions.

Process Variables	Measurement Area	Relative Density (%)	Hardness (GPa)	Fracture Toughness (MPa·m ^{1/2})
5 vol. % TiO ₂ 4 min	Edge 1	96.67	31.15±0.19	5.62±0.06
	Edge 2	96.21	30.88±0.16	5.86±0.06
	Edge 3	96.03	30.62±0.22	6.06±0.04
	Edge 4	95.82	30.12±0.25	6.49±0.08
	Edge 5	95.40	29.56±0.18	6.72±0.10
	Edge 6	95.40	29.11±0.19	6.85±0.11
	Edge Av	95.92	30.24	6.26
	Center	96.51	31.29±0.18	5.99±0.08
5 vol. % TiO ₂ 6 min	Edge 1	98.66	31.92±0.22	5.38±0.07
	Edge 2	98.39	31.75±0.26	5.76±0.06
	Edge 3	98.28	31.65±0.24	5.96±0.09
	Edge 4	98.21	30.85±0.20	6.37±0.09
	Edge 5	98.11	30.33±0.20	6.68±0.12
	Edge 6	97.88	29.42±0.18	6.27±0.11
	Edge Av	98.25	30.98	6.07
	Center	98.62	32.50±0.20	5.88±0.06
10 vol. % TiO ₂ 4 min	Edge 1	96.07	29.96±0.25	5.65±0.09
	Edge 2	95.67	29.65±0.23	5.92±0.09
	Edge 3	95.61	29.45±0.22	6.16±0.13
	Edge 4	95.21	28.68±0.20	6.34±0.10
	Edge 5	95.03	28.55±0.25	6.89±0.06
	Edge 6	94.84	28.06±0.25	6.61±0.11
	Edge Av	95.40	29.05	6.26
Center	96.21	31.10±0.22	6.03±0.09	

Furthermore, when 5 vol. % TiO₂ added samples are considered, one can see that there is an obvious correlation between the hardness and porosity. The regions with lower relative density values showed lower hardness values. Moshtaghioun et al. reported that the hardness mechanism is to be controlled by dislocation motion, because dislocation activity is reported to occur in this material under mechanical load [183,184]. In addition, they also mentioned that they found relatively lower hardness values in the samples with lower density and concluded that hardness was less

influenced by the grain size rather than the porosity level. Thus, the samples with the density lower than theoretical density do not follow the well-known Hall–Petch relationship and the lower hardness resulted from porous regions providing no resistance to applied load [183].

Also, increment in soaking time from 4 min to 6 min in spark plasma sintered 5 vol. % TiO₂ containing boron carbide samples resulted in higher hardness values. This can also be explained by the findings of Moshtaghioun et al [183]. With improved densification, the hardness values increased.

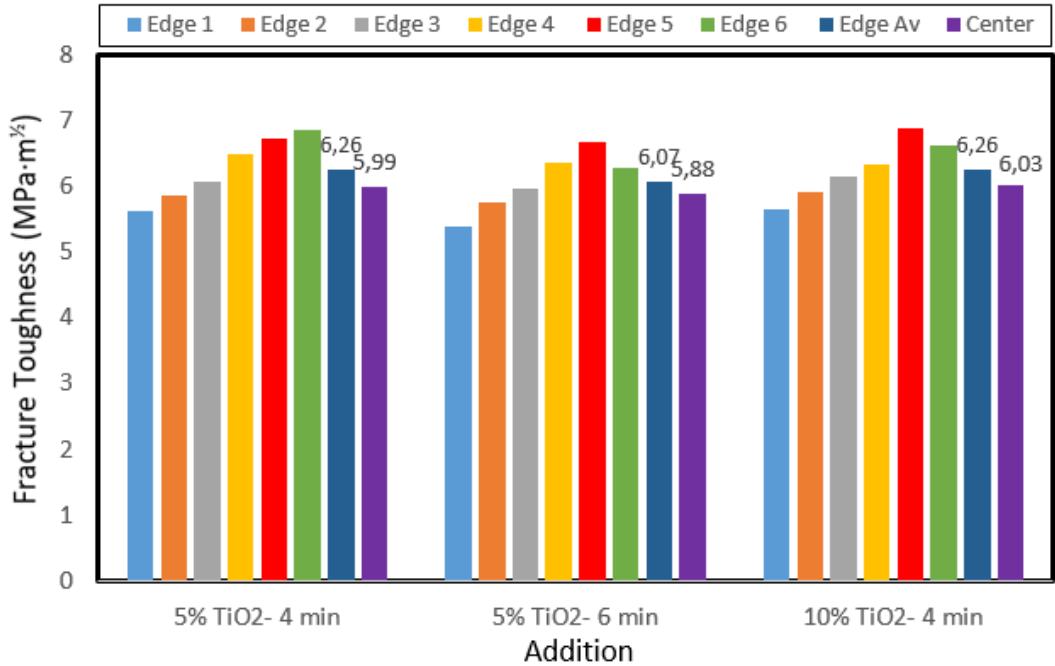


Figure 6.34 : Fracture toughness values of 5 and 10 vol. % TiO₂ added hexagonal boron carbide ceramics which were spark plasma sintered at 1550 °C for 4 or 6 min under an applied pressure of 40 MPa.

When the fracture toughness values attained in the center and edge regions of 5 and 10 vol. % TiO₂ added samples are analyzed, one can conclude that center regions showed lower fracture toughness values compared to edges. Because neither of the specimen can succeed in reaching teorethical density values in TiO₂ containing boron carbide, instead of smaller grain size, pores are seemed to be more effective to increase the fracture toughness. As Moshtaghioun et al [183] stated pores could behave as crack arrestors, contributing to increased fracture toughness.

Although in Ti-LP and Ti-SP 10 vol. % Ti addition resulted in higher fracture toughness values compared to 5 vol. % Ti content, in TiO₂ addition the results were

very close to each other and no distinct difference can be obtained. 10 vol. % TiO₂ added hexagonal boron carbide showed 6.03 MPa·m^{1/2} in its center, while 5 vol. % TiO₂ which were spark plasma sintered in exactly same conditions showed 5.99 MPa·m^{1/2} fracture toughness. However, increment in soaking time from 4 to 6 min in 5 vol. % TiO₂ added hexagonal boron carbide, which was spark plasma sintered at 1550 °C under a pressure of 40 MPa, affected the fracture toughness more negatively and resulted in a slight reduction and showed 5.88 MPa·m^{1/2} in the center of the sample.

6.4 Microstructural Investigations of Boron Carbide Ceramic Composites

6.4.1 Microstructural investigations of cylindrical boron carbide ceramics

Fracture surface microstructure studies of the monolithic boron carbide ceramics and 2 vol. % C- black or CNT added boron carbide samples with cylindrical geometry produced by spark plasma sintering method were carried out using JEOL JSM 7000F brand field emission scanning electron microscope (SEM). The microstructures of monolithic boron carbide ceramics which were heated with 150 °C/min and spark plasma sintered at 1650 and 1725 °C for 5 min under an applied pressure of 40 MPa in vacuum atmosphere is given in Figure 6.35.

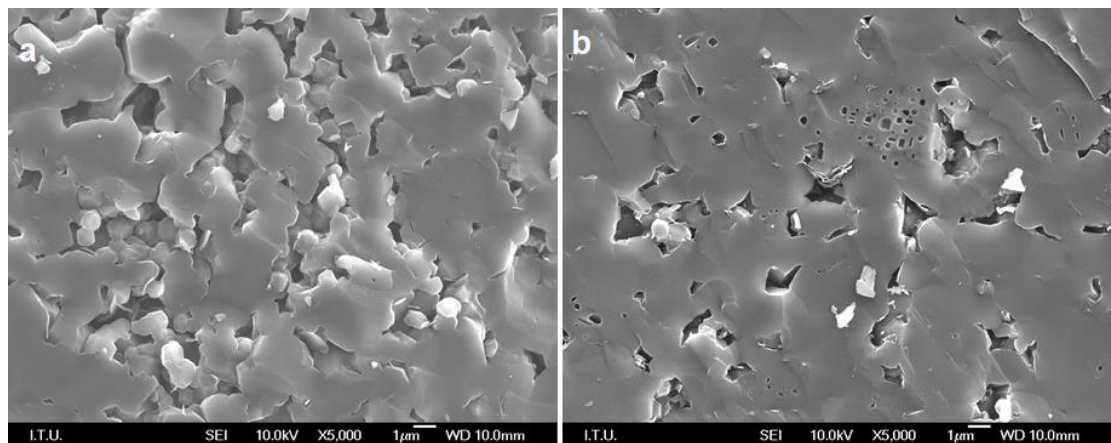


Figure 6.35 : SEM micrographs of fracture surfaces of monolithic boron carbide ceramics spark plasma sintered at: (a) 1650 °C; (b) 1725 °C for 5 min under a pressure of 40 MPa in vacuum atmosphere.

Increasing sintering temperature resulted in better densification, as expected. However, still enclosed pores is remained in the microstructure as can be seen in Figure 6.26 (b). Here, the emphasize should be given to the possibility to sinter boron

carbide in such low temperatures compared to conventional techniques such as hot pressing or pressureless sintering.

Moshtaghioun et al tried to decide upon whether heating or electric current is the main factor controlling enhanced sintering in spark plasma sintering technique [183]. Then, they sintered boron carbide ceramics by using hot pressing in same temperatures and in same conditions. As a result, no sintering is obtained at the temperatures such as 1700 °C. Accordingly, they concluded that, besides the applied temperature, the mechanism which promotes sintering during spark plasma sintering is rather complex. According to them, not just one of the below but all of them is responsible factors for controlling the efficiency of sintering and grain growth. Joule heating, local plasma current-induced processes at the grain boundaries, pulsed electric field effects or overheating produce by non-linear dependence of conductivity could be responsible for this [183].

The microstructures of boron carbide with 2 vol. % C-black which were heated with 150 °C/min and spark plasma sintered at 1650 and 1725 °C for 5 min under an applied pressure of 40 MPa in vacuum atmosphere is given in Figure 6.36.

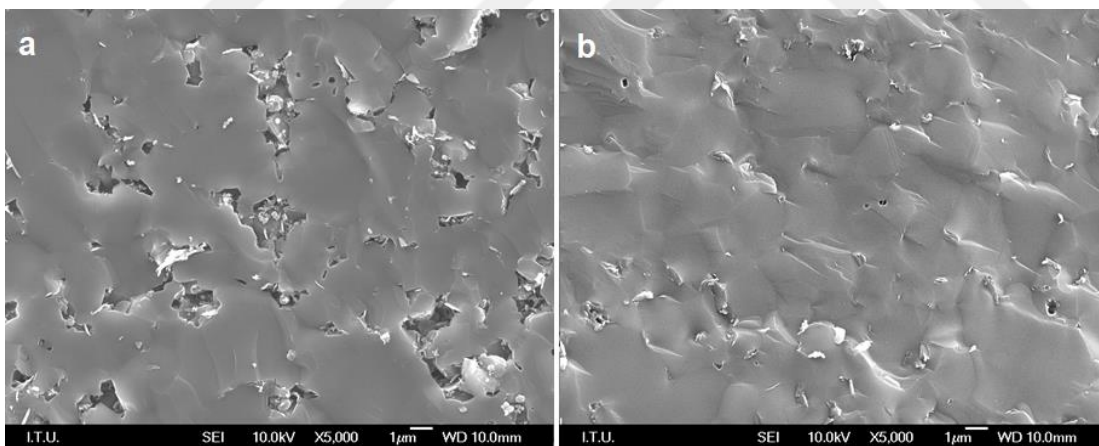


Figure 6.36 : SEM micrographs of fracture surfaces of boron carbide with 2 vol. % C-black spark plasma sintered at: (a) 1650 °C; (b) 1725 °C for 5 min under a pressure of 40 MPa in vacuum atmosphere.

If the microstructures seen in Figure 6.36 is analyzed, the positive effect of increasing temperature on the densification can be seen clearly. Also, when compared with monolithic boron carbide samples which were spark plasma sintered in the same conditions, C-black addition can be regarded as beneficial for promoting the densification of boron carbide.

In addition, the fracture surface of these completely dense samples shows predominantly mixed brittle fracture modes: transcrystalline and intercrystalline mechanisms (Figure 6.27-b), but mostly transcrystalline (transgranular) mechanisms in sample which were spark plasma sintered at higher temperatures. Moshtaghioun linked the fracture mechanism change to the grain sizes. Larger grained samples tend to form transcrystalline (transgranular) fracture mechanisms while smaller particles tend to have more intercrystalline mechanisms [183].

The microstructural investigation of boron carbide with 2 vol. % CNT addition which were heated with 150 °C/min and spark plasma sintered at 1650 and 1725 °C for 5 min under an applied pressure of 40 MPa in vacuum atmosphere is demonstrated in Figure 6.37.

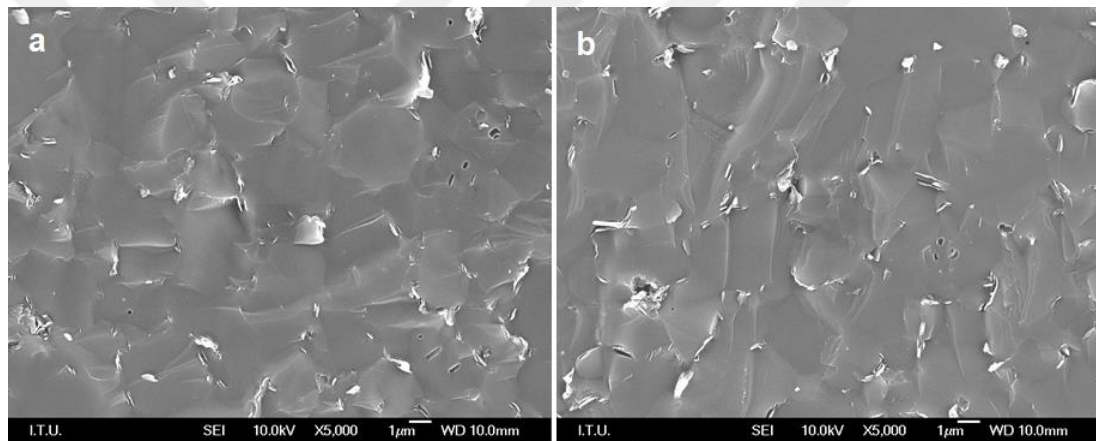


Figure 6.37 : SEM micrographs of fracture surfaces of boron carbide with 2 vol. % CNT spark plasma sintered at: (a) 1650 °C; (b) 1725 °C for 5 min under a pressure of 40 MPa in vacuum atmosphere.

As can be seen from Figure 6.28, the micrographs illustrate the trend of increasing density with the addition of CNT and increasing spark plasma sintering temperature. Almost all of the enclosed pores in the monolithic boron carbide structure has been successfully removed with 2 vol. % CNT addition. Again in CNT added sample, predominantly mixed brittle fracture modes: transcrystalline and intercrystalline mechanisms are observed.

In this study, composites containing 2 vol.% CNT, the CNTs are homogeneously dispersed but not fibrous. In the literature, in composites containing 2 and 3 wt. % CNT, there are studies which show a fibrous structure of the CNTs clearly visible. This fibrous structure of CNTs has the effect of increasing fracture toughness by bridging between cracks [116,180].

6.4.2 Microstructural investigations of hexagonal boron carbide ceramic composites

6.4.2.1 Microstructural investigations of hexagonal monolithic boron carbide ceramics

The microstructural investigations of hexagonal boron carbide ceramics are carried out for the center and one edge of the sample. The edge which subjected to SEM studies was tried to be chosen as having the most different characteristics in terms of densification, hardness and fracture toughness. Figure 6.38 shows microstructures of the center and edge of the hexagonal monolithic boron carbide sample which was heated with 100 °C/min and spark plasma sintered at 1550 °C for 4 min under an applied pressure of 40 MPa in vacuum atmosphere.

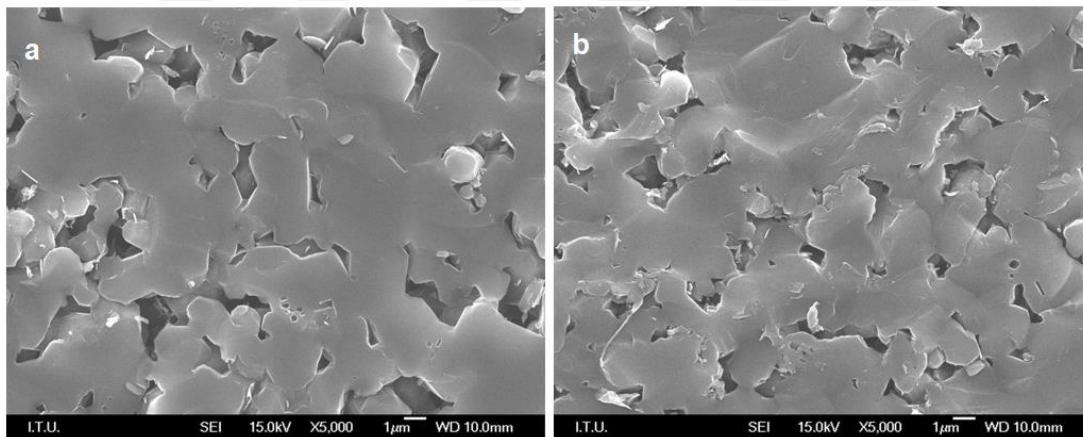


Figure 6.38: SEM fracture surface micrographs of (a) center (b) edge region of hexagonal monolithic boron carbide spark plasma sintered at 1550 °C for 4 min under a pressure of 40 MPa in vacuum atmosphere.

According to Figure 6.38, not a very significant difference between the edge and center of the monolithic boron carbide can be obtained. The edge density was measured to be 93.90 %, whereas the relative density of center was found out to be 95.34 % in this sample. However, it is possible to say that the grains were smaller in the edge of the hexagonal boron carbide sample.

Although no significant differences could be observed in this study in terms of microstructure, Klotz et al [137] showed a very different microstructures in monolithic boron carbide samples which was produced by the plasma pressure compaction which is another name of spark plasma sintering. They manufactured samples in cylindrical shapes with 25.4 mm in diameter and they obtained a rather porous area in the bottom

of the sample compared to the top of the sample. They related the density differences to the nonuniform temperatures in the die assembly itself. They reported that due to friction between the punches and the inner die walls as pressure is applied, one punch can sometimes push further into the die than the other. Observations of temperature gradients across the die during consolidation runs using an optical pyrometer showed that when a punch was inserted more on one side of the die, that region experienced a lower temperature. The side of the consolidated sample in this region, showed a greater amount of porosity and a lower overall density when examined by microscopy [137]. In our study, no difference in any sample of hexagonal shaped boron carbide is attained between the bottom and top of the sample. All of the samples were sintered by using the same die assembly and placed to the spark plasma sintering apparatus carefully. Also, all of the powders are placed in the dies concerning the die positions and the powders were poured according to these.

Furthermore, Klotz et al sintered iron and tungsten powders which are electrically conductive materials and they did not observe any density gradients in their samples. However, boron carbide is a semiconductor and has been affected from the problems seen in die assembly more compared to conductive powders due to the current pathway followed in boron carbide sample. A greater amount of the applied current is flowing through the graphite die as opposed to the powder, in the powders such as boron carbide. Also, they stated that the densification gradients can be removed by the additions of sintering aids such as Al_2O_3 , graphite or TiB_2 to the boron carbide [137].

In addition, Sairam et al investigated the microstructures of spark plasma sintered monolithic boron carbide ceramics processed in similar temperatures [185]. However they produced a final product with 17 mm. They reported that they observed locally melted structures at the contact point between the particles, which is a direct evidence for the dominance of Joules heating effect during spark plasma sintering. Also, the open porosities and the neck-like regions between particles in lower temperatures such as $1400\text{ }^\circ\text{C}$ showed the densification process that comprises the first stage of sintering. While in higher temperatures like $1600\text{ }^\circ\text{C}$, discrete densified regions bounded with interconnected porosities is observed. Joules heating results in rapid rise in temperatures at localized regions that would contribute towards the formation of dense regions. This fact represents the methodology of densification process in spark plasma

sintering [185]. In this study, the densification is observed to be homogeneous and no discrete densified regions is seen.

6.4.2.2 Microstructural investigations of hexagonal boron carbide ceramic composites with different C sources

Figure 6.39 shows microstructures of the center and edge of the hexagonal boron carbide with 2vol. % C-black which was heated with 100 °C/min and spark plasma sintered at 1550 °C for 4 min under an applied pressure of 40 MPa in vacuum atmosphere.

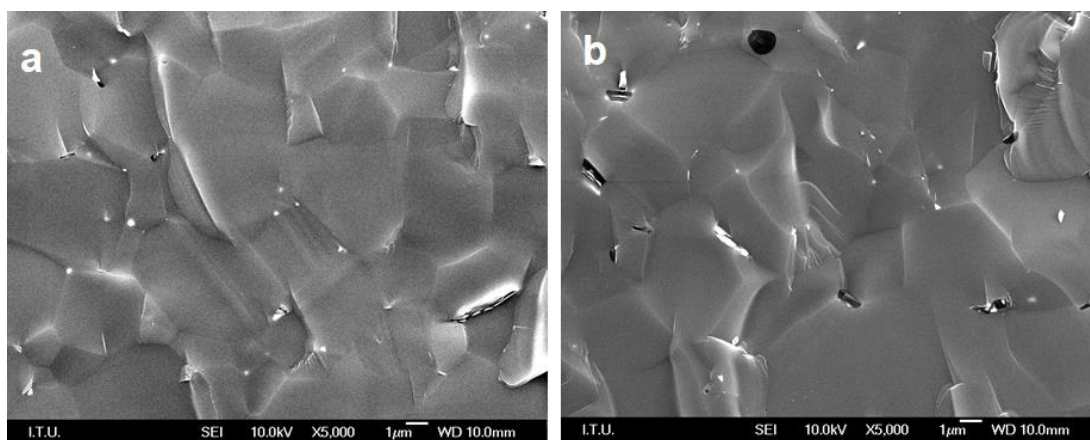


Figure 6.39 : SEM fracture surface micrographs of (a) center (b) edge region of hexagonal boron carbide with 2 vol. % C-black spark plasma sintered at 1550 °C for 4 min under a pressure of 40 MPa in vacuum atmosphere.

As can be seen from Figure 6.39, C-black addition to boron carbide structure resulted in a dense microstructure even in such lower spark plasma sintering temperatures like 1550 °C. As Suri et al mentioned in their review that addition of a small amount of carbon to B₄C plays an important role in eliminating the surface oxide layer, thereby achieving higher densities with fine grains and improved mechanical properties. However they also concluded that the quantity and the method of carbon addition have to be carefully chosen to avoid free carbon in the sintered body [17]. Because, with increasing carbon content, the unique characteristics of boron carbide starts to become ordinary. 2 vol. % C-black addition seem to be beneficial for promoting the densification of hexagonal boron carbide. Also, when the center and edge of the hexagonal boron carbide with 2 vol. % C-black addition is compared, it is obvious that the center showed a microstructure with less porosity, while pores between the grains remained in edge center of the hexagonal sample.

Figure 6.40 demonstrates the microstructures of the center and edge of the hexagonal boron carbide with 2 vol. % CNT which was heated with 100 °C/min and spark plasma sintered at 1550 °C for 4 min under an applied pressure of 40 MPa in vacuum atmosphere.

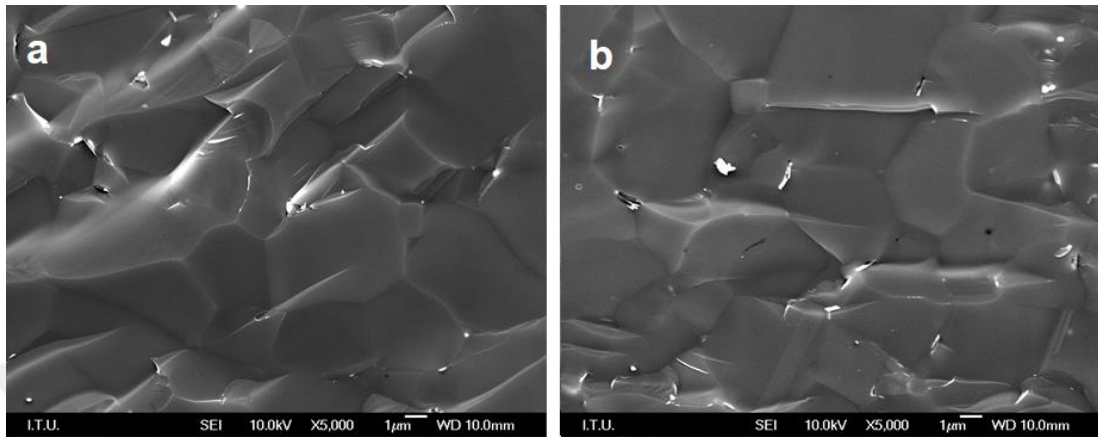


Figure 6.40 : SEM fracture surface micrographs of (a) center (b) edge region of hexagonal boron carbide with 2 vol. % CNT spark plasma sintered at 1550 °C for 4 min under a pressure of 40 MPa in vacuum atmosphere.

When the microstructures observed from the center and edge regions of boron carbide sample with 2 vol. % CNT are considered, it can be seen that dense microstructures are obtained compared to monolithic boron carbide which was spark plasma sintered exactly in same conditions. However, the grain sizes can not be comparable. As Wei et al reported in their study that multi-walled CNTs can be destroyed under the hot pressing or spark plasma sintering conditions [186]. In this study, 40 MPa pressure is applied to the boron carbide powder with 2 vol. % CNT and a portion of multi-walled CNT is probably destroyed however it is clear that the residual MWCNTs significantly affected the properties of boron carbide as in study of Wei et al [186]. Especially the promotion of densification is very clear. In addition, both C-black and CNT added boron carbide samples showed a transgranular fracture like monolithic boron carbide. It can be concluded that neither of these additions affected the fracture mode of B₄C.

6.4.2.3 Microstructural investigations of hexagonal boron carbide ceramic composites with light weight metallic additives

Al addition

Figure 6.41 gives the microstructural investigation of the center and edge of the hexagonal boron carbide with 5 vol. % Al which was heated with 100 °C/min and

spark plasma sintered at 1550 °C for 4 min under an applied pressure of 40 MPa in vacuum atmosphere. According to the microstructural observations seen in Figure 6.41, Al addition resulted in a denser microstructure compared to monolithic boron carbide which is spark plasma sintered at 100 °C higher temperatures. As parallel to relative density measurements, center regions of the hexagonal sample exhibited a microstructure with less porosity. It is known that combining the B₄C with a metal can mitigate the problems associated with brittleness. As Hulbert et al indicated that aluminium can be regarded as one of the most common used metal for this purpose because it is lightweight, readily available, cost-effective and wets B₄C well at elevated temperatures [134]. Accordingly, 5 vol. % Al addition did not just proved the spark plasma sintering temperature, but also resulted in improved mechanical properties.

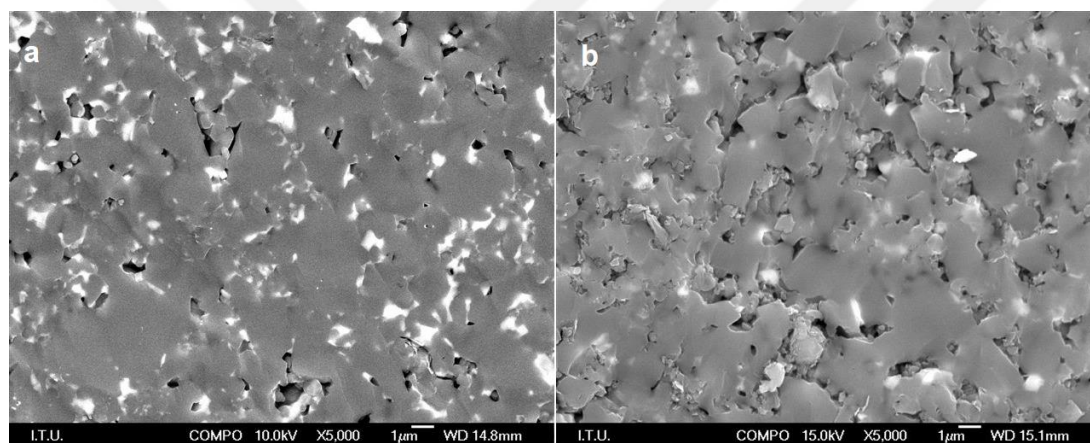


Figure 6.41 : SEM fracture surface micrographs of (a) edge (b) center region of hexagonal boron carbide with 5 vol. % Al spark plasma sintered at 1450 °C for 4 min under a pressure of 40 MPa in vacuum atmosphere.

According to EDS analysis, the gray areas in the microstructure is found out to be boron carbide, which also seen as the matrix of the sample in Figure 6.32. Furthermore, the white areas are investigated as Al-rich areas in EDS analysis. Aluminium forms binary and tertiary phases when in contact with B₄C such as Al₃BC, AlB₁₀ and Al₄C₃ which helps bond the metal to the carbide matrix and generally improve the mechanical properties [134]. According to the microstructures which can be seen in Figure 6.32, Al is dispersed in the boron carbide matrix homogeneously. Although Hulbert et al [187] mentioned that the presence of twins is very common in the fracture surface of the fully dense side of Al containing boron carbide sample, the reason for not observing any twins in these microstructures can be explained like the full densification could not been obtained in this study.

Si addition

Figure 6.42 demonstrates the microstructural observations of the center and the edge regions of 5 vol. % Si added hexagonal boron carbide samples which was heated with 100 °C/min and then spark plasma sintered at 1500 °C for 4 min under an applied pressure of 40 MPa in vacuum atmosphere.

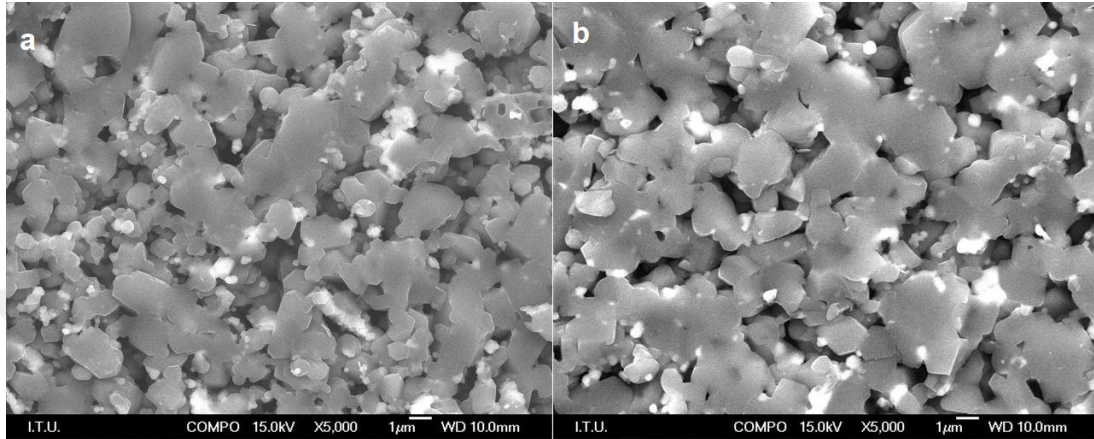


Figure 6.42 : SEM fracture surface micrographs of (a) center (b) edge region of hexagonal boron carbide with 5 vol. % Si spark plasma sintered at 1500 °C for 4 min under a pressure of 40 MPa in vacuum atmosphere.

According to Figure 6.42, it is obvious that the center region of the spark plasma sintered hexagonal boron carbide with 5 vol. % Si, showed lower porosity compared to the edge of the sample. However, it can be concluded that the desired densification could not be obtained in this sample. With the EDS analysis, it is proved that gray areas are boron carbide matrix, whereas white areas are SiC phase. Because the density of SiC is higher than that of boron carbide, these results are expected. SiC phases formed homogeneously in the boron carbide matrix. In the samples generated from B₄C and 5 vol. % Si starting powders, Si reacts with the free carbon present in B₄C above the melting temperature first and then forms B₁₂(B,C, Si)₃ by dissolving up to 2.5 % Si in B₄C structure [188]. SiC precipitate from this solid solution and the SiC amount is increased with increasing amounts of Si in the boron carbide. According to Ye et al, the grain refinement is presumably attributed to the resultant SiC, which can pin migrating grain boundaries and hence inhibiting the growth of B₄C grains. Their EDX analysis indicated the dissolution of Si in B₄C and its solid solubility increased from 1.38 to 1.8 at.% with increasing the amount of Si from 4 to 10 wt% [128].

Although B₄C, SiC₆ and SiC were expected to form in the structure according to literature [125], B₄C, SiC and carbon were found in the XRD analyzes. However, in

the XRD analyzes, $B_{12}(B,C,Si)_3$ phase coincides with B_4C peaks. When the carbon excess caused by graphite molds is taken into consideration, in excess carbon environment phases, only B_4C , SiC and C are obtained. However, the EDS analysis of the sample in the dark region shows that the B_4C matrix contains a small amount of Si dissolved in the dark matrix area. The Si content originates from Si displaceable by C in the B_4C matrix. Although the atomic radius is similar to B and C, Si enters the B_4C lattice and the lattice parameter changes and internal tension due to swelling in the lattice, causing the material to become brittle. However, since boron and carbon are light element, the quantitative values obtained from EDS analysis is not appropriate.

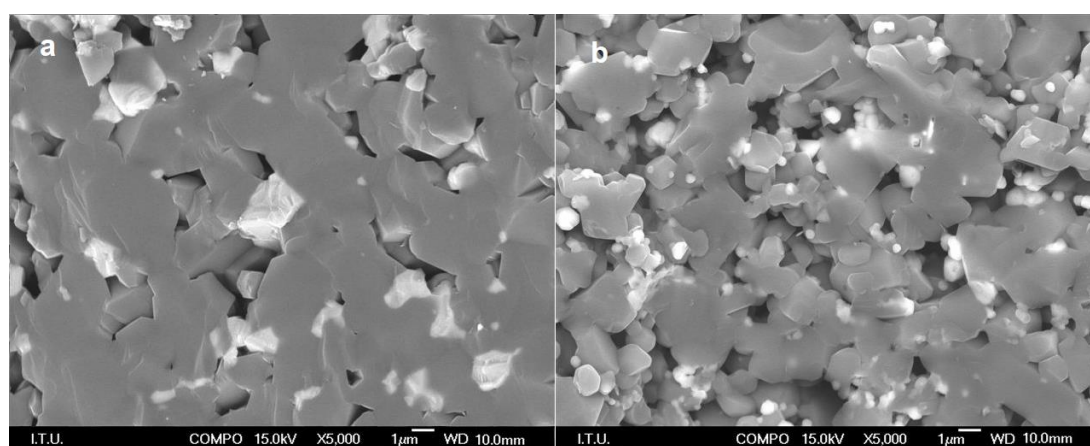


Figure 6.43 : SEM fracture surface micrographs of (a) center (b) edge region of hexagonal boron carbide with 5 vol. % Si spark plasma sintered at 1500 °C for 4 min under a pressure of 60 MPa in vacuum atmosphere.

Further experiments were applied in order to improve the densification of 5 vol. % Si added boron carbide. However, due to the sticking problems in higher temperatures, it is decided to increase the applied pressure. Figure 6.43 gives the microstructural observations of the center and the edge regions of 5 vol. % Si added hexagonal boron carbide samples which was heated with 100 °C/min and then spark plasma sintered at 1500 °C for 4 min under an applied pressure of 60 MPa in vacuum atmosphere. Increment in applied pressure from 40 to 60 MPa resulted in higher densification in 5 vol. % Si added boron carbide samples. Also, increase in pressure resulted in higher grained microstructure. Again in both center and edge of the hexagonal sample, SiC is dispersed homogeneously, however lower porosity structure is attained in the center of the hexagonal sample. SEM and EDS studies of samples obtained by spark plasma sintering of B_4C and 5 vol. % Si powders showed that Si is dissolved in the B_4C lattice, and $B_{12}(B,C,Si)_3$ structure is formed. The Si content in boron carbide activates

sintering by increasing the amount of liquid phase formed. Then, Si reacts with the carbon found in the mold structure, and the carbon bound to the B_4C . Si addition inhibits the movement of grain boundaries and also causes sintering to take place at lower temperatures. Also, the fracture mode in 5 vol. % Si-added structure is through the grain, in other words transgranular, although it was expected to be intergranular.

6.4.2.4 Microstructural investigations of hexagonal boron carbide ceramic composites with Ti and TiO_2 additives

Ti-LP addition

The study of Cengiz [118] explains the behavior of Ti in boron carbide structure very detailly. As it is known, in spark plasma sintering the microscopic electrical discharges in the gaps between the powder particles generate plasma (higher temperature areas) and causing sintering in lower temperatures [60,61]. Although the spark plasma sintering temperature was chosen to be $1550\text{ }^\circ\text{C}$, the actual temperature between the particles was above melting temperature of Ti during the sintering procedure.

Figure 6.44 demonstrates the behavior of Ti in B_4C microstructure. Figure 6.44 demonstrates that in the first stage of the spark plasma sintering, the metallic Ti particles were solid. However due to lower melting temperature ($T_{m,Ti}=1668\text{ }^\circ\text{C}$; $T_{m,B_4C}=2450$) compared to boron carbide phase, with increasing temperature Ti melts and surrounds the boron carbide grains.

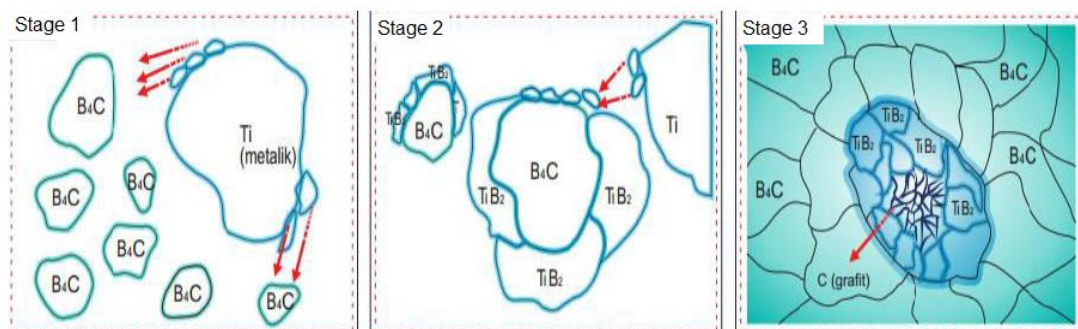


Figure 6.44 : The schematic demonstration of microstructural development occurred between Ti and B_4C during spark plasma sintering [118].

In Stage 2 of Figure 6.44, the formation of TiB_2 can be seen in consequence of the reaction between liquid Ti and B_4C . During the reaction, the boron is reduced, while free carbon come out. After the nucleation of Ti liquid phase in the boron carbide structure, the newly formed TiB_2 form granules of similar size to the B_4C grain size.

The process continues until the coarse-grained Ti melts and completely turns into small TiB_2 grains, resulting in agglomerate TiB_2 structure in which graphite is present in the center of TiB_2 clusters.

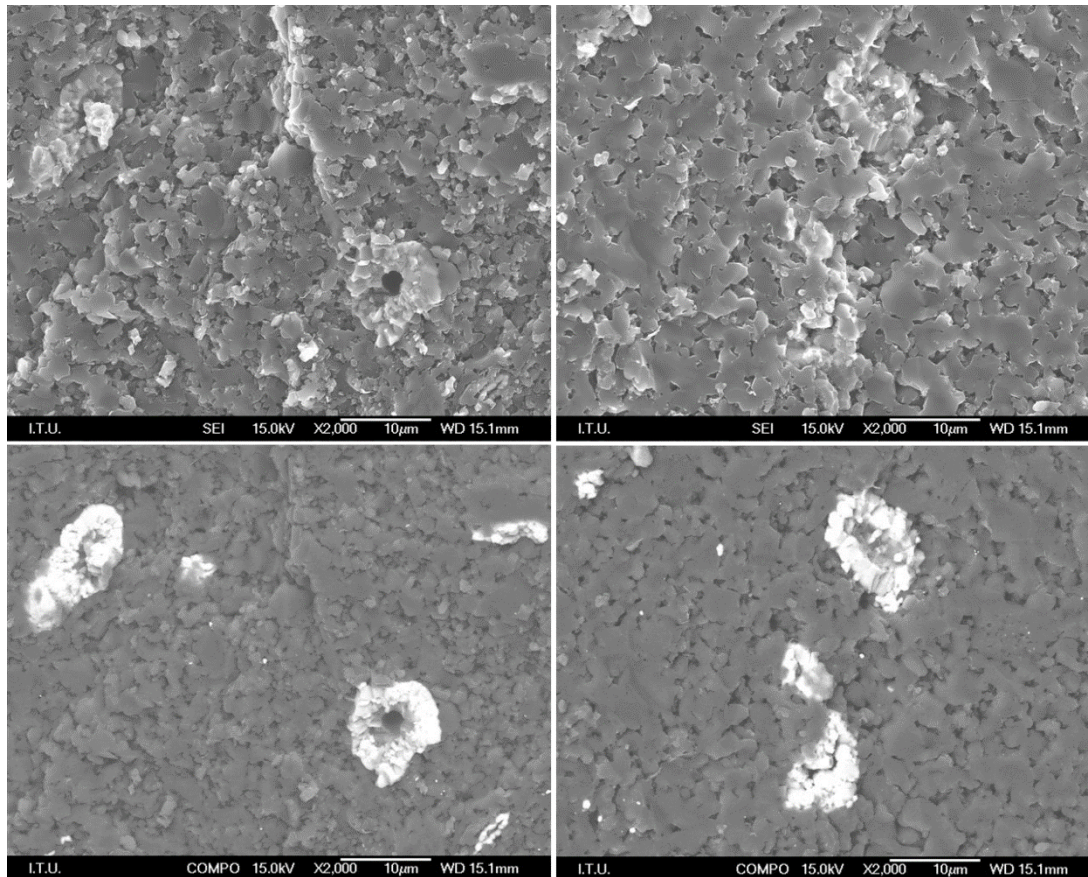


Figure 6.45 : (a) center, SEI; (b) edge, SEI; (c) center, COMPO; (d) edge, COMPO SEM fracture surface micrographs of hexagonal boron carbide with 5 vol. % Ti-LP spark plasma sintered at 1550 °C for 4 min under a pressure of 40 MPa.

Two different Ti powders which have different particle sizes were used in the Ti added boron carbide composites. Figure 6.45 gives the microstructural observations of 5 vol. % Ti-LP added boron carbide spark plasma sintered at 1550 °C for 4 min under an applied pressure of 40 MPa in vacuum atmosphere. In order to see the TiB_2 distribution in the structure, the microstructures reflecting wider areas are given. As can be seen from Figure 6.45, 5 vol. % Ti addition resulted in formation of white TiB_2 clusters, forming C in the center of agglomerates. The center of hexagonal boron carbide with 5 vol. % Ti showed a microstructure with lower porosity compared to the edge of the sample. Also, any grain growth due to large particle size of Ti starting powder is not observed.

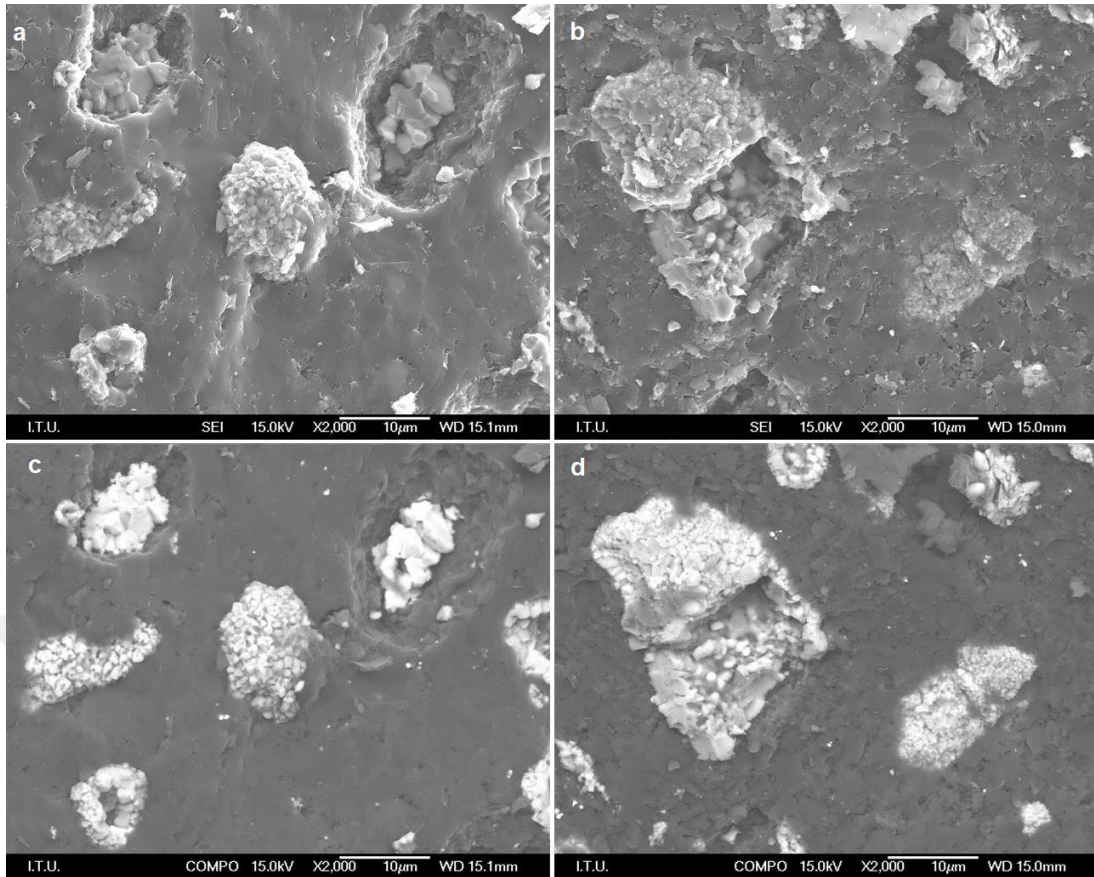


Figure 6.46 : (a) center, SEI; (b) edge, SEI; (c) center, COMPO; (d) edge, COMPO SEM fracture surface micrographs of hexagonal boron carbide with 10 vol. % Ti-LP spark plasma sintered at 1550 °C for 4 min under a pressure of 40 MPa.

Figure 6.46 demonstrates the microstructures of edge and center of hexagonal 10 vol. % Ti added boron carbide composites which was spark plasma sintered at 1550 °C for 4 min under a pressure of 40 MPa in vacuum. With increased Ti content, the white agglomerate amount seen in the microstructure increased and the densification is promoted. When compared with 5 vol. % Ti, microstructures with lower porosity is attained in 10 vol. % Ti containing sample. Again, the center of 10 vol. % Ti included boron carbide showed better densification compared to its edge. On the other hand, the newly formed TiB_2 grains were larger in 10 vol. % Ti added boron carbide compared to 5 vol. % Ti including sample.

Figure 6.47 demonstrates the 20 vol. % Ti-LP added boron carbide sample which was spark plasma sintered at 1550 °C for 4 min under an applied pressure of 40 MPa in vacuum atmosphere. To show a meaningful microstructure, the magnification is arranged to X1000.

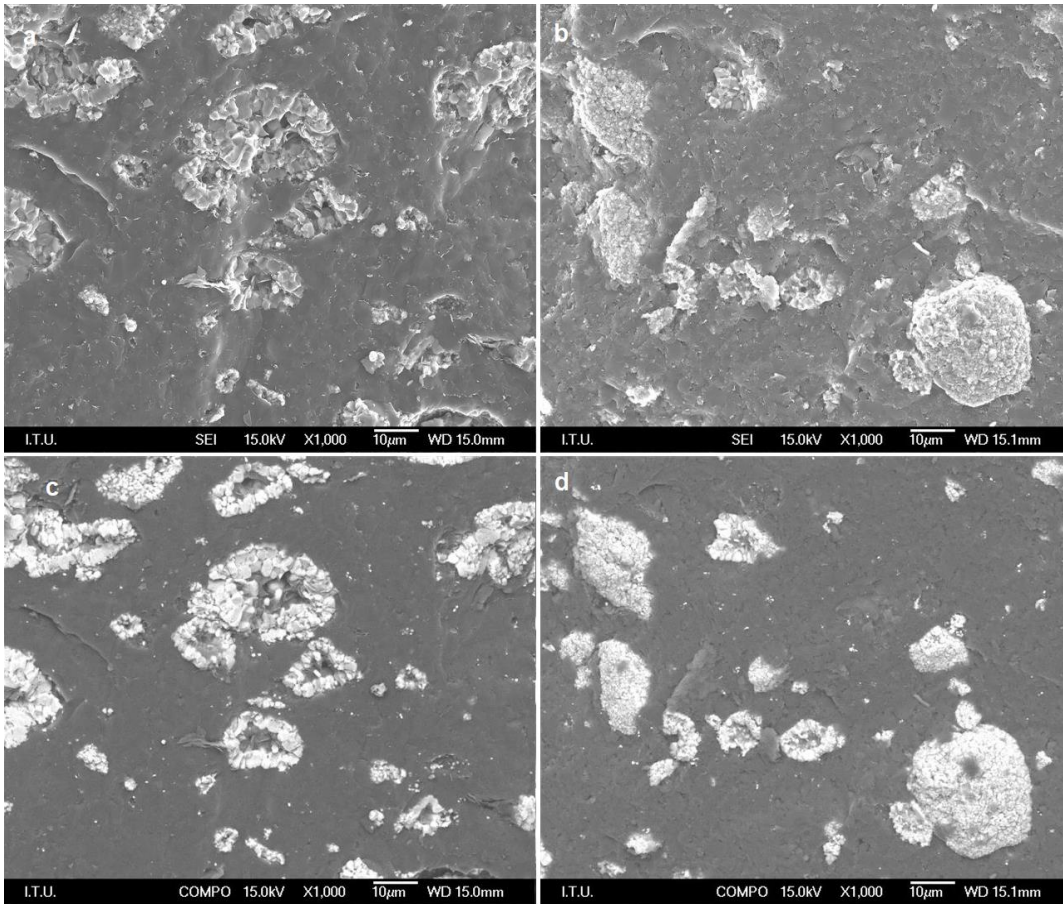


Figure 6.47 : (a) center, SEI; (b) edge, SEI; (c) center, COMPO; (d) edge, COMPO SEM fracture surface micrographs of hexagonal boron carbide with 5 vol. % Ti-SP spark plasma sintered at 1550 °C for 4 min under a pressure of 40 MPa..

When Figure 6.47 is analyzed, one can clearly see that the white phases which represents TiB_2 is increased in content, with increasing Ti amount in boron carbide structure. In addition, TiB_2 is again formed as clusters in the microstructure resulting free carbon in the center of the agglomerates. 20 vol. % Ti-LP included boron carbide showed both large and small agglomerates but one can conclude that with increasing Ti content, the agglomerate dimensions tend to get larger. Both edge and center of hexagonal boron carbide ceramic containing 20 vol. % Ti have homogenous distribution of agglomerates. Also, no significant difference in terms of porosity could be obtained when the edge and center of the spark plasma sintered hexagonal composite is compared.

Ti- SP addition

Figure 6.48 shows the edge and center of 5 vol. % Ti containing hexagonal boron carbide samples which were heated with 100 °C/min and spark plasma sintered at 1550

°C for 4 min under a pressure of 40 MPa. In order to see the TiB_2 distribution in the structure, the microstructures reflecting wider areas are given.

When the compositions seen in 5 vol %Ti- SP added boron carbide sample are investigated, a white, a grey and a black phase in the center of the white clusters can be seen clearly. When these samples are subjected to EDS analysis, the white phase is found out to be TiB_2 , whereas the grey area is boron carbide matrix, the darkest area at the center of the white cluster can be regarded as carbon.

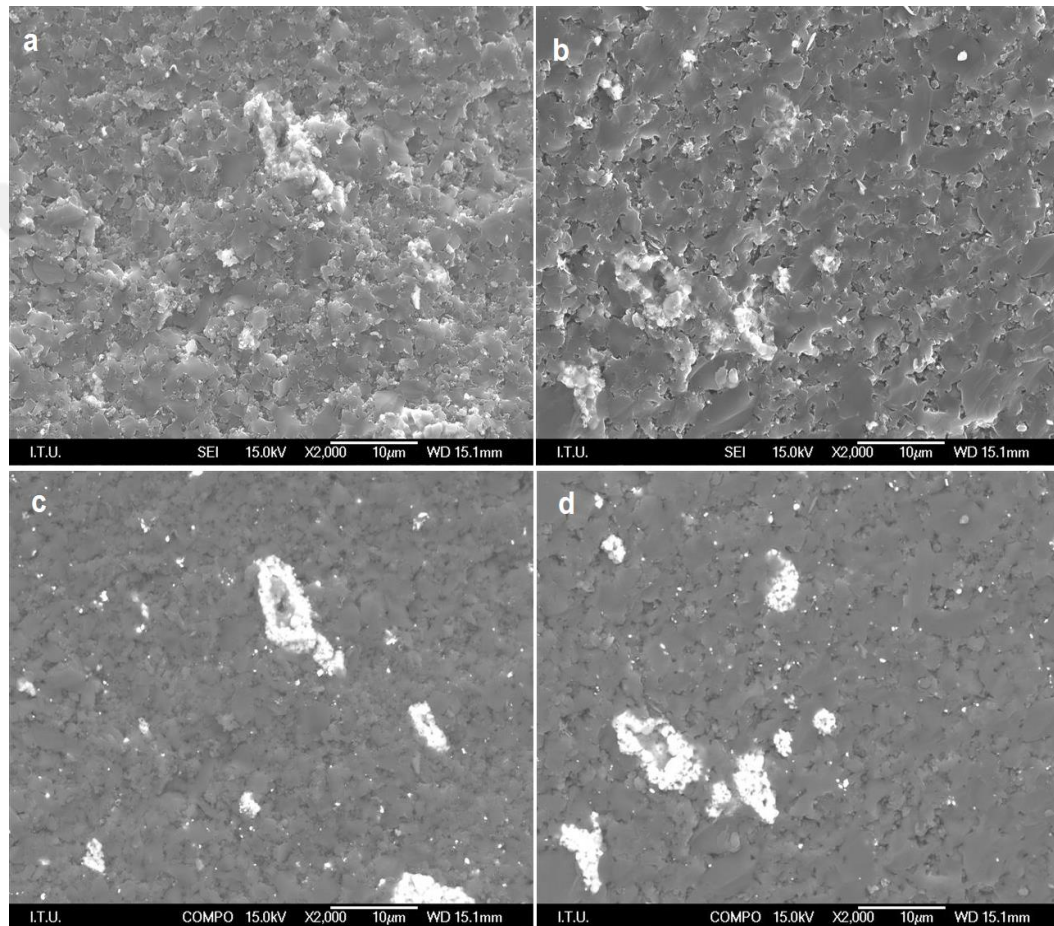
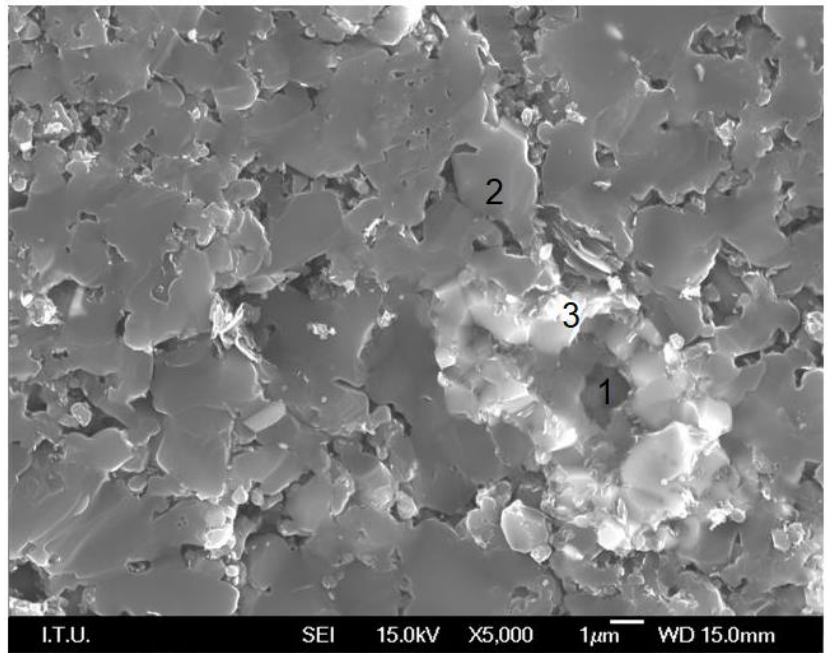
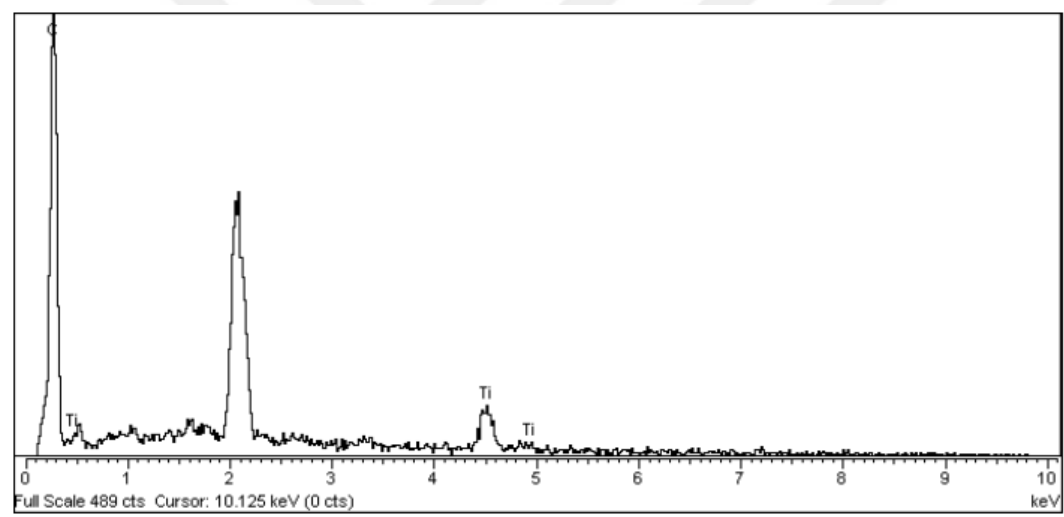


Figure 6.48: (a) center, SEI; (b) edge, SEI; (c) center, COMPO; (d) edge, COMPO SEM fracture surface micrographs of hexagonal boron carbide with 5 vol. % Ti-SP spark plasma sintered at 1550 °C for 4 min under a pressure of 40 MPa.

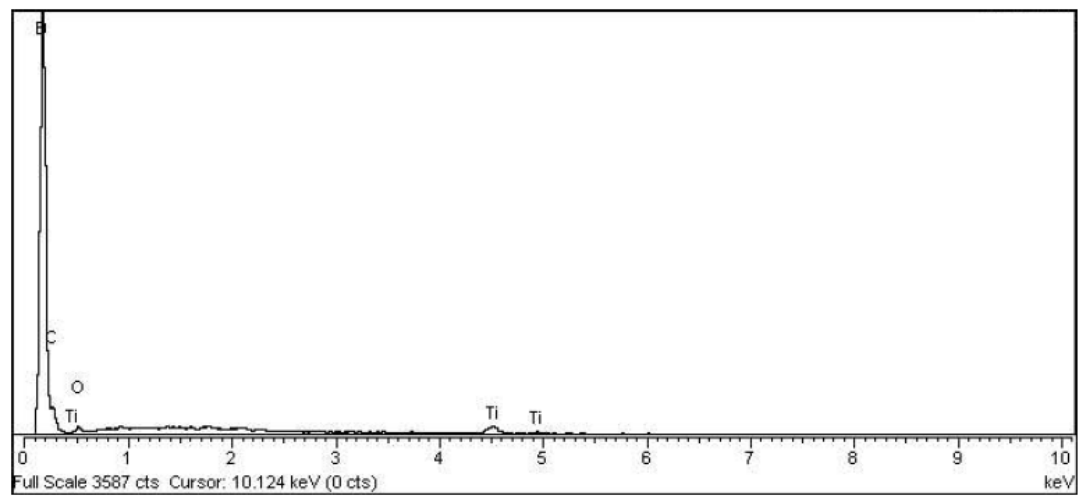
The detailed EDS analysis of an edge of 5 vol. % Ti-SP added boron carbide is given in Figure 6.49. The elemental analysis results are shown in EDS spectrums are detailed in Table 6.12.



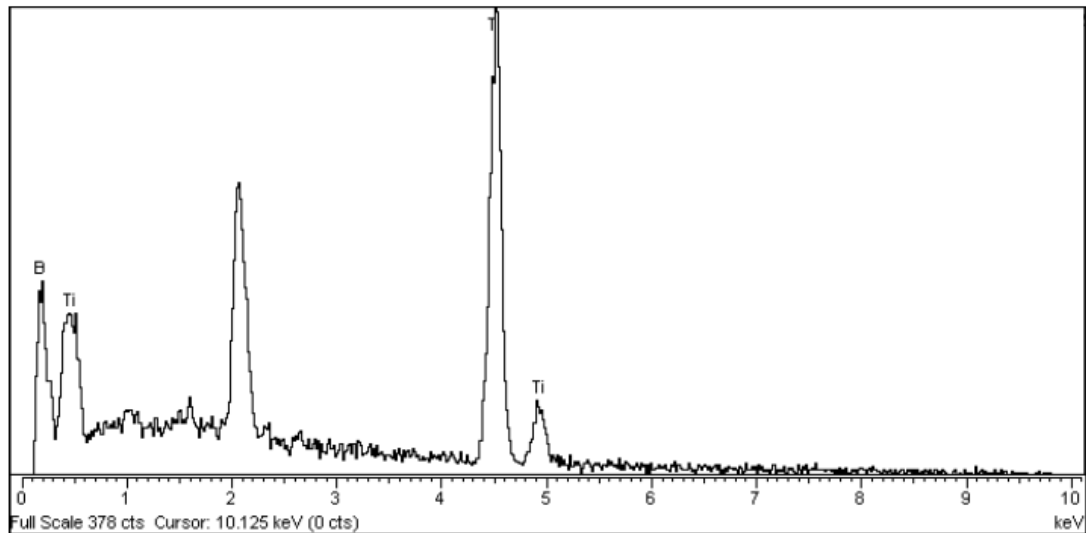
(a)



(b)



(c)



(d)

Figure 6.49 : The (a) SEM micrograph and (b) Region 1; (c) Region 2 and (d) Region 3 EDS analysis of 5 vol. % Ti-SP containing sample which was spark plasma sintered at 1550 °C for 4 min under a pressure of 40 MPa pressure.

Table 6.12 : EDS elemental analysis results of 5 vol. % Ti-SP containing sample which was spark plasma sintered at 1550 °C for 4 min under a pressure of 40 MPa.

Measurement Area	B	C	O	Ti	Total
Region 1	-	88.21	-	11.79	100.00
Region 2	78.33	16.60	1.60	7.55	100.00
Region 3	25.56	-	-	74.44	100.00

The center and edge of 5 vol. % Ti-SP added hexagonal boron carbide sample which was heated with 100 °C/min and spark plasma sintered at 1550 °C for 6 min under a pressure of 40 MPa in vacuum atmosphere the attained microstructures are given in Figure 6.50.

In order to see the effect of holding time on densification of Ti-SP added boron carbide, the experiments were repeated in the same conditions but with 6 min soaking time. It is shown that the increase in soaking time, more densified microstructures with less porosity in a continuous structure is obtained. As Sairam et al reported in their study that the density increases rapidly with increasing holding time of sintering operation even in 1 minute [185]. They investigated that increase in sinterability is due to faster sintering kinetics under the influence of electric field. The electro-migration of ions is a prime driving mode behind enhancing the kinetics of the diffusion process [185]. However Mamedov stated that the holding time in final stage of sintering, the porosity is minimal and there are no barriers for grain movement process [189].

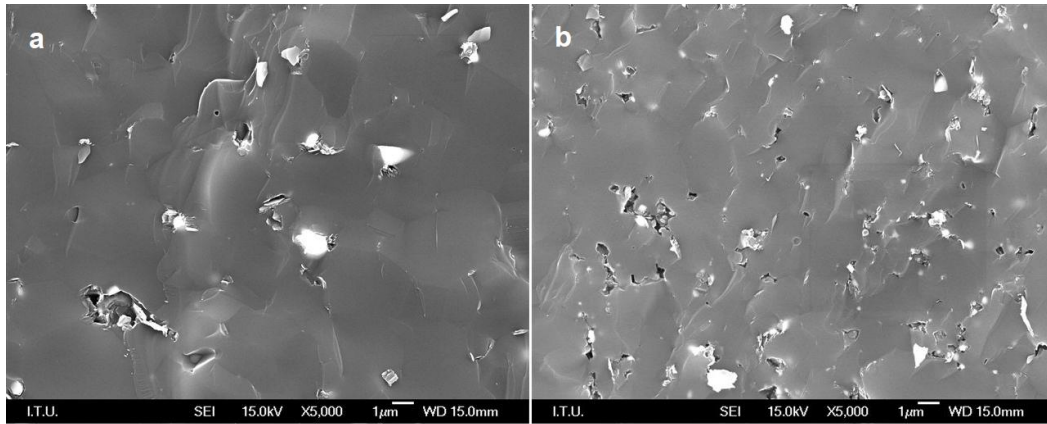


Figure 6.50 : SEM fracture surface micrographs of (a) center (b) edge region of hexagonal boron carbide with 5 vol. % Ti-SP spark plasma sintered at 1550 °C for 6 min under a pressure of 40 MPa in vacuum atmosphere.

Furthermore, the increase in Ti-SP content to 10 vol. %, is investigated. Figure 6.51 demonstrates the center and the edges of hexagonal B₄C composites with 10 vol. % Ti-SP which was heated with 100 °C/min and spark plasma sintered at 1550 °C for 5 min. It can be concluded that the formation of white clusters on the boron carbide matrix is obtained to be more distinct with the increased Ti content in starting powder. Also, again three phases with different colors are obtained in the microstructures of 10 vol. % Ti-SP added sample; white, gray and dark, which can be regarded as TiB₂, B₄C and C respectively. 10 vol % Ti-SP added B₄C composite showed a microstructure with lower porosity which corresponds well with the density results. With the increased Ti-SP content, the sintering is promoted and the porosities in the structure could be removed.

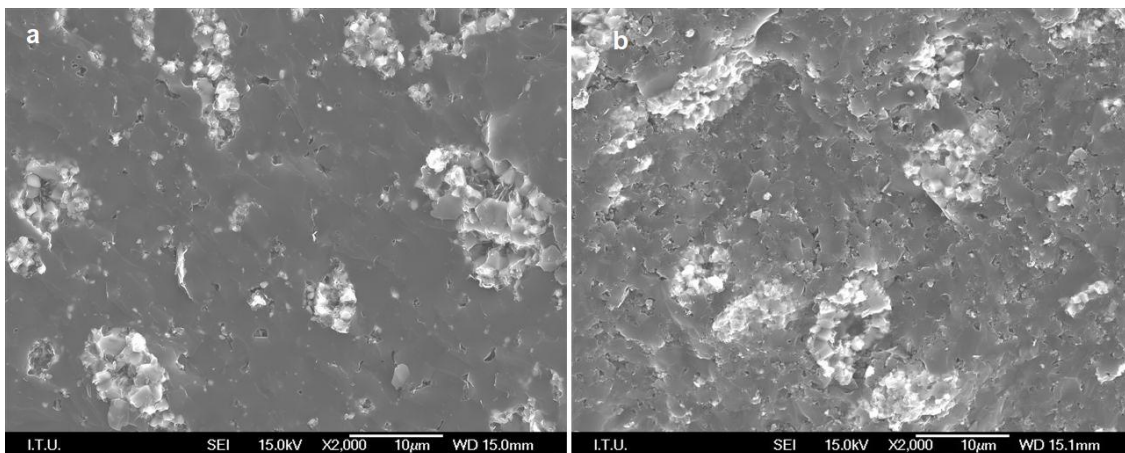


Figure 6.51 : SEM fracture surface micrographs of (a) center (b) edge region of hexagonal boron carbide with 10 vol. % Ti-SP spark plasma sintered at 1550 °C for 4 min under a pressure of 40 MPa in vacuum atmosphere.

TiO₂ addition

Figure 6.52 shows the edge and center of 5 vol. % TiO₂ containing hexagonal boron carbide samples which were heated with 100 °C/min and spark plasma sintered at 1550 °C for 4 min under a pressure of 40 MPa.

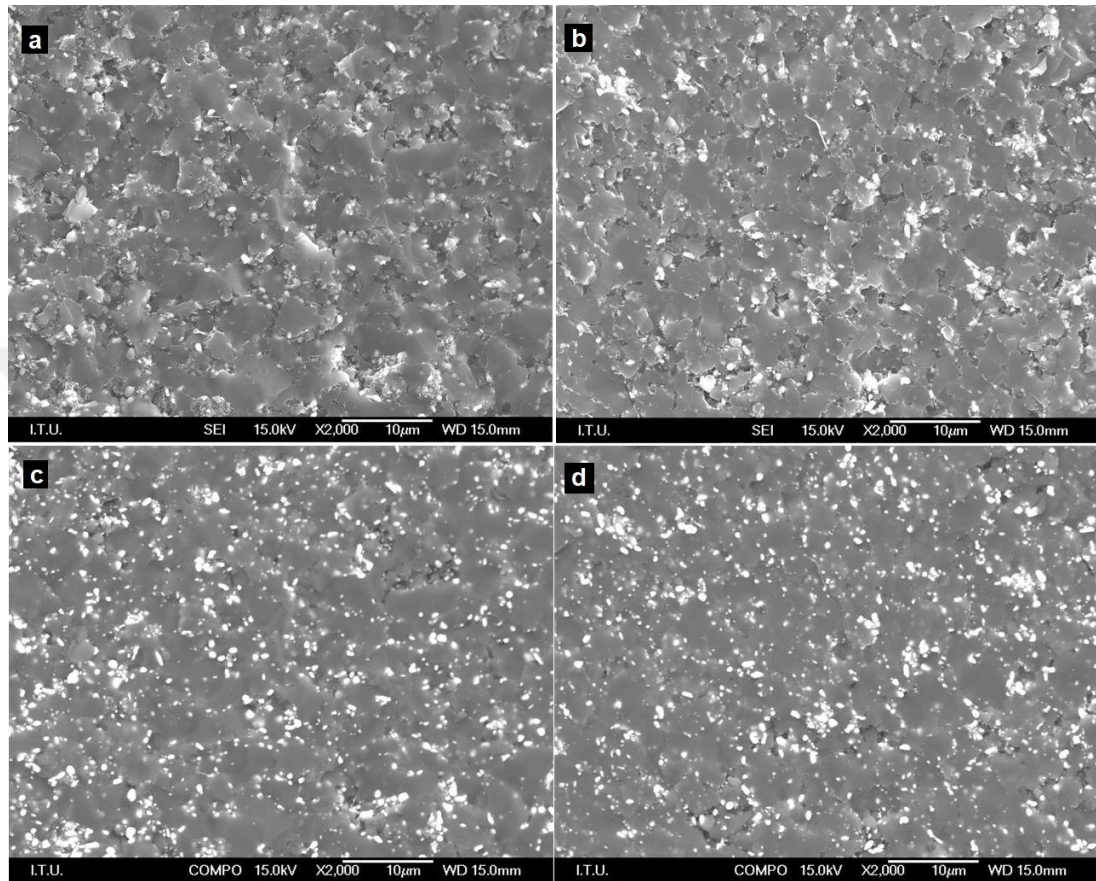


Figure 6.52 : (a) center, SEI; (b) edge, SEI; (c) center, COMPO; (d) edge, COMPO SEM fracture surface micrographs of hexagonal boron carbide with 5 vol. % TiO₂ spark plasma sintered at 1550 °C for 4 min under a pressure of 40 MPa.

According to Figure 6.52 (a) and (b), it can be mentioned that the center of hexagonal boron carbide showed microstructure with lower porosity compared to the edge. Although both Ti and TiO₂ addition results in TiB₂ formation in B₄C structure, the microstructures are obtained to be very different. TiO₂ addition results in spherical small TiB₂ grains, and no carbon can be seen in the structure, whereas in Ti added case, a cluster of TiB₂ contains a carbon phase in the center of each cluster.

It can be concluded that the formed TiB₂ dispersed in boron carbide matrix homogeneously in the samples with TiO₂ added starting powders. In addition, EDS analysis is performed for the edge of hexagonal boron carbide with 5 vol. % TiO₂ and the results were given in Figure 6.53. Only two phases can be obtained. While the grey

Table 6.13 : EDS elemental analysis results of 5 vol. % TiO₂ containing sample which was spark plasma sintered at 1550 °C for 4 min under a pressure of 40 MPa.

Measurement Area	B	C	O	Ti	Total
Region 1	33.45	6.90	-	59.66	100.00
Region 2	77.56	22.44	-	-	100.00

After these experiments, in order to see the soaking time effect and give reaction more time to take place the soaking time increased to 6 min. The microstructures of center and edge of 5 vol. % TiO₂ added B₄C composites which were heated with 1550 °C for 6 min is shown in Figure 6.54. When the edges of 5 vol. % TiO₂ added boron carbide with 4 min soaking time (Figure 6.52 (a)) and 6 min soaking time (Figure 6.54 (a)) are compared, it can be stated that with the soaking time increase resulted in a microstructure which contains less porosity and a more densified compact matrix structure is attained. Again, TiB₂ formation due to TiO₂ addition, is seem to be spherical and TiB₂ is dispersed homogenously in the boron carbide matrix. Except from TiB₂ and B₄C, no phases could be observed.

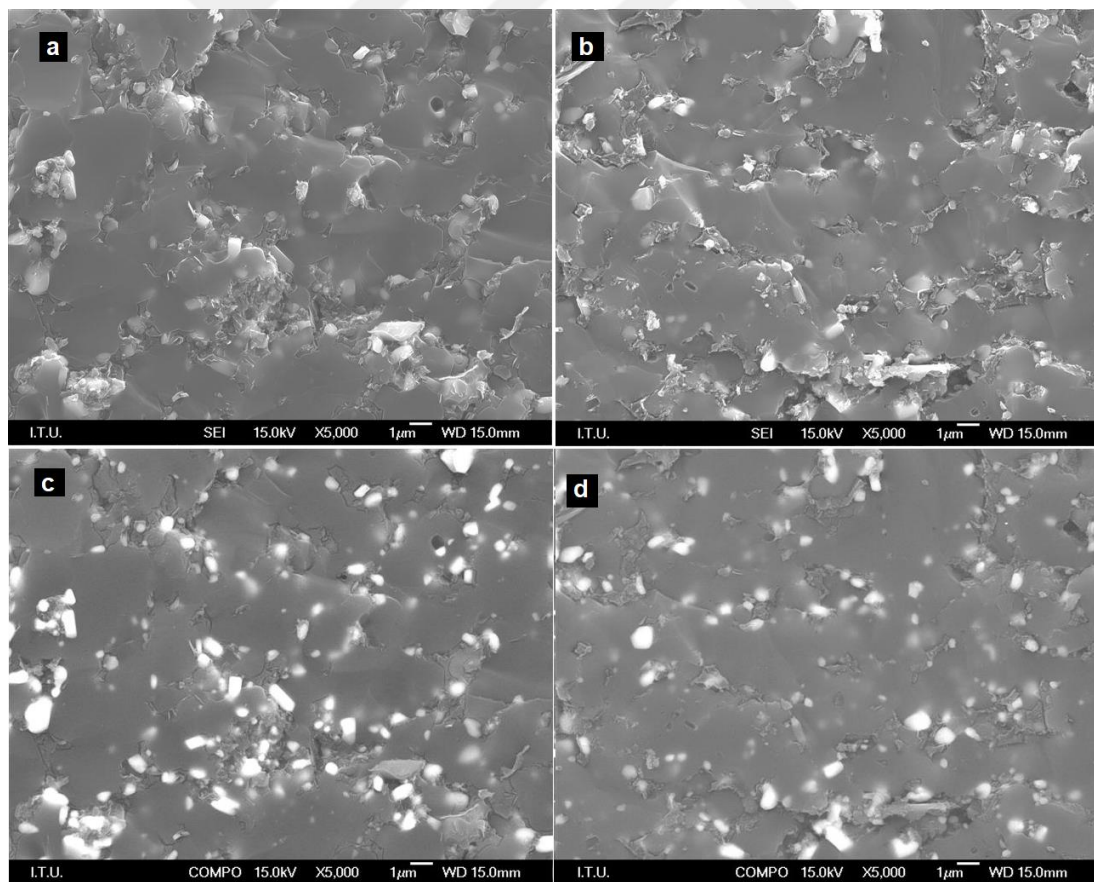


Figure 6.54 : (a) center, SEI; (b) edge, SEI; (c) center, COMPO; (d) edge, COMPO SEM fracture surface micrographs of hexagonal boron carbide with 5 vol. % TiO₂ spark plasma sintered at 1550 °C for 6 min under a pressure of 40 MPa.

Figure 6.55 demonstrates the the edge and center of 10 vol. % TiO₂ added hexagonal boron carbide composites which was heated with 100 °C/min and spark plasma sintered at 1550 °C for 4 min under a pressure of 40 MPa in vacuum atmosphere.

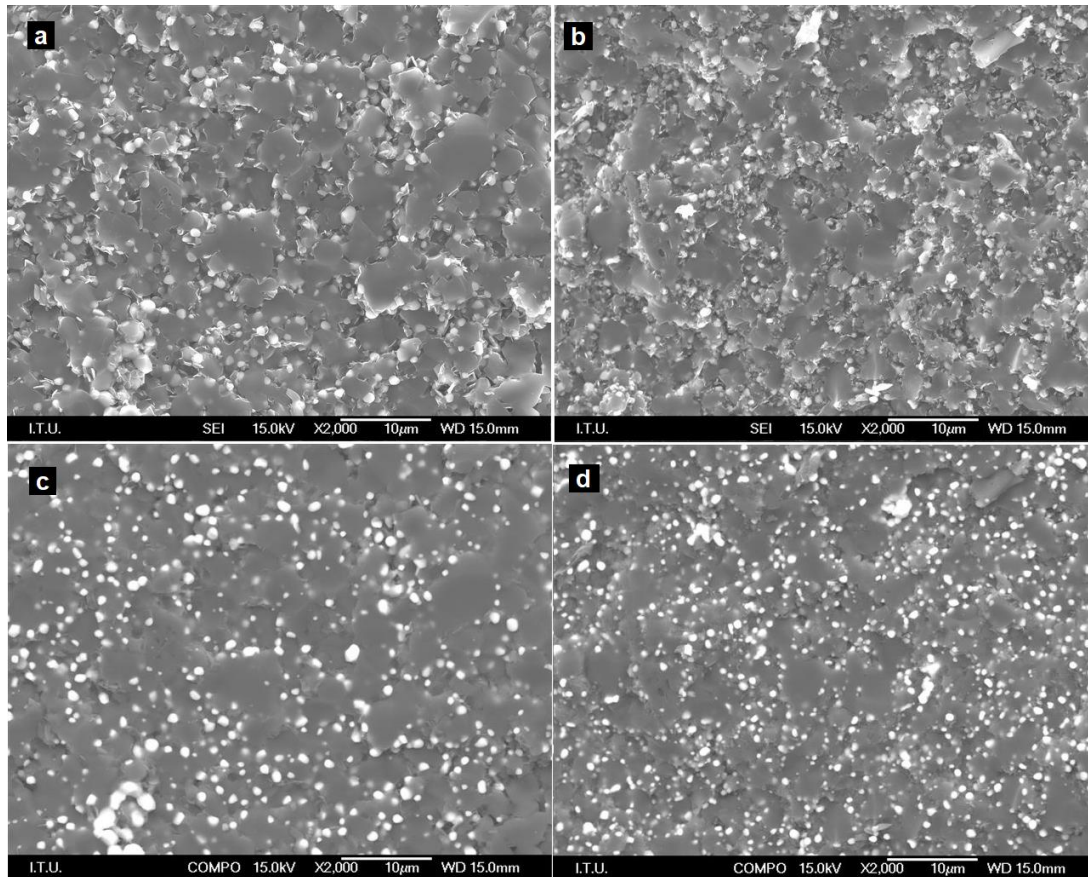


Figure 6.55 : (a) center, SEI; (b) edge, SEI; (c) center, COMPO; (d) edge, COMPO SEM fracture surface micrographs of hexagonal boron carbide with 10 vol. % TiO₂ spark plasma sintered at 1550 °C for 4 min under a pressure of 40 MPa.

With the increase in TiO₂ content in boron carbide structure, the SEM micrographs started to show more white areas, which can be seen from Figure 6.55. One can find out that, again spherical TiB₂ particles are attained in boron carbide structure. Also, when Figure 6.55 (a) and (b) are compared, it can be mentioned that hexagonal boron carbide with 10 vol. % TiO₂ showed a microstructure with finer grain size in its edges, rather than its center.

Furthermore, it is known that forming TiB₂ structure in boron carbide results in higher fracture toughness values. The improvement of fracture toughness is attributed to the crack deflection mechanism triggered by internal stresses due to the thermal expansion coefficient mismatch of B₄C matrix and TiB₂ dispersed phases. Figure 6.56 (a, b, c) shows the path of a crack produced by Vickers indentation on the polished surface of

spark plasma sintered monolithic B_4C . With the addition of 5 vol. % Ti (Figure 6.56 d and e) and with the addition of 5 vol % TiO_2 , (Figure 6.56 f,g and h) the crack mode changes from transgranular to intergranular. It should be stated that by forming and incorporating TiB_2 into B_4C , the cracks were deflected considerably and consequently their propagation was inhibited in the case of the composite, while crack deflection rarely occurred in the monolithic B_4C . The crack deflection was thought to be caused by the residual stress generated by the difference in the thermal expansion coefficient between B_4C and TiB_2 in the composites [190].

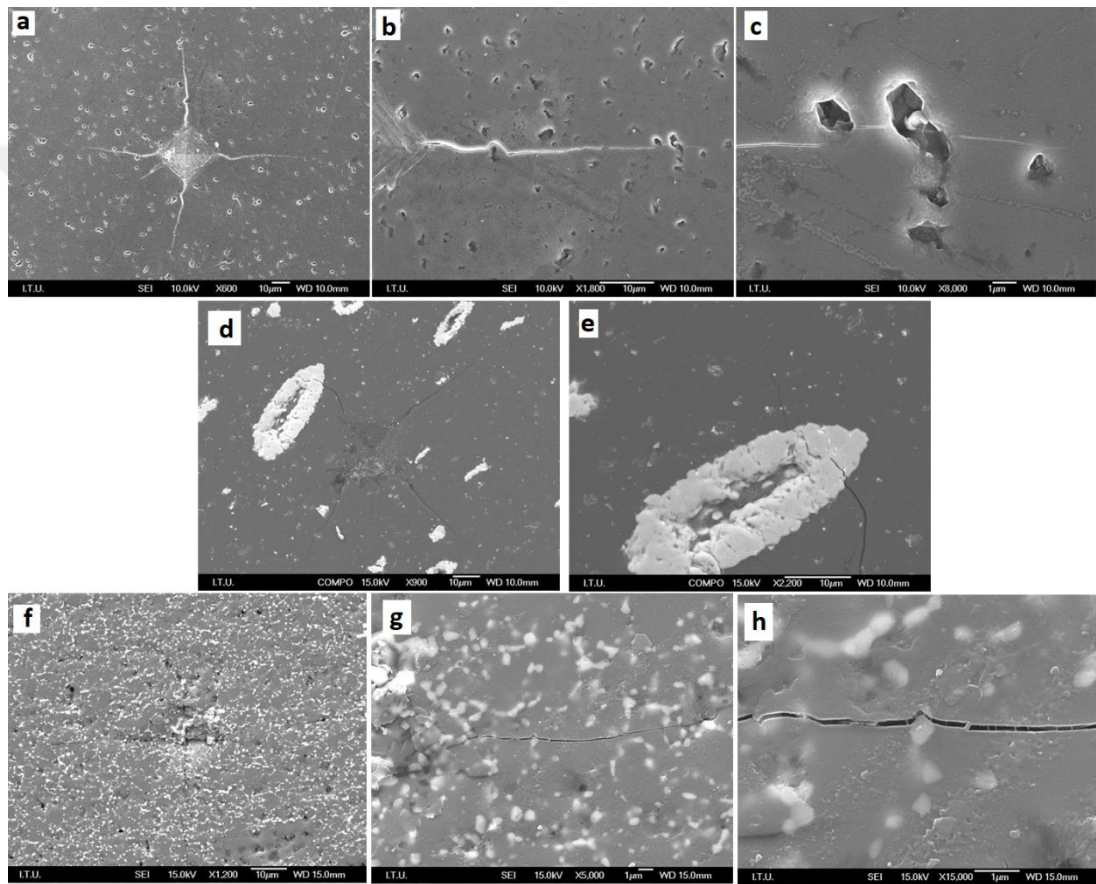


Figure 6.56 : SEM micrographs of fracture surfaces of (a,b,c) monolithic, (d,e) 5 vol. % Ti containing and (f,g,h) 5 vol. % TiO_2 added B_4C .

The polished surfaces of 5% TiO_2 added B_4C specimens are subjected to Vickers indentation test with 9.8 N load. When Figure 6.47 (b) is analyzed, one can see that the crack is propagated and gone through the B_4C grains and showed a transgranular fracture whereas when faced with TiB_2 grains, crack has been got around the TiB_2 grains and showed intergranular fracture. Also, as can be seen from Figure 6.47 (c), the pores in the structure changes the direction of crack and result in obtaining lower fracture toughness values.

6.5 Ballistic Behaviors of Boron Carbide Ceramic Composites

As mentioned earlier, the aim of this study is to produce a final boron carbide ceramic and/or composite which can be used as a ballistic armor. Because of dimension capability of spark plasma sintering method, a study like this one does not exist in the literature. In this study, hexagonal final products with 62 mm diagonal which is suitable for final use as an armor material could have been produced by spark plasma sintering successfully and the results according to ballistic performances of the materials are given in this section.

Boron carbide ceramic armors can be used as body armors and light armors. Body armor is intended to protect individuals primarily against fragments from high-explosive artillery shells, grenades, fragmenting mines, as well as projectiles from small arms. In the category of light armor, applications such as seats in helicopters (protection against ground fire) and the protection of light vehicles and airplanes can be listed. It is also important to evaluate the armor performance in terms of its areal density, that is, the weight per unit area required to offer a specific ballistic protection. For vehicular and aircraft applications, the ceramic armor (alumina, boron carbide, silicon carbide, etc.) backed by a ductile materials has been quite successful against small arms fire and shell fragments [191].

First, two reference shots have been made in Ballistic Protection Center, ROKETSAN A.Ş., Ankara, according to NIJ 0101.04 standards. In the experiments, 7.62x50 mm NATO armour piercing bullets were used and the velocity of the bullet was 868 ± 15 m/s. This velocity can be regarded as intermediate velocity and at intermediate velocities penetration into the ceramic is initiated [191]. Furthermore, a ductile material, aluminum 5083 alloy has been chosen as a backing material, in order to see and be able to make the comparison of the occurred depths in backing material more clearly. The informations related to reference shots can be followed from Table 6.14.

Table 6.14 : The parameters seen during reference shots.

Shot	V_m (muzzle velocity)	$V_{17.6m}$ (final velocity)	DOP (mm)
Reference #1	887.3 m/s	873.1 m/s	50.39 ± 0.14
Reference #2	885.9 m/s	866.6 m/s	50.18 ± 0.09

Without any protection, the depth of penetration value obtained on the surface of aluminum backing material is found out to be higher than 50 mm. Because one piece

of backing material with required thickness could not be found in ROKETSAN laboratory, two pieces of aluminum backing material with 28.5 and 35.5 mm thickness. The reference shot pierced first backing block and made a very significant penetration on the second backing block. The photos related to reference shots can be seen in Figure 6.57.

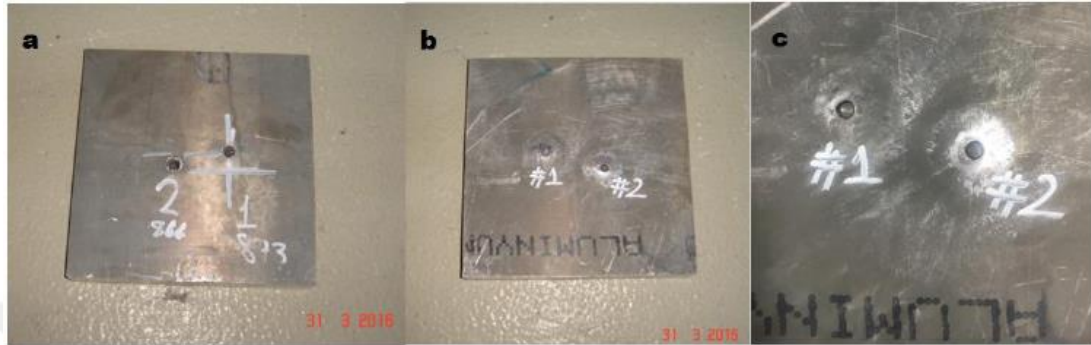


Figure 6.57 : View of the target plate after ballistic impact: (a) Front face and (b) Rear face of 5083 Al alloy plate with a thickness of 25.5 mm; (c) front face of second plate welded first block with 38.5 mm thickness.

After the reference shot, hexagonal boron carbide tiles are placed to the aluminium backing material with 38.5 mm thickness, as can be seen from Figure 6.49.

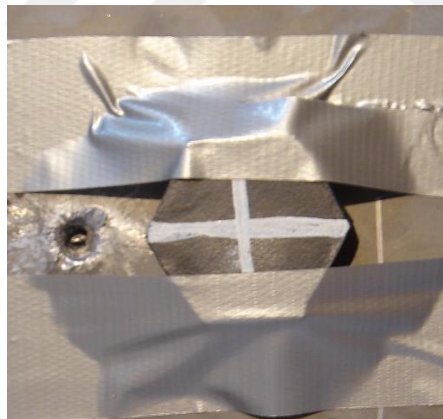


Figure 6.58 : View of hexagonal tile on aluminium backing alloy.

The bullets were fired with 868 ± 15 m/s velocities. The depth of penetration (DOP) on the 5083 aluminum alloy plate occurred was measured and the results were examined. During the ballistic tests of the composites obtained by spark plasma sintering method, high speed camera is used for displaying the damage formed during the hit of projectile to the ceramic composite armor. Again, the brand and model information of the camera used by ROKETSAN A.Ş. due to its corporate policy has not been acquired. The images are given in Figure 6.59.

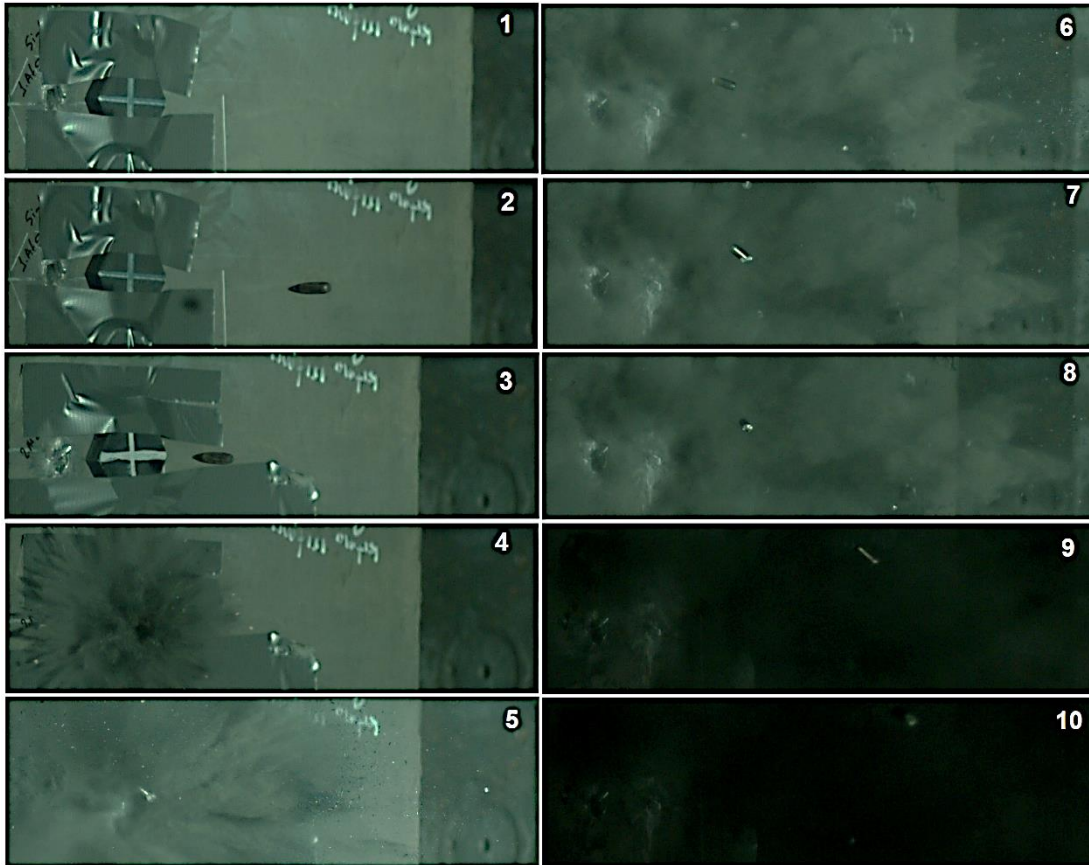


Figure 6.59 : High speed photographs of boron carbide ceramic tile subjected to ballistic test.

As can be seen from Figure 6.59, the bullet is targeted to the center of the ceramic tile and hit exactly from the center. After the hit, the ceramic armor is damaged, then explodes, splinters and spreads over while the projectile is damaged and also broken into pieces, spins around itself and draws away from the hit point. When the target is brittle material, projectile creates a conoid, which is ejected. If the ceramic armors undergo damage by stresses due to the projectile, then projectile tip is plastically deformed by the same time. The comminuted ceramic is ejected from the target through the orifice created by projectile. This creates room for the continued penetration of the projectile [191].

During the ballistic tests, armour-piercing projectiles with explosive charge is used. The charge detonates after the projectile has penetrated the target. The charge amount is very critical because it directly affects the velocity of projectile. As it is known, the kinetic energy is proportional to the square of velocity. As the velocity of impact is increased, the region of damage is decreases, and one progresses from structural effects

to local effects [191]. Accordingly, the explosive amount injected to the projectile is very significant and given in Table 6.15.

Table 6.15 : Some critical parameters considered during ballistic test.

Sample	Weight of projectile body (g)	Weight of explosive (g)	Yawing angle (°)
B ₄ C	9.41	2.98	2
B ₄ C- 2 vol. % C	9.44	3.02	0.5
B ₄ C- 2 vol. % CNT	9.51	3.03	3
B ₄ C- 2 vol. % CNT	9.42	3.05	3
B ₄ C- 5 vol. % Al	9.45	3.03	1
B ₄ C- 5 vol. % Al	9.51	3.02	1
B ₄ C- 5 vol. % Al	9.42	3.05	1
B ₄ C- 5 vol. % Si - 40MPa	9.40	3.05	0.5
B ₄ C- 5 vol. % Si - 60 MPa	9.40	3.05	0.5
B ₄ C- 5 vol. % Ti	9.44	2.98	0.5
B ₄ C- 5 vol. % Ti	9.46	3.03	0.5
B ₄ C- 10 vol. % Ti	9.47	2.98	0.5
B ₄ C- 10 vol. % Ti	9.45	3.02	2
B ₄ C- 15 vol. % Ti	9.47	3.01	0.5
B ₄ C- 20 vol. % Ti	9.49	3.02	0.5

During the ballistic tests, the projectile cores produced by Makine Kimya Endüstrisi is used and the explosive amounts given in Table 6.13 injected to the French Army projectile bodies. With this way, the yawing and obliquity is tried to be minimized. After the shots, yawing angles are measured and compared with yawing standard precision gauge. According to the standards, the yawing angle should be lower than 5° which is higher than all yawing angles obtained in this study. Accordingly, all of the experiments were acceptable.

As mentioned earlier, the explosive amount is very important to arrange the velocity of projectile. The velocities of projectile is measured for three times; muzzle time (the moment that projectile exit the weapon); at 2.2 m and 10.4 m. The velocity at the time of hit is calculated with the interpolation method using these velocities. Table 6.16 demonstrates the measured and calculated velocity values. According to NIJ 0101.06 Level IV standards, the velocity of the projectile at the hit time should be 868±15 m/s. All of the velocities obtained in ballistic experiments was conformant to the related standard.

Table 6.16 : The projectile velocities obtained during ballistic tests.

Sample	V ₀ (m/s)	V _{2.2} (m/s)	V _{10.4} (m/s)	V _{17.6} (m/s)
B ₄ C	880.0	878.5	872.8	867.9
B ₄ C- 2 vol. % C	885.1	883.0	875.0	868.1
B ₄ C- 2 vol. % CNT	884.5	882.9	876.9	871.6
B ₄ C- 2 vol. % CNT	893.5	889.5	885.2	882.5
B ₄ C- 5 vol. % Al	900.4	898.1	889.8	882.6
B ₄ C- 5 vol. % Al	891.5	890.0	884.2	879.1
B ₄ C- 5 vol. % Al	876.4	874.7	868.4	862.9
B ₄ C- 5 vol. % Si - 40MPa	877.5	875.5	868.0	861.4
B ₄ C- 5 vol. % Si - 60MPa	892.2	890.2	883.0	876.7
B ₄ C- 5 vol. % Ti	875.2	873.5	867.1	861.5
B ₄ C- 5 vol. % Ti	871.0	869.6	864.2	859.6
B ₄ C- 10 vol. % Ti	875.2	860.6	858.3	853.6
B ₄ C- 10 vol. % Ti	873.0	861.2	859.6	854.0
B ₄ C- 15 vol. % Ti	880.8	879.3	874.0	869.3
B ₄ C- 20 vol. % Ti	872.8	871.8	867.1	863.3

Boron carbide ceramics without any addition is subjected to ballistic test and the damage occurred on the aluminium 5083 backing alloy with the protection of boron carbide can be seen in Figure 6.60.

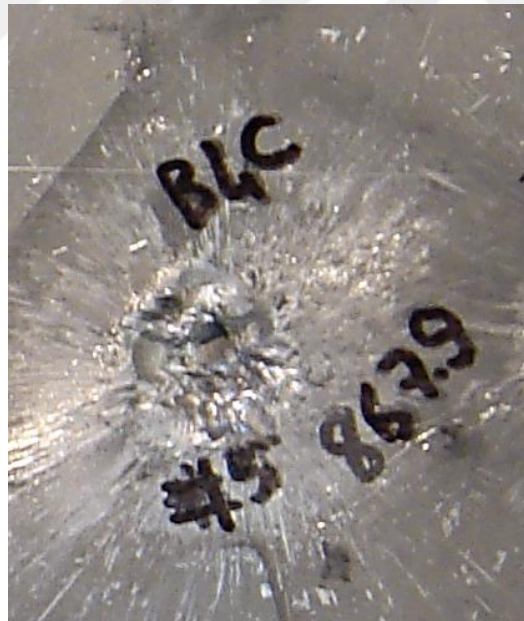


Figure 6.60 : The damage occurred on the Al backing alloy surface after the hit with the protection of monolithic boron carbide ceramic tile which was spark plasma sintered at 1550 °C for 4 min under a pressure of 40 MPa in vacuum atmosphere.

Unfortunately, the projectile after the hit could not be found in this experiment. As can be seen from Figure 6.60, the projectile does not cause a distinct radial deformation on the surface of Al 5083 backing alloy, however spalling occurred and the penetration of bullet to the backing block is measured to be 3.87 mm.

Then, the ballistic tests are continued with 2 vol. % C-black added boron carbide hexagonal samples which was spark plasma sintered at 1550 °C for 4 min under a pressure of 40 MPa in vacuum atmosphere. Figure 6.61 shows the view of the damage occurred after the protection of 2 vol. % C-black containing boron carbide. As can be seen from the projectile and target interaction in Figure 6.61, the projectile caused a radial and a deeper damage compared to Figure 6.60. It can be stated that 2 vol. C-black addition resulted in a deterioration in ballistic performance of boron carbide. DOP (depth of penetration) value is measured to be 6.86 mm.



Figure 6.61 : The damage occurred on the Al backing alloy surface after the hit with the protection of 2 vol. % C-black added boron carbide tile which was spark plasma sintered at 1550 °C for 4 min under a pressure of 40 MPa in vacuum atmosphere.

Figure 6.62 gives the view of damage occurred on the surface of Al-5083 backing alloy which was protected by hexagonal boron carbide with 2 vol. % CNT which was spark plasma sintered at 1550 °C for 4 min under a pressure of 40 MPa in vacuum atmosphere. The ballistic test is applied twice for increased accuracy however, both experiments resulted in high DOP values. Although the relative density, hardness and fracture toughness were both attained higher compared to monolithic boron carbide ceramics produced exactly in same conditions. DOP values on the surface of backing material protected with 2 vol. % CNT added boron carbide tile are found out to be 10.15 mm and 9.50 mm. Also, as can be seen from Figure 6.62 a radial damage with a certain depth is formed on the target plate.

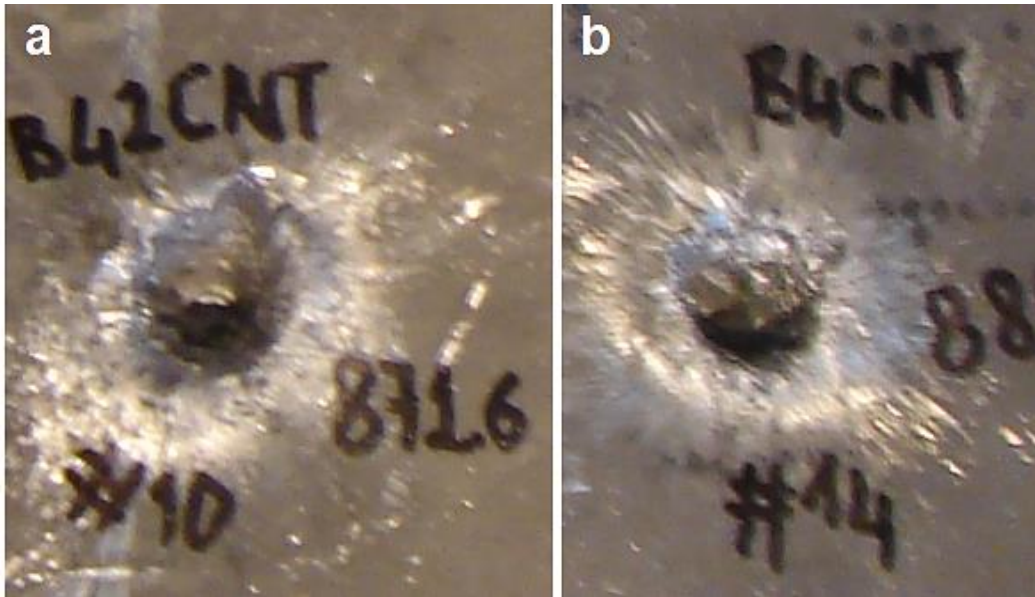


Figure 6.62 : The damages occurred on the Al backing alloy surface after the (a) first (b) second hit with the protection of 2 vol. % CNT added boron carbide tile which was spark plasma sintered at 1550 °C for 4 min under a pressure of 40 MPa in vacuum atmosphere.

Figure 6.63 shows the the interaction between the projectile and Al -5083 backing block when the boron carbide ceramic composite tile containing 5 vol. % Al is used as an armour. These experiments have been applied for three times in order to increase the occuracy. Also, the second experiment erroneously targeted the edge of the center and the projectile hit the edge. Compared to first and third, second shot resulted in deeper penetration and DOP value is found out to be higher. Al added boron carbide composite tiles showed similar ballistic performance values when compared with monolithic boron carbide. The measured DOP values on the backing block surface after the protection of 5 vol. % Al containing boron carbide was 3.10; 4.25 and 3.75 mm. On the other hand, spalling on the surface was more distinct on the backing block surface under the protection of monolithic boron carbide, while a distinct radial damage is obtained under the protection of 5 vol. % Al added boron carbide composites which were spark plasma sintered at 1450 °C for 5 min under a pressure of 40 MPa in vacuum atmosphere. The reason of this can be linked to introducing more ductile phase, Al to boron carbide ceramic and creating a ceramic composite with a more ductile structure. Although the fracture toughness improved and ballistic performances are remained similar, when the target is ductile, a projectile tends to form hole growth on the surface of the backing alloy [191].

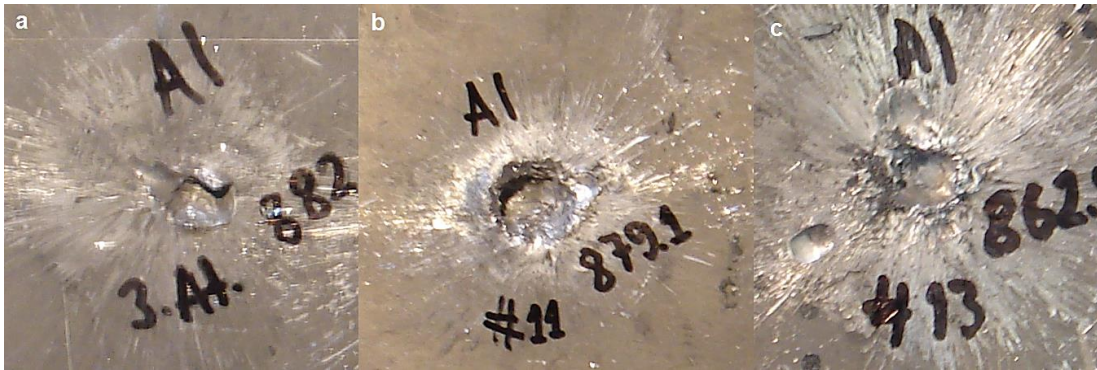


Figure 6.63 : The damages occurred on the Al backing alloy surface after the (a) first (b) second (c) third hit with the protection of 5 vol. % Al added boron carbide tile which was spark plasma sintered at 1450 °C for 4 min under a pressure of 40 MPa in vacuum atmosphere.

Figure 6.64 gives the view of Si backing block surface after the shots with the 5 vol. % Si containing boron carbide tiles which were spark plasma sintered at 1500 °C for 4 min under a pressure of 40 MPa or 60 MPa in vacuum atmosphere. DOP value attained in the Al surface protected by 5 vol. % Si added boron carbide produced under 40MPa pressure in spark plasma sintering was 11.55 mm which was highest DOP value between all spark plasma sintered ceramic and composite tiles. Also, DOP values improved to 8.52 mm in boron carbide sample with 5 vol. % Si spark plasma sintered under 60 MPa pressure. As like relative density, hardness and fracture toughness, ballistic performance is improved with the increased applied pressure to 5 vol. % Si included boron carbide.

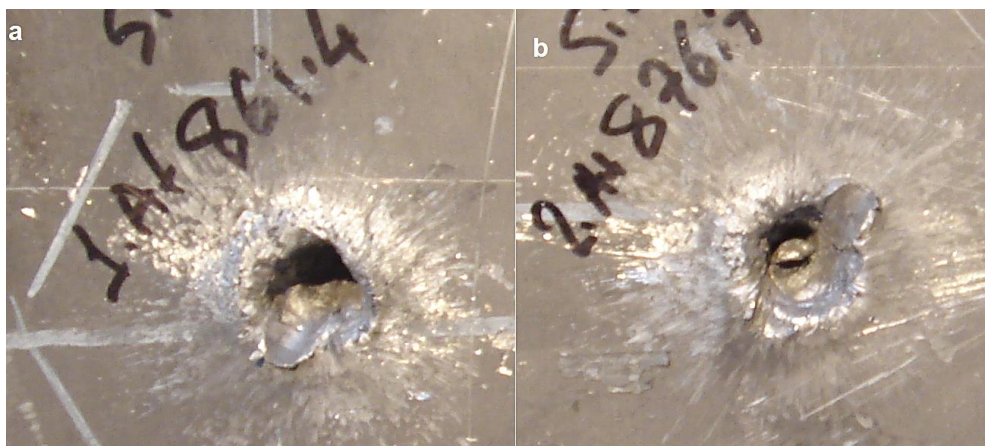


Figure 6.64 : The damages occurred on the Al backing alloy surface after the protection of 5 vol. % Si added boron carbide tile which were spark plasma sintered at 1450 °C for 4 min under a pressure of (a) 40 MPa; (b) 60 MPa in vacuum.

Figure 6.65 demonstrates the Al backing block surface after interaction of projectile and the 5 vol. % Ti- LP added boron carbide target which was spark plasma sintered

at 1550 °C for 4 min under a pressure of 40 MPa in vacuum atmosphere. The lowest DOP value as 0.80 mm is attained in Ti addition when compared to same amount Al or Si light weight metallics containing boron carbide. This DOP value was also lower than monolithic boron carbide sample which was spark plasma sintered under exactly same conditions. As can be seen from Figure 6.65, no hole or radial damage is occurred, just scratches are obtained on the Al surface when protected with 5 vol. % Ti-LP included hexagonal boron carbide composite armor.

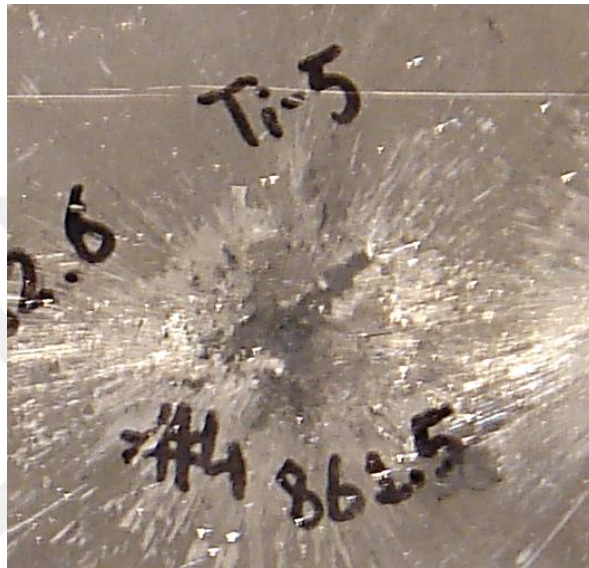


Figure 6.65 : The damage occurred on the Al backing alloy surface after the hit with the protection of 5 vol. Ti-LP added boron carbide composite tile which was spark plasma sintered at 1550 °C for 4 min under a pressure of 40 MPa in vacuum.

Figure 6.66 shows the damages occurred on the surface of Al-5083 backing alloy under the protection of 10 vol. % Ti-LP included boron carbide composites which were spark plasma sintered at 1550 °C for 4 min under an applied pressure of 40 MPa in vacuum. As can be seen from Figure 6.66 (a) again just scratches occurred on the surface of backing block. However because the second hit targeted the center of the composite tile erroneously again a deeper penetration resulting in a radial damage on the Al surface occurred. The DOP value in first hit which centered the 10 vol. % Ti containing sample was found out to be 0.88 mm while 1.84 mm is attained as a DOP value when the projectile hit the composite tile from its edge. When compared with 5 vol. % Ti containing boron carbide, the change in DOP value can be regarded as low; however with the addition of 5 vol. % more Ti to the boron carbide structure, the total weight increase from 67.53 g to 70.10 g. In light-weight armours, the most important factor besides the ballistic performance is the weight of the armor.

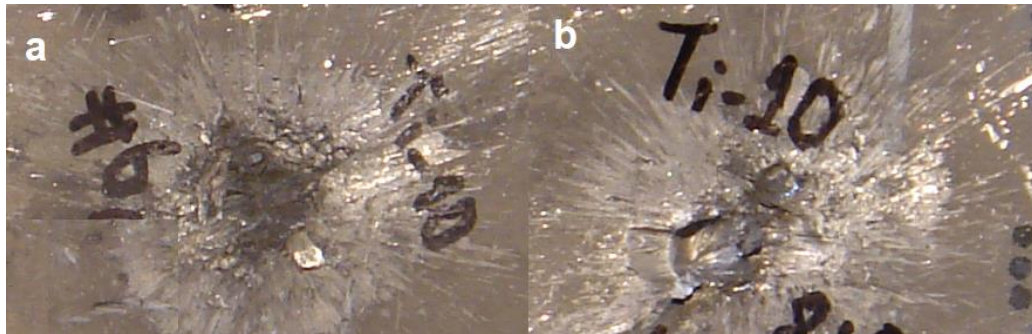


Figure 6.66 : The damages occurred on the Al backing alloy surface after (a) first and (b) second hit with the protection of 10 vol. Ti-LP added boron carbide composite tile which was spark plasma sintered at 1550 °C for 4 min under a pressure of 40 MPa in vacuum.

Figure 6.67 demonstrates the damages occurred on the surface of Al-5083 backing alloy under the protection of 15 vol. % Ti-LP included boron carbide composites which were spark plasma sintered at 1550 °C for 4 min under an applied pressure of 40 MPa in vacuum. This time DOP value is attained to be 0.92 mm which was higher than 5 and 10 vol. % Ti containing boron carbide composite protection. When Figure 6.67 is analyzed, one can see that no hole or radial damage is formed with the interaction of bullet and composite tile on the surface of Al backing block, only the scratches are obtained. However, the damage area was wider compared to 5 vol. % Ti included boron carbide protection. Also, with 15 vol. % Ti addition, the weight of hexagonal boron carbide composite tile increased to 72.64 g.



Figure 6.67 : The damage occurred on the Al backing alloy surface after the hit with the protection of 15 vol. Ti-LP added boron carbide composite tile which was spark plasma sintered at 1550 °C for 4 min under a pressure of 40 MPa in vacuum.

Figure 6.68 shows the damage occurred on the Al-5083 backing block surface after the hit with the protection of 20 vol. % Ti added hexagonal boron carbide composite tile which was spark plasma sintered at 1550 °C for 4 min under a pressure of 40 MPa in

vacuum. The DOP value attained on the Al backing surface was 0.87 mm which is very similar DOP value obtained under the protection of 5 and 10 vol. % Ti included samples. However, the weight increase should be considered and should be known that with the addition of 20 vol. % Ti, the weight of hexagonal armor is increased to 75.20 g. When the damage in Figure 6.68 is analyzed, it can be concluded that with increasing Ti content the scratches and the damage on the Al surface is increased.



Figure 6.68 : The damage occurred on the Al backing alloy surface after the hit with the protection of 20 vol. Ti-LP added boron carbide composite tile which was spark plasma sintered at 1550 °C for 4 min under a pressure of 40 MPa in vacuum.

Furthermore, unfortunately all of the projectile after each test could not be found in testing area. However, the found projectiles are given in Figure 6.69. When the DOP values occurred due to the interaction of projectile and target are compared with the final conditions of projectiles, it is very difficult to make a conclusion.

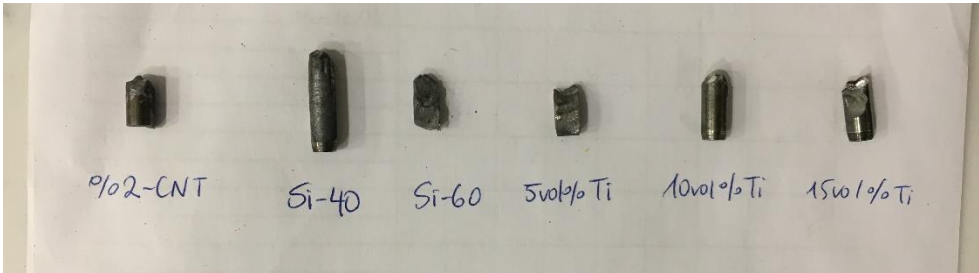


Figure 6.69 : The pieces of the broken shots of the projectile.

In Table 6.17 the depth of penetration (DOP) values obtained after 10 measurements are compared with the relative density values of hexagonal spark plasma sintered boron carbide ceramic composites and the final velocity values of projectiles are also given.

Table 6.17 : The comparison of center relative density values of hexagonal spark plasma sintered ceramics with velocity and DOP values.

Armour Sample	Relative Density (%)	Velocity of Projectile (m/s)	DOP (mm)
B ₄ C	95.34	867.9	3.87±0.09
B ₄ C- 2 vol. % C	96.75	868.1	6.86±0.12
B ₄ C- 2 vol. % CNT	97.26	871.6	10.15±0.14
B ₄ C- 2 vol. % CNT	97.26	882.5	9.50±0.11
B ₄ C- 5 vol. % Al	98.16	882.6	3.10±0.08
B ₄ C- 5 vol. % Al	98.16	879.1	4.25±0.10
B ₄ C- 5 vol. % Al	98.16	862.9	3.75±0.09
B ₄ C- 5 vol. % Si - 40MPa	96.31	861.4	11.55±0.16
B ₄ C- 5 vol. % Si - 60MPa	97.54	876.7	8.52±0.11
B ₄ C- 5 vol. % Ti	99.18	861.5	0.80±0.03
B ₄ C- 10 vol. % Ti	99.35	853.6	0.88±0.04
B ₄ C- 10 vol. % Ti	99.35	854.0	1.84±0.08
B ₄ C- 15 vol. % Ti	99.68	869.3	0.92±0.05
B ₄ C- 20 vol. % Ti	100	863.3	0.87±0.03

According to Table 6.17 it can be concluded that boron carbide ceramic or composite tiles which show higher relative density values tend to show better ballistic performances. Although all additions resulted an improvement in densification of composites, ballistic properties did not improve in all of the samples. When the additions are compared, Ti and Al seems to improve the ballistic performance of boron carbide, whereas C-black, CNT and Si addition hindered the ballistic properties. The lowest depth of penetration value as 0.80 mm is obtained in the sample containing 5 vol. % Ti which was heated with 100 °C/min and spark plasma sintered at 1550 ° for 4 min under a pressure of 40 MPa in vacuum atmosphere.

The results obtained from the ballistic tests of monolithic boron carbide ceramics are in line with the values given in the study of Savio et al. [192]. When a shot with an average speed of 802 m/s is made on 40 mm diameter circular section with an average thickness of 9.4 mm boron carbide samples without any additive, Savio et al. measured a trace depth of between 2 and 5 mm on a 6063-T6 aluminum sheet [192]. This work was carried out at higher speeds (868 ± 15 m/s), and the projectile left a mark with 3.87 mm depth on Al 5083 backing alloy when monolithic boron carbide ceramics armor material was used.

Furthermore, it is clearly seen that neither C-black nor CNT addition resulted in better ballistic performance in boron carbide ceramics. The DOP value attained in the monolithic boron carbide ceramics which were produced in the same conditions by

spark plasma sintering was lower compared to C-black or CNT added B₄C samples. However as Medvedovski stated in his study that the presence of the small carbon inclusions and their amounts and distribution in the dense carbide ceramics structure may be important factors affecting fracturing and decrease of ballistic performance, especially under the action of harder projectiles [193]. Also as Gao et al mentioned the free carbon in the dense product could reduce the Hugoniot elastic limit (HEL) and enhance the chance of fracture through shear-induced amorphization [194].

As shown in Table 6.17, when boron carbide composites containing 5 vol. % Si were produced by spark plasma sintering at 1500 °C under 40 MPa pressure, the relative density reached 96.31%. The Si additive has a higher trace depth value after shot at the Al 5083 backing alloy, although the densification is increased compared to monolithic boron carbide ceramics in the case of producing at 1550 °C under the same pressure. It was determined that Si additive negatively affected the ballistic performance of the boron carbide. Although the effect of Si addition on the ballistic performance of boron carbide does not exist in the literature, Karandikar et al highlighted the possibility of phase transformation of residual Si under a high pressure and concluded that this could have adverse effects on the impact resistance of boron carbide ceramics that contains residual Si in its structure [195]. Although, all Si is thought to be transformed to SiC in the structure, very low amount of residual Si may remained in the B₄C structure and may have not been detected by XRD.

On the other hand, one can expect that both C-black, CNT or Si addition to result in better ballistic performance due to the increased relative density, hardness and fracture toughness results given above sections. However, as Hallam et al stated in their study that while B₄C containing SiC appears superior in properties such as fracture toughness and hardness measured by loading low loads, monolithic boron carbide can be achieved as a superior material in structures subjected to a very high density impact such as ballistic performance. They found out in their analysis that as the amount of load increases, the amount of damage on the monolithic boron carbide ceramics is getting smaller [196]. In addition, Holmquist and Johnson showed that the computed results (high hardness and fracture toughness bring better ballistic performance) did not compare well to the experimental results. In general, the monolithic B₄C behavior was too weak for low impact velocities and too strong for high velocities [197,198].

Furthermore, both Al and Ti additions resulted in lower depth of penetration values. Compared with monolithic boron carbide, the trace depth on the surface of Al 5083 alloy after ballistic test in Al containing composites decreased from 3.87 mm to 3.10 mm. The addition of 5, 10, 15 and 20 vol. % Ti to the B₄C structure resulted in a considerable increase in the ballistic performance of the boron carbide. In monolithic boron carbide ceramics produced by spark plasma sintering system using the same temperature, pressure, atmosphere and heating rates, the trace depth was 3.87 mm, while for Ti-added composites this value decreased to 0.80, 0.88, 0.92 and 0.87 mm, respectively. The TiB₂ phase formed by the addition of Ti activate the mechanisms to stop crack propagation not only at low loads (the loads used during the hardness and fracture toughness measurements) but also at very strong dynamic loads.

When the dynamic properties of boron carbide materials and responses to sudden impacts are examined in the literature, localized softening and even melting of the area exposed to the impact have been reported [199,200]. However post-processing characterizations of ballistic tested materials have been performed first by Chen et al [201]. More recently, the idea that cause this unexpected behavior of boron carbide is due to the phase transformation occurring at high pressure has been proposed by Mashimo and Uchino [202].

Chen and his colleagues used a high-resolution electron microscope (HREM) to examine the boron carbide fragments obtained after ballistic test [201]. Hot pressed boron carbide ceramics are subjected to ballistic tests with armor piercing bullets at speeds of 750 to 1000 m/s. Very small parts which are evolved as a result of cleavage during ballistic testing have very thin corners with good electron permeability for TEM examination. When the specimens shot at a speed of 907 m/s were examined, damaged areas with 100 - 200 nm length and a thickness of 1 - 3 nm were observed and it was proven that no crystalline structure was found in these areas using HREM. In the crystal matrix of boron carbide, reciprocal lattice appearance proving the rhombohedral structure was obtained. However, a typical amorphous phase appeared in the damaged areas of the sample studied by FFT (Fast Fourier transforms), and it was determined that the crystalline structure was lost in these regions. When the chemical compositions were compared, no differences were found in these regions. This shows that local amorphous phases do not originate from any chemical reaction or decomposition but may be caused by high pressure effect [201]. However Reinhart et al reported that

although there are suggestions about the possibility of the existence of one or more phase transitions in high impact loaded boron carbide, none including them could demonstrate phase transition conclusively [203].

When evaluating the ballistic performance of an armor ceramic, the differential efficiency factor must be calculated as well as the depth of penetration values obtained after the shot:

$$DEF = \frac{\rho_b \times (P_o - P_b)}{\rho_c \times t} \quad (6.1)$$

where, ρ_c is the density of the ceramic material; ρ_b is the density of the backing material; P_o is the reference depth of penetration in the backing material; P_b is the residual depth of penetration in the backing material; t is the thickness of the ceramic target material. The differential efficiency factors calculated according to these are given in Table 6.18.

Table 6.18 : Differential efficiency factors of spark plasma sintered hexagonal boron carbide ceramics and composites.

Armour Sample	Thickness (mm)	DOP (mm)	DEF
B ₄ C	10.551	3.87±0.09	4.88
B ₄ C- 2 vol. % C	10.224	6.86±0.12	4.65
B ₄ C- 2 vol. % CNT	10.122	9.50±0.11	4.39
B ₄ C- 5 vol. % Al	10.263	3.10±0.08	4.93
B ₄ C- 5 vol. % Si - 40MPa	10.505	11.55±0.16	4.06
B ₄ C- 5 vol. % Si - 60MPa	10.252	8.52±0.11	4.43
B ₄ C- 5 vol. % Ti	10.153	0.80±0.03	5.00
B ₄ C- 10 vol. % Ti	10.113	0.88±0.04	4.82
B ₄ C- 15 vol. % Ti	10.166	0.92±0.05	4.60
B ₄ C- 20 vol. % Ti	10.125	0.87±0.03	4.46

When Table 6.18 is analyzed, it can be concluded that only 5 vol. % Al and 5 vol. % Ti including boron carbide composite material showed better differential efficiency factor which means in terms of weight, only these two composites show better ballistic performance compared to monolithic boron carbide ceramics.

Furthermore, the debris of the projectile and spark plasma sintered boron carbide tiles produced during the ballistic tests were collected for each experiment. The collected powders were analysed for the particle size distribution by sieving with a sieve shaker having sieves with BSS Nos. 4, 8, 30 and 100, which corresponds to 4.0, 2.0, 0.5 and 0.15 mm, respectively. The powder retained in each sieve is collected, weighed and

the relative weight percentages according to total collected powder is calculated. The powder analysis result with respect to the ballistic experiment of spark plasma sintered hexagonal monolithic B₄C, 2 vol. % C-black or CNT added B₄C, 5 vol. % Al or Si added B₄C and 5, 10, 15 and 20 vol. % Ti added B₄C is given in Table 6.19 and Figure 6.70.

Table 6.19 : Particle size distribution of the impact fractured powder for spark plasma sintered hexagonal boron carbide tiles according to sieve sizes (BSS No.).

Armour Sample	+4	+8	+30	+100	-100
B ₄ C	10.6	13.9	39.4	22.6	13.5
B ₄ C- 2 vol. % C	11.4	14.9	40.2	20.9	12.6
B ₄ C- 2 vol. % CNT	12.0	16.5	40.1	19.8	11.6
B ₄ C- 5 vol. % Al	8.1	13.4	41.3	23.0	14.2
B ₄ C- 5 vol. % Si - 40MPa	13.3	17.0	40.4	19.1	10.2
B ₄ C- 5 vol. % Si - 60MPa	11.5	16.2	41.0	20.0	11.3
B ₄ C- 5 vol. % Ti	5.3	11.5	40.6	25.2	17.4
B ₄ C- 10 vol. % Ti	6.4	12.2	41.1	24.1	16.2
B ₄ C- 15 vol. % Ti	7.4	12.6	40.6	23.9	15.5
B ₄ C- 20 vol. % Ti	6.1	11.8	41.5	24.1	16.5

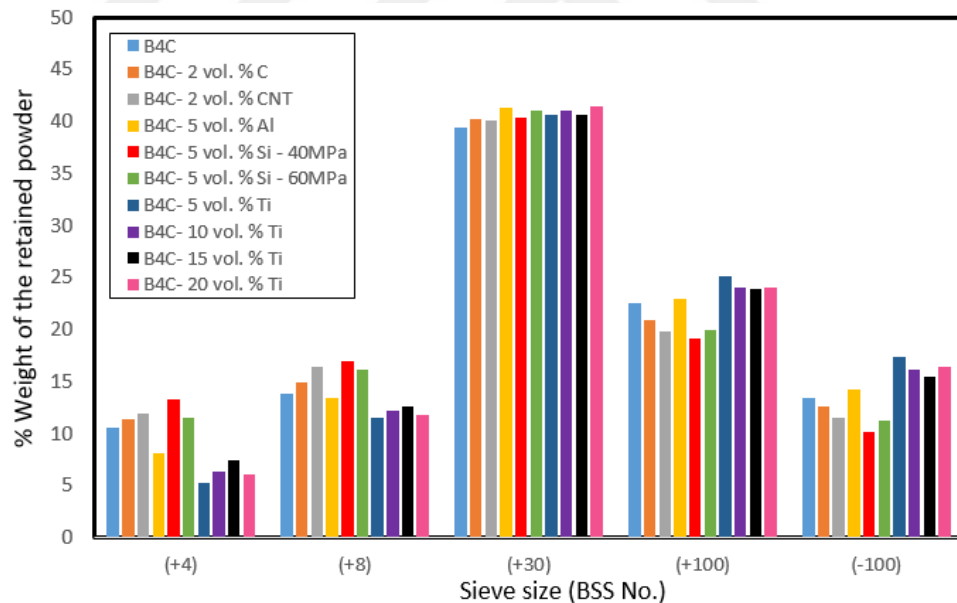


Figure 6.70 : Particle size distribution of the impact fractured powder for spark plasma sintered hexagonal boron carbide tiles according to sieve sizes (BSS No.).

According to Figure 6.70, one can state that the percentage weight of retained coarser particles is highest in 5 vol. % Si containing hexagonal boron carbide composite tile which was spark plasma sintered at 1500 °C for 4 min under a pressure of 40 MPa in vacuum atmosphere and the lowest percentage weight of retained coarser particles is attained in 5 vol. % Ti added boron carbide sample which was spark plasma sintered

at 1550 °C for 4 min under a pressure of 40 MPa in vacuum. Also, when the finest particles are considered, the relative amount of finer particles was highest in 5 vol. % Ti added B₄C whereas it was lowest in 5 vol. % Si added sample. When all the results are analyzed, it can be concluded that finer powders are attained after the ballistic tests which showed lower DOP values and coarser particles are obtained after the shots which resulted higher DOP values. In other words, in the composites which show better protection against the projectile causes to form finer particles. When compared with the study of Savio et al [192], the results are parallel. They mentioned that tiles with higher thickness result in forming finer particles, where they show lower DOP values.

6.6 Phase Analysis of Boron Carbide Ceramic Composites After Ballistic Tests

6.6.1 XRD analysis of hexagonal monolithic boron carbide ceramics

Figure 6.71 shows the XRD analysis of monolithic boron carbide before and after the ballistic tests. The boron carbide sample was heated with 100 °C/min and spark plasma sintered at 1550 °C for 4 min under an applied pressure of 40 MPa in vacuum.

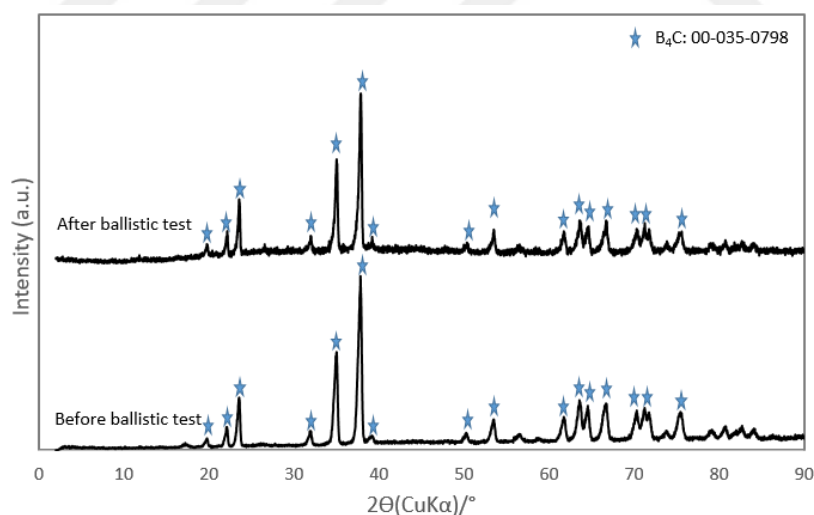


Figure 6.71 : XRD analysis of spark plasma sintered monolithic hexagonal B₄C before and after ballistic test.

Boron carbide powders did not show any other phase transformation after spark plasma sintering due to increasing temperature, as expected. In addition, in some conditions with increasing temperature, the oxidation of boron carbide has been reported [204, 205]. The XRD analysis of spark plasma sintered boron carbide did not reveal any solid oxidation products including B₂O₃. This could be related to spark plasma

sintering which is carried out in vacuum atmosphere. At the temperatures above 1200 °C, the B₂O₃ vaporizes and results in a weight decrease [205]. However, to follow and conclude an oxide formation is impossible in spark plasma sintering procedure due to a lot of existing other factors which results in powder losses during mold preparing stage.

After the ballistic test application, a slight increase in background can be seen, when the peaks observed by XRD are evaluated in detail. Also, when compared with before ballistic test XRD peaks, observed peaks were shifted left to very slightly after the ballistic test. According to Bragg's Law, a left shift in peaks means that d spacing value is increased, so that the lattice distortion with the ballistic impact can be mentioned [206].

According to Ge et al [207] due to the limited number of dislocation slip systems in boron carbide, even after hardness test, a hardness indenter triggers amorphization along the preferred crystallographic directions or a localized distortion-induced disordering. Also, Ge et al referred another study which concerns a phase transition from the rhombohedral to denser and more compressible orthorhombic structure in boron carbide at a hydrostatic pressure of ~20 GPa. However, the existence of phase transformation and amorphous phase transition have not been independently confirmed and the detailed lattice information of the high-pressure phase has never been reported in the literature. Ge et al concluded that additional characterization is required to clarify the existence of a high-pressure phase transformation in boron carbide during contact loading and the precise reason for appearance of new Raman bands [207].

Yan et al [208] investigated the Raman spectra of B₄C acquired with the loading pressures gradually increasing from the ambient up to 50 GPa. Again, they could not obtain any new peak appearance or crystalline peak disappearance induced by phase transitions. Although they concluded that the depressurization amorphization of B₄C shows an unusual manner that is caused by irreversible lattice distortion at high pressures, they could not prove it with Raman spectra [208].

6.6.2 XRD analysis of hexagonal boron carbide ceramics with different C additions

Figure 6.72 demonstrates the XRD analysis of boron carbide containing 2 vol. % C-black which was heated with 100 °C/min and spark plasma sintered at 1550 °C for 4

min under an applied pressure of 40 MPa in vacuum. The XRD analysis is applied to the composite before and after the ballistic test.

As can be seen from Figure 6.72, only B₄C and C peaks could be obtained in the XRD analysis of 2 vol. % C-black containing boron carbide. According to the literature, XRD diagram of pure graphite has a sharp characteristic peak at $2\theta = 26.6^\circ$. This peak belongs to the (002) diffraction plane [209]. Moreover, this time the shift after the ballistic test was not too distinctive as it is in monolithic boron carbide. However, after the ballistic test, it appears that the peak belongs to C-black has lost its sharpness and rounded off. It can be stated that, with the tremendous dynamic load applied during ballistic test affects not only boron carbide structure, but also changes the structure of additions.

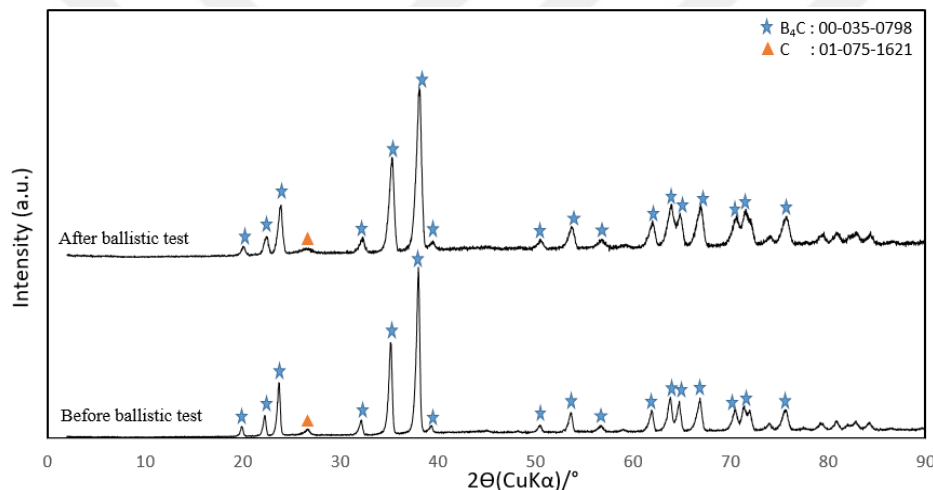


Figure 6.72 : XRD analysis of spark plasma sintered hexagonal B₄C with 2vol. % C-black before and after ballistic test.

Figure 6.73 gives the XRD analysis of boron carbide containing 2 vol. % CNT which was heated with 100 °C/min and spark plasma sintered at 1550 °C for 4 min under an applied pressure of 40 MPa in vacuum. The XRD analysis is applied to the composite before and after the ballistic test.

As mentioned before XRD diagram of pure graphite has a sharp characteristic peak at $2\theta = 26.6^\circ$. In the XRD diagram of single-walled CNT, it was determined that the peak expanded and the intensity of the characteristic peak is decreased. Also, the peak position was shifted from 26.6° to 26° [180]. The peak position of the multi-walled CNT is obtained at 26.38° in this study. In the obtained XRD analyzes, it is thought that the free carbon in B₄C structure as an impurity and the peaks of CNT coincide.

Also, again after the ballistic test a slight shift to the left in boron carbide peaks is obtained clearly, whereas CNT peak slightly moved to right.

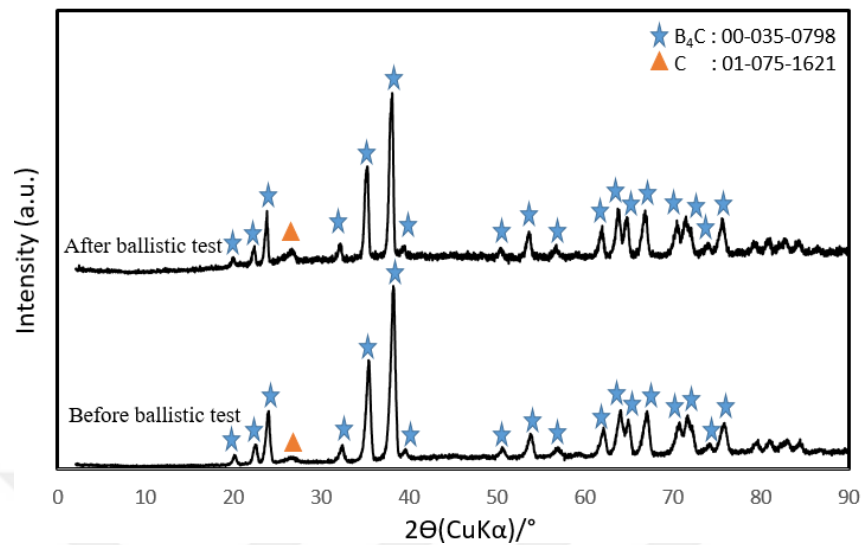


Figure 6.73 : XRD analysis of spark plasma sintered hexagonal B₄C with 2 vol. % CNT before and after ballistic test.

6.6.3 XRD analysis of hexagonal boron carbide ceramics with light-weight metallic additions

In order to benefit from the light weight advantage of boron carbide, the ceramics are aimed to strengthen with low density metallic additions such as aluminum and silicon. The hardness, fracture toughness and ballistic test results obtained in this thesis study showed that aluminium is beneficial addition under both quasi-static and dynamic loading conditions. Also in the literature, Al is regarded as a ductile phase toughening boron carbide effectively both in quasi-static and dynamic loading conditions [210].

Figure 6.74 shows X-ray diffractograms of a boron carbide composite containing 5 vol. % Al heated at a heating rate of 100 °C/ in for 4 minutes at spark plasma sintering temperature of 1450 °C. Besides the 35-0798 card numbered B₄C and 26-1076 card numbered C as an impurity of B₄C, it was observed that 36-0148 card numbered Al₂OC and 35-8216 card numbered Al₈B₄C₇ phases were formed after the spark plasma sintering process.

The phases mentioned above, obtained after spark plasma sintering are also quite common in Al-added B₄C composites in the literature [211-215]. Apart from them, in the literature six ternary phases have been discovered, B₄₀AlC₄ and B₄₈Al₂C₈, which have a B₄C structure and thus are probably B₁₂(B,C,Al)₃ solid solutions, orthorombic

$B_{51}Al_2C_8$, hexagonal and orthorhombic $B_{48}Al_3C_8$, and hexagonal B_4Al_8C [13]. The temperature stabilities of these phases are not known. In particular, the presence of the $Al_8B_4C_7$ phase in the structure is known for increasing the sinterability of boron carbide and results in achieving higher relative density values. It is pointed out that the $Al_8B_4C_7$ phase exhibited lower shrinkage temperatures during sintering if it is formed in the structure and the final product performed better mechanical properties [211-213].

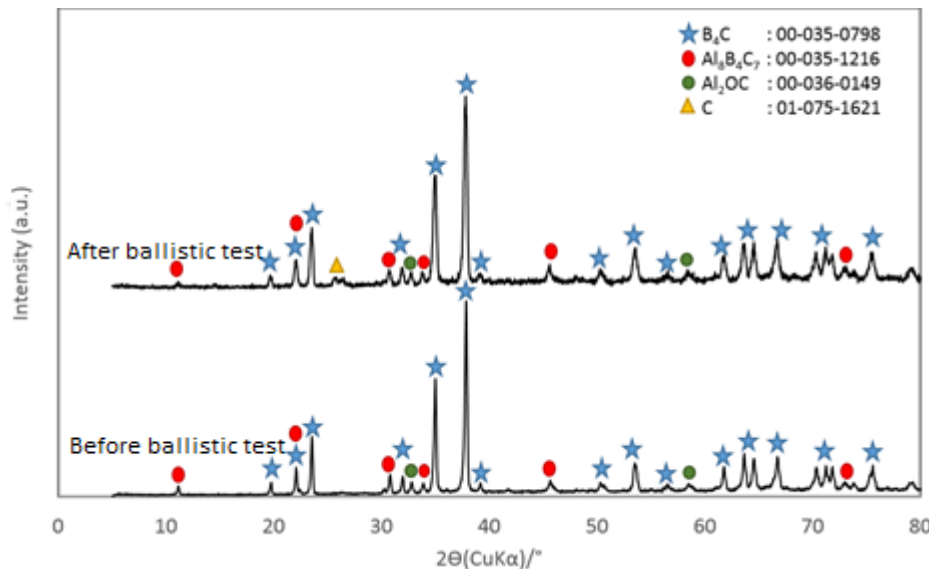


Figure 6.74 : XRD analysis of spark plasma sintered hexagonal B_4C with 5 vol. % Al before and after ballistic test.

Moreover, the reason for the formation of Al_2OC phase is thought to be due to the easy oxidation of the Al additive added to the structure. Gao et al [213] studied XRD peaks of Al added boron carbide and found out that the formation of Al_2OC is originated from the starting powders. Al metal and the oxide layer on the surface of the starting powders combine with the carbon, which is released possibly during the formation of $Al_8B_4C_7$ phase, and results in the formation of Al_2OC [213].

The presence of more noisy regions in the X-ray diffractogram of boron carbide composites containing 5 vol. % Al exposed to ballistic damage is due to the material being exposed to ballistic impact, which is a high-intensity impact. However, not all of the sample subjected to the ballistic test became amorphous and very distinct peaks were obtained under X-rays. Although X-ray diffractograms can not prove that the structure is amorphous, it is known that boron carbides show local amorphous behavior when subjected to high loads due to the studies in the literature [101,201,207,216,217].

The characteristic peak of boron carbide is shifted from 37.82° to 37.70° , whereas the highest intensity peak of $\text{Al}_8\text{B}_4\text{C}_7$ phase moved from 45.72° to 45.48° .

Figure 6.75 demonstrates the XRD peaks obtained from before and after ballistic test of spark plasma sintered boron carbide with 5 vol. % Si which was heated with $100^\circ\text{C}/\text{min}$ and sintered at 1500°C for 4 min under a pressure of 40 MPa. It can be clearly seen that all Si in the starting powder transformed into SiC. However, no free boron phase can be observed. This can be due the spark plasma sintering process which is performed with graphite molds. Also, the wear obtained in the surfaces of graphite die and molds prove that not only boron carbide, but also graphite molds are used as a C source for Si to transform to SiC.

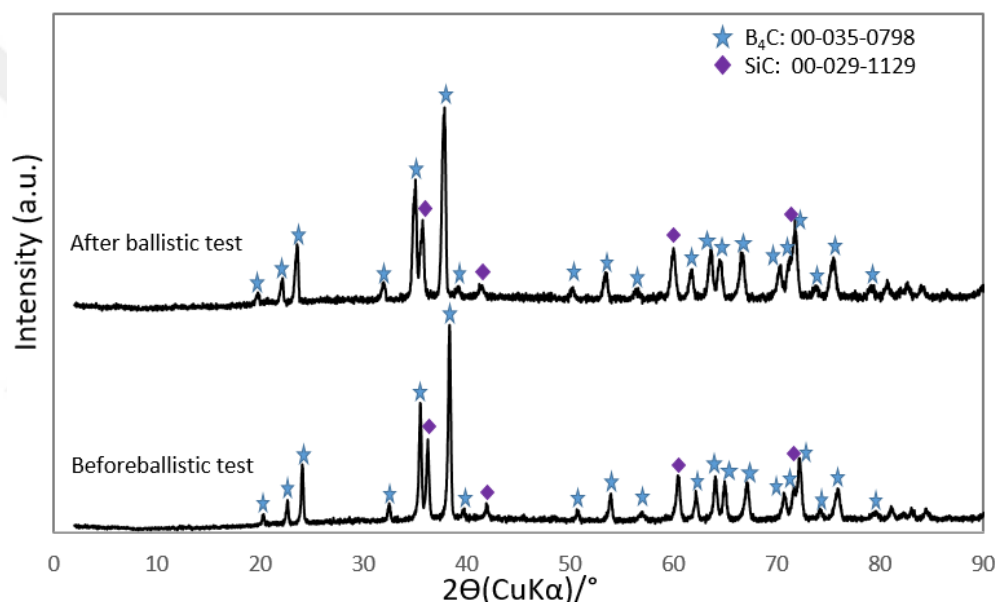


Figure 6.75 : XRD analysis of spark plasma sintered hexagonal B_4C with 5 vol. % Si before and after ballistic test.

The characteristics of B-C-Si system as evaluated, include the stability of a $\text{B}_{12}(\text{B,C,Si})_3$ solid solution with a maximum of 2.5 vol. % Si. As described by Telle and Petzow [218], the diffusion of Si into the B_4C lattice reaches 2.5 % at 2050°C , under conditions where B_4C and Si coexist. When Si enters the B_4C lattice, it replaces with C and forms $\text{B}_{12}(\text{B,C,Si})_3$. By displacement of Si with C, SiC layers collapse around the $\text{B}_{12}(\text{B,C,Si})_3$ grains during the liquid phase hot pressing and prevents excessive grain growth [218]. No other ternary phases exist in B-C-Si system [13].

One other possibility is the presence of the SiB_6 phase which is related to the C ratio in the environment. The formation of a solid solution of $\text{B}_{12}(\text{B,C,Si})_3$ is accompanied by

the precipitation of SiC which melts eutectically with SiB₆ and residual solid Si above 1380 °C. Where the C atomic % value in the medium is above 18.5 %, the phases present in the B-C-Si system are only B₄C and SiC. As a Si incorporation into the boron carbide lattice always results in the release of C or the simultaneous formation of SiC if Si is present in excess. It may be concluded that Si substitutes for C assuming that there is no carbon in boron carbide on interstitial sites [13]. Therefore, when the SPS experimental setup system is considered, Si, which is liquefied by increasing temperature, forms SiC by taking carbon from the graphite molds. Graphite molds, caused the B-C-Si balance to increase in the C ratio, thus allowing the B₄C + SiC region to stay in the equilibrium diagram of B-Si-C system. For this reason, instead of the expected SiB₆ phase, B₄C + SiC are the only phases existed after spark plasma sintering.

Moreover, when the XRD peaks are analysed, one can realize that again noisy regions are obtained after the ballistic impact. Also, the characteristic peak with highest intensity of boron carbide is shifted to left from 38.34 ° to 37.74 which can be concluded as a distortion in the boron carbide lattice. On the other hand, the SiC peak with highest intensity showed a move from 36.22° to 35.60° after the ballistic impact applied to B₄C-Si structure.

6.6.4 XRD analysis of hexagonal boron carbide ceramics with Ti or TiO₂ additions

Figure 6.76 demonstrates the X-ray diffractograms obtained from before and after ballistic tests of hexagonal boron carbide containing 5 vol. % Ti which was spark plasma sintered at 1550 °C for 4 min under a pressure of 40 MPa in vacuum atmosphere.

According to Figure 6.76, one can clearly see that all Ti added to the system is transformed into TiB₂ in boron carbide structure. No ternary phases have been discovered related to Ti-B-C system. Only, the ternary solid solubility of the particular binary compounds except TiC_{0.81}B_{0.17} is generally less than 1 at. % TiB₂ coexists with TiC_{1-x} in a quasi-binary eutectic equilibrium at 2620 ± 15 °C. It can be concluded that TiC is not stable in the presence of B₄C but reacts to form TiB₂ + C. On the other hand, in the literature there are studies which composed TiB₂-B₄C composites from TiC and

B powders by reaction sintering [13]. Spark plasma sintering at 1550 °C for 4 min resulted in TiB₂ formation in boron carbide structure.

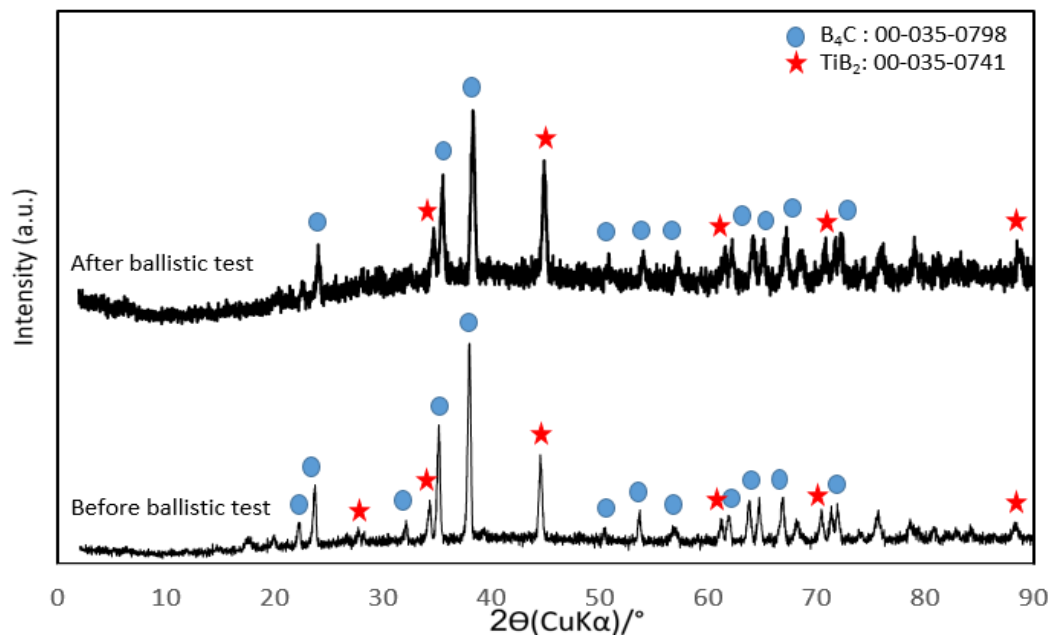


Figure 6.76 : XRD analysis of spark plasma sintered hexagonal B₄C with 5 vol. % Ti-LP before and after ballistic test.

When the XRD peaks obtained from the 5 vol % Ti including composite after the ballistic test is investigated, very distinct noisy regions can be seen. No other phases are obtained however again shifts in the peaks are evaluated. When the boron carbide peaks are investigated more closely, the peak with highest intensity is moved from 38.00 ° to 38.36 and TiB₂ characteristic peak is moved from 44.56 to 44.88. All the peaks obtained as mentioned before tend to shift to the left after the ballistic test, whereas 5 vol. % Ti-LP containing sample resulted in a shift to right.

The atomic plane spacings are used as "strain gauges" to measure changes due to elastic load. The idea is that (1) stress creates strain; (2) strain alters d-spacings; and (3) changes in d-spacings cause changes in diffraction peak positions. Since there is no preferred orientation of the carbide grains, the same averaged diffraction pattern will be seen no matter how the sample is oriented in the beam. Thus, peak position and peak shape do not change as a function of sample orientation in the beam even though there are significant variations from point to point within a grain, and from grain to grain. However, the distinction between a mechanically hydrostatic and a diffraction hydrostatic stress state is in the shape of the diffraction peak [219]. Accordingly, in

case of strain resulting from a planar stress, peaks will be shifted to lower angle for compressive stress and to higher angle for tensile stress.

Figure 6.77 shows the XRD analysis results of hexagonal boron carbide with 10 vol. % Ti-LP before and after the ballistic test. The ceramic composite was manufactured by using spark plasma sintering at 1550 °C for 4 min under a pressure of 40 MPa in vacuum.

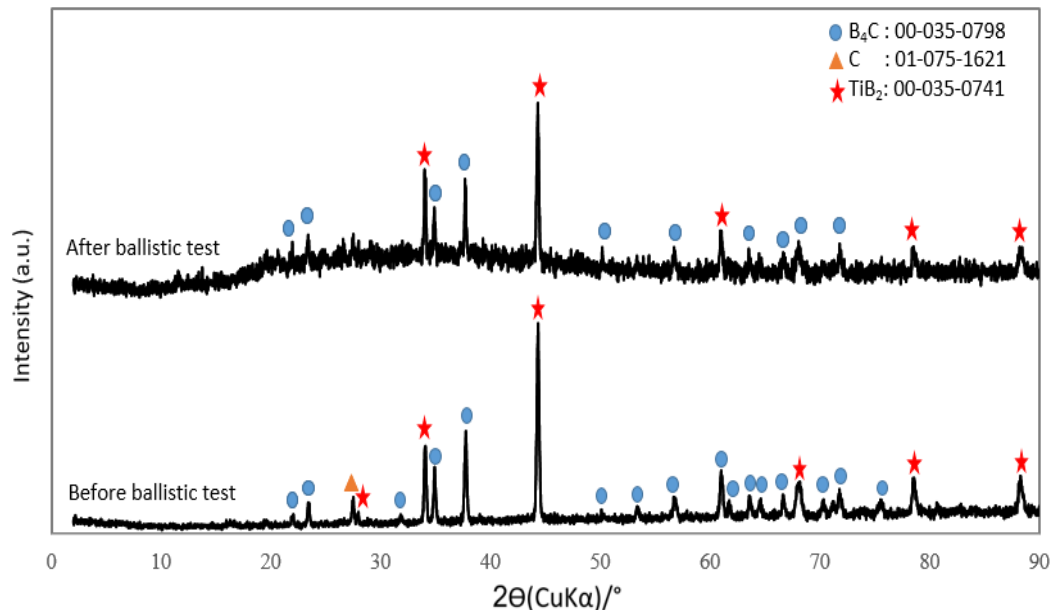


Figure 6.77 : XRD analysis of spark plasma sintered hexagonal B₄C with 10 vol. % Ti-LP before and after ballistic test.

When Figure 6.76 and 6.77 are compared, one can state that with increasing Ti amount in the boron carbide structure, the peak intensities of TiB₂ is increased., as expected. After spark plasma sintering, again no other phases could be obtained except from TiB₂ , B₄C and C. The reaction between Ti and B₄C caused to form TiB₂ and free C in the structure and all peaks could be observed regarding to these phases. Also, again with the high impact applied during the ballistic test, the noisy region became apparent and both peaks showed a shift to the left. For instance, the peak with highest intensity which belongs to TiB₂ phase is slightly shifted from 48.32 ° to 48.26 °.

Figure 6.78 shows the XRD patterns obtained from the hexagonal boron carbide with 20 vol. % Ti-LP containing sample before and after ballistic test which was spark plasma sintered at 1550 °C for 4 min under a pressure of 40 MPa for 4 min in vacuum atmosphere.

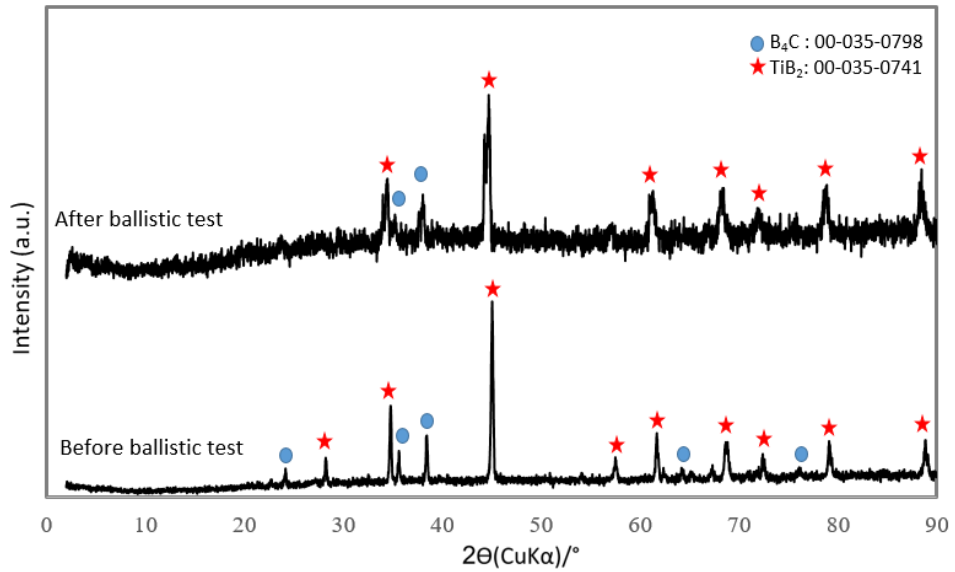


Figure 6.78 : XRD analysis of spark plasma sintered hexagonal B_4C with 20 vol. % Ti-LP before and after ballistic test.

Figure 6.69 clearly demonstrates the change in peak intensities with increasing Ti content in the starting powder mixture. With increased Ti content, the peaks which belong to B_4C started to disappear, whereas TiB_2 peak intensities increased. Unfortunately, no C phase could be observed before or after ballistic test of 20 vol. % Ti containing sample, although a severe C peak is expected. Again when after and before ballistic test XRD results are compared, the peaks got noisy and a slight shift to left is observed. The TiB_2 characteristic peak with highest intensity is moved from 45.06° to 44.76° . It can be concluded that a distinct distortion in the lattice of material is obtained due to the drastic damage occurred on the structure during the ballistic impact.



7. CONCLUSIONS

The general results obtained in this study in terms of cylindrical boron carbide samples are listed below in detail.

1. In this study, monolithic boron carbide ceramics, 2 vol. % C and % CNT added boron carbide are produced in cylindrical final shape with 50 mm diameter and 5 mm thickness. These experiments could be designated as preliminary works for further experiments which helped to determine the spark plasma sintering procedure conditions.
2. Monolithic boron carbide ceramics, 2 vol. % C-black and 2 vol. % CNT added boron carbide are heated with approximately 150 °C/min and spark plasma sintered at 1650 and 1725 °C for 5 min under an applied pressure of 40 MPa in vacuum atmosphere. The samples were achieved in one piece without any melting or mold adhesion.
3. Monolithic B₄C started to shrink at 1595 °C, whereas the shrinking temperature was reduced to 1525 °C in C-black and CNT containing samples. Densification curves clearly demonstrated that both C-black and CNT additions were effective in enhancing the sintering process.
4. Addition of both 2 vol. % C-black and CNT resulted in higher density values. The relative density differences were more distinct in the samples which were spark plasma sintered at 1650 °C for 5 min under a pressure of 40 MPa in vacuum atmosphere.
5. Increasing spark plasma sintering temperature accelerated diffusion and improved sintering. Approximately 99 % relative density was obtained for 2 vol. % CNT included boron carbide composites which was spark plasma sintered at 1725 °C for 5 min under a pressure of 40 MPa in vacuum atmosphere.
6. When the monolithic boron carbide and 2 vol. % C-black and CNT added samples which were produced exactly in the same conditions were compared, it could be seen that both additions resulted in a significant improvement in hardness of the

ceramics. The lowest hardness value was belong to boron carbide with poor densification which was spark plasma sintered at 1650 °C as 24.6 GPa. However with 2 vol. % C-black and CNT addition increased the hardness values to 34.2 and 34.6 GPa, respectively.

7. The highest hardness value between the cylindrical shaped samples was attained in the boron carbide sample with 2 vol. % CNT addition as 36.3 GPa.

8. With the addition of 2 vol. % C-black or CNT addition to boron carbide body, fracture toughness values were also tended to increase. The highest fracture toughness, $4.5 \text{ MPa} \cdot \text{m}^{1/2}$, was achieved with the addition of 2 vol. % CNT to boron carbide which was spark plasma sintered at 1725 °C for 5 min under a pressure of 40 MPa in vacuum atmosphere.

9. When the microstructures of cylindrical samples are considered, increasing the spark plasma sintering temperature and additions of 2 vol. % C-black and CNT resulted in microstructures with lower porosities. The CNTs in the microstructures are homogeneously dispersed but not fibrous.

The general results obtained in this study in terms of hexagonal boron carbide samples are listed below in detail.

1. Monolithic boron carbide ceramics and 2 vol. % C-black, 2 vol. % CNT, 5 vol. % Al, 5 vol. % Si, 5, 10, 15 and 20 vol. % Ti and 5 and 10 vol. % $\text{TiO}_2 + \text{C}$ containing boron carbide ceramic composites are produced by using spark plasma sintering technique in an hexagonal shape with 62 mm diagonal, 31.5 mm length and 10 mm thickness which are suitable dimensions for final ballistic use.

2. Monolithic boron carbide ceramics, 2 vol. % C-black, 2 vol. % CNT, 5, 10, 15 and 20 vol. % Ti and 5 and 10 vol. % TiO_2 containing boron carbide ceramic composites are heated with 100 °C/min and spark plasma sintered at 1550 °C for 4 min under a pressure of 40 MPa in vacuum atmosphere.

3. Due to the sticking problems and low melting temperatures of Al and Si, 5 vol. % Al and Si including samples are spark plasma sintered at lower temperatures. The spark plasma sintering temperatures were 1450 and 1500 °C, respectively. The samples were heated with 100 °C/min and the soaking time was chosen to be 4 min, applied pressure was 40 MPa, and the vacuum atmosphere is used.

4. Both of the edges and the centers of the hexagonal ceramics and ceramic composites are examined in terms of density, hardness and fracture toughness. The average of edge results is calculated and compared with the center values. When the electrical properties of boron carbide is considered, the centers of the sample showed better performances compared to the edges of the same sample because the current passed through the powder sample and the die and the center of the sample reached higher temperatures during spark plasma sintering procedure.
5. Monolithic boron carbide ceramic which was spark plasma sintered at 1550 °C for 4 min under a pressure of 40 MPa in vacuum showed an average edge relative density of 94.72 % and center relative density of 95.34%.
6. 2 vol. % C-black and CNT addition resulted in higher densification in spark plasma sintered boron carbide ceramics at 1550 °C for 4 min under a pressure of 40 MPa in vacuum. The average edge relative density was found to be 95.89 % for C-black added sample and 96.17 % for CNT added sample and the center relative density values was measured to be 96.75 and 97.26 %, respectively.
7. When the displacement curves for cylindrical and hexagonal samples are compared, the shrinkage temperature difference can be seen very remarkably. 2 vol. % C and CNT added boron carbide samples start to shrink 1525 °C in cylindrical molds, whereas the shrinkage temperature in hexagonal molds is 1286°C in CNT containing sample which is nearly 250 °C lower.
8. 5 vol. % Al added boron carbide composite which was spark plasma sintered at 1450 °C for 4 min under a pressure of 40 MPa in vacuum atmosphere showed average edge relative density of 97.71 % and center relative density 98.16 %. Al addition to boron carbide leads to liquid phase sintering and the formed liquid removes the inhomogeneities and results in homogen densification. Al addition decreased the shrinkage starting temperature to 1188 °C.
9. 5 vol. % Si addition is made under two different applied pressures; 40 and 60 MPa. The reason for increase in applied pressure is poor densification of 5 vol. % Si added boron carbide composite which was spark plasma sintered at 1500 °C for 4 min under a pressure of 40 MPa in vacuum atmosphere. The average edge relative density was found out to be 94.58 % and the center relative density was 96.31 %. With increased applied pressure, the relative density of edge and center is improved to 96.41 and 97.54

% respectively. Because of sticking problems, higher spark plasma sintering temperatures could not be used in Si added boron carbide composites.

10. In this study, two different Ti with an average particle size of 26.46 μm (Ti-LP) and 5.12 μm (Ti-SP) is used. Ti-LP addition were made 5, 10, 15 and 20 vol. % to boron carbide whereas only 5 and 10 vol. % Ti-SP were added to boron carbide. With increased Ti-LP addition from 5 to 10, 15 and 20 vol. %, the relative density values tend to increase to 99.18, 99.35, 99.68 and 100 % in the center regions of the samples, respectively. When Ti-SP powders are used, 99.40 and 99.90 % relative density values are attained in the center regions of 5 and 10 vol. % Ti-SP added B_4C samples which were spark plasma sintered at 1550 $^\circ\text{C}$ for 4 min. When the soaking time is increased to 6 min, the theoretical density is attained in the center of the 5 vol. % Ti-SP containing sample.

11. When 5 and 10 vol. % $\text{TiO}_2 + \text{C}$ additions were made to B_4C , the center relative density values were found out to be 96.51 and 96.21 %, respectively. However, 5 vol. % TiO_2 added boron carbide which was spark plasma sintered at 1550 $^\circ\text{C}$ for 6 min under a pressure of 40 MPa in vacuum showed a relative density of 98.62 % in its center region. Increasing the soaking time from 4 to 6 minutes resulted in higher relative density values both in edges and center of the sample. Also, the sintering is observed to be more homogenous in the sample with 6 minute soaking time.

12. The hardness of monolithic hexagonal boron carbide is measured as 28.71 GPa in the center, whereas the average edge hardness was found out to be 27.39 GPa. The hardness of hexagonal monolithic boron carbide showed higher values in measurement regions where the relative density values are higher, the hardness is prominently dependent to density, with increasing density the hardness values increased.

13. With increasing relative density and hardness, fracture toughness values tend to decrease. The average fracture toughness value for edges is measured as 3.41 $\text{MPa}\cdot\text{m}^{1/2}$ which is higher than the more densified region, center of the sample, as 3.23 $\text{MPa}\cdot\text{m}^{1/2}$ in monolithic boron carbide which was spark plasma sintered at 1550 $^\circ\text{C}$ for 4 min under a pressure of 40 MPa in vacuum atmosphere.

14. When 2 vol. % C-black or CNT additions were made to boron carbide, the hardness values of the samples were increased to 32.81 and 33.66 in the center regions

of the samples, respectively in the samples which were spark plasma sintered at 1550 °C for 4 min under a pressure of 40 MPa in vacuum.

15. The center of 2 vol. % C- black containing boron carbide ceramic 3.69 MPa·m^{1/2} in and 4.46 MPa·m^{1/2} fracture toughness is attained in the center of 2 vol. % CNT containing boron carbide. These increases corresponds to approximately 15 % and 38 % increase in fracture toughness values of 2 vol. % C and CNT added boron carbide samples compared to monolithic boron carbide produced exactly in the same conditions, respectively.

16. The edge hardness values of 5 vol. % Al containing boron carbide, which was spark plasma sintered at 1450 °C for 4 min under a pressure of 40 MPa in vacuum, were ranged between 29.68 to 31.65 GPa, with an average of 30.93 GPa, whereas the center hardness was found out to be 31.96 GPa.

17. The hardness and fracture toughness values attained in edge regions of hexagonal boron carbide sample with 5 vol. % Al are found out to be inversely proportional. However the hardness values are observed to be directly proportional with the relative density values. The highest hardness is obtained in the center region of the 5 vol. % Al containing hexagonal boron carbide which is also the most densified part of the sample. Also, the lowest hardness value was seen in Edge 6, which can be regarded as the part with lowest density. The highest fracture toughness was seen in the Edge 6 as 6.06 MPa·m^{1/2} whereas this edge showed the lowest hardness value of whole sample, also the relative density was lowest in this part of the sample.

18. With the increasing applied pressure, the hardness values increased in 5 vol. % Si containing sample which were spark plasma sintered at 1500 °C for 4 min. 40 MPa pressure resulted in 31.88 GPa hardness in the center and 28.22 GPa hardness is calculated for the average edge hardness. However, the highest hardness is attained in the center of 5 vol. % Si containing sample which was spark plasma sintered under 60 MPa pressure as 32.32 GPa, and the average edge hardness was found out to be 29.97 GPa.

19. With the increased applied pressure from 40 to 60 MPa during spark plasma sintering, the fracture toughness of 5 vol. % Si added boron carbide composites are also increased. In addition, the hexagonal geometry effect is very clear in 5 vol. % Si containing boron carbide composites. The highest fracture toughness values are

attained in edge regions with lowest density and the average edge fracture toughness is found to be higher than the center fracture toughness values. The average edge fracture toughness is attained in the sample with 5 vol. % Si, which was spark plasma sintered at 1500 °C for 4 min under a pressure of 60 MPa in vacuum, as 5.71 MPa·m^½.

20. With increasing Ti-LP content in B₄C structure from 5 to 10, 15 and 20 vol. %, the densification is promoted however the hardness values is decreased. Hardness is observed to be increased compared to monolithic boron carbide and after adding 15 and 20 vol.% Ti, it diminishes. The highest hardness is attained in the center region of vol. % Ti-LP containing sample which was heated with 100 °C/min and spark plasma sintered at 1550 °C for 4 min under a pressure of 40 MPa as 32.23 GPa while the average center hardness is found out to be 30.80 GPa.

21. When all the hardness and fracture toughness values of Ti-LP containing samples are considered particularly, hardness can be defined as higher in the regions where relative density is higher whereas fracture toughness is generally lower in the regions where densification is higher. The highest fracture toughness is observed in 10 vol. % Ti-LP added sample as 6.25 MPa·m^½ in the center and 6.51 MPa·m^½ as an edge average. All Ti additions with different contents resulted in higher fracture toughness values compared to monolithic boron carbide ceramics. The main reason for the increase in toughness is linked to the different thermal expansion coefficients between B₄C and TiB₂.

22. With increasing Ti-SP amount from 5 to 10 vol. %, the hardness value for both center and edges are decreased. The center hardness value of 5 vol. % Ti-SP is found out to be 32.7 GPa and the average edge hardness is measured 31.07 GPa, whereas the center hardness of 10 vol. % Ti-SP were 31.89 and the average hardness was measured 30.78 GPa. In all samples with different Ti-SP contents, edge regions exhibited lower hardness values compared to center of the sample.

23. Between all fracture toughness values obtained in this thesis, the highest fracture toughness belongs to 10 vol. % Ti-SP containing sample which was spark plasma sintered at 1550 °C for 5 min under a pressure of 40 MPa with 6.54 MPa·m^½ value in its center.

24. With increasing TiO₂ amount in hexagonal boron carbide, the hardness values in both center and edge is decreased. This can be due to the lower hardness of the

reaction product, TiB_2 , than that of B_4C according to the rule of mixtures. The highest hardness value is seen in the center of the hexagonal boron carbide sample with 5 vol. % Ti-LP which were spark plasma sintered at 1550 °C, as 32.50 GPa, whereas the average edge is calculated to be 30.98 GPa.

25. The center regions of 5 and 10 vol. % TiO_2 added samples showed lower fracture toughness values compared to edges. Because neither of the specimen can succeed in reaching theoretical density values in TiO_2 containing boron carbide, instead of smaller grain size, pores are seemed to be more effective to increase the fracture toughness. The fracture toughness values were found out to be very close ranging between 5.62 and 6.89 $\text{MPa}\cdot\text{m}^{1/2}$.

26. The ballistic tests were held according to NIJ 0101.04 standards. In the experiments, 7.62 x 50 mm NATO armour piercing bullets were used and the velocity of the bullet was 868 ± 15 m/s. Under the protection of the monolithic hexagonal boron carbide sample which was spark plasma sintered at 1550 °C for 4 min under a pressure of 40 MPa, the projectile does not cause a distinct radial deformation on the surface of Al 5083 backing alloy, however spalling occurred and the penetration of bullet to the backing block is measured to be 3.87 mm.

27. 2 vol. % C- black addition resulted in a deterioration in ballistic performance of boron carbide. DOP (depth of penetration) value is measured to be 6.86 mm. DOP value on the surface of backing material protected with 2 vol. % CNT added boron carbide tile are found out to be 9.50 mm. Although better density, hardness and fracture toughness were observed in 2 vol. % CNT added sample compared to monolithic boron carbide ceramics produced exactly in same conditions, the DOP values are found out to be higher.

28. The measured DOP values was measured to be 3.10 mm on the backing block surface after the protection of 5 vol. % Al containing boron carbide which was spark plasma sintered at 1450 °C for 5 min under a pressure of 40 MPa in vacuum. Although the fracture toughness improved and ballistic performances are remained similar compared to monolithic boron carbide, when the target became ductile with the addition of Al, a different damage type occurred on the backing alloy surface. The projectile formed hole growth on the surface of the backing alloy.

29. DOP value attained in the Al surface protected by 5 vol. % Si added boron carbide produced under 40 MPa pressure in spark plasma sintering was 11.55 mm which was highest DOP value between all spark plasma sintered ceramic and composite tiles. Also, DOP values improved to 8.52 mm in boron carbide sample with 5 vol. % Si spark plasma sintered under 60 MPa pressure.

30. The lowest DOP value in this study is attained as 0.80 mm under the protection of 5 vol. % Ti containing hexagonal boron carbide sample which was spark plasma sintered at 1550 °C for 4 min under a pressure of 40 MPa in vacuum. No hole or radial damage is occurred, just scratches are obtained on the Al surface.

31. Under the protection of 10 vol. % Ti-LP included boron carbide composites which were spark plasma sintered at 1550 °C for 4 min under an applied pressure of 40 MPa in vacuum, the DOP value was found out to be 0.88 mm. When compared with 5 vol. % Ti containing boron carbide, the change in DOP was low; however with the total weight increase was remarkable. In light-weight armours, the most important factor besides the ballistic performance is the weight of the armor.

32. No hole or radial damage is formed with the interaction of bullet and composite tile on the surface of Al backing block, only the scratches are obtained under the protection of 15 vol. % Ti-LP added boron carbide which was spark plasma sintered at 1550 °C for 4 min under a pressure of 40 MPa in vacuum. The DOP caused by the protection of 15 vol. % Ti-LP added boron carbide was 0.92 mm.

33. The DOP value attained on the Al backing surface was 0.87 mm under the protection of 20 vol. % Ti included sample. However, the weight increase should be considered and should be known that with the addition of 20 vol. % Ti, the weight of hexagonal armor is increased to 75.20 g.

34. When the ballistic efficiency factors of both samples are calculated, only 5 vol. % Al and 5 vol. % Ti including boron carbide composite material showed better differential efficiency factor which means in terms of weight, only these two composites show better ballistic performance compared to monolithic boron carbide ceramics.

35. After the ballistic test, the collected particles and powders were subjected to sieve analysis. The percentage weight of retained coarser particles is highest in 5 vol. % Si containing hexagonal boron carbide composite tile which was spark plasma sintered at 1500 °C for 4 min under a pressure of 40 MPa in vacuum atmosphere and

the lowest percentage weight of retained coarser particles is attained in 5 vol. % Ti added boron carbide sample which was spark plasma sintered at 1550 °C for 4 min under a pressure of 40 MPa in vacuum. Finer powders are attained after the ballistic tests which showed lower DOP values and coarser particles are obtained after the shots which resulted higher DOP values.

36. When the XRD analysis were made to hexagonal ceramic and ceramic composite tiles before and after the ballistic test, neither of the samples showed amorphous phase . However in both samples, a noisy background is obtained after the ballistic tests. Also, when compared with before ballistic test XRD peaks, observed peaks were shifted left to very slightly after the ballistic tests. According to Bragg's Law, a left shift in peaks means that dspacing value is increased, so that the lattice distortion with the ballistic impact can be mentioned.

37. After spark plasma sintering at 1550 °C, no new phase transformations is obtained in monolithic boron carbide or 2 vol. % C or CNT added boron carbide sample.

38. Spark plasma sintering at 1450 °C for 4 min of 5 vol. % Al addition resulted in to form $Al_8B_4C_7$ and Al_2OC phases. $Al_8B_4C_7$ phase in the structure is known for increasing the sinterability of boron carbide and results in achieveing higher relative density values. reason for the formation of Al_2OC phase is thought to be due to the easy oxidation of the Al additive added to the structure.

39. XRD peaks obtained from spark plasma sintered boron carbide with 5 vol. % Si which was heated with 100 °C/min and sintered at 1500 °C for 4 min under a pressure of 40 MPa showed that all Si in the starting powder transformed into SiC. However, no free boron phase could be observed.

40. All Ti added to the system is transformed into TiB_2 in boron carbide structure in the samples with 5, 10, 15 and 20 vol. % Ti-LP and 5 and 10 vol. % Ti-SP. No ternary phases have been discovered related to Ti-B-C system. When the microstructures of Ti containing sample are examined, it can be seen that melted Ti surrounded the boron carbide grains and TiB_2 is formed around the B_4C grains as agglomerates which causes to form free C areas in the center of the agglomerates. After the nucleation of Ti liquid phase in the boron carbide structure, the newly formed TiB_2

form granules of similar size to the B_4C grain size. The process continues until the coarse-grained Ti melts and completely turns into small TiB_2 grains.

41. The addition of 5 or 10 vol. % TiO_2 resulted in the formation of TiB_2 in the boron carbide structure. Also, C phase is also obtained in XRD analysis of the samples which were spark plasma sintered at 1550 °C for 4 or 6 min under a pressure of 40 MPa in vacuum.

42. With increasing Ti-SP or Ti-LP content, the peak intensities of TiB_2 tend to increase, whereas the B_4C peak intensities get smaller. The same trend is also obtained in TiO_2 included boron carbide samples. When Ti-LP, Ti-SP and TiO_2 peaks are considered, a difference in the peak intensities can be observed. TiO_2 addition resulted in higher peak intensities compared to same amount of Ti-SP containing sample and Ti-SP addition resulted in higher peak intensities compared to same amount of Ti-LP containing sample.

REFERENCES

- [1] **Thévenot, F.** (1990). Boron carbide—a comprehensive review. *Journal of the European Ceramic Society*, 6 (4), 205-225.
- [2] **Pierson, H. U.** (1996). *Handbook of Refractory Carbides and Nitrides*. United States: Noyes Publications.
- [3] **Makarenko, G. N.** (1977). Borides of the IVB Group. In *Boron and Refractory Borides* (pp. 310-330). Berlin Heidelberg: Springer.
- [4] **Tabor, D.** (2000). *The hardness of metals*. London: Oxford University Press.
- [5] **Oliver, W. C., & Pharr, G. M.** (1992). An improved technique for determining hardness and elastic modulus using load and displacement sensing indentation experiments. *Journal of Materials Research*, 7 (6), 1564-1583.
- [6] **Domnich, V., Reynaud, S., Haber, R. A., & Chhowalla, M.** (2011). Boron carbide: structure, properties, and stability under stress. *Journal of the American Ceramic Society*, 94 (11), 3605-3628.
- [7] **Lee H., & Speyer R.F.** (2002). Hardness and Fracture Toughness of Pressureless-Sintered Boron Carbide (B₄C). *J. Am. Ceram. Soc.*, 85 (5), 1291–1293.
- [8] **Gadow, R., & Von Niessen, K.** (2006). Lightweight ballistic with additional stab protection made of thermally sprayed ceramic and cermet coatings on aramide fabrics. *International Journal of Applied Ceramic Technology*, 3 (4), 284-292.
- [9] **Medvedovski, E. (Ed.)**. (2006). *Ceramic Armor and Armor Systems*. Ohio: Ceramic Transactions - American Ceramic Society.
- [10] **Orlovskaya N., Lugovy M., Subbotin V., Rachenko O., Adams J., Chheda M.,, Yarmolenko S.** (2004). Design and manufacturing B₄C-SiC layered ceramics for armor applications. *Ceramic Armor and Armor Systems*, 151, 59-70.
- [11] **Skaggs, S. R.** (2008). A brief history of ceramic armor development. *27th Annual Cocoa Beach Conference on Advanced Ceramics and Composites: A: Ceramic Engineering and Science Proceedings*, 24 (3), 337-349. John Wiley & Sons, Inc.
- [12] **Speyer, R. F., & Lee, H.** (2003). Improved pressureless densification of B₄C. *Ceramic Armor and Armor Systems*, 151, 71-82.
- [13] **Riedel, R. (Ed.)** (2000). *Handbook of Ceramic Hard Materials*. Darmstadt: Wiley VCH.
- [14] **Zhang, Z. H., Liu, Z. F., Lu, J. F., Shen, X. B., Wang, F. C., & Wang, Y. D.** (2014). The sintering mechanism in spark plasma sintering—Proof of the occurrence of spark discharge. *Scripta materialia*, 81, 56-59.

- [15] **Bouchacourt, M., & Thevenot, F.** (1981). Analytical investigations in the B₄C system. *Journal of the Less Common Metals*, 82, 219-226.
- [16] **Conard, J., Bouchacourt, M., Thevenot, F., & Hermann, G.** (1986). ¹³C and ¹¹B nuclear magnetic resonance investigations in the boron carbide phase homogeneity range: A model of solid solution. *Journal of the Less Common Metals*, 117 (1-2), 51-60.
- [17] **Suri, A. K., Subramanian, C., Sonber, J. K., & Murthy, T. C.** (2010). Synthesis and consolidation of boron carbide: a review. *International Materials Reviews*, 55 (1), 4-40.
- [18] **Mohanty, R. M., Balasubramanian, K., & Seshadri, S. K.** (2011). Evolution of Crystallographic Structures and Phases in Micropyretically Formed Boron Rich Boron Carbide—a New Material System. In *Advances in Ceramics-Characterization, Raw Materials, Processing, Properties, Degradation and Healing*. InTech.
- [19] **Cardarelli, F.** (2008). *Materials handbook: a concise desktop reference*. Springer Science & Business Media.
- [20] **Kovalev D.Y. & Konovalihin S.V.** (2017). Boron Carbide. In *Concise Encyclopedia of Self-Propagating High-Temperature Synthesis*, Elsevier.
- [21] **Jimbou, R., Saidoh, M., Nakamura, K., Akiba, M., Suzuki, S., Gotoh, Y., ... & Morita, K.** (1996). New composite composed of boron carbide and carbon fiber with high thermal conductivity for first wall. *Journal of Nuclear Materials*, 233, 781-786.
- [22] **Jimbou, R., Kodama, K., Saidoh, M., Suzuki, Y., Nakagawa, M., Morita, K., & Tsuchiya, B.** (1997). Thermal conductivity and retention characteristics of composites made of boron carbide and carbon fibers with extremely high thermal conductivity for first wall armour. *Journal of Nuclear Materials*, 241, 1175-1179.
- [23] **Gosset, D., & Provot, B.** (2001). Boron carbide as a potential inert matrix: an evaluation. *Progress in Nuclear Energy*, 38 (3-4), 263-266.
- [24] **Mortensen, M. W., Sørensen, P. G., Björkdahl, O., Jensen, M. R., Gundersen, H. J. G., & Bjørnholm, T.** (2006). Preparation and characterization of Boron carbide nanoparticles for use as a novel agent in T cell-guided boron neutron capture therapy, *Applied Radiation and Isotopes*, 64 (3), 315-324.
- [25] **Medvedovski, E.** (2003). Silicon Carbide-Based Ceramics for Ballistic Protection. *Ceramic Armor and Armor Systems*, 151, 19-35.
- [26] **Kaufmann, C., Cronin, D., Worswick, M., Pageau, G., & Beth, A.** (2003). Influence of material properties on the ballistic performance of ceramics for personal body armour, *Shock and Vibration*, 10 (1), 51-58.
- [27] **Cho, N.** (2006). *Processing of boron carbide*. (Doctoral dissertation). Georgia Institute of Technology, GEORGIA.
- [28] **Alizadeh, A., Taheri-Nassaj, E., & Ehsani, N.** (2004). Synthesis of boron carbide powder by a carbothermic reduction method. *Journal of the European Ceramic Society*, 24 (10), 3227-3234.

- [29] **Sheng, Y., Li, G., Meng, H., Han, Y., Xu, Y., Wu, J., ... & Zhang, X.** (2018). An improved carbothermal process for the synthesis of fine-grained boron carbide microparticles and their photoelectrocatalytic activity, *Ceramics International*, *14*, 1052-1058.
- [30] **Weimer, A. W.** (1997). Thermochemistry and kinetics. In *Carbide, nitride and boride materials synthesis and processing*. Netherlands: Springer.
- [31] **Wiley, C. S.** (2011). *Synergistic methods for the production of high-strength and low-cost boron carbide*. Georgia Institute of Technology, GEORGIA.
- [32] **Turan, A.** (2014). Production of TiB₂ based advanced technology ceramics by utilizing domestic raw materials (Doctoral dissertation). Istanbul Technical University, ISTANBUL.
- [33] **Aghaie, A., Falamaki, C., Yekta, B. E., & Afarani, M. S.** (2002). Effect of seeding on the synthesis of B₄C by the magnesiothermic reduction route, *Ind. Ceram.*, *22* (2), 121–125.
- [34] **Asgarian, P., Nourbakhsh, A., Amin, P., Ebrahimi-Kahrizsangi, R., & MacKenzie, K. J.** (2014). The effect of different sources of porous carbon on the synthesis of nanostructured boron carbide by magnesiothermic reduction. *Ceramics International*, *40* (10), 16399-16408.
- [35] **Jain, A., Anthonysamy, S., Ananthasivan, K., Ranganathan, R., Mittal, V., Narasimhan, S. V., & Rao, P. V.** (2008). Characterization of electrodeposited elemental boron. *Materials Characterization*, *59* (7), 890-900.
- [36] **Yamada, K.** (1996). Boron Carbide Particles Formed from an Amorphous Boron/Graphite Powder Mixture Using a Shock-Wave Technique. *Journal of the American Ceramic Society*, *79* (4), 1113-1116.
- [37] **Rahaman, M., & Rahaman, M. N.** (2006). *Ceramic processing*. CRC press.
- [38] **Carter, C. B., & Norton, M. G.** (2007). *Ceramic Materials: Science and Engineering*. Springer Science & Business Media.
- [39] **Fang, Z. Z.** (Ed.). (2010). *Sintering of Advanced Materials*. Elsevier.
- [40] **German, R. M.** (1996). *Sintering theory and practice*. New York: John Wiley and Sons.
- [41] **Castro, R., & van Benthem, K.** (Eds.). (2012). *Sintering: mechanisms of convention nanodensification and field assisted processes* (Vol. 35). Springer Science & Business Media.
- [42] **German, R. M.** (2013). *Liquid phase sintering*. New York, USA: Springer Science & Business Media.
- [43] **Moya, J. S., Baudin, C., & Miranzo, P.** (2003). Sintering. *Encyclopedia of Physical Science and Technology, Eighteen-Volume Set*, 865-878.
- [44] **German, R. M.** (2014). *Sintering: from empirical observations to scientific principles*. New York, USA: Butterworth-Heinemann.

- [45] **Brook, R. J.** (Ed.). (2012). *Concise encyclopedia of advanced ceramic materials*. Elsevier.
- [46] **Gupta N., Basu B.** (2018). *Hot pressing and spark plasma sintering techniques of intermetallic matrix composites*, In *Intermetallic Matrix Composites*, Woodhead Publishing.
- [47] **Harmer M.P.** (1991). *Hot Pressing: Technology and Theory*, In *Concise Encyclopedia of Advanced Ceramic Materials*, Pergamon, 222-225.
- [48] **Hu, C., Li, F., Qu, D., Wang, Q., Xie, R., Zhang, H., ... & Zhou, Y.** (2014). Developments in hot pressing (HP) and hot isostatic pressing (HIP) of ceramic matrix composites. *Advances in Ceramic Matrix Composites*, 164-189.
- [49] **Garay, J. E.** (2010). Current-activated, pressure-assisted densification of materials. *Annual review of materials research*, 40, 445-468.
- [50] **Technische Universitat Darmstat, FAST School, Guillon O.** (2010). *Technological aspects of FAST*. [PowerPoint slides].
- [51] **Grasso, S., Sakka, Y., & Maizza, G.** (2009). Electric current activated/assisted sintering (ECAS): a review of patents 1906–2008. *Science and Technology of Advanced Materials*, 10 (5), 053001.
- [52] **Munir, Z. A., Anselmi-Tamburini, U., & Ohyanagi, M.** (2006). The effect of electric field and pressure on the synthesis and consolidation of materials: a review of the spark plasma sintering method. *Journal of Materials Science*, 41 (3), 763-777.
- [53] **Yang Y. F. & Qian M.** (2015). *Spark plasma sintering and hot pressing of titanium and titanium alloys*, In *Titanium Powder Metallurgy*, Butterworth-Heinemann, 219-235.
- [54] **Zhang, D., Zhang, L., Guo, J., & Tuan, W. H.** (2006). Direct evidence of temperature variation within ceramic powder compact during pulse electric current sintering. *Journal of the American Ceramic Society*, 89 (2), 680-683.
- [55] **Anselmi-Tamburini, U., Garay, J. E., & Munir, Z. A.** (2006). Fast low-temperature consolidation of bulk nanometric ceramic materials. *Scripta materialia*, 54 (5), 823-828.
- [56] **Bernard, F. I. G. S., Spinassou, N., Paris, S., Gaffet, E., Woolman, J. N., & Munir, Z. A.** (2004). Dense nanostructured materials obtained by spark plasma sintering and field activated pressure assisted synthesis starting from mechanically activated powder mixtures. *Science of Sintering*, 36 (3), 155-164.
- [57] **Langer, J., Quach, D. V., Groza, J. R., & Guillon, O.** (2011). A comparison between FAST and SPS apparatuses based on the sintering of oxide ceramics. *International Journal of Applied Ceramic Technology*, 8 (6), 1459-1467.
- [58] **Chaim, R.** (2007). Densification mechanisms in spark plasma sintering of nanocrystalline ceramics. *Materials Science and Engineering: A*, 443 (1), 25-32.

- [59] **Luke M.T.** (2009). *Microstructural Evolution of Nickel During Spark Plasma Sintering*. (Doctoral Dissertation). Boise State University. IDAHO.
- [60] **Zhang, Z. H., Liu, Z. F., Lu, J. F., Shen, X. B., Wang, F. C., & Wang, Y. D.** (2014). The sintering mechanism in spark plasma sintering—Proof of the occurrence of spark discharge. *Scripta materialia*, 81, 56-59.
- [61] **Perera, D. S., Tokita, M., & Moricca, S.** (1998). Comparative study of fabrication of Si₃N₄/SiC composites by spark plasma sintering and hot isostatic pressing. *Journal of the European Ceramic Society*, 18 (4), 401-404.
- [62] **Song, S. X., Wang, Z., & Shi, G. P.** (2013). Heating mechanism of spark plasma sintering. *Ceramics International*, 39 (2), 1393-1396.
- [63] **Tang, Y., Xue, J. X., Zhang, G. J., Wang, X. G., & Xu, C. M.** (2014). Microstructural differences and formation mechanisms of spark plasma sintered ceramics with or without boron nitride wrapping. *Scripta Materialia*, 75, 98-101.
- [64] **Zhang, F., Mihoc, C., Ahmed, F., Lathe, C., & Burkel, E.** (2011). Thermal stability of carbon nanotubes, fullerene and graphite under spark plasma sintering. *Chemical physics letters*, 510 (1), 109-114.
- [65] **Omori, M.** (2000). Sintering, consolidation, reaction and crystal growth by the spark plasma system (SPS). *Materials Science and Engineering: A*, 287 (2), 183-188.
- [66] **Hulbert, D. M., Anders, A., Andersson, J., Lavernia, E. J., & Mukherjee, A. K.** (2009). A discussion on the absence of plasma in spark plasma sintering. *Scripta Materialia*, 60 (10), 835-838.
- [67] **Hulbert, D. M., Anders, A., Dudina, D. V., Andersson, J., Jiang, D., Unuvar, C., ... & Mukherjee, A. K.** (2008). The absence of plasma in “spark plasma sintering”. *Journal of Applied Physics*, 104 (3), 033305.
- [68] **Olevsky, E., Kandukuri, S., & Froyen, L.** (2008). Analysis of mechanisms of spark-plasma sintering. *Key Engineering Materials*, 368, 1580-1584.
- [69] **Technische Universitat Darmstat, FAST School, Anselmi-Tamburini, U.** (2010). Mechanisms in FAST sintering. [PowerPoint slides].
- [70] **Anselmi-Tamburini, U., Gennari, S., Garay, J. E., & Munir, Z. A.** (2005). Fundamental investigations on the spark plasma sintering/synthesis process: II. Modeling of current and temperature distributions. *Materials Science and Engineering: A*, 394 (1), 139-148.
- [71] **Carney, C. M., & Mah, T. I.** (2008). Current isolation in spark plasma sintering of conductive and nonconductive ceramics. *Journal of the American Ceramic Society*, 91 (10), 3448-3450.
- [72] **Zavaliangos, A., Zhang, J., Krammer, M., & Groza, J. R.** (2004). Temperature evolution during field activated sintering. *Materials Science and Engineering: A*, 379 (1), 218-228.
- [73] **Vanmeensel, K., Laptev, A., Hennicke, J., Vleugels, J., & Van der Biest, O.** (2005). Modelling of the temperature distribution during field assisted sintering. *Acta Materialia*, 53 (16), 4379-4388.

- [74] **Technische Universitat Darmstat, FAST School, Zavaliangos, A.** (2010). Finite Element Modeling of FAST. [PowerPoint slides].
- [75] **Tiwari, D., Basu, B., & Biswas, K.** (2009). Simulation of thermal and electric field evolution during spark plasma sintering. *Ceramics International*, 35 (2), 699-708.
- [76] **Dobedoe, R. S., West, G. D., & Lewis, M. H.** (2005). Spark plasma sintering of ceramics: understanding temperature distribution enables more realistic comparison with conventional processing. *Advances in Applied Ceramics*, 104 (3), 110-116.
- [77] **Voisin, T., Durand, L., Karnatak, N., Le Gallet, S., Thomas, M., Le Berre, Y., ... & Couret, A.** (2013). Temperature control during spark plasma sintering and application to up-scaling and complex shaping. *Journal of Materials Processing Technology*, 213 (2), 269-278.
- [78] **Riedel, R., & Chen, I. W. (Eds.)**. (2013). *Ceramics Science and Technology, Volume 2: Materials and Properties*. John Wiley & Sons.
- [79] **Kuzenkova, M. A., Kislyi, P. S., Grabchuk, B. L., & Bodnaruk, N. I.** (1979). The structure and properties of sintered boron carbide. *Journal of the Less Common Metals*, 67 (1), 217-223.
- [80] **Dole, S. L., Prochazka, S., & Doremus, R. H.** (1989). Microstructural coarsening during sintering of boron carbide. *Journal of the American Ceramic Society*, 72 (6), 958-966.
- [81] **Zorzi, J. E., Perottoni, C. A., & Da Jornada, J. A. H.** (2005). Hardness and wear resistance of B₄C ceramics prepared with several additives. *Materials Letters*, 59 (23), 2932-2935.
- [82] **Roy, T. K., Subramanian, C., & Suri, A. K.** (2006). Pressureless sintering of boron carbide. *Ceramics International*, 32 (3), 227-233.
- [83] **Speyer, R. F., Lee, H., & Bao, Z.** (2009). *U.S. Patent No. 7,592,279*. Washington, DC: U.S. Patent and Trademark Office.
- [84] **Schwetz, K. A., & Grellner, W.** (1981). The influence of carbon on the microstructure and mechanical properties of sintered boron carbide. *Journal of the Less Common Metals*, 82, 37-47.
- [85] **Telle, R., & Petzow, G.** (1988). Strengthening and toughening of boride and carbide hard material composites. *Materials Science and Engineering: A*, 105, 97-104.
- [86] **Vlajic, M. D., & Krstic, V. D.** (1998). *U.S. Patent No. 5,720,910*. Washington, DC: U.S. Patent and Trademark Office.
- [87] **Sigl, L., Thaler, H., & Schwetz, K. A.** (1996). *U.S. Patent No. 5,505,899*. Washington, DC: U.S. Patent and Trademark Office.
- [88] **Baharvandi, H. R., Hadian, A. M., Abdizadeh, A., & Ehsani, N.** (2006). Investigation on addition of ZrO₂-3mol% Y₂O₃ powder on sintering behavior and mechanical properties of B₄C. *Journal of materials science*, 41 (16), 5269-5272.

- [89] **Baharvandi, H. R., Hadian, A. M., Abdizade, H., & Ehsani, N.** (2006). Investigation on addition of talc on sintering behavior and mechanical properties of B₄C. *Journal of materials engineering and performance*, 15 (3), 280-283.
- [90] **Sano, T., Vargas-Gonzalez, L., LaSalvia, J., & Hogan, J. D.** (2017). Dynamic Failure and Fragmentation of a Hot-Pressed Boron Carbide. *Journal of Dynamic Behavior of Materials*, 3, 1-9.
- [91] **Swab, J. J., Meredith, C. S., Casem, D. T., & Gamble, W. R.** (2017). Static and dynamic compression strength of hot-pressed boron carbide using a dumbbell-shaped specimen. *Journal of Materials Science*, 52 (17), 10073-10084.
- [92] **Savio, S. G., & Madhu, V.** (2017). Effect of Tile Thickness and Projectile Velocity on the Ballistic Performance of Boron Carbide Against 12.7 mm AP. *Procedia Engineering*, 173, 286-292.
- [93] **Hogan, J. D., Farbaniec, L., Mallick, D., Domnich, V., Kuwelkar, K., Sano, T., ... & Ramesh, K. T.** (2017). Fragmentation of an advanced ceramic under ballistic impact: Mechanisms and microstructure. *International Journal of Impact Engineering*, 102, 47-54.
- [94] **Sedlák, R., Kovalčíková, A., Balko, J., Rutkowski, P., Dubiel, A., Zientara, D., ... & Dusza, J.** (2017). Effect of graphene platelets on tribological properties of boron carbide ceramic composites. *International Journal of Refractory Metals and Hard Materials*, 65, 57-63.
- [95] **Ekbon, L. B., & Amundin, C.** (1981). Microstructural evaluation of sintered boron carbides with different compositions. *Proc. 11 th International Conf. on Science of Ceramics held at Stenungsund, Sweden, June 14-17, 1981*. Edited by R. Carlsson and S. Karlsson. *Swedish Ceram. Soc.*, Gothenburg, Sweden, 237-243.
- [96] **Champagne, B., & Angers, R.** (1979). Mechanical Properties of Hot-Pressed B-B₄C Materials. *Journal of the American Ceramic Society*, 62, 149-153.
- [97] **Larsson, P., Axen, N., & Hogmark, S.** (2000). Improvements of the microstructure and erosion resistance of boron carbide with additives. *Journal of materials science*, 35 (14), 3433-3440.
- [98] **Mikijelj, B., Victor, G., & Schwetz, K. A.** (2007). *U.S. Patent No. 7,309,672*. Washington, DC: U.S. Patent and Trademark Office.
- [99] **Larker, H. T., Hermansson, L., & Adlerborn, J.** (1988). Hot Isostatic Pressing and its applicability To silicon carbide and boron carbide. *J. Ind. Ceram.*, 8 (1), 17-25.
- [100] **Schwetz, K. A., Sigl, L. S., & Pfau, L.** (1997). Mechanical properties of injection molded B₄C-C ceramics. *Journal of solid state chemistry*, 133 (1), 68-76.
- [101] **Ghosh, D., Subhash, G., Sudarshan, T. S., Radhakrishnan, R., & Gao, X. L.** (2007). Dynamic indentation response of fine-grained boron carbide. *Journal of the American Ceramic Society*, 90 (6), 1850-1857.

- [102] **Kim, K. H., Chae, J. H., Park, J. S., Kim, K. D., Shim, K. B., & Lee, B. H.** (2007). Methanol washing effects on spark plasma sintering behavior and mechanical properties of B₄C ceramics. *Journal of Ceramic Processing Research*, 8 (4), 238-242.
- [103] **Anselmi-Tamburini, U., Munir, Z. A., Koodera, Y., Imai, T., & Ohyanagi, M.** (2005). Influence of synthesis temperature on the defect structure of boron carbide: experimental and modeling studies. *Journal of the American Ceramic Society*, 88 (6), 1382-1387.
- [104] **Zhang, M., Yuan, T., Li, R., Xie, S., Wang, M., & Weng, Q.** (2018). Densification mechanisms and microstructural evolution during spark plasma sintering of boron carbide powders. *Ceramics International*, 44 (4), 3571-3579.
- [105] **Ma, L., Xie, K. Y., Toksoy, M. F., Kuwelkar, K., Haber, R. A., & Hemker, K. J.** (2017). The effect of Si on the microstructure and mechanical properties of spark plasma sintered boron carbide. *Materials Characterization*, 134, 274-278.
- [106] **Liu, J. A., Zeng, F., Zou, Z., Li, Y., Gu, Y., Zhang, F., & Liang, T.** (2017). Continuum modeling of B₄C densification during Spark Plasma Sintering. *Journal of Materials Research*, 32 (17), 1-9.
- [107] **Kunka, C., Awasthi, A., & Subhash, G.** (2017). Evaluating boron-carbide constituents with simulated Raman spectra. *Scripta Materialia*, 138, 32-34.
- [108] **Innocent, J. L., Portehault, D., Gouget, G., Maruyama, S., Ohkubo, I., & Mori, T.** (2017). Thermoelectric properties of boron carbide/HfB₂ composites. *Materials for Renewable and Sustainable Energy*, 6 (2), 6.
- [109] **Moskovskikh, D. O., Paramonov, K. A., Nepapushev, A. A., Shkodich, N. F., & Mukasyan, A. S.** (2017). Bulk boron carbide nanostructured ceramics by reactive spark plasma sintering. *Ceramics International*, 43 (11), 8190-8194.
- [110] **Belon, R., Antou, G., Pradeilles, N., Maître, A., & Gosset, D.** (2017). Mechanical behaviour at high temperature of spark plasma sintered boron carbide ceramics. *Ceramics International*, 43 (8), 6631-6635
- [111] **Ghasali, E., Alizadeh, M., Niazmand, M., & Ebadzadeh, T.** (2017). Fabrication of magnesium-boron carbide metal matrix composite by powder metallurgy route: Comparison between microwave and spark plasma sintering. *Journal of Alloys and Compounds*, 697, 200-207.
- [112] **Bouchacourt, M., & Thevenot, F.** (1981). The properties and structure of the boron carbide phase. *Journal of the Less Common Metals*, 82, 227-235.
- [113] **Suzuki, H., Hase, T., & Maruyama, T.** (1979). Effect of carbon on sintering of boron carbide. *Yogyo Kyokai-Shi*, 87 (1008), 430-433.
- [114] **Zhang, F., Fu, Z. Y., Zhang, J. Y., Wang, H., Wang, W. M., & Wang, Y. C.** (2009). Reinforcement of B₄C ceramics with multi-walled carbon nanotubes. *Advanced Materials Research*, 66, 41-44.

- [115] **Yadhukulakrishnan, G. B., Rahman, A., Karumuri, S., Stackpoole, M. M., Kalkan, A. K., Singh, R. P., & Harimkar, S. P.** (2012). Spark plasma sintering of silicon carbide and multi-walled carbon nanotube reinforced zirconium diboride ceramic composite. *Materials Science and Engineering: A*, 552, 125-133.
- [116] **Yavas, B., Sahin, F., Yucel, O., & Goller, G.** (2015). Effect of particle size, heating rate and CNT addition on densification, microstructure and mechanical properties of B₄C ceramics. *Ceramics International*, 41 (7), 8936-8944.
- [117] **Chawla, K. K.** (1998). Ceramic matrix composites. In *Composite Materials* (pp. 212-251). Springer New York.
- [118] **Cengiz, M.** (2016). Production and characterization of B₄C based composites from B₄C/Me starting powders by using spark plasma sintering (SPS) method. (Doctoral dissertation). Istanbul Technical University, ISTANBUL.
- [119] **Viala, J. C., Bouix, J., Gonzalez, G., & Esnouf, C.** (1997). Chemical reactivity of aluminium with boron carbide. *Journal of Materials Science*, 32 (17), 4559-4573.
- [120] **Hulbert, D. M., Jiang, D., Anselmi-Tamburini, U., Unuvar, C., & Mukherjee, A. K.** (2008). Continuous functionally graded boron carbide - aluminum nanocomposites by spark plasma sintering. *Materials Science and Engineering: A*, 493 (1), 251-255.
- [121] **Arslan, G., & Kalemtaş, A.** (2009). Processing of silicon carbide–boron carbide–aluminium composites. *Journal of the European Ceramic Society*, 29 (3), 473-480.
- [122] **Xu, C. M., Zeng, H., & Zhang, G. J.** (2013). Pressureless sintering of boron carbide ceramics with Al–Si additives. *International Journal of Refractory Metals and Hard Materials*, 41, 2-6.
- [123] **Kang, P. C., Cao, Z. W., Wu, G. H., Zhang, J. H., Wei, D. J., & Lin, L. T.** (2010). Phase identification of Al–B₄C ceramic composites synthesized by reaction hot-press sintering. *International Journal of Refractory Metals and Hard Materials*, 28 (2), 297-300.
- [124] **Chen, H. S., Wang, W. X., Li, Y. L., Zhang, P., Nie, H. H., & Wu, Q. C.** (2015). The design, microstructure and tensile properties of B₄C particulate reinforced 6061Al neutron absorber composites. *Journal of Alloys and Compounds*, 632, 23-29.
- [125] **Werheit, H., Kuhlmann, U., Laux, M., & Telle, R.** (1994). Solid solutions of silicon in boron-carbide-type crystals. *Journal of alloys and compounds*, 209 (1), 181-187.
- [126] **Sahani, P., Karak, S. K., Mishra, B., Chakravarty, D., & Chaira, D.** (2016). A Comparative Study on SiC–B₄C–Si Cermet Prepared by Pressureless Sintering and Spark Plasma Sintering Methods. *Metallurgical and Materials Transactions A*, 47 (6), 3065-3076.
- [127] **Rehman, S. S., Ji, W., Khan, S. A., Fu, Z., & Zhang, F.** (2015). Microstructure and mechanical properties of B₄C densified by spark plasma sintering with Si as a sintering aid. *Ceramics International*, 41 (1), 1903-1906.

- [128] **Ye, F., Hou, Z., Zhang, H., & Liu, L.** (2010). Densification and mechanical properties of spark plasma sintered B₄C with Si as a sintering aid. *Journal of the American Ceramic Society*, 93 (10), 2956-2959.
- [129] **Feng, B., Martin, H. P., Hempel-Weber, R., & Michaelis, A.** (2012, June). Preparation and thermoelectric properties of B₄C-Si-B composites. In *AIP Conference Proceedings* (Vol. 1449, No. 1, pp. 315-318). AIP
- [130] **Heydari, M. S., & Baharvandi, H. R.** (2015). Comparing the effects of different sintering methods for ceramics on the physical and mechanical properties of B₄C-TiB₂ nanocomposites. *International Journal of Refractory Metals and Hard Materials*, 51, 224-232.
- [131] **Nikzad, L., Orrù, R., Licheri, R., & Cao, G.** (2013). Influence of mechanical and electric current activation on the mechanism of formation and the properties of bulk B₄C-TiB₂ composites obtained by reactive sintering. *Chemical Engineering Transactions*, 32, 1669-1674.
- [132] **Dudina, D. V., Hulbert, D. M., Jiang, D., Unuvar, C., Cytron, S. J., & Mukherjee, A. K.** (2008). In situ boron carbide-titanium diboride composites prepared by mechanical milling and subsequent Spark Plasma Sintering. *Journal of Materials Science*, 43 (10), 3569-3576.
- [133] **Nikzad, L., Licheri, R., Ebadzadeh, T., Orrù, R., & Cao, G.** (2012). Effect of ball milling on reactive spark plasma sintering of B₄C-TiB₂ composites. *Ceramics International*, 38 (8), 6469-6480.
- [134] **Hulbert, D. M., Jiang, D., Dudina, D. V., & Mukherjee, A. K.** (2009). The synthesis and consolidation of hard materials by spark plasma sintering. *International Journal of Refractory Metals and Hard Materials*, 27 (2), 367-375.
- [135] **Uygun, B., Göller, G., Yücel O., & Sahin, F. C.** (2010). Production and characterization of boron carbide-titanium diboride ceramics by spark plasma sintering method. In *Advances in Science and Technology* (Vol. 63, pp. 68-73). Trans Tech Publications.
- [136] **Huang, S. G., Vanmeensel, K., Malek, O. J. A., Van der Biest, O., & Vleugels, J.** (2011). Microstructure and mechanical properties of pulsed electric current sintered B₄C-TiB₂ composites. *Materials science and engineering: A*, 528(3), 1302-1309.
- [137] **Klotz, B. R., Cho, K. C., & Dowding, R. J.** (2004). Sintering aids in the consolidation of boron carbide (B₄C) by the plasma pressure compaction method. *Materials and Manufacturing Processes*, 19 (4), 631-639.
- [138] **Xu, C., Cai, Y., Flodström, K., Li, Z., Esmailzadeh, S., & Zhang, G. J.** (2012). Spark plasma sintering of B₄C ceramics: the effects of milling medium and TiB₂ addition. *International Journal of Refractory Metals and Hard Materials*, 30 (1), 139-144.
- [139] **Çakır, E., Ergun, C., Şahin, F. Ç., & Erden, I.** (2010). In situ synthesis of B₄C/TiB₂ composites from low cost sugar based precursor. In *Defect and Diffusion Forum* (Vol. 297, pp. 52-56). Trans Tech Publications.

- [140] **Skorokhod, V., Vlajić, M. D., & Krstić, V. D.** (1998). Pressureless sintering of B₄C-TiB₂ ceramic composites. In *Materials science forum* (Vol. 282, pp. 219-224). Trans Tech Publications.
- [141] **Baharvandi, H. R., Hadian, A. M., & Alizadeh, A.** (2006). Processing and mechanical properties of boron carbide–titanium diboride ceramic matrix composites. *Applied Composite Materials*, 13(3), 191-198.
- [142] **de Rocha, R. M., & de Melo, F. C. L.** (2012). Effect of TiO₂ and TiB₂ on Pressureless Sintering of B₄C. In *Materials Science Forum* (Vol. 727, pp. 1022-1027). Trans Tech Publications.
- [143] **Huang, S. G., Vanmeensel, K., Van der Biest, O., & Vleugels, J.** (2011). In situ synthesis and densification of submicrometer-grained B₄C–TiB₂ composites by pulsed electric current sintering. *Journal of the European Ceramic Society*, 31(4), 637-644.
- [144] **Yue, X. Y., Zhao, S. M., Yu, L., & Ru, H. Q.** (2010). Microstructures and Mechanical Properties of B₄C-TiB₂ Composite Prepared by Hot Pressure Sintering. In *Key Engineering Materials* (Vol. 434, pp. 50-53). Trans Tech Publications.
- [145] **Wang, Y. J., Peng, H. X., Feng, Y. E., & Yu, Z.** (2011). Effect of TiB₂ content on microstructure and mechanical properties of in-situ fabricated TiB₂/B₄C composites. *Transactions of Nonferrous Metals Society of China*, 21, s369-s373.
- [146] **Skorokhod, V., & Krstic, V. D.** (2000). High strength-high toughness B₄C-TiB₂ composites. *Journal of materials science letters*, 19(3), 237-239.
- [147] **Advanced ceramic powders.** (2017). Retrieved December 04, 2017, from https://www.hcstarck.com/hcadmin/file/8a8181e225548334012554ce05db17e4.de.0/advanced_ceramicpowder_03_%202017.pdf;jsessionid=43182EDB4222152B477BAE79BC27F725.s2
- [148] **Multiwalled carbon nanotubes.** (2018). Retrieved January 05, 2018, from <https://polymer-additives.specialchem.com/product/a-carbon-ntf-21-carbon-nt-f-21-mt-mw-010-020>.
- [149] **Mitsubishi Carbon Black.** (2017). Retrieved December 05, 2017 from http://www.carbonblack.jp/en/product/list1_04.html#05.
- [150] **Wissler, M.** (2006). Graphite and carbon powders for electrochemical applications. *Journal of Power Sources*, 156(2), 142-150.
- [151] **Malvern Zetasizer Product.** (2017). Retrieved December 05, 2017 from <https://www.malvern.com/en/products/product-range/zetasizer-range/zetasizer-nano-range>.
- [152] **Lankford, J.** (1982). Indentation microfracture in the Palmqvist crack regime: implications for fracture toughness evaluation by the indentation method. *Journal of Materials Science Letters*, 1 (11), 493-495.
- [153] **Strecker, K., Ribeiro, S., & Hoffmann, M. J.** (2005). Fracture toughness measurements of LPS-SiC: a comparison of the indentation technique and the SEVNB method. *Materials Research*, 8 (2), 121-124.

- [154] *Ballistic resistance of personal body armor*. (2008). NIJ Standard–0101.06: National Institute of standards and technology.
- [155] **Demir, T., Übeyli, M., & Yıldırım, R. O.** (2008). Investigation on the ballistic impact behavior of various alloys against 7.62 mm armor piercing projectile. *Materials & Design*, 29 (10), 2009-2016.
- [156] **Apak, B., & Sahin, F. C.** (2015). C-CNT Produced by Spark Plasma Sintering. *Acta Physica Polonica A*, 127 (4), 1029-1031.
- [157] **Yamamoto, G., Omori, M., Yokomizo, K., & Hashida, T.** (2008). Mechanical properties and structural characterization of carbon nanotube/alumina composites prepared by precursor method. *Diamond and Related Materials*, 17(7), 1554-1557.
- [158] **Munoz, S., & Anselmi-Tamburini, U.** (2010). Temperature and stress fields evolution during spark plasma sintering processes. *Journal of Materials Science*, 45 (23), 6528-6539.
- [159] **Lagrenaudie, J.** (1953). A Study of the Properties of Boron. *J. Phys.-Paris*, 14, 14–18.
- [160] **Werheit, H.** (2006). On excitons and other gap states in boron carbide. *Journal of Physics: Condensed Matter*, 18 (47), 10655-10662.
- [161] **Dekura, H., Shirai, K., & Yanase, A.** (2010). Metallicity of boron carbides at high pressure. *Journal of Physics: Conference Series*, 215, (1) 012117.
- [162] **Kim, K. T., Cha, S. I., Hong, S. H., & Hong, S. H.** (2006). Microstructures and tensile behavior of carbon nanotube reinforced Cu matrix nanocomposites. *Materials Science and Engineering: A*, 430 (1), 27-33.
- [163] **Kim, K. T., Cha, S. I., & Hong, S. H.** (2007). Hardness and wear resistance of carbon nanotube reinforced Cu matrix nanocomposites. *Materials Science and Engineering: A*, 449, 46-50.
- [164] **Lahiri, D., Singh, V., Keshri, A. K., Seal, S., & Agarwal, A.** (2010). Carbon nanotube toughened hydroxyapatite by spark plasma sintering: microstructural evolution and multiscale tribological properties. *Carbon*, 48 (11), 3103-3120.
- [165] **Cha, S. I., Kim, K. T., Lee, K. H., Mo, C. B., & Hong, S. H.** (2005). Strengthening and toughening of carbon nanotube reinforced alumina nanocomposite fabricated by molecular level mixing process. *Scripta Materialia*, 53 (7), 793-797.
- [166] **German, R. M., Suri, P., & Park, S. J.** (2009). liquid phase sintering. *Journal of materials science*, 44 (1), 1-39.
- [167] **Frage, N., Hayun, S., Kalabukhov, S., & Dariel, M. P.** (2007). The effect of Fe addition on the densification of B₄C powder by spark plasma sintering. *Powder Metallurgy and Metal Ceramics*, 46 (11), 533-538.
- [168] **Panasyuk, A. D., Oreshkin, V. D., & Maslennikova, V. R.** (1979). Kinetics of the reactions of boron carbide with liquid aluminum, silicon, nickel, and iron. *Powder Metallurgy and Metal Ceramics*, 18 (7), 487-490.

- [169] **Wells, J. M.** (2007). Progress in the nondestructive analysis of impact damage in TiB₂ armor ceramics. *Advances in Ceramic Armor II: Ceramic Engineering and Science Proceedings*, 27 (7) 198-209.
- [170] **Rodriguez, S., Munoz, V. B., Esquivel, E. V., Murr, L. E., & Rupert, N. L.** (2002). Microstructural characterization of TiB₂ armor targets. *Journal of materials science letters*, 21 (21), 1661-1666.
- [171] **Wells, J. M., Rupert, N. L., & Green, W. H.** (2002). Progress in the 3-D visualization of interior ballistic damage in armor ceramics. *Ceramic transactions*, 134, 441-450.
- [172] **Gupta, N., Basu, B., Prasad, V. B., & Vemuri, M.** (2012). Ballistic studies on TiB₂-Ti functionally graded armor ceramics. *Defence Science Journal*, 62 (6), 382-389.
- [173] **Kang, E. S., & Kim, C. H.** (1990). Improvements in mechanical properties of TiB₂ by the dispersion of B₄C particles. *Journal of Materials Science*, 25 (1), 580-584.
- [174] **Heydari, M. S., & Baharvandi, H. R.** (2015). Effect of different additives on the sintering ability and the properties of B₄C–TiB₂ composites. *International Journal of Refractory Metals and Hard Materials*, 51, 61-69.
- [175] **Baharvandi, H. R., & Hadian, A. M.** (2008). Pressureless sintering of TiB₂-B₄C ceramic matrix composite. *Journal of Materials Engineering and Performance*, 17 (6), 838-841.
- [176] **Levin, L., Frage, N., & Dariel, M. P.** (1999). The effect of Ti and TiO₂ additions on the pressureless sintering of B₄C. *Metallurgical and Materials Transactions A*, 30(12), 3201-3210.
- [177] **Skorokhod, V. V.** (2000). Processing, Microstructure, and Mechanical Properties of B₄C–TiB₂ Particulate Sintered Composites. Part I. Pressureless Sintering and Microstructure Evolution. *Powder Metallurgy and Metal Ceramics*, 39 (7), 414-423.
- [178] **Skorokhod, V. V.** (2000). Processing, Microstructure, and Mechanical Properties of B₄C–TiB₂ Particulate Sintered Composites. Part II. Fracture and Mechanical Properties. *Powder Metallurgy and Metal Ceramics*, 39 (9), 504-513.
- [179] **Hirota, K., Nakayama, Y., Kato, M., Nakane, S., & Nishimura, T.** (2009). The Study on Carbon Nanofiber (CNF)-Dispersed B₄C Composites. *International Journal of Applied Ceramic Technology*, 6 (5), 607-616.
- [180] **Yavas, B.** (2014). Production and Characterization of Monolithic and Reinforced Boroncarbide Ceramics Prepared by Spark Plasma Sintering (SPS) (Master of Science dissertation). Istanbul Technical University, ISTANBUL.
- [181] **Bhattacharya, A. K., & Petrovic, J. J.** (1992). Ductile phase toughening and R-curve behaviour in a B₄C-Al cermet. *Journal of Materials Science*, 27 (8), 2205-2210.

- [182] **Mashhadi, M., Taheri-Nassaj, E., & Sglavo, V. M.** (2010). Pressureless sintering of boron carbide. *Ceramics International*, 36 (1), 151-159.
- [183] **Moshtaghion, B. M., Cumbreira-Hernández, F. L., Gómez-García, D., de Bernardi-Martín, S., Domínguez-Rodríguez, A., Monshi, A., & Abbasi, M. H.** (2013). Effect of spark plasma sintering parameters on microstructure and room-temperature hardness and toughness of fine-grained boron carbide (B_4C). *Journal of The European Ceramic Society*, 33 (2), 361-369.
- [184] **Abzianidze, T. G., Eristavi, A. M., & Shalamberidze, S. O.** (2000). Strength and creep in boron carbide (B_4C) and aluminum dodecaboride ($\alpha-AlB_{12}$). *Journal of Solid State Chemistry*, 154 (1), 191-193.
- [185] **Sairam, K., Sonber, J. K., Murthy, T. C., Subramanian, C., Fotedar, R. K., Nanekar, P., & Hubli, R. C.** (2014). Influence of spark plasma sintering parameters on densification and mechanical properties of boron carbide. *International Journal of Refractory Metals and Hard Materials*, 42, 185-192.
- [186] **Wei, H. K., Zhang, Y. J., & Gong, H. Y.** (2009). Preparation and characteristics of multiwalled carbon nanotubes reinforced boron carbide composites. *Materials Research Innovations*, 13 (1), 70-73.
- [187] **Hulbert, D. M., Jiang, D., Anselmi-Tamburini, U., Unuvar, C., & Mukherjee, A. K.** (2008). Experiments and modeling of spark plasma sintered, functionally graded boron carbide–aluminum composites. *Materials Science and Engineering: A*, 488 (1), 333-338.
- [188] **Jannotti, P., Subhash, G., Zheng, J. Q., Halls, V., Karandikar, P. G., Salamone, S., & Aghajanian, M. K.** (2015). Raman spectroscopic characterization of the core-rim structure in reaction bonded boron carbide ceramics. *Applied Physics Letters*, 106 (4), 041903.
- [189] **Mamedov, V.** (2002). Spark plasma sintering as advanced PM sintering method. *Powder Metallurgy*, 45 (4), 322-328.
- [190] **Deng, J., Zhou, J., Feng, Y., & Ding, Z.** (2002). Microstructure and mechanical properties of hot-pressed $B_4C/(W,Ti)C$ ceramic composites. *Ceramics international*, 28 (4), 425-430.
- [191] **Meyers, M. A.** (1994). *Dynamic behavior of materials*. United States: John Wiley & Sons.
- [192] **Savio, S. G., Ramanjaneyulu, K., Madhu, V., & Bhat, T. B.** (2011). An experimental study on ballistic performance of boron carbide tiles. *International Journal of Impact Engineering*, 38 (7), 535-541.
- [193] **Medvedovski, E.** (2010). Ballistic performance of armour ceramics: Influence of design and structure. Part 1. *Ceramics International*, 36 (7), 2103-2115.
- [194] **Gao, Y., Etzold, A., Munhollon, T., Rafaniello, W., & Haber, R.** (2016). Processing factors influencing the free carbon contents in boron carbide powder by rapid carbothermal reduction. *Diamond and Related Materials*, 61, 14-20.

- [195] **Karandikar, P. G., Evans, G., Wong, S., Aghajanian, M. K., & Sennett, M.** (2009). A review of ceramics for armor applications. *Adv. Ceram Armor IV Ceram Eng Sci Proc*, 29 (6), 163-75.
- [196] **Hallam, D., Heaton, A., James, B., Smith, P., & Yeomans, J.** (2015). The correlation of indentation behaviour with ballistic performance for spark plasma sintered armour ceramics. *Journal of the European Ceramic Society*, 35 (8), 2243-2252.
- [197] **Holmquist, T. J., & Johnson, G. R.** (2006). Characterization and evaluation of boron carbide for plate-impact conditions. *Journal of applied physics*, 100 (9), 093525.
- [198] **Johnson, G. R., & Holmquist, T. J.** (1999). Response of boron carbide subjected to large strains, high strain rates, and high pressures. *Journal of Applied Physics*, 85 (12), 8060-8073.
- [199] **Grady, D. E.** (1980). Shock deformation of brittle solids. *Journal of Geophysical Research: Solid Earth*, 85 (12), 913-924.
- [200] **Grady, D. E.** (1998). Shock-wave compression of brittle solids. *Mechanics of Materials*, 29 (3), 181-203.
- [201] **Chen, M., McCauley, J. W., & Hemker, K. J.** (2003). Shock-induced localized amorphization in boron carbide. *Science*, 299 (5612), 1563-1566.
- [202] **Mashimo, T., & Uchino, M.** (1997). Heterogeneous free-surface profile of B₄C polycrystal under shock compression. *Journal of Applied Physics*, 81 (10), 7064-7066.
- [203] **Reinhart, W. D., Vogler, T. J., & Chhabildas, L. C.** (2003). Dynamic behavior of boron carbide. *Journal of Applied Physics*, 95 (8), 4173-4183.
- [204] **Lavrenko, V. A., & Gogotsi, Y. G.** (1988). Influence of oxidation on the composition and structure of the surface layer of hot-pressed boron carbide. *Oxidation of metals*, 29 (3), 193-202.
- [205] **Lavrenko, V. A., Pomytkin, A. P., Kislyj, P. S., & Grabchuk, B. L.** (1977). Kinetics of high-temperature oxidation of boron carbide in oxygen. *Oxidation of Metals*, 10 (2), 85-95.
- [206] **Moore, D. M., & Reynolds, R. C.** (1989). *X-ray Diffraction and the Identification and Analysis of Clay Minerals* (Vol. 378, p. 155). Oxford: Oxford university press.
- [207] **Ge, D., Domnich, V., Juliano, T., Stach, E. A., & Gogotsi, Y.** (2004). Structural damage in boron carbide under contact loading. *Acta Materialia*, 52 (13), 3921-3927.
- [208] **Yan, X. Q., Tang, Z., Zhang, L., Guo, J. J., Jin, C. Q., Zhang, Y., ... & Chen, M. W.** (2009). Depressurization amorphization of single-crystal boron carbide. *Physical review letters*, 102 (7), 075505.
- [209] **Jung, C. H., Lee, M. J., & Kim, C. J.** (2004). Preparation of carbon-free B₄C powder from B₂O₃ oxide by carbothermal reduction process. *Materials letters*, 58 (5), 609-614.

- [210] **Palfey, W.** (2000). *The mechanical response of boron carbide-aluminum composites during compressive loading* (No. LA-UR-00-3408). Los Alamos National Lab., NM (US).
- [211] **Mashhadi, M., Taheri-Nassaj, E., Sglavo, V. M., Sarpoolaky, H., & Ehsani, N.** (2009). Effect of Al addition on pressureless sintering of B₄C. *Ceramics International*, 35 (2), 831-837.
- [212] **Arslan, G., Kara, F., & Turan, S.** (2003). Quantitative X-ray diffraction analysis of reactive infiltrated boron carbide–aluminium composites. *Journal of the European Ceramic Society*, 23 (8), 1243-1255.
- [213] **Gao, Y., Huang, Z., Fang, M., Liu, Y. G., Huang, S., & Ouyang, X.** (2012). Synthesis of Al₈B₄C₇ ceramic powder from Al/B₄C/C mixtures. *Powder Technology*, 226, 269-273.
- [214] **Suvorov, S. A., Musevich, V. A., & Iksanov, F. R.** (2007). Carbonated pericalse refractories with functional additives. *Refractories and Industrial Ceramics*, 48 (2), 133-137.
- [215] **Cui, P., Yuan, W. J., Deng, C. J., Zhu, H. X., & Li, J.** (2013). Synthesis of Al₈B₄C₇ from Aluminum, Boron Trioxide and Activated Carbon Mixed Powders. In *Advanced Materials Research* (Vol. 634, pp. 2383-2387). Trans Tech Publications.
- [216] **Subhash, G., Ghosh, D., Blaber, J., Zheng, J. Q., Halls, V., & Masters, K.** (2013). Characterization of the 3-D amorphized zone beneath a Vickers indentation in boron carbide using Raman spectroscopy. *Acta Materialia*, 61 (10), 3888-3896.
- [217] **Dandekar, D. P.** (2001). *Shock response of boron carbide* (No. ARL-TR-2456). Army Research Lab Aberdeen Proving Ground Md.
- [218] **Telle, R., & Petzow, G.** (1986). Mechanisms in the liquid phase sintering of boron carbide with silicon based melts. *High Tech Ceramics.(Part A)*, 961-973.
- [219] **Sarin, V.** (2014). *Comprehensive hard materials*. Newnes: New York, US.

CURRICULUM VITAE



Name Surname : Burcu APAK GÜLSEVER

Place and Date of Birth : Istanbul, 21.01.1988

E-Mail : apakb@itu.edu.tr

EDUCATION :

- B.Sc. : 2009, Istanbul Technical University, Faculty of Chemical and Metallurgical Engineering, Metallurgical and Materials Engineering Department.
- M.Sc. : 2011, Istanbul Technical University, Graduate School of Science Engineering and Technology, Production Metallurgy and Technologies Department.
- M.Sc. : 2015, University of Warwick, Warwick Manufacturing Group, WMG, Engineering Business Management.

PROFESSIONAL EXPERIENCE:

- December 2011 – September 2017: Research and Teaching Assistant in Istanbul Technical University, Faculty of Chemical and Metallurgical Engineering, Metallurgical and Materials Engineering Department 34469 Maslak/Istanbul.
- May 2010 – November 2012: Project Assistant in TUBITAK Project coded 109M584, ITU Prof. Dr. Adnan Tekin Materials Sciences and Production Technologies Applied Research Center 34469 Maslak/Istanbul.

PUBLICATIONS, PRESENTATIONS AND PATENTS ON THE THESIS:

- Apak B., Sahin F., “B₄C-CNT produced by Spark Plasma Sintering”, Acta Physica Polonica A Volume 127, Issue 4, 1 April 2015, Pages 1029-1031. (Article Published in International Peer-Review Periodicals (SCI)).
- Apak B., Goller G., Yucel O., Sahin F., “The Effects of Additives on Ballistic Performance of the Spark Plasma Sintered Boron Carbide Ceramics”, IMMC

2016 Proceeding Book, pp:129-133, (Paper Submitted to International Meetings and Published in Proceeding Books).

- Apak B., Goller G., Yucel O., Sahin F., “Light weight metallic additive effect on ballistic performance of spark plasma sintered B₄C”, ECERS 2017 Abstract Book, p. 16. (Abstract Submitted to International Meetings and Published in Proceeding Books).
- Guney B., Sara R., Ersan F.D., Apak B., Karadayi I. A., Goller G., Yucel O., Sahin F.C., Fracture toughness properties of spark plasma sintered boron carbide ceramics using Ti and TiO₂, ECERS 2017 Abstract Book, p. 106. (Abstract Submitted to International Meetings and Published in Proceeding Books).
- Sahin F., Apak B., Cengiz M., Yavas B., Özer S.C. , Göller G., Yücel O. ,Turan S., Balazsi K., B₄C based ceramic composites prepared by spark plasma sintering, ECERS 2017 Abstract Book, p. 628. (Abstract Submitted to International Meetings and Published in Proceeding Books).

OTHER PUBLICATIONS, PRESENTATIONS AND PATENTS:

- Sahin F. C., Kanbur H. E., Apak B., “Preparation of AlON ceramics via reactive spark plasma sintering”, Journal of the European Ceramic Society 32 (2012) 925–929. (Article Published in International Peer-Review Periodicals (SCI))
- Sahin F.C., Apak B., Akin I., Kanbur H., Genckan D., Turan A., Goller G., Yucel O., “Spark plasma sintering of B₄C- SiC composites”, Volume 14, Issues 11–12, November 2012, Pages 1660–1663. (Article Published in International Peer-Review Periodicals (SCI))
- Apak B., Kanbur H.E., Zayim E. O., Goller G., Yucel O., Sahin F.C., “Transparent Polycrystalline Alumina Obtained by SPS: Single and Double Doping Effect”, TMS 2012. (Paper Submitted to International Meetings and Published in Proceeding Books).
- Apak B., Kanbur H.E., Zayim E. O., Sahin F.C., “Dopant Effects on Transparent Alumina by Spark Plasma Sintering”, Proceedings of the 12th Conference of the European Ceramic Society – ECerS XII Stockholm, Sweden – 2011. (Paper Submitted to International Meetings and Published in Proceeding Books).
- Kanbur H. E., Apak B., Sahin F.C., “AlON Ceramics Prepared by Spark Plasma Sintering”, Proceedings of the 12th Conference of the European Ceramic Society – ECerS XII Stockholm, Sweden – 2011. (Paper Submitted to International Meetings and Published in Proceeding Books).
- Apak B., Goller G., Yucel O., Sahin F.C., “Nano boyuttaki Al₂O₃ Seramiklerinin Spark Plazma Sinterleme Yöntemi ile Üretimi”, 15th International Metallurgy and Materials Congress, pp. 2252-2258 (2010). (Paper Submitted to International Meetings and Published in Proceeding Books).
- Apak B., Goller G., Yucel O., Sahin F.C., “The effects of codoping Y₂O₃ on MgO doped Spark Plasma Sintered Al₂O₃”, Advances in Science and Technology Vol. 63 (2010) pp 74-78, 12th International Ceramic Congress CIMTEC, Haziran 2010, Montecatini Terme/İtalya. (Paper Submitted to International Meetings and Published in Proceeding Books).

- Apak B., Goller G., Yucel O., Sahin F.C., “The effects of heating rate on magnesia doped alumina prepared by SPS”, 34th International Conference and Exposition on Advanced Ceramics and Composites, pp. 3-8, Daytona Beach, FL/ABD, 2010. (Paper Submitted to International Meetings and Published in Proceeding Books).
- Apak B., Zayim E. O., Goller G., Yucel O., Sahin F.C., “Transparent polycrystalline alumina prepared by spark plasma sintering”, ECERS, 13th Conference of the European Ceramic Society Abstract Book, p. 200. (Abstract Submitted to International Meetings and Published in Proceeding Books)
- Apak B., Turan A., Kanbur H.E., Uygun B., Celik Y., Genckan D., Goller G., Yucel O., Sahin F. C., “A General Investigation of Boron Compounds Densified by Spark Plasma Sintering”, 17th International Symposium on Boron, Borides and Related Materials Abstract Book, p. 138-139, 2011. (Abstract Submitted to International Meetings and Published in Proceeding Books).
- Apak B., Balazsi C., Horvath A., Şahin F.C., Göller G., Yücel O., “Preparation of FeB added ODS steels”, 17th International Symposium on Boron, Borides and Related Materials Abstract Book, p. 126, 2011. (Abstract Submitted to International Meetings and Published in Proceeding Books).

